

DISS. ETH NO. 23431

Protein structure determination and methods
development for Solid - State NMR

A thesis submitted to attain the degree of
DOCTOR OF SCIENCES of ETH ZURICH
(Dr. sc. ETH Zurich)

presented by
FRANCESCO RAVOTTI
Physics University of Turin

born on 13.05.1985

Citizen of
Italy

Accepted on the recommendation of

Prof. Dr. Beat H. Meier

Prof. Dr. Roland Riek

Dr. Anja Böckmann

2016

Contents

Abbreviations	5
Abstract	6
Sommario	8
1 General introduction	11
1.1 Interactions in solid - state NMR	11
1.2 Recoupling techniques in solid - state NMR	13
1.3 Sequential assignment	15
I Structure Calculation	16
2 Structure determination of the Amyloid β (1-42) fibril	17
2.1 Introduction	17
2.2 Results and discussion	18
2.2.1 Screening of conditions	18
2.2.2 Sequential assignment	20
2.2.3 Secondary structure determination	25
2.2.4 Distance restraints spectra	28
2.2.5 Mass-per-length measurement	30
2.2.6 The 3D structure of A β (1-42) fibril	32
2.3 Conclusions	39
2.4 Experimental Methods	40
2.4.1 Expression and purification	40
2.4.2 Rotor filling	41
2.4.3 Solid - state NMR spectroscopy	41
2.4.4 Structure calculation	41
3 Structure determination of the mouse ASC-PYD filament	47
3.1 Introduction	47
3.1.1 Biological context	48

3.2	Results and discussion	48
3.2.1	NMR screening of the filaments	48
3.2.2	Sequential assignment	52
3.2.3	Secondary structure determination	59
3.2.4	Distance restraints spectra	61
3.2.5	Structure calculation of the mouse ASC - PYD filament	62
3.2.6	The structure of mouse ASC filament	69
3.2.7	The CARD domain	74
3.3	Conclusions	76
3.4	Experimental methods	76
3.4.1	Expression and purification	76
3.4.2	Rotor filling	77
3.4.3	Solid - state NMR spectroscopy	77
II	Methods development for solid - state NMR	80
4	Higher resolution ^{13}C spectra by removing the J - couplings	81
4.1	Introduction	81
4.2	Theoretical background	82
4.2.1	The S^3E building block	83
4.2.2	The DS^3E building block	86
4.3	Results and discussion	91
4.3.1	Sequence optimization	91
4.3.2	Applications of S^3E and DS^3E	96
4.4	Conclusions	110
4.5	Experimental methods	110
4.5.1	Sample preparation	110
4.5.2	Solid - state NMR spectroscopy	111
5	Applications of TEDOR sequence	113
5.1	Introduction	113
5.2	Theoretical background	114
5.3	Results and discussion	119
5.3.1	^1H detected TEDOR	119
5.3.2	Intermolecular restraints	124
5.4	Conclusions	133
5.5	Experimental methods	133
5.5.1	Sample preparation	133
5.5.2	Solid - state NMR spectroscopy	134

III	Conclusions and Outlook	135
	Appendix	139
A	Structure determination of the Amyloid β (1-42) fibril	139
A.1	Screening of conditions	139
A.2	Dot blot measurement	141
A.3	Chemical shifts comparison	142
A.4	H/D exchange	145
A.5	Dilution analysis	147
A.6	Limited proteolysis	148
B	Methods development	150
B.1	Selective π pulses optimization	150
B.2	Comparison of ^{13}C and ^{15}N MISSISSIPI experiment	152
B.3	Assignment of ^2H - 100% back - exchanged HET-s(218-289)	152
	Curriculum Vitae	161

Abbreviations

1D	one-dimensional
2D	two-dimensional
3D	three-dimensional
CP	cross-polarisation
AD	Alzheimer's disease
A β	amyloid beta
APP	amyloid precursor protein
AHT	average Hamiltonian theory
CP	cross polarization
CS	chemical shift
CSA	chemical shift anisotropy
DCP	double cross-polarization
EM	electron microscopy
FL	full length
HD	hydrogen/deuterium
INEPT	insensitive nuclei enhanced by polarization transfer
MAS	magic angle spinning
MPL	mass-per-length
MQ	multiple - quantum
MW	molecular weight
MW _{Theor}	theoretical molecular weight
NA	natural abundance
NS	number of scans
NMR	nuclear magnetic resonance
OD	optical density
REDOR	rotational-echo double-resonance
RF	radio frequency
STEM	scanning transmission electron microscopy
TEDOR	transferred-echo double-resonance
TSAR	third spin assisted recoupling
UL	uniformly labeled
upl	upper distance limit
w/v	weight over volume

Abstract

Proteins are large macromolecules consisting in one or more chains of amino acids. Their role is of great importance in cells, accomplishing specific tasks which are coded in the genes. To understand the function of a protein, knowing its 3D structure is a key point. Solid - state NMR provides powerful techniques that can be applied to determine the structure of protein fibrils and protein complexes that cannot be solved with standards methods, as X - ray crystallography and solution - state NMR. In fact, solid - state NMR does not require the protein to form nice crystal for diffraction or high solubility of the sample.

Structure calculation based on NMR data combines chemical information from the sample (amino acid sequence, bond length and bond angles) with restraints and constraints derived from experimental data. The most commonly used classes of constraints and restraints are torsion angle restraints and distance restraints and constraints. These data can be obtained from the analysis of solid - state NMR spectra.

In the first part of the thesis we present two examples of applications of solid - state NMR methods for protein structure determination. In Chapter 1 we present the structure of the Amyloid β (1 - 42) fibrils. This protein belongs to the amyloid fibrils family, which play a role in different neurodegenerative diseases, including Alzheimer's disease. Firstly, we obtained the chemical shifts of the fibrils from 2D and 3D spectra. These spectra show a well formed fibrils, with ^{13}C line width in the order of 0.5 ppm. We identified the presence of 5 β - strands in the protein and we deduced the parallel in - register β sheets architecture. The stretch of residues 11 - 14 are not rigid and invisible in solid state NMR spectra, therefore we calculated the structure of the rigid part of the protein (residues 15 - 42).

In Chapter 2 we introduced a new hybrid approach that combines solid - state NMR methods with cryo - electron microscopy data. We described this method and applied it for the structure determination of the filaments composed by the PYRIN domain of the mouse ASC protein. The two techniques provide complementary information, leading to an overall comprehensive description extending beyond the power and resolution of cryo - EM or solid - state NMR alone. In the first step of this approach, we used the dihedral angle restraints obtained from solid - state NMR together with the structural information of the cryo - EM density map. This led to a well converged structure of the backbone. To increase the precision of this approach, we refined the initial structure

adding solid - state NMR distance restraints and distance constraints. These two final steps were important to obtain more information on the side chains position.

In the second part of the thesis, we proposed two new approaches that can be applied in solid - state NMR, efficient in the fast MAS regime. In this regime, the main factor that limits resolution in ^{13}C spectra is the presence of the homonuclear J - coupling. This interaction is challenging to remove during the detection of the NMR signal. In Chapter 3 we discuss the applications of a family of J - decoupling sequences, the Spin State Selective Excitation, to obtain high resolution ^{13}C spectra. We present here possible applications of these sequences to obtain highly resolved correlation spectra that can be used for the assignment of proteins backbone atoms.

In Chapter 4 we present a new approach to obtain highly resolved ^{15}N - ^{13}C intermolecular correlations. These correlations can be used in structure determination of proteins as source of information on the stacking of the monomers. The 3D TEDOR experiment we performed combined information on long range inter molecular ^{15}N - ^{13}C contacts with a intra residue ^{15}N - ^1H correlations. The strong restriction that the ^{15}N and ^1H have to belong to the same residue allowed to dramatically reduce the ambiguities of the inter molecular ^{15}N - ^{13}C constraints, which is usually a limiting factor in distance restraints experiment. We have used the so-obtained correlations in an automatic structure calculation of the HET-s fibrils.

Sommario

Le proteine sono grosse macromolecole, consistenti in una o più catene di amino acidi. Il loro ruolo è di fondamentale importanza nelle cellule, svolgendo compiti specifici che sono codificati nei geni. Per determinare la funzione di una proteina, la conoscenza della sua struttura in 3D è un punto fondamentale. RMN stato solido fornisce potenti tecniche che possono essere applicate per determinare la struttura di fibrille e complessi di proteine che non possono essere determinate con metodi standard, come cristallografia a raggi X e RMN stato liquido. Infatti, RMN stato solido non richiede che la proteina formi cristalli per la cristallografia e non richiede una sua alta solubilità.

Il calcolo di strutture basato su dati da RMN combina informazioni chimiche del campione (sequenza di amino acidi, lunghezze dei legami e angoli dei legami) con vincoli ottenute da dati sperimentali. Le classi più comuni di vincoli sono su angoli di torsione e vincoli di distanza. Questi dati possono essere ottenuti dall'analisi degli spettri di RMN stato solido.

Nella prima parte della tesi, presentiamo due esempi di applicazioni di metodi da RMN stato solido per la determinazione di strutture di proteine. Nel Capitolo 1 presentiamo la struttura delle fibrille dell'amiloide β (1 - 42). Questa proteina risiede nella famiglia di fibrille amiloidi che giocano un ruolo nelle malattie neurodegenerative, come la sindrome di Alzheimer. In primo luogo abbiamo ottenuto gli spostamenti chimici (chemical shifts) delle fibrille da spettri in 2D e in 3D. Questi spettri presentano fibrille ben formate con una linea spettrale di 0.5 ppm. Abbiamo identificato la presenza di 5 fogli β nella proteina e abbiamo dedotto la struttura parallela in β -registrata di fogli β . I residui tra 11 - 14 non sono rigidi e sono invisibili negli spettri di RMN stato solido, dunque abbiamo calcolato la struttura della parte rigida della proteina (residui 15 - 42).

Nel Capitolo 2 abbiamo introdotto un nuovo approccio ibrido che combina metodi di RMN stato solido con dati di crio - microscopia elettronica. Abbiamo descritto questo metodo e applicato per la determinazione di struttura dei filamenti composti dal dominio PYRIN della proteina ASC del topo. Le due tecniche forniscono informazioni complementari, portando a una descrizione di insieme che va oltre il potere di risoluzione della singola crio - microscopia elettronica o di RMN stato solido. Nel primo passo di questo approccio, abbiamo usato i vincoli per gli angoli diedri ottenuti da RMN stato solido con le informazioni strutturali della densità elettronica della crio - microscopia elettronica. Questo ha portato a una struttura convergente della catena dorsale (backbone). Per

aumentare la precisione di questo approccio, abbiamo rifinito la struttura iniziale aggiungendo vincoli di distanza da RMN stato solido. Questi due passi finali sono importanti per ottenere più informazioni sulla posizione delle catene laterali.

Nella seconda parte della tesi, abbiamo proposto due nuovi approcci che possono essere applicati nella RMN stato solido, efficienti nel regime di MAS veloce. In questo regime, il fattore principale che limita la risoluzione negli spettri di ^{13}C è la presenza del accoppiamento J omonucleare. Questa interazione è complessa da rimuovere durante la detezione del segnale di RMN. Nel Capitolo 3 discutiamo le applicazioni di una famiglia di sequenze per il disaccoppiamento J durante l'acquisizione in spettri di ^{13}C , le sequenze di eccitazione selettiva di stati di spin. Presentiamo qui possibili applicazioni di queste sequenze per ottenere spettri di correlazione ad alta risoluzione che possono essere usati per l'assegnazione di atomi del bacbone delle proteine.

Nel Capitolo 4 presentiamo un nuovo approccio per ottenere correlazioni intermolecolari tra ^{15}N - ^{13}C ad alta risoluzione. Queste correlazioni possono essere usate per il calcolo di strutture di proteine come una sorgente di informazioni sulla simmetria dei monomeri. L'esperimento in 3D TEDOR che abbiamo misurato combina informazioni su contatti a lunga distanza fra differenti molecole di ^{15}N - ^{13}C con correlazioni nello stesso residuo di ^{15}N - ^1H . La stringente restrizione che il ^{15}N e il ^1H debbano appartenere allo stesso residuo ha permesso di ridurre drasticamente le ambiguità dei vincoli intermolecolari tra ^{15}N - ^{13}C , che solitamente rappresenta un fattore limitante negli esperimenti di vincoli di distanza. Abbiamo utilizzato le correlazioni così ottenute in un calcolo di struttura automatico delle fibrille del HET-s.

Chapter 1

General introduction

1.1 Interactions in solid - state NMR

The relevant interactions for a spin-1/2 can be described with a Hamiltonian

$$\hat{\mathcal{H}} = \hat{\mathcal{H}}_Z + \hat{\mathcal{H}}_{CS} + \hat{\mathcal{H}}_{RF} + \hat{\mathcal{H}}_D + \hat{\mathcal{H}}_J. \quad (1.1)$$

where $\hat{\mathcal{H}}_Z$ is the Zeeman Hamiltonian, which describes the interaction of the spins with the static magnetic field B_0 , $\hat{\mathcal{H}}_{RF}$ is the radio frequency (RF) Hamiltonian, which describes the interaction of the spins with an applied RF field, $\hat{\mathcal{H}}_{CS}$ is the chemical shift (CS) Hamiltonian, $\hat{\mathcal{H}}_D$ is the dipolar coupling Hamiltonian, which describes the through space interactions between spins and $\hat{\mathcal{H}}_J$ is the isotropic J-coupling Hamiltonian, which describes the interaction mediated by binding electrons. The CS Hamiltonian, $\hat{\mathcal{H}}_{CS}$, can be written as

$$\begin{aligned} \hat{\mathcal{H}}_{CS} &= - \sum_k \gamma_k \hat{I}_k \underline{\sigma}_k \vec{B}_0 = \\ &= \sum_k \gamma_k (\hat{I}_{kx}, \hat{I}_{ky}, \hat{I}_{kz}) \begin{pmatrix} \sigma_{xx}^{(k)} & \sigma_{xy}^{(k)} & \sigma_{xz}^{(k)} \\ \sigma_{yx}^{(k)} & \sigma_{yy}^{(k)} & \sigma_{yz}^{(k)} \\ \sigma_{zx}^{(k)} & \sigma_{zy}^{(k)} & \sigma_{zz}^{(k)} \end{pmatrix} \begin{pmatrix} 0 \\ 0 \\ B_0 \end{pmatrix}. \end{aligned} \quad (1.2)$$

Here γ_k is the gyromagnetic ratio of the nucleus k , \hat{I}_k represents the nuclear spin angular momentum operator and $\underline{\sigma}_k$ is the chemical-shift tensor. The anisotropy δ of the tensor is defined by

$$\delta = \sigma_{zz}^{(k)} - \bar{\sigma}, \quad (1.3)$$

where $\bar{\sigma}$ is the trace of the tensor. The asymmetry η is given by

$$\eta = \frac{\sigma_{yy}^{(k)} - \sigma_{xx}^{(k)}}{\delta}. \quad (1.4)$$

The CS observed in the spectrum depends therefore on the orientation of the chemical shift tensor with respect to the external magnetic field.

The dipolar coupling Hamiltonian, $\hat{\mathcal{H}}_D$, can be written as

$$\hat{\mathcal{H}}_D = \sum_{ij, i < j} d_{i,j} \left(2\hat{I}_{iz}\hat{I}_{jz} - \frac{1}{2}(\hat{I}_i^+\hat{I}_j^- + \hat{I}_i^-\hat{I}_j^+) \right) \quad (1.5)$$

for the homonuclear case, where $d_{i,j}$ is

$$d_{i,j} = \frac{\delta_D^{(i,j)}}{2} \frac{1 - 3 \cos^2 \theta_{i,j}}{2} \quad (1.6)$$

and the dipolar coupling constant $\delta_D^{(i,j)}$ is

$$\delta_D^{(i,j)} = -2 \frac{\mu_0 \gamma_i \gamma_j \hbar}{4\pi r_{ij}^3}, \quad (1.7)$$

where γ_i represents the gyromagnetic ratio of spin i , r_{ij} the distance between spins i and j , μ_0 the magnetic permeability constant, \hbar the Planck's constant and θ_{ij} the angle between the vector joining the spins and the external magnetic field B_0 .

Equation 1.5 can be simplified in the heteronuclear case to

$$\hat{\mathcal{H}}_D = \sum_{ij, i < j} d_{i,j} 2\hat{I}_{iz}\hat{I}_{jz} \quad (1.8)$$

since the terms $\hat{I}_i^+\hat{I}_j^- + \hat{I}_i^-\hat{I}_j^+$ become time dependent due to the different Larmor frequencies and can be neglected as non-secular.

In the general case, the J-coupling Hamiltonian, $\hat{\mathcal{H}}_J$, can be written as follows

$$\hat{\mathcal{H}}_J^{(i,j)} = 2\pi J_{(i,j)} \hat{I}_i \cdot \hat{S}_j, \quad (1.9)$$

where $J_{(i,j)}$ is the J-coupling constant between atom i and j . In the heteronuclear case, the Hamiltonian can be simplified into

$$\hat{\mathcal{H}}_J^{(i,j)} = 2\pi J_{(i,j)} \hat{I}_{iz} \hat{S}_{jz}, \quad (1.10)$$

In the case of nuclei $\frac{1}{2}$ in solution, the anisotropic part of the CS tensor (Equation 1.2) as well as the dipolar coupling (Equation 1.5) are averaged out because of molecular tumbling. In the case of a powder sample, in which all possible orientation of the molecules are present, the angular dependence of these interactions have to be taken into account. Static spectra of samples containing multiple spins are challenging to investigate, due to severe overlapping and line broadening. To circumvent this issue, Magic-Angle Spinning (MAS) was introduced in the 1950s [1], [2]: the sample is spun at an angle $\theta_M \approx 54.7^\circ$ with respect to the static magnetic field B_0 . Under this condition, the angular dependence of the dipolar interaction as well as the anisotropy of the chemical shifts are averaged out zero in a first-order approximation. This approximation is only valid if spinning rate is much higher than the strength of the interactions.

Nowadays, MAS frequencies up to 130 *kHz* are achievable [3]. Under this condition, the anisotropy part of the chemical shift tensor as well as the dipolar interaction between low γ nuclei (e.g. ^{13}C and ^{15}N) are averaged out in first order approximation.

The ^1H - ^{13}C and ^1H - ^{15}N dipolar coupling, on the other hand, is not averaged out efficiently by MAS alone. Therefore, additional decoupling must be applied on ^1H to obtain high resolved ^{13}C and ^{15}N spectra. Examples of the multi pulse sequences commonly used in solid state NMR are SPINAL-64 [4], TPPM [5], XiX [6]. Under slow MAS condition ($\nu_r \leq 40$ kHz) the rf power used in these decoupling sequences is ~ 100 kHz. On the other hand, if $\nu_r \geq 50$ kHz, low - power decoupling can be applied [7], [8], as shown in Chapter 4 and 5. The strong ^1H - ^1H dipolar coupling is also not completely averaged out on this MAS regime. Therefore, to obtain high resolution ^1H spectra, it is necessary to dilute the proton network (i.e. by partial deuteration [9]) or to set the MAS frequency to $\nu_r \geq 100$ kHz.

1.2 Recoupling techniques in solid - state NMR

To transfer the magnetization between nuclei, one can choose to use dipolar based or J - coupling based experiment. In solid - state NMR the first type of transfer is normally preferred, since the strength of the dipolar coupling is usually higher than the J - coupling and permits faster transfer. On the other hand, INEPT [10] based experiment can be implemented in fully protonated samples to obtain information on the flexible regions. Since the MAS averages out in a first - order approximation the dipolar couplings, we need to design experiments to recouple this interaction. The most common recoupling experiment in solid - state NMR is the cross polarization (CP) [11], which transfers magnetization between different type nuclei (i.e. ^1H - ^{13}C). Under MAS the resonance condition is

$$n_I\omega_I + n_S\omega_S + n_r\omega_r = 0, \quad (1.11)$$

where ω_I , ω_S are the rf fields applied on the I and S spin, respectively, ω_r is the MAS frequency and n_I , n_S , n_r are natural numbers. To obtain dipolar recoupling n_I , n_S can have the value of ± 1 , while n_r can be ± 1 or ± 2 .

At the chosen resonance condition, the magnetization oscillates between I and S and the frequency of this oscillation is given by the dipolar coupling constant δ_D , defined in Equation 1.7. Due to the orientation dependence of the dipolar coupling, for a powder sample a super position of the different transfer curves is observed. The maximum transfer efficiency for the CP is 73%, while for long mixing time an equilibrium at 50% is eventually reached. The transfer efficiency can reach 100% using an adiabatic version of the CP, as shown in [12]. Another possibility to transfer magnetization directly reintroducing the dipolar coupling is the TEDOR [13], as discussed in Chapter 5.

In literature, several mechanisms for homonuclear transfer are proposed and can be divided roughly in two groups. The first group reintroduces directly the dipolar coupling

in the first - order average Hamiltonian theory. In the heteronuclear case, the CP and TEDOR mentioned above belong to this group.

In these experiment, an interference between the rf applied and the MAS frequency is created, leading to a non-zero effective dipolar coupling Hamiltonian. A frequently used first order recoupling sequence is the DREAM experiment [14], in which one sweeps through the HORROR condition ($\omega_{HORROR} = \frac{\omega_r}{2}$ in an adiabatic way. Possible applications of this sequence are shown in Chapter 2 and 3 and leads to transfer mainly between directly bonded ^{13}C nuclei. The reason is that first - order recoupling techniques are subjected to dipolar truncation.

Dipolar truncation is the effect that in the presence of a strong dipolar coupling, the transfer of magnetization between spins which are weakly coupled (i.e. longer distance) is strongly attenuated [15]. An easy way to understand this effect is to look at the effect of a first - order dipolar recoupling techniques in a 3 - spins system, with $r_{13} \gg r_{12}$. A possible example would be to use a sequence which creates a zero - quantum first order Hamiltonian on the form ([16], [17], [18])

$$\mathcal{H}_{ZQ}^{(1)} = \sum_{i,j=1,i < j}^3 d_{i,j} [\hat{I}_i^+ \hat{I}_j^- + \hat{I}_i^- \hat{I}_j^+] \quad (1.12)$$

The density operator for this system, after having set the coupling between 2 and 3 (d_{23}) to zero, can be calculated using the Liouville von Neumann equation,

$$\frac{d}{dt} \hat{\rho}(t) = -i[\mathcal{H}, \hat{\rho}(t)] \quad (1.13)$$

which gives the solution

$$\hat{\rho}(t) = \exp(-i\mathcal{H}t) \hat{\rho}(0) \exp(i\mathcal{H}t) \quad (1.14)$$

for a time independent Hamiltonian. We can now calculate the transfer between spin 1 to 2 and 3 evaluating the density operator $\hat{\rho}(t)$ using Equation 1.14, with $\hat{\rho}(0) = \hat{I}_{1z}$. Thus, we obtain the magnetization of spin 2 and 3 as

$$\langle \hat{I}_{2z} \rangle = \frac{d_{12}^2}{d_{12}^2 + d_{13}^2} \sin^2(\omega t) \quad (1.15)$$

$$\langle \hat{I}_{3z} \rangle = \frac{d_{13}^2}{d_{12}^2 + d_{13}^2} \sin^2(\omega t) \quad (1.16)$$

with $\omega t = \sqrt{d_{12}^2 + d_{13}^2}$.

We can evaluate now the ratio between $\langle \hat{I}_{2z} \rangle$ and $\langle \hat{I}_{3z} \rangle$ as, since the dipolar coupling constant is proportional to r^{-3}

$$\frac{\langle \hat{I}_{2z} \rangle}{\langle \hat{I}_{3z} \rangle} = \left(\frac{r_{13}}{r_{12}} \right)^6 \quad (1.17)$$

According to equation 1.17, if $r_{13} \gg r_{12}$, the transfer from spin 1 to spin 3 is greatly quenched. Therefore, to measure long distance ^{13}C contacts in UL proteins, another

approach has to be applied. The second family of recoupling techniques, the so called second - order recoupling experiments, have been developed for this purpose. Additional examples of these sequences are used in Chapter 2 and 3.

1.3 Sequential assignment

Solid - state NMR techniques can be used for protein structure determination. However the information on the chemical shifts of the ^{13}C and ^{15}N are essential to achieve this goal. The procedure, called sequential assignment, can be described by the following steps:

- (i) Identify CS of backbone atoms belonging to the same residue (spin system)
- (ii) Connect different spin system sequentially
- (iii) Complete the assignment of spin system with side chains CS.

The goal is to identify chains of spin systems of sufficient length with a particular amino acid sequence that happens only once in a protein. For small proteins, this procedure can be obtained by 2D spectroscopy. However, for larger system, one needs a combination of 2D and 3D spectroscopy, as shown in Chapter 2 and 3. The identification of CS of backbone of the same residue can be achieved by a combination of 2D NCA and 3D NCACB: both NCA and the CA-CB DREAM transfer the magnetization between directly bonded atoms, rendering possible the identification of the N, the $C\alpha$ and $C\beta$ of the same residue. For deuterated protein, an assignment strategy based on 2D [^{15}N - ^1H] can be used [19]. Additional 3D experiment, namely NCACO, CANCO and NCOCA allow to connect different spin systems sequentially. The procedure is to keep two known CS fixed (i.e. N and $C\alpha$ of the same residue, found in the NCACB) and find the third connected frequency in the chosen experiment (i.e. the C' of the previous residue in the CANCO).

As shown in Chapter 3, the small dispersion of CS in the carbonyl region can cause severe overlap and increase the difficulty in the sequential assignment procedure. Therefore, another set of experiments can be measure in which the C' frequency is not recorded, adding an additional transfer step. Examples of these experiment are the N(CO)CACB and CAN(CO)CA.

The assignment of the residues can be completed by the CS of the side chains. To accomplish this task, additional 2D and 3D experiment can be measured, namely 2D DARR and CCC and the relayed N(CA)CBCX, in which the $C\alpha$ dimension is not recorded. With the information on the CS of the backbone atoms, the assignment of the side chains can be obtained in a similar way as for the backbone walk (i.e. two known frequency used to connect with one unknown CS).

Part I

Structure Calculation

Chapter 2

Structure determination of the Amyloid β (1-42) fibril

This chapter is based on two manuscripts by Francesco Ravotti, Marielle A. Wälti, Peter Güntert, Roland Riek, Anja Böckmann, B. H. Meier and by Marielle A. Wälti, Francesco Ravotti, Hiromi Arai, Charles Glabe, Joseph Wall, Anja Böckmann, Peter Güntert, Beat H. Meier and Roland Riek.

Marielle prepared the samples for the screening and the one used for the assignment and structure calculation. I measured the NMR spectra used for the assignment and the structure calculation. Together with Marielle, we have assigned the protein and analysed the distance restraints spectra. Together with Marielle and Peter, we have performed the structure calculation and written the initial manuscripts.

2.1 Introduction

Alzheimer's disease (AD) is a neurodegenerative disorder with still no known cure and increasing incidence. The disease is characterized by the development and accumulation of extracellular plaques in the brain. The senile plaques consist mainly of amyloid beta ($A\beta$) fibrils [20], [21]. The $A\beta$ is a peptide of 39-43 amino-acid residues and is generated from the amyloid precursor protein (APP) by the proteolytic activities of β - and α -secretase [22].

The amyloid fibrils of $A\beta$ are a pathological hallmark of AD disease and may play a central role in cell-to-cell transmissibility (reviewed in [23]) while their precise role in toxicity is unclear. The characterization of the structure of $A\beta$ fibrils is therefore crucial for a detailed understanding of the aggregation process and the AD disease, as well as for devising strategies for the development of interacting compounds.

The $A\beta$ (1-42) fragment is the dominant $A\beta$ species in the amyloid plaques of AD patients [24], [25], [26], [27]. Although a generalized discussion of the biological activity of $A\beta$ is complicated by the presence of different polymorphs, $A\beta$ (1-42) typically displays a higher

propensity to form amyloid fibrils in vitro [28] [29], [30], and appears to be a more toxic species than A β (1-40) and to aggregate faster. Most high-resolution structural studies have been performed on A β (1-40) amyloid fibrils [31], [32], [33].

In addition to low resolution structural information on A β (1-42) fibrils from methods such as mutagenesis studies, H/D exchange measurements, electron microscopy, solid - state NMR, and X-ray fiber diffraction [34], [35], [36], [37], [38], [39], [40] recently a solid - state NMR-based structural model based on 11 long-range distance restraints became available [41]. It shows a single A β (1-42) molecule within a protofilament of the fibril comprising a double horseshoe-like cross- β -sheet structure. Interestingly, a familial mutant of A β (1-40) amyloid fibril shows a similar fold [33].

In this chapter we determine the 3D structure of a disease-relevant polymorph of A β (1-42) amyloid fibrils at atomic resolution using solid - state NMR techniques combined with supplementary methods.

2.2 Results and discussion

2.2.1 Screening of conditions

Biophysical investigations of A β amyloids often indicate the presence of several polymorphs within a single sample. On the mesoscopic scale polymorphs distinguish themselves by the amount of twisting observed by electron microscopy (EM), the number of filaments per fibril, and the diameter and MPL of the fibrils [42].

In solid - state NMR spectra different chemical-shift fingerprints and mixtures of polymorphs can be distinguished by the appearance of more than one resonance line per spin probe [43], [44]. Therefore differences on the atomic scale can be detected, leading to a NMR-guided optimization of the fibrillization conditions using seeding steps.

In a first trial uniformly [^{13}C , ^{15}N]-labeled A β (1-42) was fibrillized in phosphate buffer (condition 0, Appendix A.1). We performed a 2D [^{13}C - ^{13}C] 20ms DARR spectrum [45], [46] on this condition, as shown in Figure 2.1 **A - D**, where the serine-containing part of the 2D spectrum is highlighted. A β (1-42) comprises two serines and concomitantly two $^{13}\text{C}\alpha$ - $^{13}\text{C}\beta$ cross peaks are expected, but under these conditions at least 6 cross peaks are observed (Figure 2.1 **A**). This indicates the presence of at least three polymorphs under this conditions.

We made a second attempt using 100 mM sodium chloride (NaCl) and seeding decreased the polymorphism in the sample dramatically. However, still six serine peaks were observable (Figure 2.1 **C**).

In contrast, A β (1-42) at concentrations of either 30 or 100 M in phosphate buffer with 100 mM NaCl and 100 M ZnCl exhibited a single set of cross peaks as demonstrated for the two serine cross peaks assigned to Ser 8 and Ser 26 (Appendix A.1, conditions 2 and 4; Figure 2.1 **B - D**). Finally, we choose condition 2 for further studies because the seeds

were prepared under identical buffer conditions and yielded reproducible solid - state NMR spectra of high quality without batch-to-batch variability. Moreover, as shown in Appendix A.2, there are evidences that the chosen condition is relevant for AD disease. Fibrils treated with heparin (condition 1, Appendix A.1), although clearly visible by EM, did not sediment by centrifugation, and therefore no spectra could be recorded.

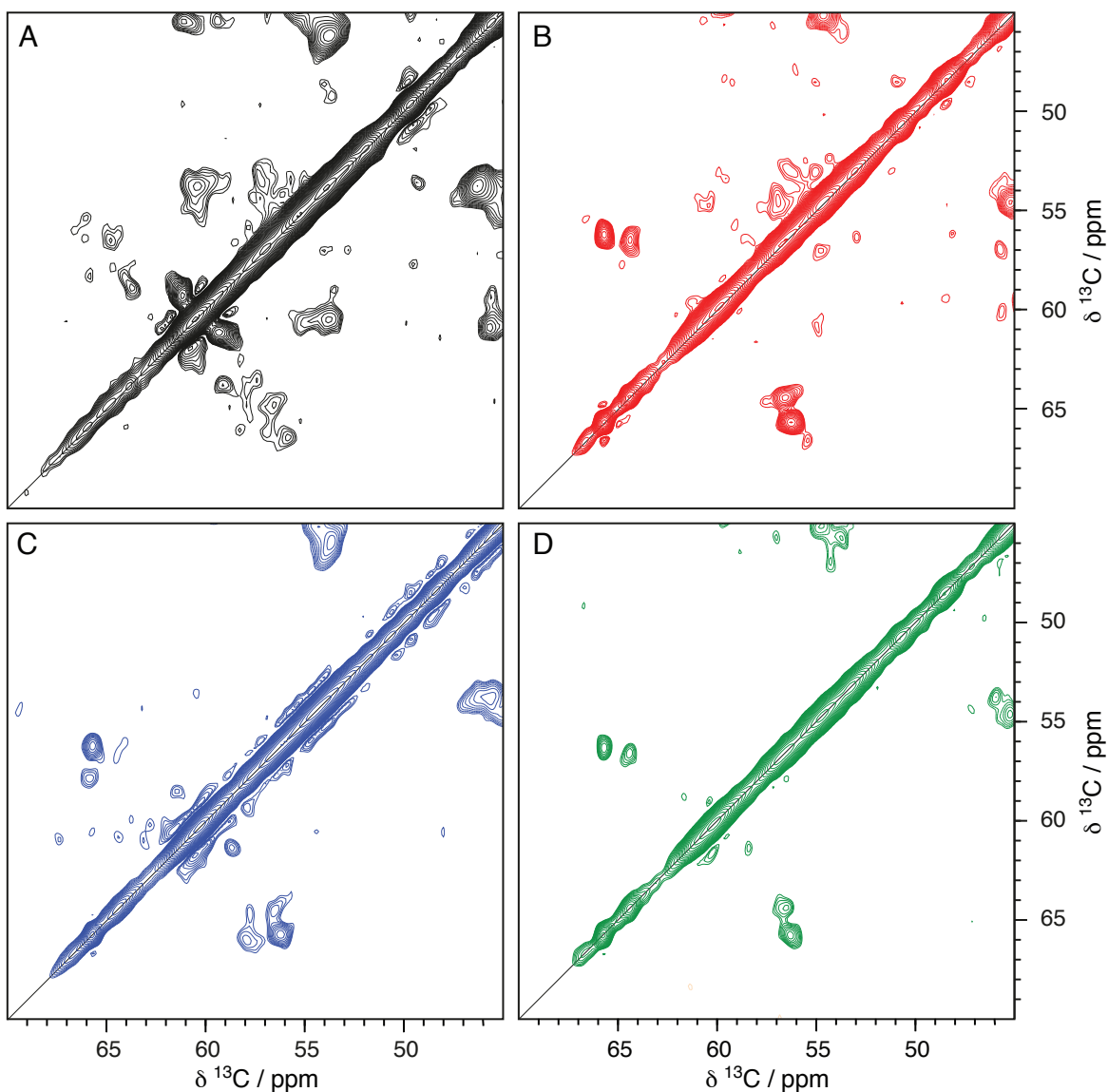


Figure 2.1: Particular of serine's region of 2D 20ms DARR spectra measured on different samples. The spectra were measured on the same conditions at a magnetic field of 14.0 T and MAS frequency of 13 kHz. In (A) and (C), at least 6 correlation are visible, while (B) and (D) show only 2 serine cross peaks. Details on the sample preparation are shown in Appendix A.1

2.2.2 Sequential assignment

The selected [UL ^{13}C - ^{15}N] fibrils of A β (1-42) show in average a linewidth of 0.5 ppm in [^{13}C - ^{13}C] correlation spectra (Figure 2.2).

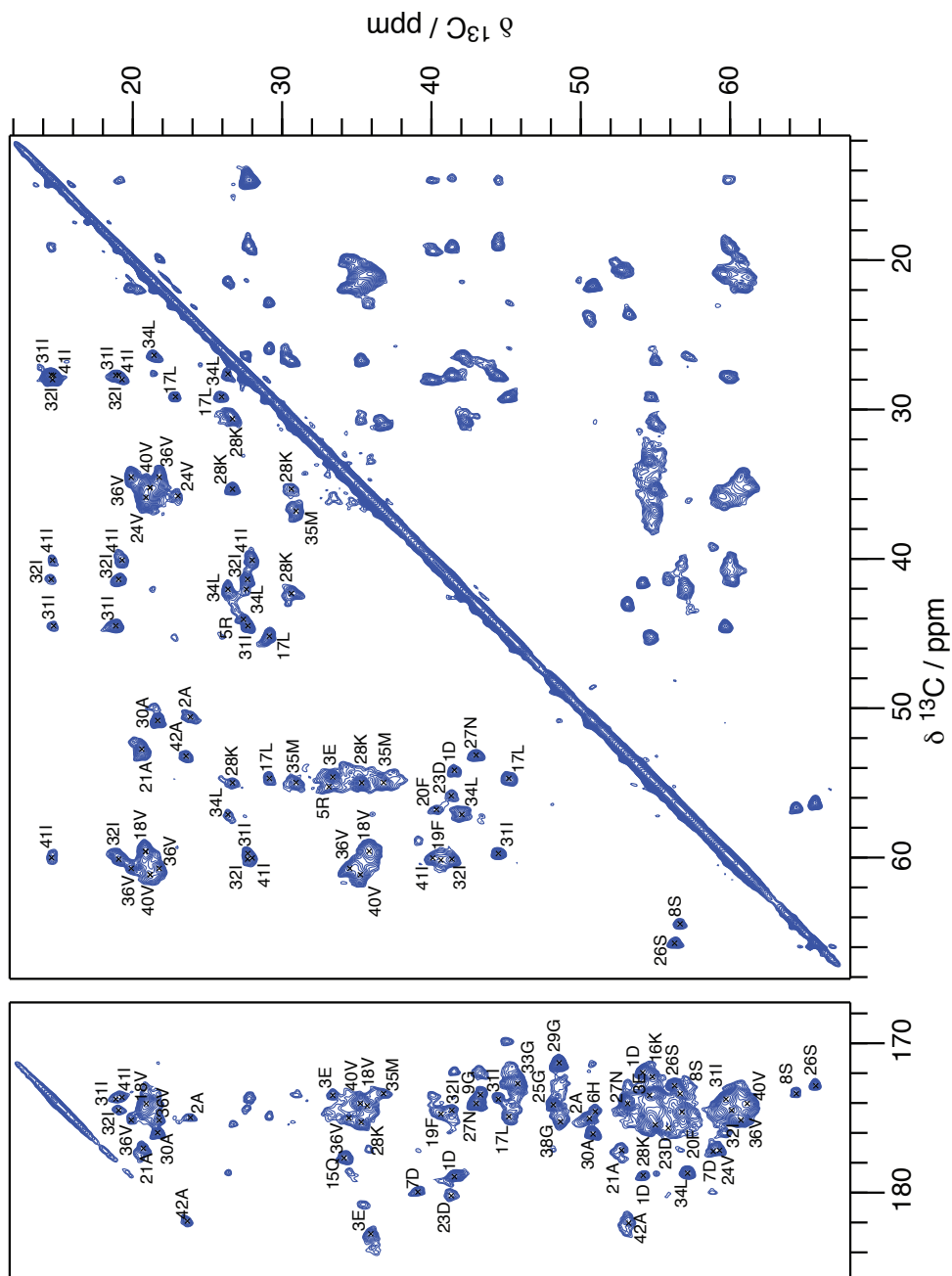


Figure 2.2: 2D [^{13}C - ^{13}C] DARR spectrum on [UL ^{13}C - ^{15}N] A β (1-42) fibrils with a mixing time of 20ms measured at a magnetic field of 20.0 T. The experiment was performed at MAS frequency of 19 kHz. The sequence specific assignment were derived from the sequential backbone walk performed on 3D spectra, as shown in Figure 2.4

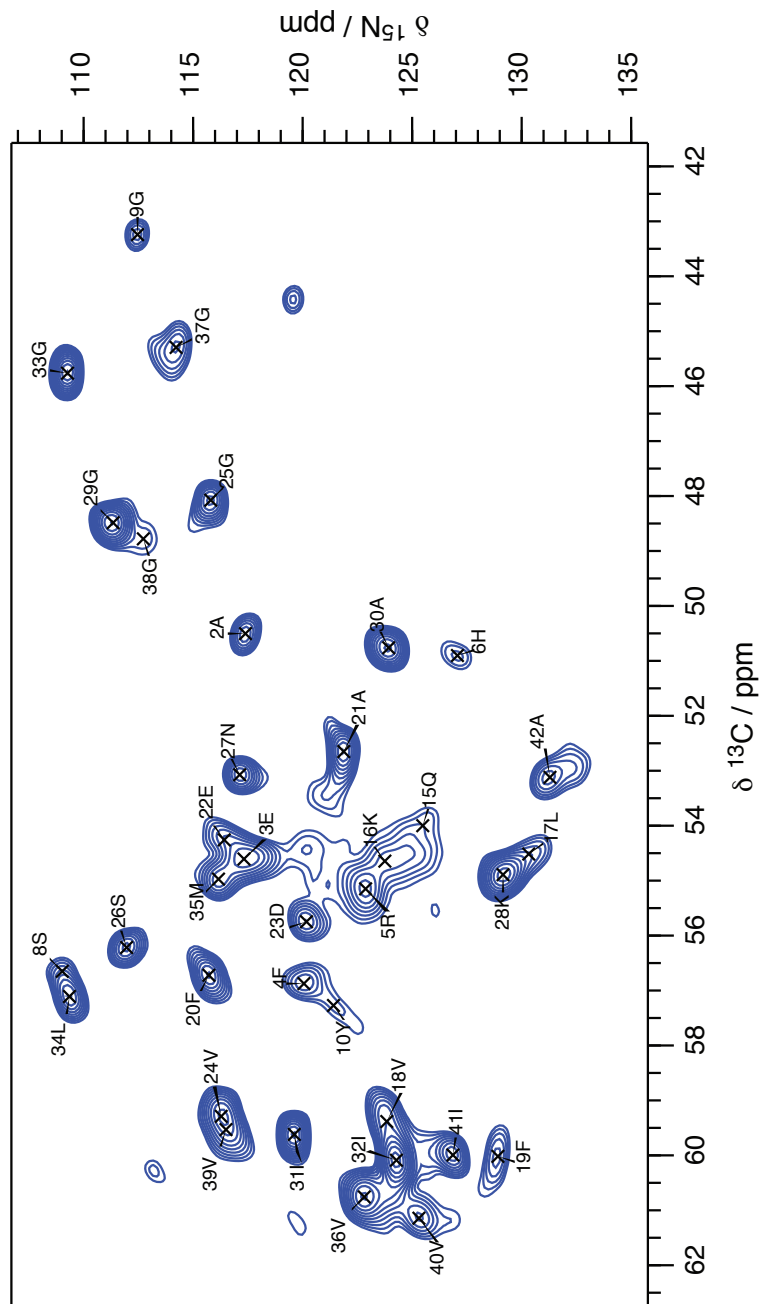


Figure 2.3: 2D [^{13}C - ^{15}N] NCA spectrum on [UL ^{13}C - ^{15}N] A β (1-42) fibrils measured at a magnetic field of 20.0 T. The experiment was performed at MAS frequency of 19 kHz. The sequence specific assignment were derived from the sequential backbone walk performed on 3D spectra, as shown in Figure 2.4

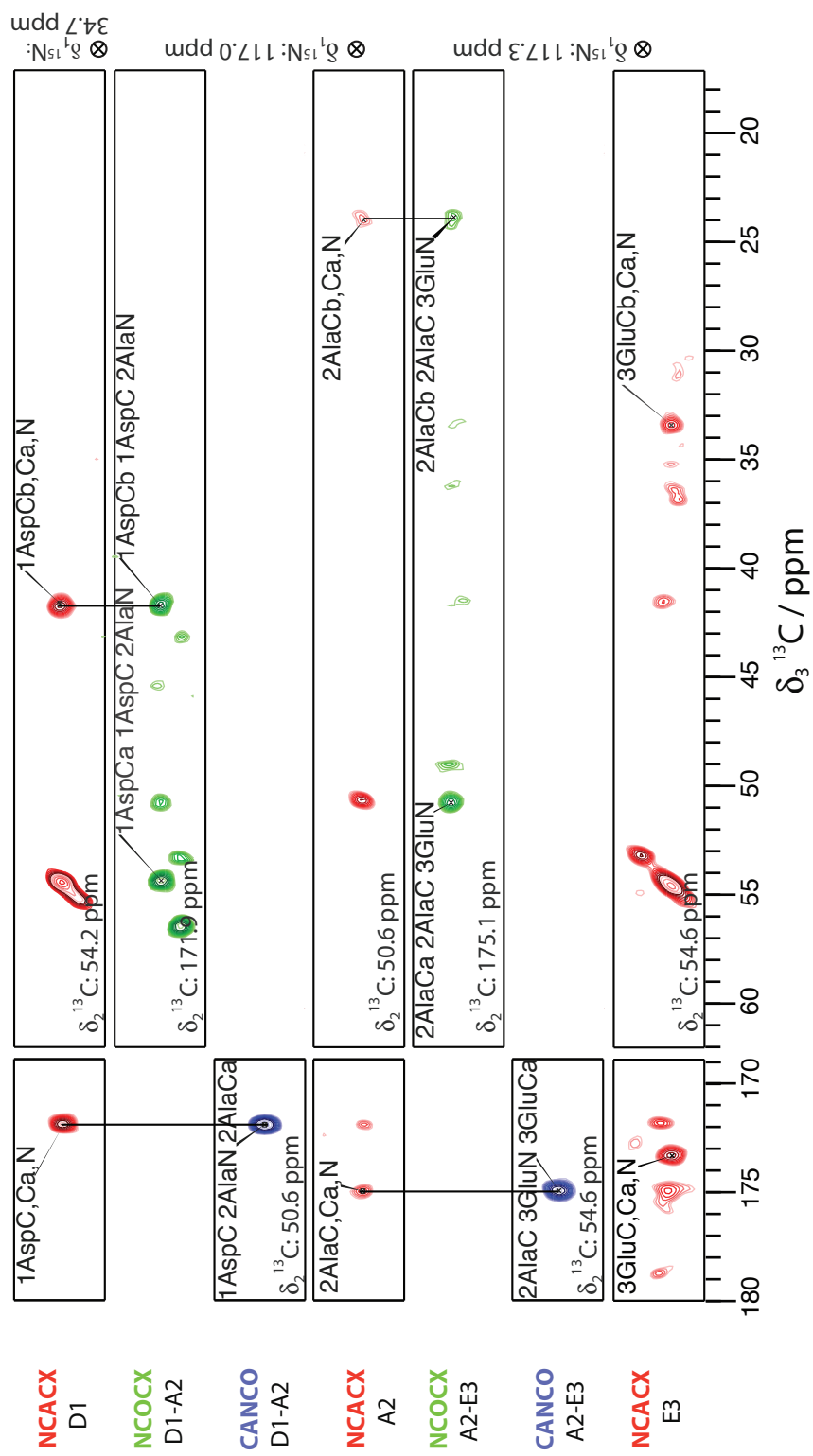


Figure 2.4: Strips extracted from the 3D NCACX (red), NCOCX (green) and CANCO (blue) spectra of [UL ¹³C-¹⁵N] Aβ (1-42) fibrils. Vertical lines were added to aid following the backbone walk starting at the N-terminus of the protein

Residue	N	N γ	N η	N ζ	C	C α	C β	C γ	C δ	C ϵ	C ζ
1 Asp	34.7	-	-	-	171.8	54.1	41.6	179.0	-	-	-
2 Ala	117.3	-	-	-	175.0	50.5	23.8	-	-	-	-
3 Glu	120.3	-	-	-	173.5	54.6	33.5	35.8	182.9	-	-
4 Phe	122.8	-	-	-	175.3	56.9	41.7	139.5	132.8	130.73	127.6
5 Arg	127.0	-	69.8	-	174.6	55.3	33.1	27.4	44.1	-	159.7
6 His	125.8	-	-	-	171.8	50.8	29.9	134.4	116.7	-	-
7 Asp	109.0	-	-	-	117.2	58.9	38.8	180.0	-	-	-
8 Ser	112.3	-	-	-	173.4	56.6	64.3	-	-	-	-
9 Gly	120.8	-	-	-	173.5	43.3	-	-	-	-	-
10 Tyr	-	-	-	-	174.7	57.1	35.7	129.1	133.2	117.4	157.8
11 Glu	-	-	-	-	-	-	-	-	-	-	-
12 Val	-	-	-	-	-	-	-	-	-	-	-
13 His	-	-	-	-	-	-	-	-	-	-	-
14 His	-	-	-	-	-	-	-	-	-	-	-
15 Gln	123.9	-	107.5	-	173.9	54.1	31.5	34.1	177.7	-	-
16 Lys	129.8	-	-	-	172.2	54.8	37.6	-	-	-	-
17 Leu	123.7	-	-	-	174.9	54.7	45.2	29.1	25.86, 22.8	-	-
18 Val	128.5	-	-	-	174.2	60.0	35.7	20.9	-	-	-
19 Phe	115.4	-	-	-	174.7	60.2	40.6	140.0	131.0	130.0	128.4
20 Phe	121.6	-	-	-	174.6	56.7	40.5	140.0	134.1	130.7	127.4
21 Ala	116.3	-	-	-	177.2	52.7	21.4	-	-	-	-
22 Glu	120.0	-	-	-	175.4	54.4	32.4	35.5	180.8	-	-
23 Asp	116.3	-	-	-	175.7	55.9	41.5	180.2	-	-	-
24 Val	115.6	-	-	-	177.2	59.3	35.8	22.9, 20.9	-	-	-
25 Gly	111.9	-	-	-	174.1	48.1	-	-	-	-	-
26 Ser	117.0	-	-	-	172.8	56.2	65.7	-	-	-	-
27 Asn	129.2	109.9	-	-	174.0	53.1	43.0	175.4	-	-	-
28 Lys	111.1	-	-	32.2	175.6	54.9	35.3	26.7	30.7	42.2	-
29 Gly	123.6	-	-	-	171.3	48.5	-	-	-	-	-
30 Ala	119.4	-	-	-	175.9	50.8	21.6	-	-	-	-
31 Ile	124.1	-	-	-	173.7	59.7	44.7	27.8, 18.9	14.6	-	-
32 Ile	119.1	-	-	-	174.5	60.1	41.4	27.7, 19.1	14.4	-	-
33 Gly	109.2	-	-	-	172.7	45.8	-	-	-	-	-
34 Leu	116.2	-	-	-	178.7	56.9	42.0	26.3	21.2, 27.6	-	-
35 Met	122.6	-	-	-	173.4	54.8	36.6	30.9	-	17.2	-
36 Val	113.9	-	-	-	175.1	60.7	34.5	21.7	-	-	-
37 Gly	112.6	-	-	-	172.6	45.4	-	-	-	-	-
38 Gly	116.5	-	-	-	175.2	48.7	-	-	-	-	-
39 Val	125.2	-	-	-	174.1	59.5	35.8	20.9	-	-	-
40 Val	126.6	-	-	-	174.0	61.1	35.2	21.2	-	-	-
41 Ile	127.8	-	-	-	173.6	60.0	40.1	27.9, 19.2	14.6	-	-
42 Ala	130.8	-	-	-	182.0	53.3	23.7	-	-	-	-

Table 2.1: Chemical shifts of A β (1-42) fibrils in ppm

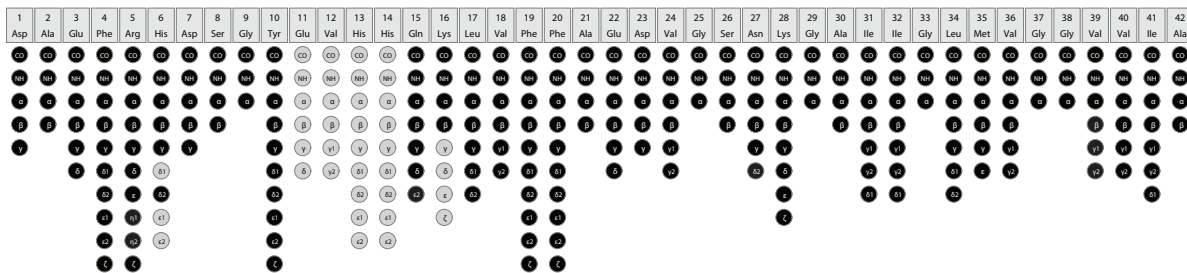


Figure 2.5: Sequential assignment graph showing all carbon and nitrogen atoms of $A\beta$ (1-42) by circles. The assigned atoms are shown in black, whereas the unassigned ones are shown in grey. The graph was designed with the software CcpNMR 2.3 analysis [47], [48]

A single set of resonances can be identified in the DARR and NCA of in Figures 2.2 and 2.3 with a few additional resonances, which were visible in 2D spectra, but not be detected in 3D spectra. We believe that these resonances represent a minor polymorph. The intensity of the intra-residue cross peaks of those resonances is less than 5% of the main form.

NCOCX, NCACX, NCACB, and CANCO spectra allowed the sequential assignment of the backbone atoms of the protein (excluding residues 11-14, which were not visible in any of the spectra). 3D CCC and 2D DARR spectra were recorded to complete the assignment of the side-chains, as proposed in [49], [50] Using this procedure, we assigned 90.5 % of the backbone and 77% of the side-chains atoms (90.5% of nitrogen, and 80.5 % of all carbon atoms, respectively). A representative sequential walk using the NCACX, NCOCX, and CANCO spectra is depicted in Figure 2.4. Furthermore, the sequential assignment graph reflecting the completeness of the assignments on a residue-per-residue basis is shown in Figure 2.5.

The experimental details are shown in Table 2.2. The assigned chemical shifts can be seen in Table 2.1.

In order to assess whether the resonances for residues 11-14 are missing due to fast dynamics, we performed a ^1H - ^{15}N INEPT-based 2D correlation experiment to check for the presence of highly flexible residues in the fibrils. However, this spectrum was devoid of any peaks. Therefore we concluded that the missing 4-residues stretch presents an intermediate range (μs correlation times) of motion, rendering it invisible in CP- as well as INEPT-based experiments.

A comparison of the chemical shifts of this $A\beta$ (1-42) with previously published $A\beta$ (1-42) and $A\beta$ (1-40) is depicted in Appendix A.3.

2.2.3 Secondary structure determination

We performed the identification of secondary structure elements by the analysis of the so-called secondary chemical shifts ($\Delta\delta C\alpha - \Delta\delta C\beta$): that is defined as the difference between measured $^{13}\text{C}\alpha$ chemical shifts and corresponding random coil $^{13}\text{C}\alpha$ chemical shifts

and subtracted the difference between measured $^{13}\text{C}\beta$ chemical shifts and corresponding random coil $^{13}\text{C}\beta$ chemical shifts [51].

In this approach, we defined a β strand by at least three consecutive resonances with a value of the secondary shifts difference $\Delta\delta\text{C}\alpha - \Delta\delta\text{C}\beta < -1.4$ ppm [51].

We could identify five β -sheets using this approach, namely between residues 2 - 6 (β_1), 15 - 18 (β_2), 26 - 28 (β_3), 30 - 32 (β_4), 39 - 42 (β_5). Just requesting that $\Delta\delta\text{C}\alpha - \Delta\delta\text{C}\beta$ is negative would add another beta strand at residues 20 - 22, as shown in light red in Figure 2.6.

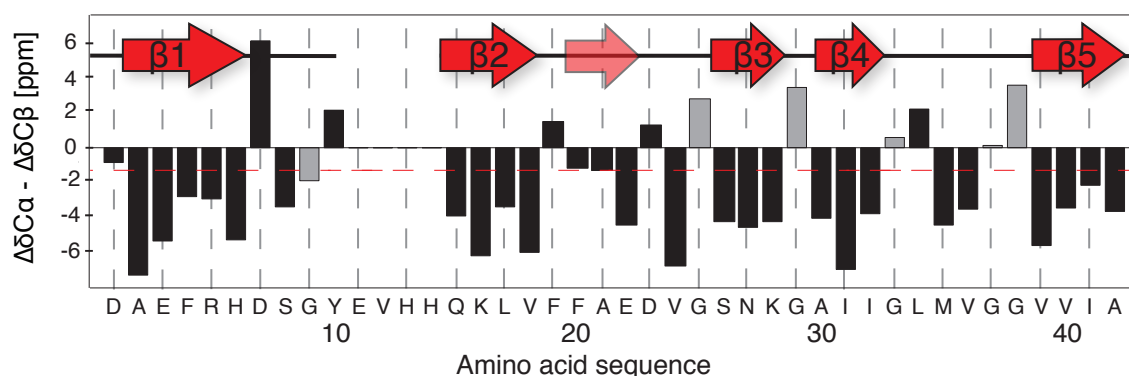


Figure 2.6: Secondary structural elements for $A\beta$ (1-42) fibrils from secondary chemical shifts. The line is interrupted where data are missing. β -strands are assumed where the secondary chemical shifts are lower than -1.4 ppm for three residues in a row (red arrows). An additional putative beta strand with three negative values in a row but not reaching the -1.4 ppm limit is indicated in light red. For the glycines, the $\Delta\delta\text{C}\alpha$ shifts are displayed in grey.

Next, we performed [^{13}C - ^{15}N]-PAIN and [^{13}C - ^{15}N]-TEDOR experiment [52] on a mixed labeled sample (ML) of fibrils composed by exclusively ^{13}C -labeled and exclusively ^{15}N -labeled $A\beta$ (1-42) monomers in a 1 : 1 ratio. We then compared the resulting spectra with a NCA spectrum of the UL sample. All the intraresidual ^{13}C - ^{15}N -cross peaks identified in the NCA spectrum and labeled with black letters in Figure 2.7 are also present in the [ML ^{13}C - ^{15}N]-PAIN spectrum. This indicates that nitrogen and carbon frequencies of the same residue, but from different monomers, are in close spatial proximity, as in the case of in-register parallel β -sheets.

This was found for β -strands β_2 to β_5 . No cross peaks belonging to β -strand β_1 could be obtained from these experiments, therefore no information about its in registry could be obtained.

In addition, no cross-peaks for the residues Leu 17, Asp 23, Met 35, Ile 41, and Ala 42 could be seen in these spectra, most of which are not located in β -strands (Figures 2.7). Full details of these experiments are shown in Table 2.3. Additional information extracted from the hydrogen/deuterium (H/D) exchange are presented in Appendix A.4.

2.2.4 Distance restraints spectra

We performed long distance [^{13}C - ^{13}C] experiments, such as 200 ms DARR, 400 ms DARR [53], 8 ms PAR [54] and 400 μs CHHC to obtain distance restraints to use in the structure calculation procedure.

We defined as restraint a spectral unambiguous (i.e. only one possibility of assignment in each dimension, with 0.2 ppm of tolerance) correlation between ^{13}C atoms which belong to amino acids that are far apart in the primary sequence (i.e. more than 3 residues).

The experiments were measure on [UL ^{13}C - ^{15}N] and on a diluted samples. The diluted sample contains uniformly [^{13}C - ^{15}N]-labeled A β (1-42) and natural abundance (NA) A β (1-42) monomers in a ratio of 1:3.

We classified restraints as inter- or intra-molecular (or ambiguous in this respect) according to the intensity ratio between the UL sample and the diluted sample. Cross-peaks were classified as intra-molecular contacts if the intensity ratio $I_{Dil}/I_{UL} > 0.8$ with a standard deviation margin above 0.4. Cross-peaks were classified as inter-molecular contacts if the intensity ratio $I_{Dil}/I_{UL} < 0.4$ with a standard deviation margin below 0.8. No classification was done in any other cases. Corresponding traces of the individual spectra of the two samples are compared in Figures 2.8 (C) and (D) . Details on the experiment condition are shown in Table 2.3.

From the dilution analysis we could identify three spectrally unambiguous inter-molecular cross peaks, defining contacts between two pairs of residues (Gln 15 - Met 35, Leu 17 - Met 35). Moreover, 7 intra-molecular correlations defining contacts between 6 residue pairs were found (Figures 2.8 (E), 2.11 (A) and Table 2.5). A detailed analysis of representative traces for the correlations can be found in Appendix A.5, while a summary of all the restraints is shown in Figure 2.9 .

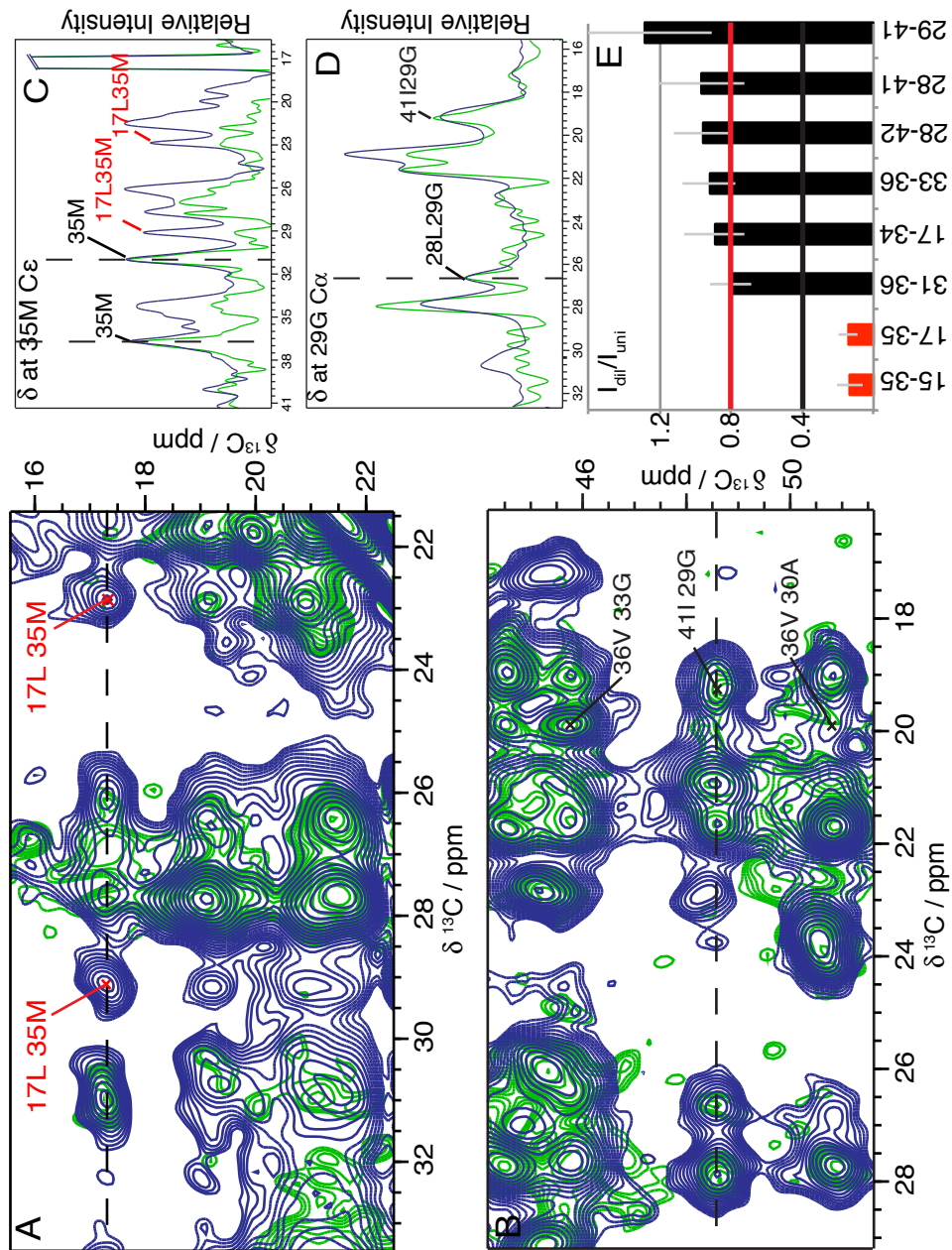


Figure 2.8: Extracts of NMR spectra that distinguish intra- from inter-molecular contacts. (A), (B) Superposition of 2D PAR spectra recorded on a $[\text{UL } ^{13}\text{C}-^{15}\text{N}]$ sample (blue contours) and on a diluted sample (green contours) of A β (1-42). (E) Intensity ratios of cross-peaks from the diluted and uniformly labeled samples. (C) Trace extracted at the Met 35 C ϵ -resonance from the PAR spectra of UL (blue) and diluted (green) samples. All cross peaks of this resonance are of inter-molecular nature. (D) Trace extracted at the Gly 29 C α resonance from the PAR spectra of UL (blue) and diluted (green) samples. All cross-peaks of this resonance are of intra-molecular nature.

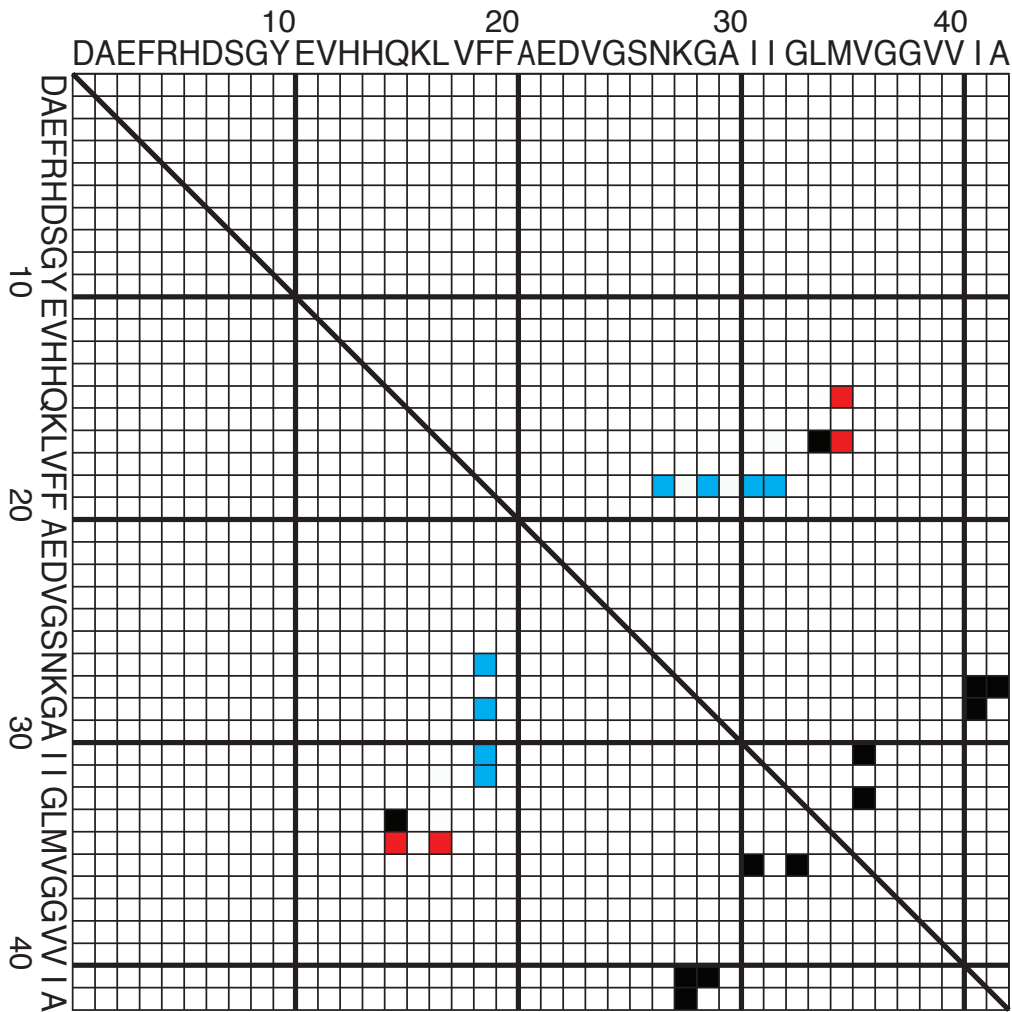


Figure 2.9: Overview of all the manually assigned distance restraints. The x- and y-axes show the amino acid sequence of A β (1-42). Filled squares display an interaction between the respective residues. Intra-molecular contacts are depicted in black and inter-molecular distances in red, whereas distances with ambiguities are colored in cyan.

2.2.5 Mass-per-length measurement

One important parameter necessary for the structure determination of an amyloid fibril is the mass-per-length (MPL) measurement using Scanning Transmission Electron Microscopy (STEM) [55], [56], [57]. The number of molecules per layer (i.e. per 0.48 nm) can be determined combining the result of this measurement with the knowledge that A β (1-42) amyloid fibrils are composed of an in-register intermolecular parallel cross- β -sheet entity with a repetition rate at every 0.48 nm (i.e. the distance between two β -strands across the β -sheets), as shown in Paragraph 2.2.3.

The MPL measurements were done on two A β (1-42) amyloid fibrils samples coming from two independent batches: one sample was fully $^{13}\text{C},^{15}\text{N}$ -labeled and the other one unlabeled. Both samples were evaluated separately (with a $MW_{\text{Theor}} = 4772$ Da for the

^{13}C , ^{15}N -labeled sample, and a $\text{MW}_{\text{Theor}} = 4517$ Da for the unlabeled sample).

A total of 537 MPL measurements were manually performed on single filaments, which were distinguished from multimeric fibrils by eye. The analysed data, visible in Figure 2.10, show a clear peak at an MPL value of $1.9 \text{ kDa}/\text{\AA}$. This suggests the presence of two $\text{A}\beta$ (1-42) molecules per 0.48 nm .

A small peak at MPL of $3.8 \text{ kDa}/\text{\AA}$, which would correspond to four molecules per 0.48 nm , was attributed to a lateral stacking of two filaments.

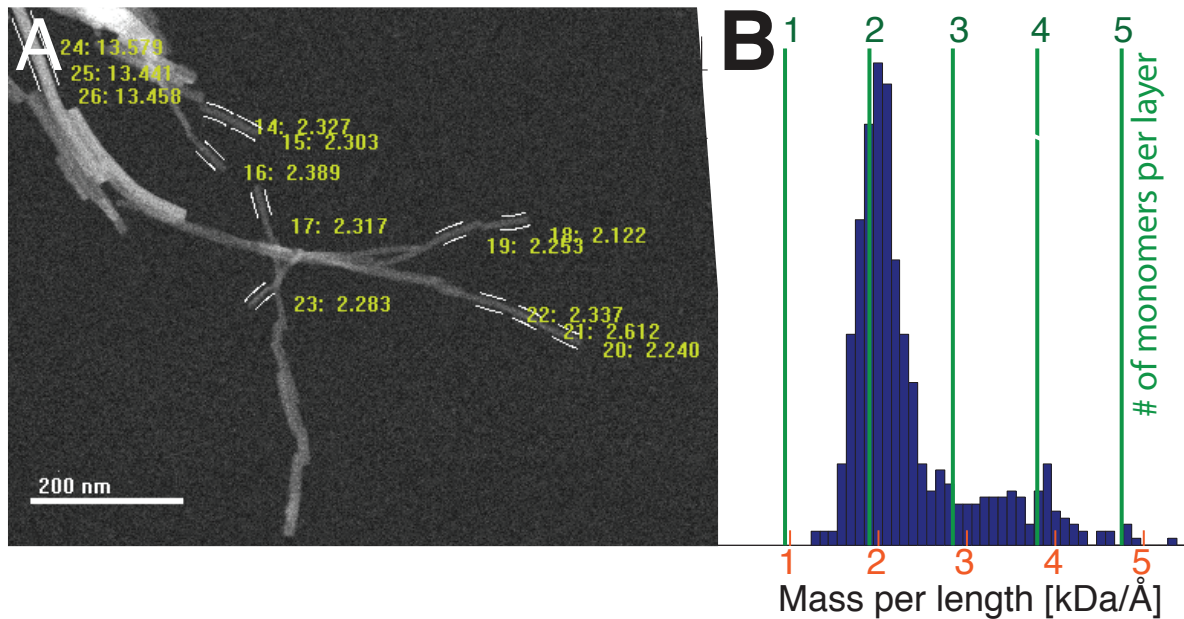


Figure 2.10: (A) STEM image of unstained, freeze-dried $\text{A}\beta$ (1-42) fibrils. Only the ends of the fibrils are used for the MPL measurements and are marked with white lines. (B) Result of the MPL experiment with number of measurements with a given mass per length as indicated. The number of monomers per layer of a cross- β -sheet fibril is highlighted with green dotted lines. The MPL measurements indicate two monomers per layer.

2.2.6 The 3D structure of A β (1-42) fibril

We used the following information for the first 3D structural model of A β (1-42) fibrils:

- (i) The measure of two molecules per layer (STEM) and the presence of a single set of resonances positions two symmetrically equivalent A β (1-42) molecules per subunit.
- (ii) Dihedral angle restraints $-200^\circ \leq \phi \leq -80^\circ$ and $40^\circ \leq \psi \leq 220^\circ$ (45) were applied for the residues involved in a β -strand, as defined in paragraph 2.2.3.
- (iii) 2 x 32 inter-molecular hydrogen bond restraints were implemented for residues in these five β -strands.
- (iv) 81 either spectrally unambiguous medium- and long-range distance restraints or restraints with low spectral ambiguity (Table 2.5) identified in 200 ms DARR, 400 ms DARR, 8 ms PAR and [ML ^{13}C - ^{15}N]-PAIN spectra.
- (v) partially unstructured N-terminus (residues 1-10), seen in the [ML ^{13}C - ^{15}N]PAIN spectrum and in limited proteolysis with proteinase K experiments. The result of this experiment is shown in Appendix A.6.

Using this information, we calculated a manual 3D structure composed of 2 x 3 A β (1-42) molecules with CYANA [58]. The restraints we used in the calculation are shown in Figure 2.11 (A) plotted onto the structure.

In a second step, we performed an automatic structure calculation using, in addition to the input data described above, automatically picked peak lists from [^{13}C - ^{13}C] CHHC, [^{13}C - ^{13}C] PAR and [ML ^{13}C - ^{15}N] PAIN spectra and assigned using an iterative process [59]. This procedure yielded 551 additional restraints (Table 2.4) and resulted in a well converged structure with an average target function of 1.90 Å² for the final bundle comprising the 10 best conformers and a backbone RMSD of 0.89 Å for residues 15 - 42 of the two molecules in the central layer, as shown in Figure 2.13-2.14-2.15 and Table 2.4.

The 3D structure of the automatic calculation superimposes well with the structure from the manual calculation (Figure 2.12). Residue pairs supported by automatically assigned cross peaks are displayed in Figure 2.11 (B).

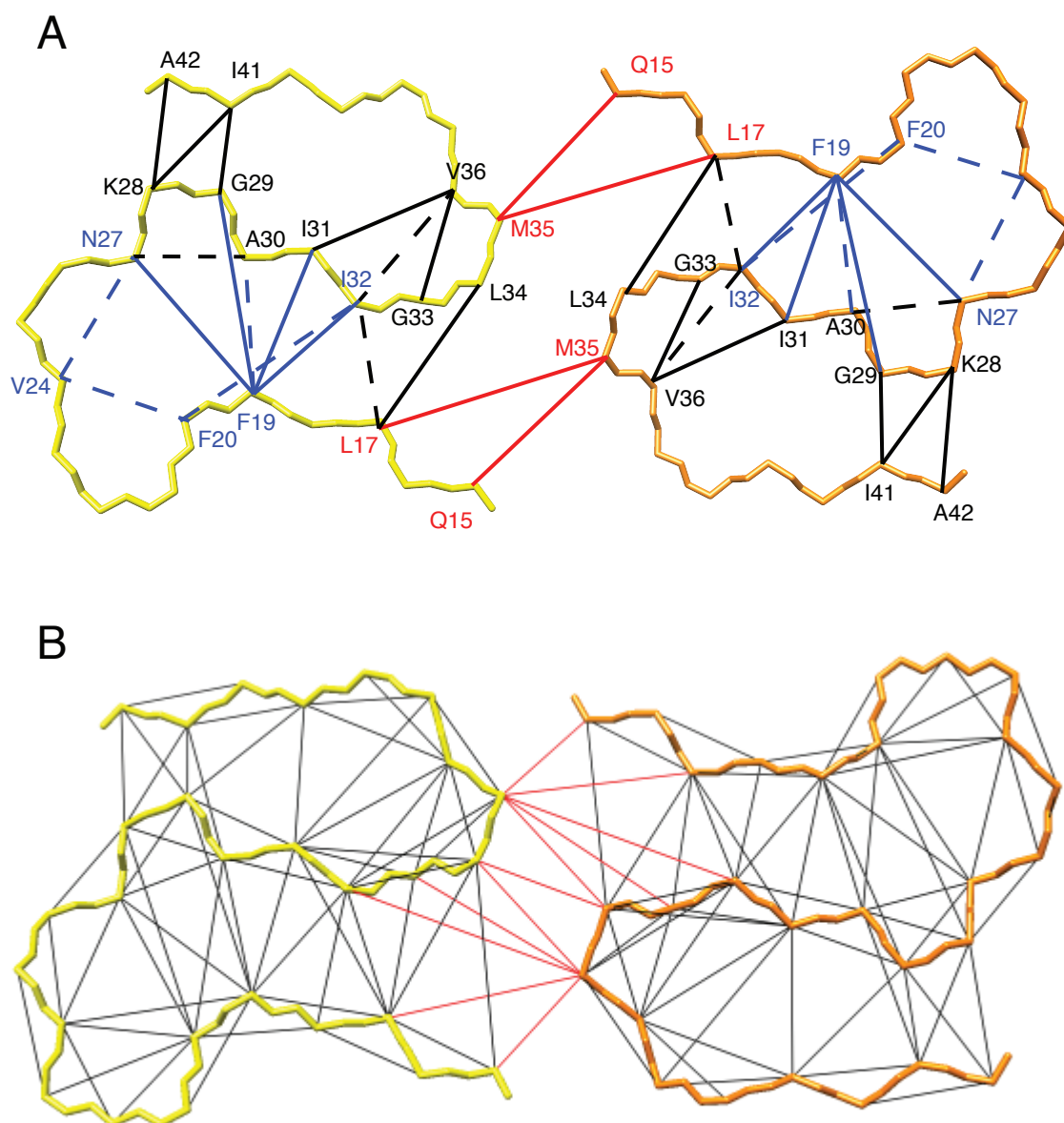


Figure 2.11: (A) Unambiguous distance restraints used for the manual structure calculations are plotted onto the final 3D structure. Distance restraints between residues (indicated by one letter code) are color coded in red for inter-molecular restraints, in black for intra-molecular ones, and in blue for unambiguous restraints, which could be either of inter- or intra-molecular nature, respectively. Solid lines indicate spectrally unambiguous restraints (within 0.2 ppm), dashed lines restraints with low ambiguity as shown in Table 2.5. The 3D structure is represented by the backbone of the two symmetric $A\beta$ (1-42) molecules in one layer color-coded yellow and orange. In (B) distance restraints assigned during the automatic structure calculation by CYANA are displayed onto its corresponding 3D structure.

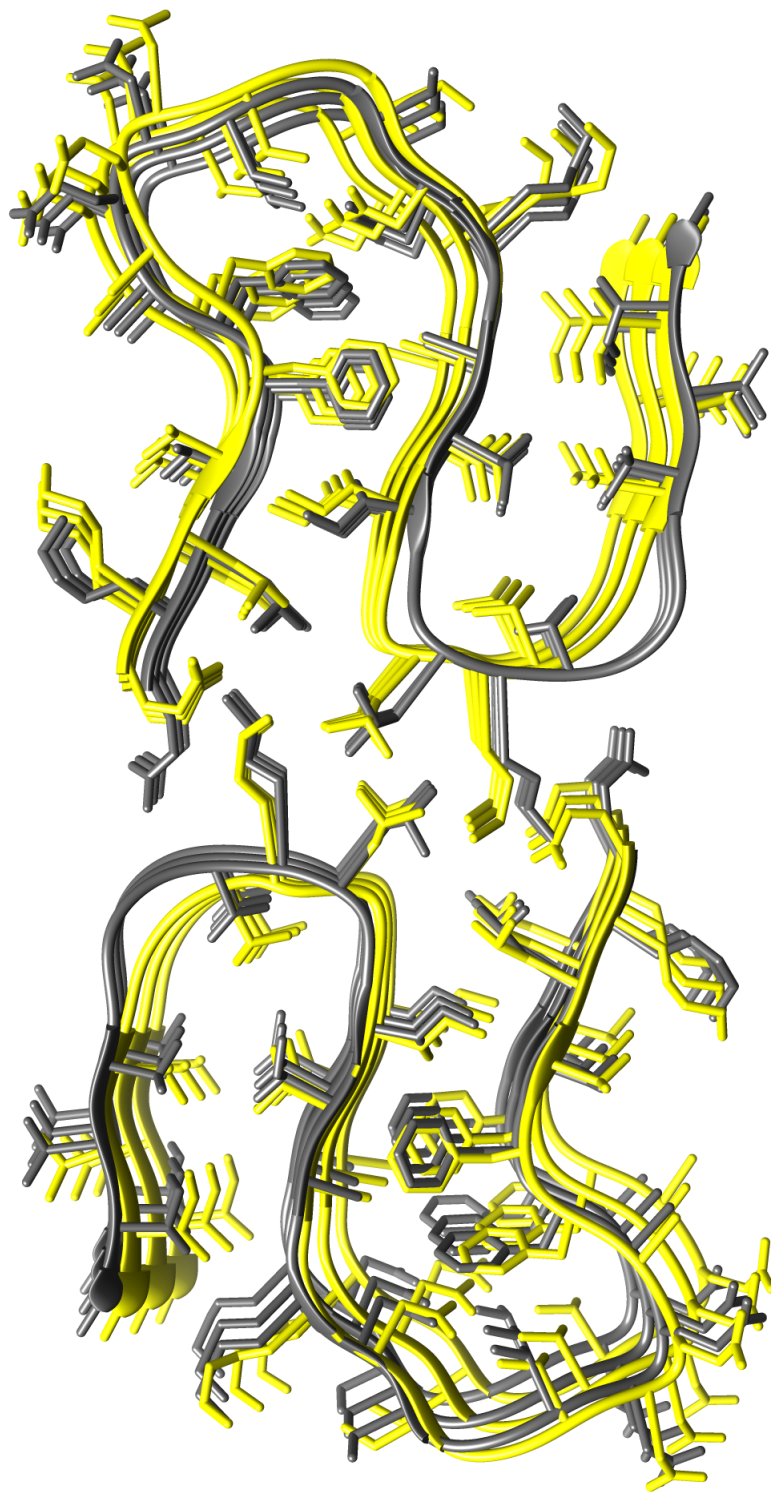


Figure 2.12: Superposition of the 3D structures of the manual calculation and the automatic one. In yellow are 3 layers of the A β (1-42) fibrils using only manually assigned peaks, whereas in grey, automatically picked peaks are included to the structure calculation. The two structures superimpose well with an RMSD of 0.98 Å

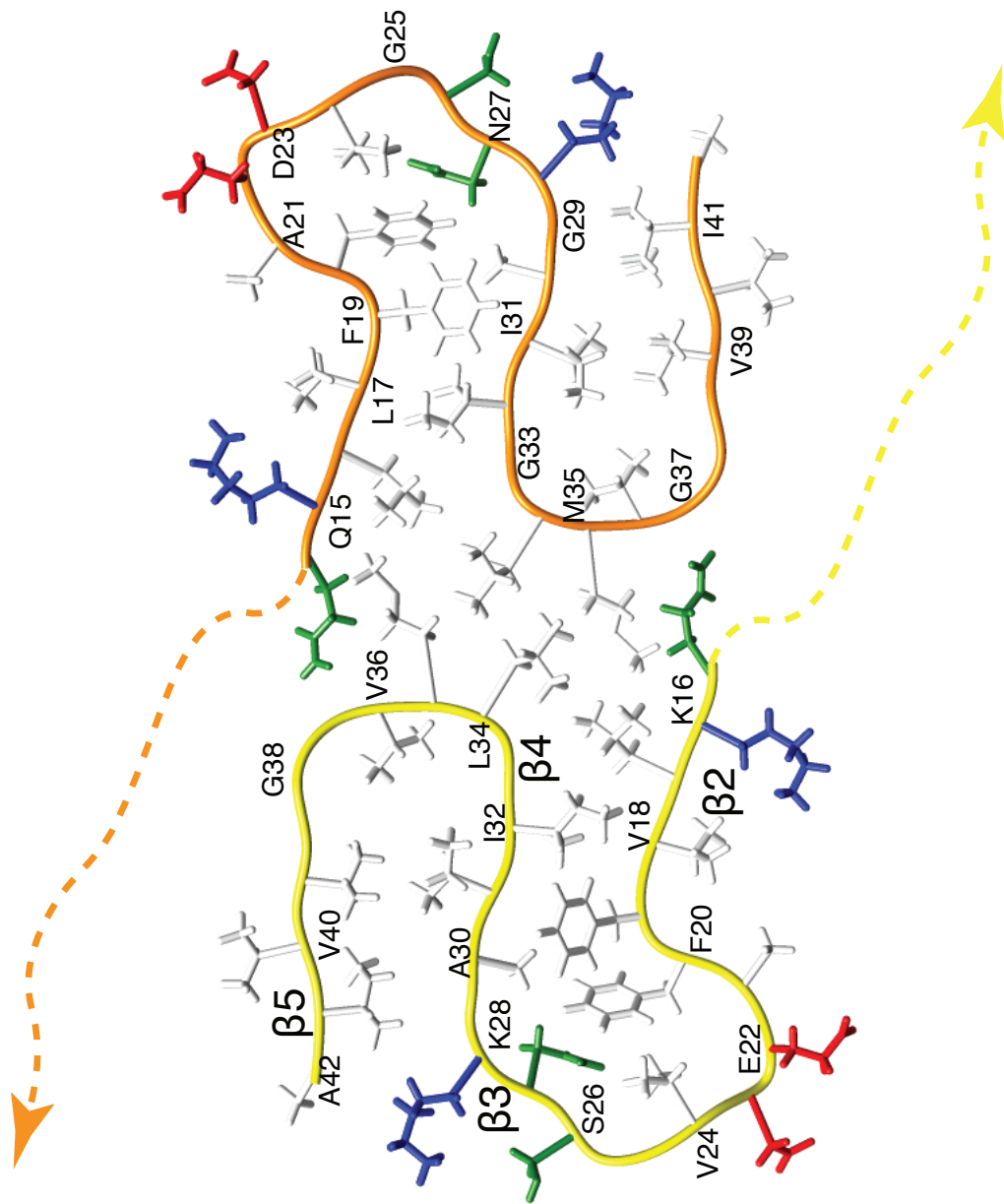


Figure 2.13: Detailed 3D structure of A β (1-42) fibrils represented with the conformer showing the smallest CYANA target function. The backbone of the two point symmetric molecules are shown as yellow and orange spines. The 3D structure of the N-terminal residues 1-14 is only indicated by dotted lines. The side-chains of the positively charge residues are shown in red, the negatively charged in blue, the hydrophobic residues in white, and polar residues (including glycine) in green, respectively. Every second residue is labeled with the one letter amino acid code.

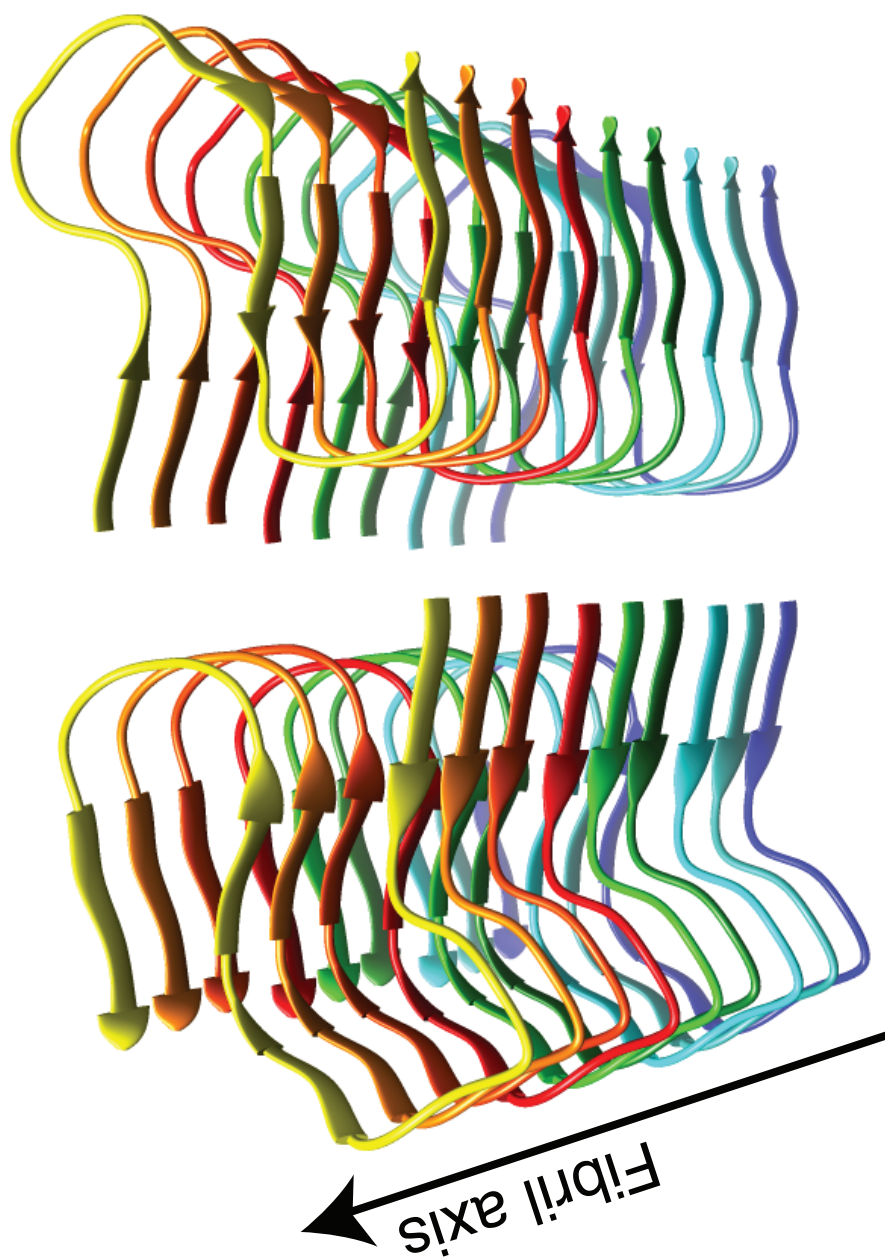


Figure 2.14: A ribbon-based cartoon of the A β (1-42) fibrils showing 9 molecules of A β (1-42) along the fibril axis. Individual molecules are colored following rainbow colors.

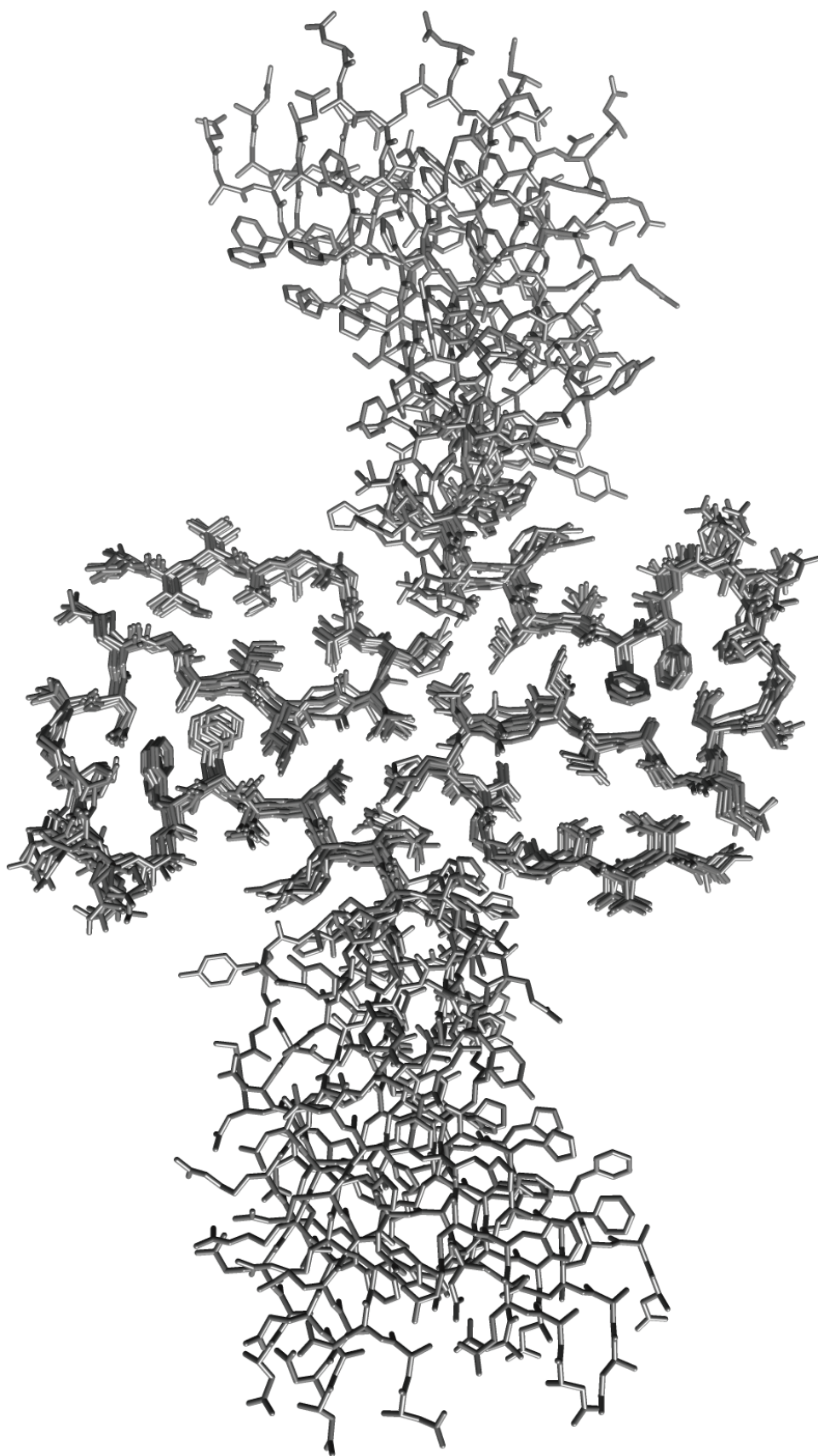


Figure 2.15: A bundle of the 10 conformers having an RMSD of 0.89 Å representing the 3D structure is shown.

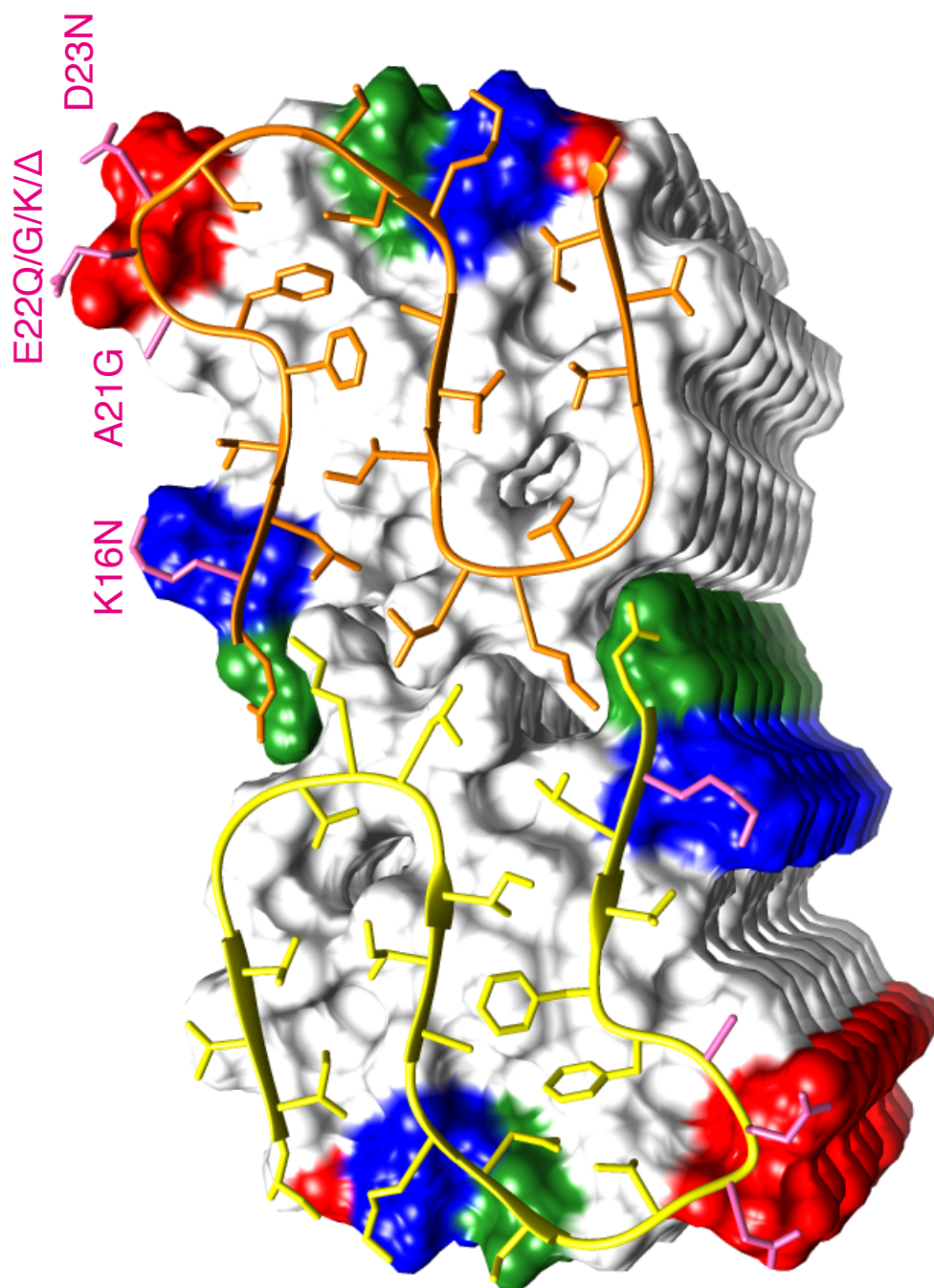


Figure 2.16: Ribbon diagram of the core structure of residues 1542 of A β (1-42) within the fibril. The two point symmetric molecules are shown as yellow and orange spines, respectively. The β -strands are indicated by arrows. The following molecules within the fibril are shown by a surface representation. Positively and negatively charged surface patches are shown in blue and red, respectively, and all hydrophobic residues in white, and polar residues (including glycine) in green. Indicated in pink and labeled accordingly are the residues with known familial Alzheimer's mutations.

2.3 Conclusions

In this chapter, we presented the sequential assignment of A β (1-42). Using 2D and 3D experiments, we fully assigned two stretches of residue 1-10 and 15-42. Intermolecular contacts coming from the [^{13}C - ^{15}N]-PAIN and [^{13}C - ^{15}N]-TEDOR experiments suggest a parallel in-register β -sheet architecture.

We performed structure calculation using input coming from STEM measurement, H/D exchange, limited proteolysis together with NMR-based data, such as dihedral angles, hydrogen bonds and distance restraints and constraints.

The dimeric double horseshoe A β (1-42) structure that we obtained, shown in Figure 2.13-2.14-2.15 and 2.16, is of much greater complexity than the peptide amyloid structures determined by X-ray crystallography [39].

It comprises some of the amyloid-typical structural motifs such as in-register cross- β -sheet secondary structures and Asn/Gln ladders, but the complexity of the fold appears to be dictated by burying maximally the hydrophobic side-chains, a feature usually assigned to soluble evolved proteins and functional amyloids [60].

If maximizing hydrophobic compactness is requested to a sequence that has not been functionally evolved, rather unique structural features may thus arise. Such as the two sequential aromatic side-chains (i.e. Phe 19 and Phe 20) facing both the hydrophobic core, or the two negatively charged side-chains (i.e. Glu 22 and Asp 23) facing both the solvent, as well as the rather now well documented cross- β -sheet motifs and Asn/Gln ladders mentioned above [39].

While not evolutionary evolved, it is noteworthy to mention that also the structure presented here has been undergoing a selection pressure (albeit a rather primitive one) through three cycles of seeded polymerization starting from a series of polymorphs, which are distinct in the core structure since there are significant differences in the chemical shifts for residues Leu 17, Ser 26, Ile 31, and Leu 34 in the various samples and polymorphs, as shown in Figure 2.1.

Further support for the indication that the presented structure is "fit" in a seeded polymerization, is the high similarities of chemical shifts and concomitantly structural similarities with the A β (1-42) fibril samples of the Ishii and the Griffin groups (Appendix A.3), which also were prepared via seeded polymerization albeit under different aggregation conditions [41], [61].

Based on this discussion, the 3D structure of Figure 2.13-2.14-2.15 and 2.16 may thus represent the conformation of a fast-replicating and "fit" polymorph. Since replication and cell-to-cell transmissibility are believed to be key mechanisms in AD [62], [63] it is not surprising that the presented A β (1-42) polymorph is recognized by the same conformation-specific antibodies as the plaques in AD brain slices (Appendix A.2). Thus, the presented 3D structure may be regarded as the culprit of A β (1-42) fibril replication in AD.

Within this hypothesis it is interesting to note that all the known familial Alzheimer’s mutations that are localized in the core of the presented core structure (i.e. K16N, A21G, E22Q, E22G, E22K, E22 Δ , D23N) may favor the determined 3D structure (Figure 2.16, pink colored side chains). While most of them may attenuate inter-molecular charge repulsion (i.e. K16N, E22Q, E22G, D23N and E22K), A21G and E22G may rather relax the backbone restraints due to the quite peculiar side-chain arrangements of F19-F20 and E22-E23 (Figure 2.13), respectively.

In contrast, the further known non AD-linked single nucleotide polymorphism within this segment that cause a missense mutation (i.e. V39I, G38V, G38S, G38C, V36M, I32V, I31V, F19L, V18M) are all conservative mutations (with the exception of G38S and G38C) without expected structural consequences on the A β (1-42) fibril structure.

In summary, we obtained a 3D structure of a A β (1-42) fibril polymorph composed of a complex interplay of hydrophobic interactions and Asn/Gln ladders, that hold together four in register cross- β -strands, may be regarded the causative agent of A β (1-42) fibril replication in AD. It could thus open an avenue for a comprehensive understanding at atomic resolution of key aspects of AD including replication, and cell-to-cell transmissibility as well as structure-assisted developments of potent anti-AD drugs and AD diagnostic markers.

2.4 Experimental Methods

2.4.1 Expression and purification

The plasmid construct containing a N-terminal His-tag followed by a solubility tag (NANP)₁₉ was inserted in *Escherichia coli* and purified as described previously [64].

The peptide was produced according to the required labeling schemes: UL peptide for the resonance assignment and collection of restraints for the structure calculation, ML peptide in a ratio of 1:1, and a diluted sample with UL monomers diluted in unlabeled ones in a ratio of 1:3 for the differentiation of intra- and inter-molecular restraints.

The lyophilized material was dissolved with 10 mM NaOH with the help of a sonication bath (3 times 30 s sonication with 50-60 % power, interrupted by 1 min cooling on ice). To remove large aggregates, the sample was ultracentrifuged for 1 h at 126,000 g. The concentration was adjusted as listed in Appendix A.1.

Further phosphate buffer was added to a final concentration of 100 mM at pH of 7.4 and the required additives were added in the sample. Fibrillization was performed under various shaking conditions at 37° as indicated in Appendix A.1. Seeding was done for 3 generations, 10% of the grand-parent generation was used as seeds for the parent generation, and again 10% for the daughter generation, respectively.

2.4.2 Rotor filling

After the last seeding step, the fibrils, made up of 1520 mg peptide, were centrifuged at 30,000 g over night (SW41-TI swinging bucket, optima L90-K, Beckmann) and re-suspended in MilliQ water. The fibrils were washed for 3 days by gentle shaking. The pellet was again centrifuged at 30,000 g over night, the supernatant was discarded and the fibrils were packed into a 3.2 mm Bruker rotor by ultracentrifugation using a filling device [65]. The drive tip was sealed with epoxy glue (Araldit blue) in order to prevent dehydration of the sample.

2.4.3 Solid - state NMR spectroscopy

The 2D NCA and DARR experiment, performed for sample screening and the TEDOR were measured on a Bruker AVANCE III 600 MHz spectrometer using a 3.2 mm triple resonance probe.

All spectra for the sequential assignment, as well as the experiments measured to derive distance restraints were measured on a Bruker Avance II+ 850 MHz using a Bruker 3.2 mm triple-resonance probe. The sample temperature was determined, using the water resonance frequency, to be around 4°C. All spectra were apodized with a Shifted Sine Bell window function (SSB of 2.2 2.7). The processing was done by TopSpin 3.1 (Bruker Biospin) and the analysis was performed with CcpNMR analysis 2.3 [47], [48].

All experimental parameters are displayed in Table 2.2 and Table 2.3.

2.4.4 Structure calculation

Structure calculations followed the protocol established for fibril structure determinations by solid - state NMR with CYANA [33].

A first structure calculation was performed using only the manually assigned distance restraints listed in Table 2.5. This structure was subsequently used as additional input for a structure calculation with automated distance restraint assignment [59].

The first cycle of combined automated distance restraint assignment and structure calculation was skipped and replaced by the aforementioned manual structure calculation. In all calculations hydrogen-bond restraints for the β -sheets, backbone torsion angle restraints, and symmetry restraints [66] were used. 500 conformers were calculated using 35,000 torsion angle dynamics steps in CYANA [58].

The final structure was calculated as a consensus structure bundle [67] of 10 conformers with lowest target function values that are used to represent the 3D structure of $A\beta$ (1-42) fibrils. Structural statistics are given in Table 2.4.

Experiment	NCACX	NCOCX	NCACB	CANCO	CCC	NCA	NCO	DARR 20ms
¹ H Larmor frequency	850 MHz	850 MHz	850 MHz	850 MHz	850 MHz	850 MHz	850 MHz	850 MHz
Isotope labeling	[UL ¹³ C- ¹⁵ N]	[UL ¹³ C- ¹⁵ N]	[UL ¹³ C- ¹⁵ N]	[UL ¹³ C- ¹⁵ N]	[UL ¹³ C- ¹⁵ N]	[UL ¹³ C- ¹⁵ N]	[UL ¹³ C- ¹⁵ N]	[UL ¹³ C- ¹⁵ N]
MAS frequency [kHz]	19	19	19	19	19	19	19	19
Transfer 1	HN-CP	HN-CP	HN-CP	HC-CP	HC-CP	HN-CP	HN-CP	HC-CP
Field [kHz] - ¹ H	80.3	80.3	80.3	90.1	80.3	80.3	80.3	74.9
Field [kHz] - X	57.4	57.4	57.4	70.2	67.8	57.4	57.4	57.6
Shape	tangent	tangent	tangent	tangent	tangent	tangent	tangent	tangent
Carrier [ppm]	-	-	-	C α	-	-	-	-
Time [ms]	1.4	1.4	1.4	0.35	0.35	1.4	1.4	0.9
Transfer 2	NC-CP	NC-CP	NC-CP	CN-CP	DREAM	NC-CP	NC-CP	DARR
Field [kHz] - ¹ H	-	-	-	-	90.1	-	-	18.7
Field [kHz] - ¹³ C	5.2	5.2	5.2	5.2	9.2	5.2	5.2	-
Field [kHz] - ¹⁵ N	22.5	22.3	22.5	22.8	-	22.5	22.3	-
Shape	tangent	tangent	tangent	tangent	tangent	tangent	tangent	-
Carrier [ppm]	C α	CO	C α	C α	52	C α	CO	-
Time [ms]	7	7	7	7	4	7	7	20
Transfer 3	DARR	DARR	DREAM	NC-CP	DARR	-	-	-
Field [kHz] - ¹ H	20.1	20.1	89.1	-	20.1	-	-	-
Field [kHz] - ¹³ C	-	-	9.1	5.2	-	-	-	-
Field [kHz] - ¹⁵ N	-	-	-	22.3	-	-	-	-
Shape	-	-	tangent	tangent	-	-	-	-
Carrier [ppm]	-	-	52	CO	-	-	-	-
Time [ms]	80	65	4	7	80	-	-	-
t ₁ increments	96	112	100	92	200	768	768	2560
Sweep width (t ₁) [kHz]	6	7	40	8	20	40	40	100
Max acq time (t ₁) [ms]	8.00	8.00	7.14	5.75	5.00	9.60	9.60	12.80
t ₂ increments	100	76	108	108	200	1536	1536	3968
Sweep width (t ₂) [kHz]	8	6	9	7	20	50	50	100
Max acq time (t ₂) [ms]	6.25	6.33	6.00	7.71	5.00	15.36	15.36	19.84
t ₃ increments	2560	2560	2048	2560	2560	-	-	-
Sweep width (t ₃) [kHz]	100	100	100	100	100	-	-	-
Max acq time (t ₃) [ms]	12.80	12.80	10.24	12.80	12.80	-	-	-
¹ H SPINAL64 Dec. [kHz]	90	90	90	90	90	90	90	90
Interscan delay [s]	2.5	2.5	2	2.9	2.1	2.5	2.5	3
Number of scans	8	8	8	8	4	16	16	8
Measurement time [h]	53.7	47.6	48.4	64.3	93.7	8.6	8.6	17.3

Table 2.2: Experimental parameters for the NMR spectra used for the sequential assignment procedure. All fields in kHz are calculated from reference fields (100 kHz, 62.5 kHz, 50.0 kHz). Actual values might deviate significantly from calculated ones.

Experiment	DARR 200ms	DARR 400ms	DARR 400ms	CHHC 400 μ s	CHHC 400 μ s	CHHC 400 μ s	PAR 8ms	PAR 8ms	PAIN 6ms	NHHC	TEDOR
¹ H Larmor frequency	850 MHz	850 MHz	850 MHz	850 MHz	850 MHz	850 MHz	850 MHz	850 MHz	850 MHz	850 MHz	600 MHz
Isotope labeling	[UL ¹³ C- ¹⁵ N]	[UL ¹³ C- ¹⁵ N]	[UL ¹³ C- ¹⁵ N]	[UL ¹³ C- ¹⁵ N]	[UL ¹³ C- ¹⁵ N]	[UL ¹³ C- ¹⁵ N]	Diluted	[ML ¹³ C- ¹⁵ N]	[ML ¹³ C- ¹⁵ N]	[ML ¹³ C- ¹⁵ N]	[ML ¹³ C- ¹⁵ N]
MAS frequency [kHz]	15	15	15	15	15	15	15	15	17	17	12.5
Transfer 1	HC-CP	HC-CP	HC-CP	HC-CP	HC-CP	HC-CP	HC-CP	HN-CP	HN-CP	HN-CP	HN-CP
Field [kHz] - ¹ H	80.3	81.2	78.5	79.4	79.4	79.4	75.8	69.1	69.1	68.3	50.0
Field [kHz] - X	63.2	63.2	67.8	68.6	67.8	67.8	65.5	55.0	55.0	56.3	40.2
Shape	tangent	tangent	tangent	tangent	tangent	tangent	tangent	tangent	tangent	tangent	tangent
Carrier [ppm]	-	-	-	Ca	Ca	Ca	-	-	-	-	-
Time [ms]	0.9	0.9	0.9	0.5	0.5	0.5	0.9	0.9	1.2	1.2	0.9
Transfer 2	DARR	DARR	DARR	H-H mixing	H-H mixing	H-H mixing	PAR	PAR	PAR	PAR	TEDOR
Field [kHz] - ¹ H	17.9	18.1	18.5	-	-	-	53.6	51.8	38.8	38.8	-
Field [kHz] - ¹³ C	-	-	-	-	-	-	52.0	52.6	36.7	36.7	50
Field [kHz] - ¹⁵ N	-	-	-	-	-	-	-	-	35.7	35.7	50
Shape	-	-	-	-	-	-	-	-	-	-	-
Carrier [ppm]	-	-	-	-	-	-	60	60	-	-	-
Time [ms]	200	400	400	0.4	0.4	0.4	8	8	6	6	0.5
t ₁ increments	2560	2048	2048	1856	1856	1856	2816	2816	2560	2560	1536
Sweep width (t ₁) [kHz]	100	100	100	100	100	100	100	100	50	50	12.5
Max acq time (t ₁) [ms]	12.80	10.24	10.24	9.28	9.28	9.28	9.28	9.28	7.68	7.68	10.24
t ₂ increments	3072	3024	2560	2816	2816	2816	2816	2816	2560	2560	1536
Sweep width (t ₂) [kHz]	100	100	100	100	100	100	100	100	100	100	50
Max acq time (t ₂) [ms]	15.36	15.12	12.80	14.08	14.08	14.08	14.08	14.08	12.80	12.80	15.36
¹ H SPINAL64 Dec. [kHz]	90	90	90	90	90	90	90	90	90	90	90
Interscan delay [s]	2	2	2	2.3	2.3	2.3	2.5	2.5	2.8	2.8	2.5
Number of scans	64	91	152	96	240	240	168	168	480	480	1024
Measurement time [h]	100.8	124.9	208.6	114.5	286.1	286.1	218.3	218.3	288.5	225.3	184.0

Table 2.3: Experimental parameters for the NMR spectra used for structure calculation. All fields in kHz are calculated from reference fields (100 kHz, 62.5 kHz, 50.0 kHz). Actual values might deviate significantly from calculated ones.

Table 2.4: Restraint and structure statistics.

Quantity	manual and automated analysis	manual analysis
Conformational restraints (per monomer): ^a		
Distance restraints from solid state NMR spectra: ^a	632	81
intraresidual	18	0
sequential ($ i - j = 1$)	215	1
medium range ($2 \leq i - j \leq 4$)	202	21
long range ($ i - j \geq 5$)	197	59
intramolecular	507	20
intra- or intermolecular	108	58
intermolecular	17	3
Restrained hydrogen bonds ^b	16	16
Dihedral angle restraints (ϕ/ψ)	38	38
Restraint violations: ^c		
CYANA target function value (\AA^2)	1.90 ± 0.04	0.95 ± 0.34
RMS distance restraint violation (\AA)	0.0023 ± 0.0005	0.0022 ± 0.0006
Maximal distance restraint violation ($^\circ$)	0.19	0.09
RMS dihedral angle restraint violation (\AA)	0.10 ± 0.08	0.018 ± 0.035
Maximal dihedral angle restraint violation ($^\circ$)	1.99	1.01
RMSD to mean for the central 2 monomers:		
Backbone of residues 15–42 (\AA)	0.89 ± 0.19	1.01 ± 0.16
All heavy atoms of residues 15–42 (\AA)	1.14 ± 0.16	1.26 ± 0.14

^aEach group of symmetrically equivalent distance restraints is counted as a single restraint. Distance restraints with multiple assignments are classified by the assignment spanning the shortest residue range.

^bEach hydrogen bond was restrained by two upper and two lower distance bounds.

^cWhere applicable, the average value and the standard deviation over the 10 conformers that represent the NMR structure are given.

PAR	ω_1	ω_2
I31,I32 - V36	I31 C γ 2 I31 C γ 2	V36 C γ 1
L17 - M35	L17 C γ	L17 C ϵ
L17 - I31, 32, 41	L17 C γ	I31 C δ 1 I32 C δ 1 I41 C δ 1

CHHC	ω_1	ω_2
K16, L17, K28, M35 - I41	K16 H α L17 H α K28 H α M35 H α	I41 Q γ 2
L17 - D23, I32	L17 H γ	D23 H β I32 H β
L17, V24 - D23, I32	L17 Q δ 1 V24 Q γ 2	D23 H β I32 H β D23 H β I32 H β
K28 - I32, I41	K28 C γ	I32 Q γ 2 I41 Q γ 2
G29 - I41	G29 Q α	I41 H β
A30, V36 - G33	A30 H β V36 Q γ 2	G33 Q α
G33 - V36	G33 Q α	V36 Q γ 1
Q15 - M35	Q15 Q ϵ	M35 Q ϵ
L17 - M35	L17 H γ	M35 Q ϵ
F19 - N27	F19 Q δ	N27 Q β
F19 - I32	F19 Q ζ	I32 H β
K28 - I41	K28 Q δ	I41 Q γ 2
I31 - V36	I31 Q γ 2	V36 Q γ 1
L17, V24 - N27	L17 Q δ 1 V24 Q γ 1	N27 Q β
V18, V24 - N27	V18 Q γ 1 V24 Q γ 1	N27 Q β

DARR	ω_1	ω_2
L17 - L34	L17 C γ	L34 C β
K28 - I41	K28 C δ	I41 C β
K28 - A42	K28 C δ	A42 C
G29 - I41	G29 C α	I41 C β
I31 - V36	I31 C β	V36 C γ_1
N27, A42 - A30	N27 C α	A30 C α
	A42 C α	
G29 - I32, I41	G29 C α	I32 C γ_2
		I41 C γ_2
Q15 - M35	Q15 C δ	M35 C ϵ
L17 - M35	L17 C γ	M35 C ϵ
L17, V24 - M35	L17 C δ_1	M35 C ϵ
	V24 C γ_2	
F19 - G29	F19 C ϵ	G29 C α
F19 - I31	F19 C δ_1	I31 C β
K28 - I41	K28 C δ	I41 C γ_2
K28 - A42	K28 C γ	A42 C
G33 - V36	G33 C α	V36 C γ_1
L17, V24 - N27	L17 C δ_1	N27 C β
	V24 C γ_2	
G29, G38 - A42	G29 C α	A42 C
	G38 C α	
L17 - I32, L34	L17 C γ	I32 C γ_1
		L34 C δ_2
F19 - A30, V36	F19 C ζ	A30 C β
		V36 C γ_2

Table 2.5: Manually assigned restraints for the structure calculation. In grey are the intra-molecular restraints, in pink the inter-molecular ones, and no color shows that the restraint can not be classified as inter- or intra-molecular. The restraints have been collected from the PAR, the CHHC or the DARR spectra as indicated and each restraint in the PAR and DARR are derived from four cross peaks.

Chapter 3

Structure determination of the mouse ASC-PYD filament

This chapter is based on two publications:

Lorenzo Sborgi, Francesco Ravotti, Venkata P. Dandey, Mathias S. Dick, Adam Mazur, Sina Reckel, Mohamed Chami, Sebastian Scherer, Matthias Huber, Anja Böckmann, Edward H. Egelman, Henning Stahlberg, Petr Broz, Beat H. Meier, and Sebastian Hiller **2015**. Structure and assembly of the mouse ASC inflammasome by combined NMR spectroscopy and cryo-electron microscopy. *Proceedings of the National Academy of Sciences of the United States of America* doi: 10.1073/pnas.1507579112.

Francesco Ravotti, Lorenzo Sborgi, Riccardo Cadalbert, Matthias Huber, Adam Mazur, Petr Broz, Sebastian Hiller, Beat H. Meier, and Anja Böckmann **2015**. Sequence-specific solid - state NMR assignments of the mouse ASC PYRIN domain in its filament form. *Biomolecular NMR Assignments* doi: 10.1007/s12104-015-9647-6. Me and Lorenzo wrote the initial manuscript, which were revised by Sebastian, Anja and Beat. I performed solid state NMR experiments and analysed the restraints spectra, Lorenzo the solution state NMR experiments and Adam performed the structure calculation, combining cryo EM and solid state NMR data.

3.1 Introduction

Inflammasomes are multiprotein complexes that control the innate immune response by activating caspase-1, thus promoting the secretion of cytokines in response to invading pathogens and endogenous triggers. Many of these complexes present a receptor to the adapter protein ASC (Apoptosis - associated speck - like protein), that plays a central role in eukaryotic innate immune response. Upon infection, multiple ASC molecules assemble to long filaments which facilitate procaspase-1 recruitment. ASC is composed of two domains, the C-terminal caspase-recruitment domain (CARD), which is involved in the recruitment of the caspase, and the N-terminal PYRIN domain (PYD), which is

responsible for the formation of the filament.

In this chapter we present the structure of the mouse ASC filament produced in vitro at atomic resolution. We describe furthermore a new hybrid approach between solid - state NMR techniques and cryo - electron microscopy (cryo - EM) that have been used to calculate the structure. Cryo - EM density maps do not recover disordered or dynamic polypeptide segments, but solid - state NMR spectroscopy renders data from both the rigid and dynamic parts of a molecular assembly. The two techniques thus can provide complementary information.

Further comparison of solid - state NMR and solution - state NMR data are used to identify the interactions sites for the formation of the filament. Finally, the characterization of the CARD domain using solid - state NMR experiments is presented.

3.1.1 Biological context

The innate immune system detects and responds to different types of pathogen - and danger - associated molecular patterns (PAMPs and DAMPs, respectively) at minimal concentrations via specific, germline - encoded pattern - recognition receptors (PRRs) [68], [69], [70]. A subset of cytosolic PRRs respond to PAMPs and DAMPs by initiating the assembly of cytosolic macromolecular inflammasome complexes [71], [72], [73] and eventually leads to an inflammatory cascade. This cascade starts with the activation of caspase-1 and the maturation of the inflammatory cytokines Interleukin 1β (IL- 1β) and Interleukin 18 (IL-18), leading eventually to apoptosis of the cell. It has been shown that the structures of inflammasome complexes are crucial for the efficiency of the immune response [71] [74]; moreover, malfunctions of such oligomers are related to human disease, such as cancer and autoimmune syndromes [75]. The signaling pathway from the PRRs to the activation of caspase-1 is mediated in many cases by the bipartite adaptor protein ASC (Apoptosis - associated speck - like protein), which consists of an N - terminal PYD and a C - terminal CARD. The structure of the PYD and ASC monomer has been determined by solution - state NMR methods ([76], [77]), showing that these domains tumble independently in solution and are connected by a flexible linker. In ASC - dependent inflammasomes, the PYD oligomerizes upon interaction with the receptor to form the so-called ASC speck, and the C-terminal CARD subsequently recruits the inflammatory caspase. The large ASC filament thus forms the structural core of the ASC - inflammasome [78].

3.2 Results and discussion

3.2.1 NMR screening of the filaments

In general, the atomic structure of filaments depends on the assembly conditions in vivo and in vitro, and polymorphism is common in some systems [44], [79]. We characterized

the homogeneity of the sample preparation by measuring solid - state NMR spectra, namely 2D ^{13}C - ^{13}C 20 ms DARR (Figure 3.1) and 2D NCA (Figure 3.2), on the filaments composed by the PYD alone (red spectra) and on the full length (FL) ASC (blue spectra). These correlation spectra of both samples present narrow lines (line width of cross peaks on the order of 0.5 ppm for ^{13}C), which is a clear indication of a homogeneous sample. The spectra of the filaments composed by the PYD alone look extremely similar to the FL filaments, indicating that the CARD domain is essentially invisible in solid - state NMR experiments. Further information on the CARD domain is shown in Paragraph 3.2.7. From the perfect correspondence of cross peaks, we can deduce that the presence of the CARD does not perturb the structure of the PYD. We can conclude from the analysis of the spectra that the scaffold of the filament is formed by the PYD alone and the two domains are independent, as also shown in [76] for the monomeric form of ASC.

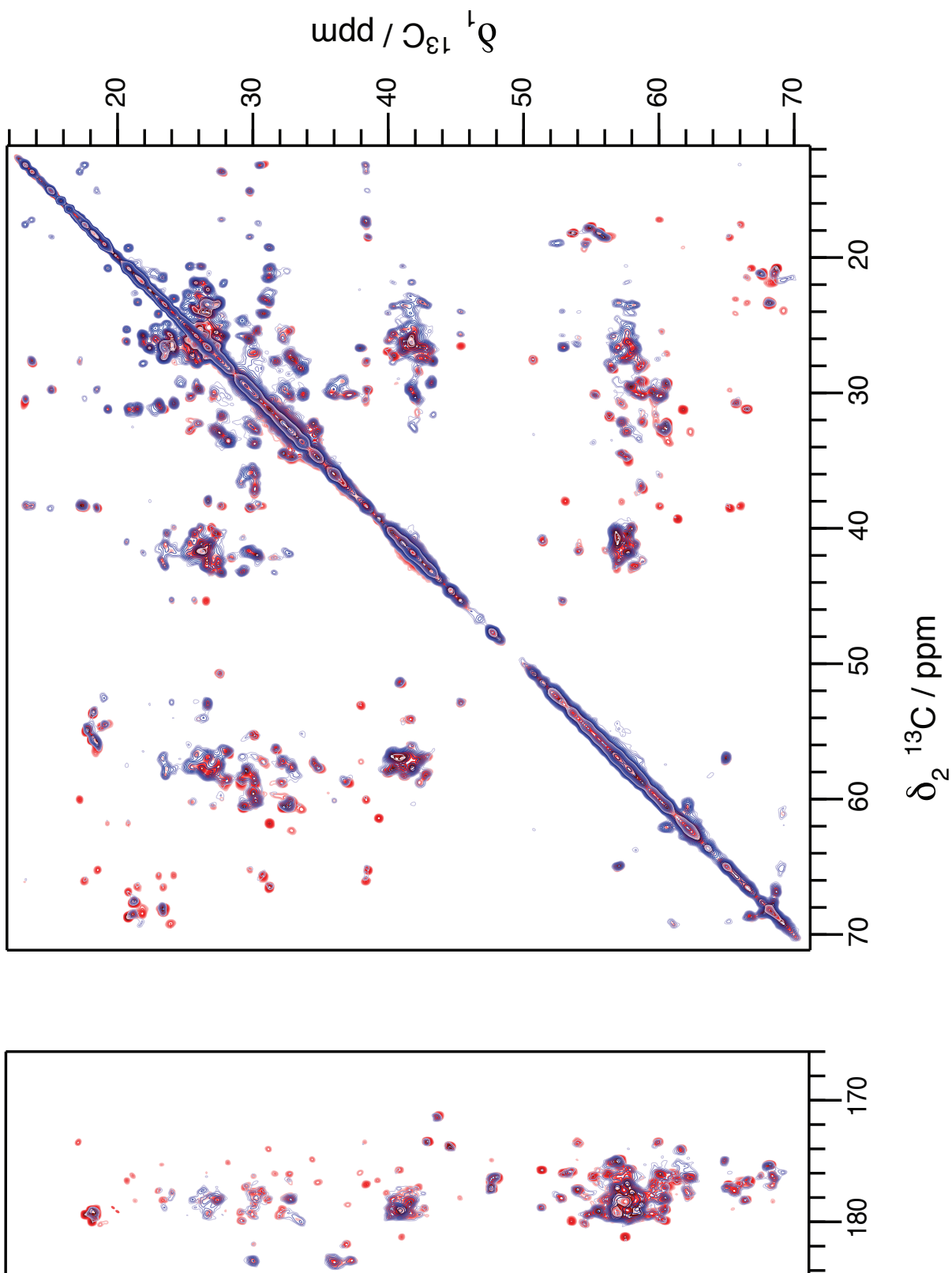


Figure 3.1: Comparison of 2D ^{13}C - ^{15}N DARR spectrum with a mixing time of 20 ms measured on uniformly [^{13}C - ^{15}N] labeled filaments of PYD alone (red) and full-length ASC (blue). Experiments were measured at 20.0 T magnetic field setting the MAS frequency to 17 kHz

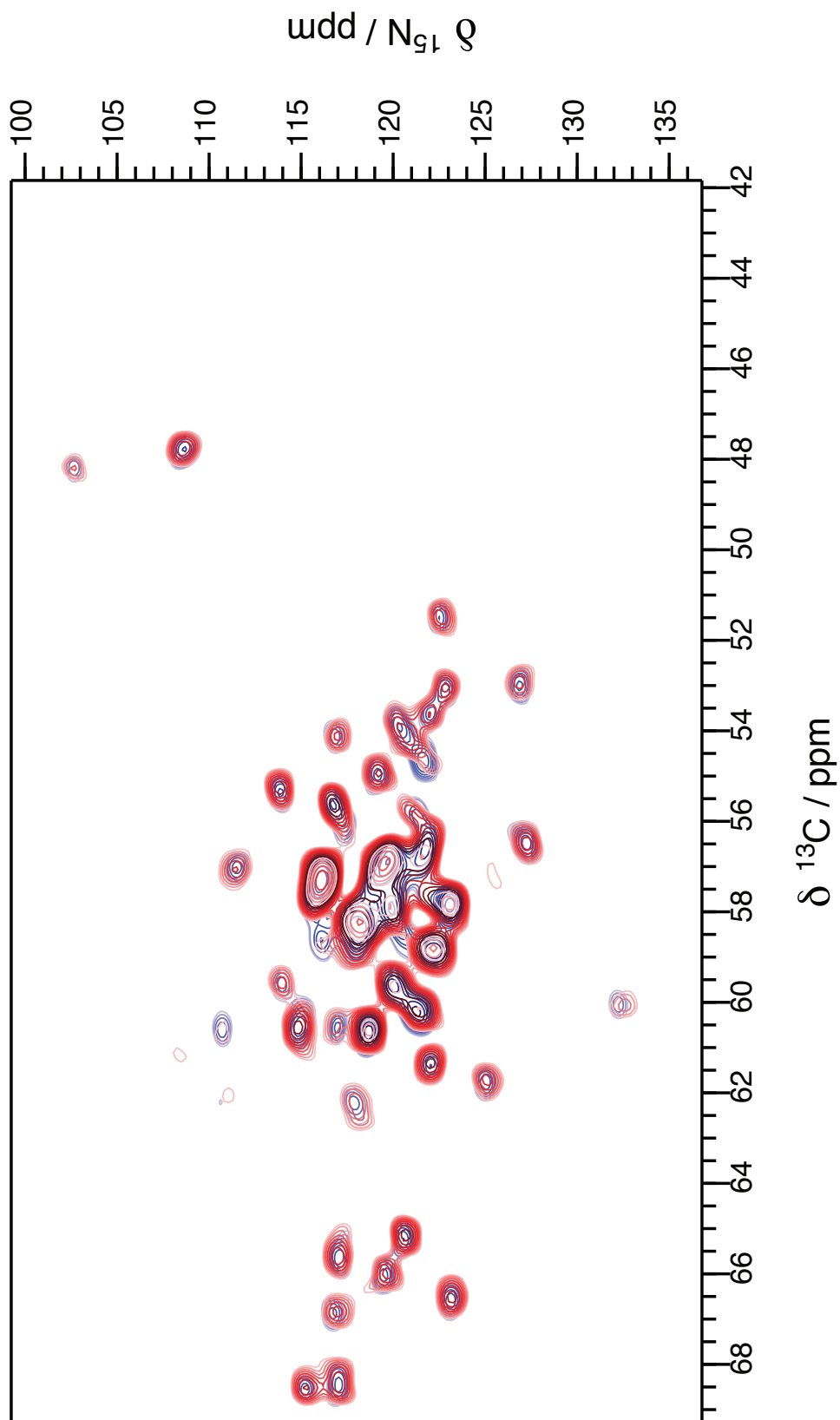


Figure 3.2: Comparison of 2D NCA spectrum measured on uniformly [^{13}C - ^{15}N] labeled filaments of PYD alone (red) and full - length ASC (blue). Experiments were measured at 20.0 T magnetic field setting the MAS frequency to 17 kHz

3.2.2 Sequential assignment

After the observations presented in Paragraph 3.2.1, we used the UL [^{13}C - ^{15}N] sample formed without the CARD domain.

We performed the standard set of 2D and 3D experiments [49], [50] to perform the backbone walk, namely NCACO, NCACB, CANCO and NCOCA. The relayed 3D experiments (NcoCACB and CANcoCA) where no evolution of the C' was recorded due to small dispersion of chemical shifts in this region, were fundamental to reduce the ambiguities in some stretches of the protein. For the C' - $C\alpha$ transfer, which is critical for these experiments, we have used the efficient band selective homonuclear cross polarization [80]. Experimental details are shown in Table 3.4.

We assigned all backbone atoms of residue 3 - 85 using these experiments. In Figure 3.3 a representative strip plot of the sequential backbone assignment is shown.

The assignment was completed by measuring 2D ^{13}C - ^{13}C DARR spectrum and 3D N(CA)CBCX and CCC, obtaining 80% of all the ^{13}C sidechains (92% of the assigned backbone residues) as shown in Figure 3.4. The missing nuclei were either not visible in the spectra due to local dynamics (as for side chains of 5 Arg 5, Met 25 $C\epsilon$, Met 70 $C\epsilon$) or not assignable due to spectral overlap (as for $C\gamma$ Asp 6, Asp 51 and Asp 54).

A summary of the assigned atoms is shown in Figure 3.5 and the assigned chemical shifts are presented in Table 3.1. The filaments present no polymorphism: all the peaks present in the 20 ms DARR (Figure 3.6) and NCA (Figure 3.7) were assigned, with the exception of two additional weak threonine signals present in the DARR. Most likely, these two signals arise from Thr 87 and Thr 88, but no nitrogen resonance and no connectivity information could be obtained from the different spectra.

The first 3 and the last 6 residues were only visible in some of the dipolar - transfer - based NMR spectra and could not be sequentially assigned with certainty. We performed an INEPT - type [^{15}N ^1H] spectrum of the ASC PYD filaments to investigate the flexibility of these stretches, but it was devoid of peaks. We concluded that these residues experience dynamics on the intermediate time scale, and are thus line - broadened below the detection limit using either solution - or solid - state NMR methods.

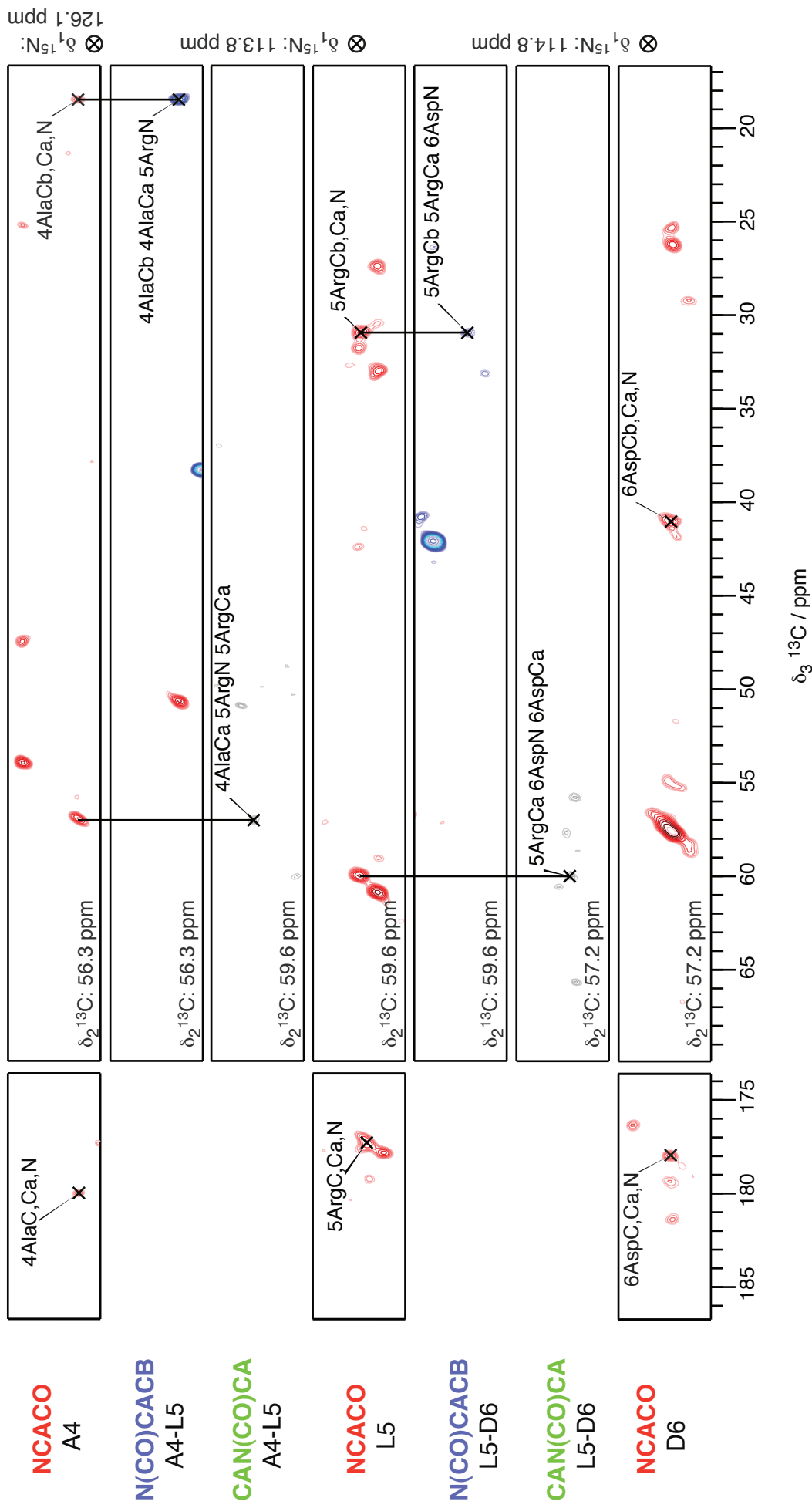


Figure 3.3: Strips extracted from the 3D NCACO (red), N(CO)CACB (blue) and CAN(CO)CA (green) spectra of [UL-¹³C-¹⁵N] PYD filaments. Vertical lines were added to aid following the backbone walk starting at the first visible residue at N-terminus of the protein

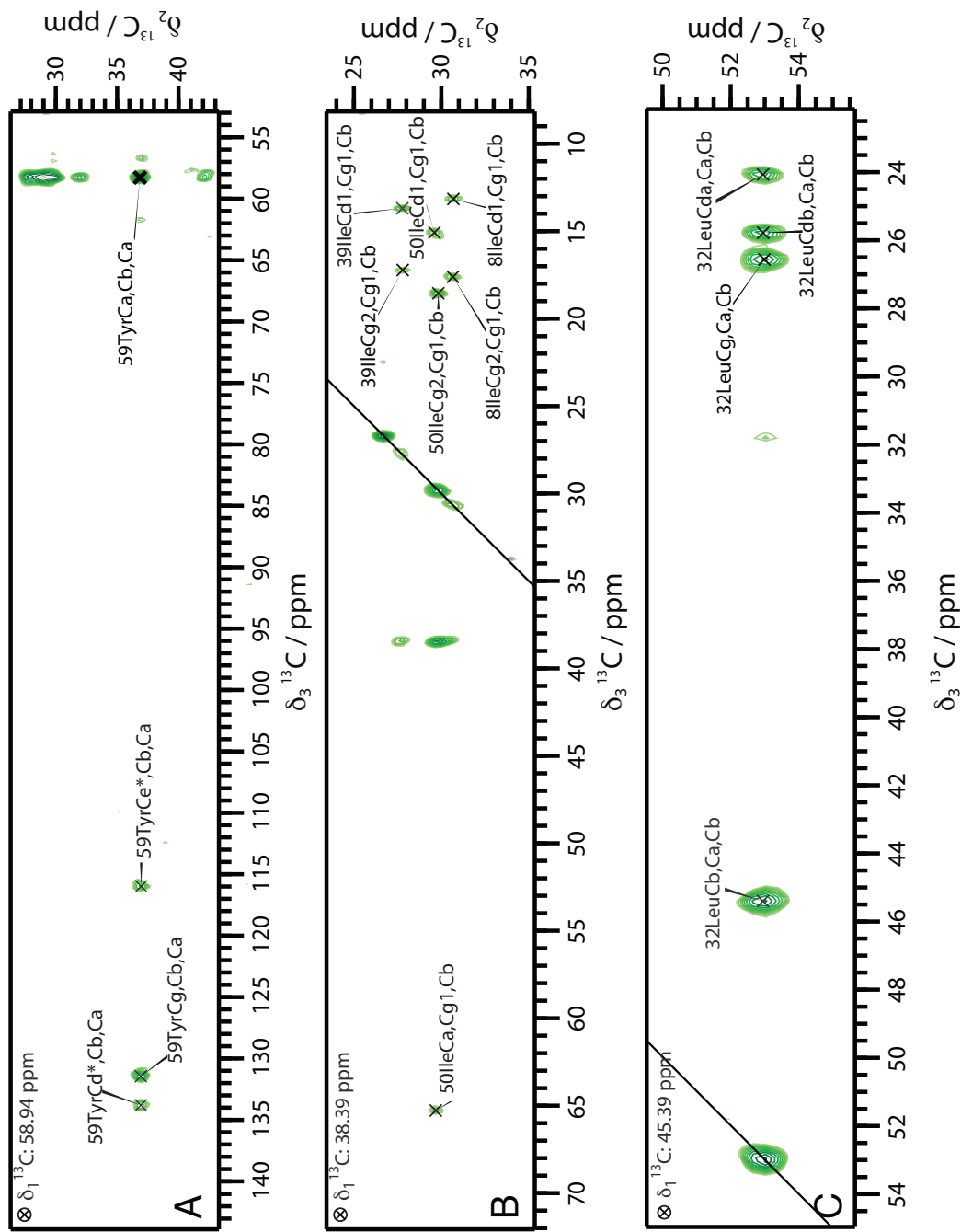


Figure 3.4: Strips extracted from the 3D CCC spectrum of ASC - PYD filaments, used for the assignment of the sidechains. In a CCC spectrum, polarization transfers are selected to mainly display $\text{C}\alpha$ resonances in the first dimension, $\text{C}\beta$ in the second and the remaining side chains in the third dimension. In (A) aromatic sidechains for Tyr 59 are shown, in (B) sidechains for different Ile and in (C) for Leu 32.



Figure 3.5: Sequential assignment graph showing all carbon and nitrogen atoms of ASC - PYD filaments by circles. The assigned atoms are shown in black, whereas the unassigned ones are shown in grey. The graph was designed with the software CcpNMR 2.3 analysis [47], [48]

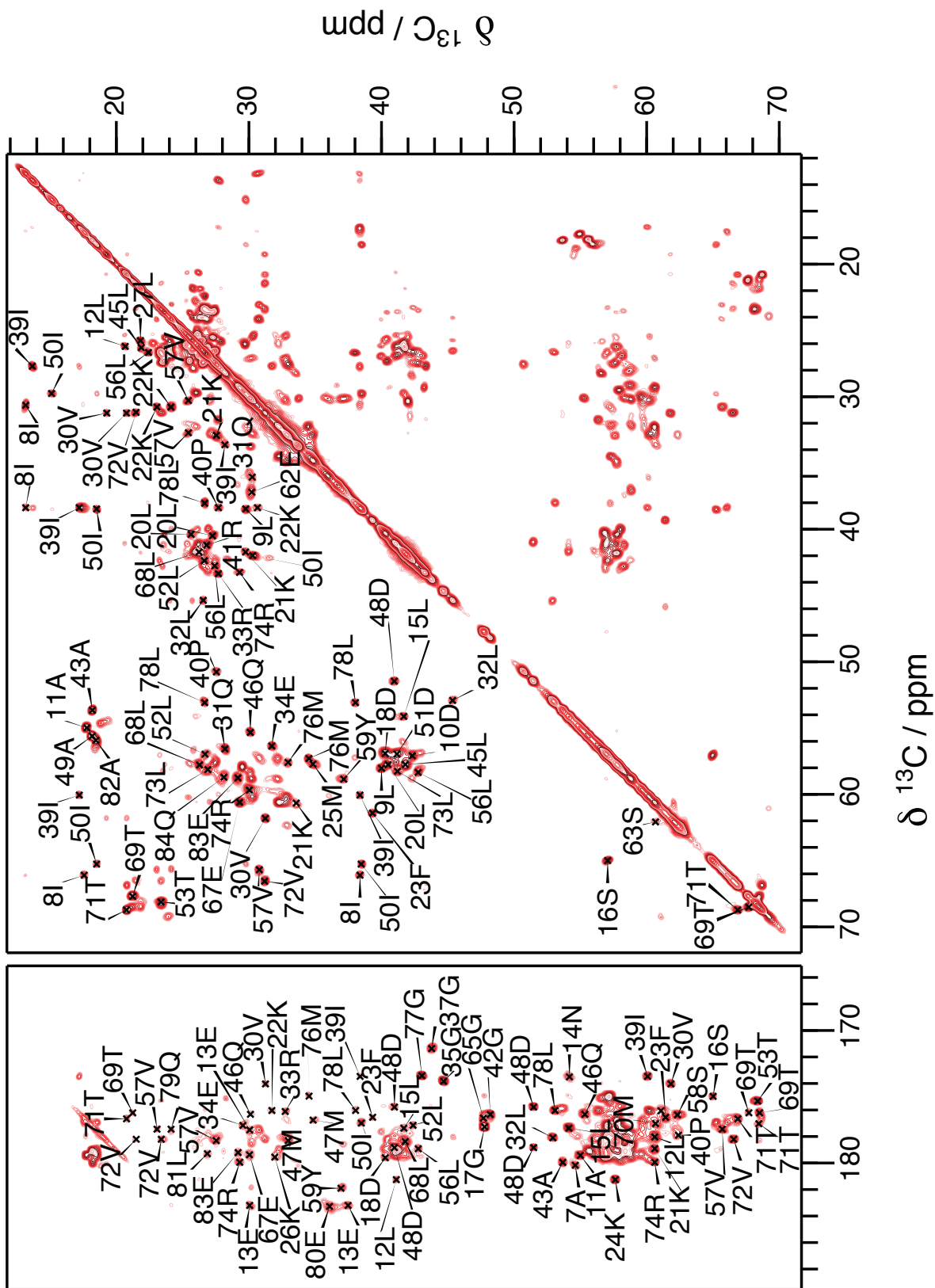


Figure 3.6: 2D ^{13}C - ^{15}N DARR spectrum with a mixing time of 20 ms measured on uniformly [^{13}C - ^{15}N] labeled filaments of PYD alone. This experiment was measured at 20.0 T magnetic field setting the MAS frequency to 17 kHz

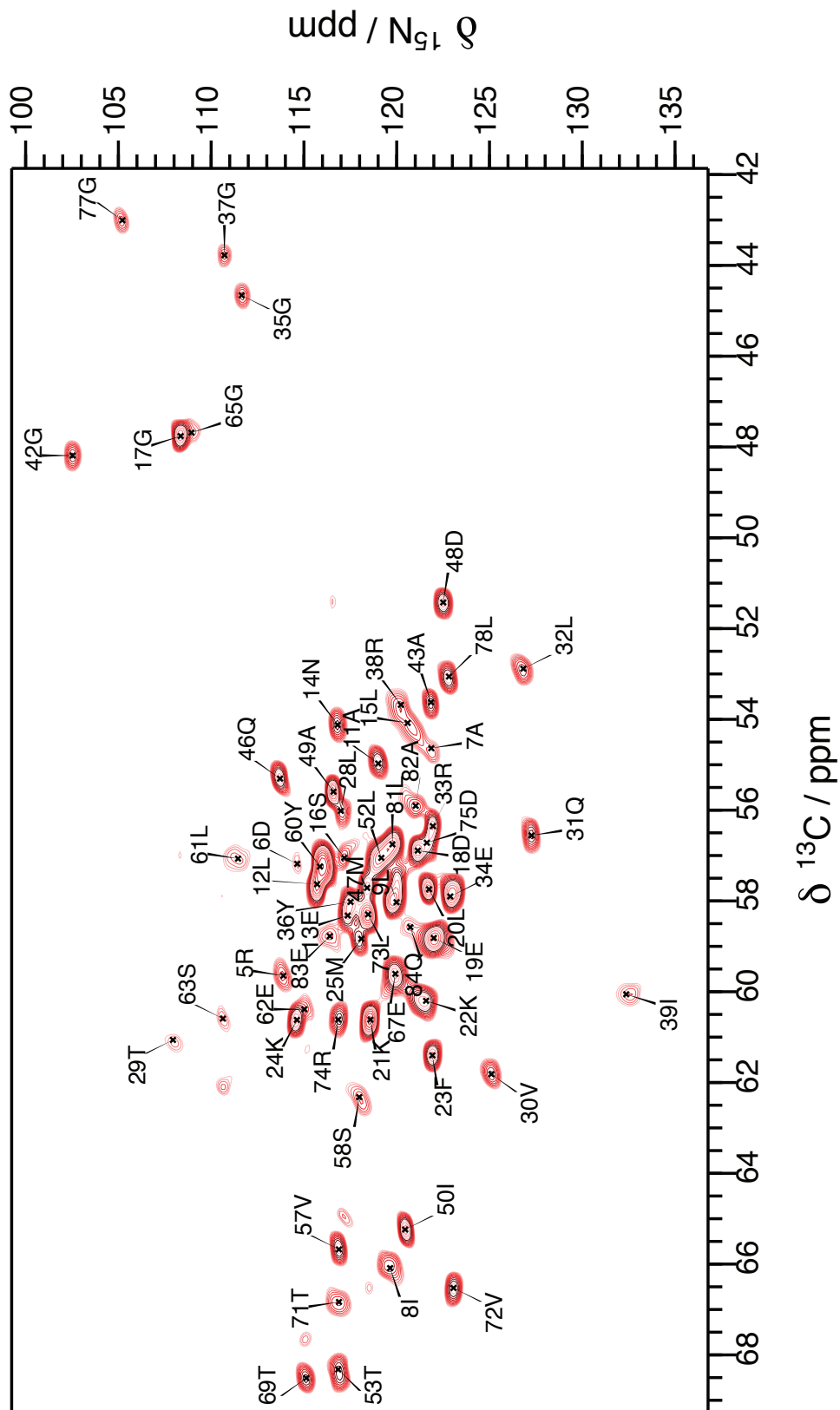


Figure 3.7: 2D NCA spectrum measured on uniformly [^{13}C - ^{15}N] labeled filaments of PYD alone. This experiment was measured at 20.0 T magnetic field setting the MAS frequency to 17 kHz

Residue	N	N γ	N η	N ζ	C	C α	C β	C γ	C δ	C ϵ	C ζ
3 Arg	-	-	-	-	177.6	-	-	-	-	-	-
4 Ala	126.1	-	-	-	179.5	56.3	18.6	-	-	-	-
5 Arg	113.8	-	-	-	177.4	59.7	30.7	-	-	-	-
6 Asp	114.8	-	-	-	178.0	57.2	40.8	-	-	-	-
7 Ala	121.8	-	-	-	180.1	54.6	19.0	-	-	-	-
8 Ile	119.7	-	-	-	176.7	66.1	38.4	30.6, 17.6	13.2	-	-
9 Leu	119.9	-	-	-	177.7	58.0	40.0	26.9	26.3, 24.1	-	-
10 Asp	116.1	-	-	-	178.1	57.1	42.3	179.5	-	-	-
11 Ala	119.0	-	-	-	179.4	55.0	17.8	-	-	-	-
12 Leu	115.7	-	-	-	181.3	57.6	41.1	26.2	20.7, 25.4	-	-
13 Glu	117.4	-	-	-	177.5	58.4	30.0	37.5	183.2	-	-
14 Asn	116.8	-	-	-	173.5	54.2	41.1	-	-	-	-
15 Leu	120.6	-	-	-	177.4	54.1	41.7	26.0	24.0, 26.3	-	-
16 Ser	117.2	-	-	-	175.0	57.1	65.0	-	-	-	-
17 Gly	108.3	-	-	-	177.3	47.8	-	-	-	-	-
18 Asp	121.1	-	-	-	179.0	57.0	40.3	179.6	-	-	-
19 Glu	122.0	-	-	-	178.6	58.8	30.2	36.9	181.9	-	-
20 Leu	121.6	-	-	-	178.2	57.7	40.5	27.3	25.5, 23.7	-	-
21 Lys	118.5	-	-	34.2	178.9	60.6	32.3	26.0	29.7	41.7	-
22 Lys	121.6	-	-	35.2	176.1	60.3	32.7	25.4	30.3	42.0	-
23 Phe	121.9	-	-	-	176.5	61.4	39.3	138.1	132.0	130.3	128.6
24 Lys	114.6	-	-	33.0	178.0	60.6	32.7	27.1	30.2	41.9	-
25 Met	118.0	-	-	-	179.5	58.8	32.1	31.5	-	-	-
26 Lys	118.7	-	-	32.6	179.5	57.3	31.9	25.5	28.3	42.2	-
27 Leu	120.0	-	-	-	178.8	56.7	40.3	27.8	25.8, 21.8	-	-
28 Leu	117.1	-	-	-	178.2	56.0	41.6	25.9	25.3, 22.8	-	-
29 Thr	107.9	-	-	-	176.0	61.1	69.2	23.9	-	-	-
30 Val	125.1	-	-	-	174.0	61.8	31.2	20.8, 19.3	-	-	-
31 Gln	127.2	-	-	-	175.1	56.6	28.2	33.6	180.3	-	-
32 Leu	126.8	-	-	-	178.1	52.9	45.4	26.5	24.0, 25.8	-	-
33 Arg	121.9	-	84.6	-	176.0	56.4	31.7	27.7	43.3	-	158.9
34 Glu	122.9	-	-	-	177.1	58.0	29.5	36.1	183.8	-	-
35 Gly	111.6	-	-	-	173.8	44.7	-	-	-	-	-
36 Tyr	117.5	-	-	-	175.7	58.0	40.1	131.5	134.2	118.2	157.8
37 Gly	110.6	-	-	-	171.4	43.8	-	-	-	-	-
38 Arg	120.2	-	-	-	175.9	53.7	31.3	-	42.1	-	159.6
39 Ile	132.3	-	-	-	173.5	60.1	38.4	27.7, 13.7	13.7	-	-
40 Pro	136.6	-	-	-	177.9	62.4	32.9	27.5	50.8	-	-
41 Arg	119.9	-	-	-	176.8	59.8	32.0	28.4	42.2	-	159.6
42 Gly	102.5	-	-	-	176.3	48.2	-	-	-	-	-

Residue	N	N γ	N η	N ζ	C	C α	C β	C γ	C δ	C ϵ	C ζ
43 Ala	121.8	-	-	-	180.0	53.7	18.2	-	-	-	-
44 Leu	119.6	-	-	-	179.7	57.9	43.0	26.8	24.2, 25.4	-	-
45 Leu	115.7	-	-	-	178.6	57.8	41.8	26.3	21.9, 25.7	-	-
46 Gln	113.7	-	-	-	176.3	55.3	30.1	33.8	180.3	-	-
47 Met	118.4	-	-	-	176.8	57.7	34.8	32.8	-	17.7	-
48 Asp	122.5	-	-	-	175.8	51.5	41.0	178.8	-	-	-
49 Ala	116.6	-	-	-	179.1	55.6	18.2	-	-	-	-
50 Ile	120.5	-	-	-	177.0	65.3	38.5	29.8, 18.5	15.1	-	-
51 Asp	119.5	-	-	-	179.5	57.0	41.1	-	-	-	-
52 Leu	119.1	-	-	-	177.2	57.1	42.4	27.4	26.7, 23.3	-	-
53 Thr	116.8	-	-	-	175.3	68.4	68.1	23.4	-	-	-
54 Asp	116.2	-	-	-	178.5	57.4	41.8	-	-	-	-
55 Lys	118.7	-	-	32.9	177.9	57.3	30.8	24.2	27.6	41.1	-
56 Leu	118.3	-	-	-	178.9	58.3	42.8	27.4	23.5, 26.5	-	-
57 Val	116.9	-	-	-	177.4	65.7	30.8	24.1, 23.1	-	-	-
58 Ser	118.0	-	-	-	176.4	62.3	62.8	-	-	-	-
59 Tyr	121.7	-	-	-	178.6	58.9	37.1	131.9	134.4	116.5	156.7
60 Tyr	115.8	-	-	-	175.5	57.3	38.0	131.4	134.2	117.9	157.6
61 Leu	111.4	-	-	-	176.0	57.1	40.6	29.3	24.7, 25.9	-	-
62 Glu	114.8	-	-	-	177.9	60.5	30.2	37.2	179.6	-	-
63 Ser	110.6	-	-	-	177.3	60.7	62.1	-	-	-	-
64 Tyr	123.0	-	-	-	176.8	57.8	35.1	129.5	132.3	117.9	155.5
65 Gly	108.9	-	-	-	176.6	47.7	-	-	-	-	-
66 Leu	122.6	-	-	-	177.8	58.8	42.3	27.7	26.5	-	-
67 Glu	119.9	-	-	-	179.4	59.7	30.0	35.7	182.8	-	-
68 Leu	123.1	-	-	-	178.3	57.8	41.8	26.3	23.8, 25.8	-	-
69 Thr	115.1	-	-	-	176.2	68.5	67.7	21.2	-	-	-
70 Met	118.5	-	-	-	177.0	60.7	35.6	32.6	-	-	-
71 Thr	116.8	-	-	-	176.7	66.9	68.7	-	-	-	-
72 Val	123.0	-	-	-	178.2	66.5	31.2	23.4, 21.5	-	-	-
73 Leu	118.5	-	-	-	179.2	58.3	41.2	26.8	23.6	-	-
74 Arg	117.0	-	-	-	179.9	60.6	29.3	26.7	43.3	-	159.3
75 Asp	121.8	-	-	-	178.4	56.8	41.5	179.8	-	-	-
76 Met	116.1	-	-	-	174.9	57.3	34.5	32.2	-	15.8	-
77 Gly	105.2	-	-	-	173.4	43.0	-	-	-	-	-
78 Leu	122.8	-	-	-	176.0	53.1	38.0	26.7	22.4	-	-
79 Gln	120.0	-	109.8	-	178.3	57.6	27.5	33.0	179.5	-	-
80 Glu	121.1	-	-	-	179.7	60.1	30.2	36.0	183.3	-	-
81 Leu	119.8	-	-	-	179.3	56.9	42.9	26.9	23.4, 22.0	-	-
82 Ala	121.0	-	-	-	179.1	55.9	18.5	-	-	-	-
83 Glu	116.4	-	-	-	179.2	58.8	29.2	36.7	183.2	-	-
84 Gln	120.3	-	110.9	-	179.5	58.7	28.1	33.5	179.9	-	-

Table 3.1: Chemical shifts of mouse ASC - PYD filaments in ppm

3.2.3 Secondary structure determination

We performed the identification of secondary structure elements by the analysis of the so-called secondary chemical shifts ($\Delta\delta C\alpha - \Delta\delta C\beta$): that is defined as the difference between measured $^{13}C\alpha$ chemical shifts and corresponding random coil $^{13}C\alpha$ chemical shifts

and subtracted the difference between measured $^{13}\text{C}\beta$ chemical shifts and corresponding random coil $^{13}\text{C}\beta$ chemical shifts [51].

In this approach, we defined a α helix by at least four consecutive resonances with value of the secondary shifts difference $\Delta\delta\text{C}\alpha - \Delta\delta\text{C}\beta > 1.4$ ppm [51]. Moreover, we perform a database analysis using the software TALOS+ [81], obtaining similar result of the secondary chemical shifts analysis, with the exception of residue 61. This residue, according to the secondary chemical shifts analysis, is the first one of the 5th helix, while TALOS+ puts it in a loop region. We resolved this issue in the structure calculation, where this residue was put outside of the 5th α helix. From the combination of these methods, 6 α helices were defined at position 3 - 14 (α_1), 17 - 29 (α_2), 41 - 46 (α_3), 49 - 59 (α_4), 62 - 76 (α_5), 80 - 84 (α_6), as shown in Figure. These locations are similar to those observed in the monomeric human ASC PYD, where helices were defined including residues 3 - 14, 17 - 26, 41 - 46, 49 - 59, 62 - 76, 80 - 89. The last helix for the mouse ASC presumably extends until residue 89, but resonances that could correspond to the segment 85 - 89 were not found in any of the spectra [77].

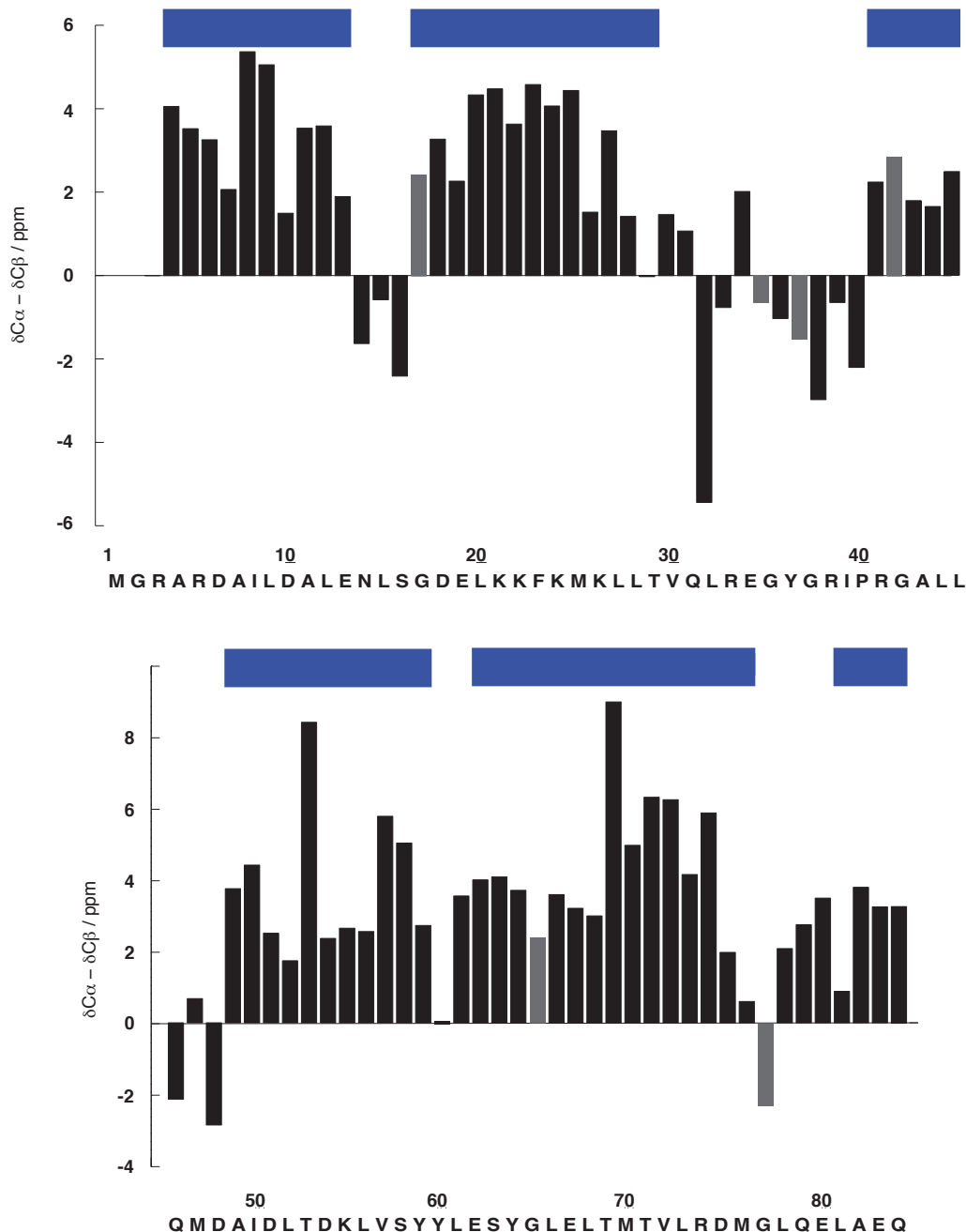


Figure 3.8: Secondary chemical shifts analysis of labeled filaments of ASC - PYD made. For glycine $\Delta\delta C\alpha$ is plotted and the corresponding bars are plotted in gray. Four consecutive resonances with value of the secondary shifts difference $\Delta\delta C\alpha - \Delta\delta C\beta > 1.4$ ppm defined a α helix. Blue squares are drawn for TALOS+ [81] predicted α - helix regions. Only residues without warning and with small dispersion of predictions were included.

3.2.4 Distance restraints spectra

We performed long distance [^{13}C - ^{13}C] experiments, namely 8 ms PAR [54] and 200 μs CHHC to obtain distance restraints to combine with the additional data from cryo - EM

CHHC	ω_1	ω_2
F23 - M76	F23 H β	M76 Q ϵ
T69 - I8	T69 H β	I8 Q δ 1
E19 - M76	E19 Q γ	M76 Q ϵ
F23 - M76	F23 H α	M76 Q ϵ
PAR	ω_1	ω_2
F23 - M76	F23 C β	M76 C ϵ
E19 - M76	E19 C γ	M76 C ϵ
F23 - V72	F23 C α	V72 C γ 1
F23 - M76	F23 C α	M76 C ϵ
I8 - T53	I8 C γ 1	T53 C β
I8 - T53	I8 C γ 2	T53 C α
F23 - T69	F23 C ζ	T69 C γ 2
F23 - V72	F23 C ϵ	V72 C γ 1
I8 - T69	I8 C γ 1	T53 C γ 2

Table 3.2: Manually assigned restraints for the structure calculation. In grey are the intra - molecular restraints that have been collected from the CHHC and PAR spectra

for the structure calculation.

We defined as restraint a spectral unambiguous (i.e. only one possibility of assignment in each dimension, with 0.2 ppm of tolerance) correlation between ^{13}C atoms which belong to amino acids that are far apart in the primary sequence (i.e. more than 3 residues).

The experiments were measure on [UL ^{13}C - ^{15}N] and on a diluted samples. The diluted sample contains uniformly [^{13}C - ^{15}N] - labeled ASC - PYD and natural abundance (NA)ASC - PYD monomers in a ratio of 1:3.

We classified restraints as inter- or intra-molecular (or ambiguous in this respect) according to the intensity ratio between the UL sample and the diluted sample. Cross-peaks were classified as intra-molecular contacts if the intensity ratio $I_{Dil}/I_{UL} > 0.8$ with a standard deviation margin above 0.4. Cross-peaks were classified as inter-molecular contacts if the intensity ratio $I_{Dil}/I_{UL} < 0.4$ with a standard deviation margin below 0.8. No classification was done in any other cases, similarly to Chapter 2. From the analysis of the spectra, we could identify 4 and 9 spectral unambiguous restraints from the CHHC and PAR experiment, respectively. All this restraints were classified as intra molecular from the dilution analysis (Figure 3.9) and are shown in Table 3.2. Experimental details are shown in Table 3.5.

3.2.5 Structure calculation of the mouse ASC - PYD filament

We proposed the following hybrid approach between solid state NMR and cryo - EM for structure determination of proteins, as shown representatively in Figure 3.10. In the first

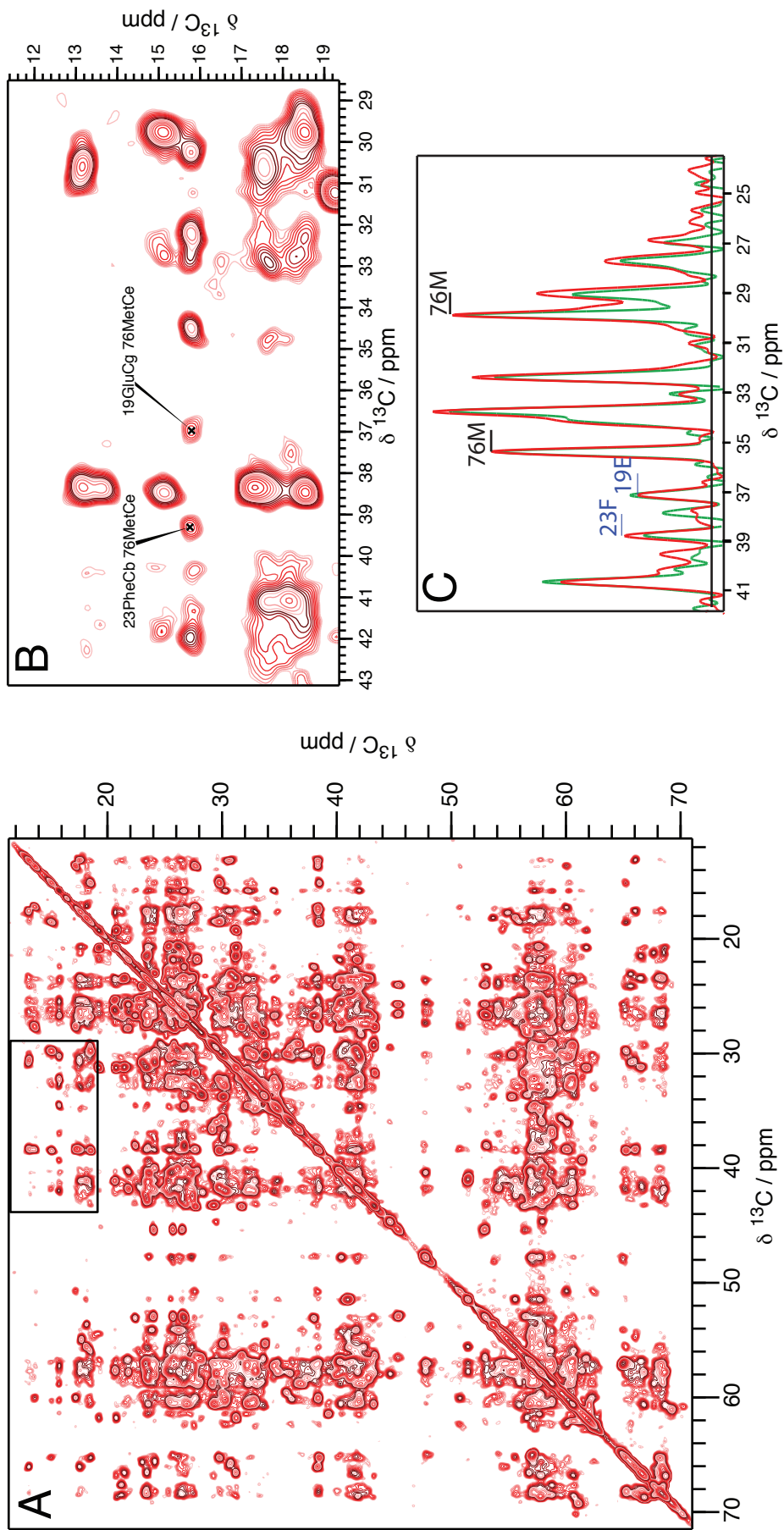


Figure 3.9: (A) 2D 8 ms PAR spectrum measured on uniformly [^{13}C - ^{15}N] labeled filaments of PYD alone. This experiment was measured at 20.0 T magnetic field setting the MAS frequency to 15 kHz. **B** Part of PAR spectrum with two spectrally unambiguous long range restraints. **C** Dilution analysis on the peaks shown in **B**. The PAR spectrum measured on the diluted sample is plotted in green and is scaled with the UL spectrum to the intra residue peak. The two restraints are classified as intra molecular

step, the cryo - EM data (shown in Figure 3.11) is combined with solid state NMR data to obtain the first of the 3 - steps model.

We obtained model 1 of the ASC - PYD filament monomer based on the EM electron density map and on the location of the six α helices in the amino acid sequence, as determined in paragraph 3.2.3. The model was built by placing the helices interactively into the cryo - EM density map using Coot [82] and connecting them as indicated by electron density. Because some of the side chains were well resolved in the electron density map, matching them allowed a tentative rotational orientation. The full - filament coordinates were created from this monomer by application of the helical symmetry (C_3 , 53° rotation, 14.2 - Å rise).

We refined the resulting model 1 further by using the X-PLOR-NIH program [83] under continuous symmetry enforcement, using the cryo - EM structure factors (i.e. the Fourier transform of the density map) as restraints, as well as the TALOS+ dihedral angles from solid - state NMR chemical shifts for a total of 70 residues and $i, i+4$ backbone hydrogen - bond restraints for residues in α - helical secondary structure, obtaining the model 2, as depicted in Figure 3.10.

In order to increase the precision of this model, we used the set of spectrally unambiguous cross - peaks found in the CHHC and PAR spectra, presented in Table 3.2. All these restraints are validated in the structure. The resulting model 2 shows a well defined backbone structure, as indicated by a backbone rmsd of 0.23 Å and an overall heavy atom rmsd of 0.94 Å for the conformer bundle.

For the final step of this procedure, we included in the calculation the automatic picked peak lists from the distance restraints spectra. The 674 correlation were assigned automatic by the CANDID [84] algorithm, using the 3D structure of model 2 as a starting point. A summary of the assigned peaks can be seen in Table 3.3.

We therefore performed a structure calculation with X-PLOR-NIH [83] under symmetry enforcement and we obtained the model 3. In model, the ensemble of the 10 lowest energy conformers of the ASC - PYD filament featured a backbone rmsd of 0.17 Å and an overall heavy atom rmsd of 0.63 Å (Figure 3.12, 3.13, 3.14).

A comparison of model 3 with model 1 showed significant improvements. The models differ by backbone and all heavy atom rmsds of 0.84 Å and 1.04 Å, respectively. The comparison of model 3 with model 2 showed only small differences overall (backbone and all heavy atom rmsds of 0.27 Å and 0.33 Å, respectively). Visual inspection showed that the improvement is not uniform but that a number of side - chain orientations were better defined in model 3 through the integration of the distance restraints.

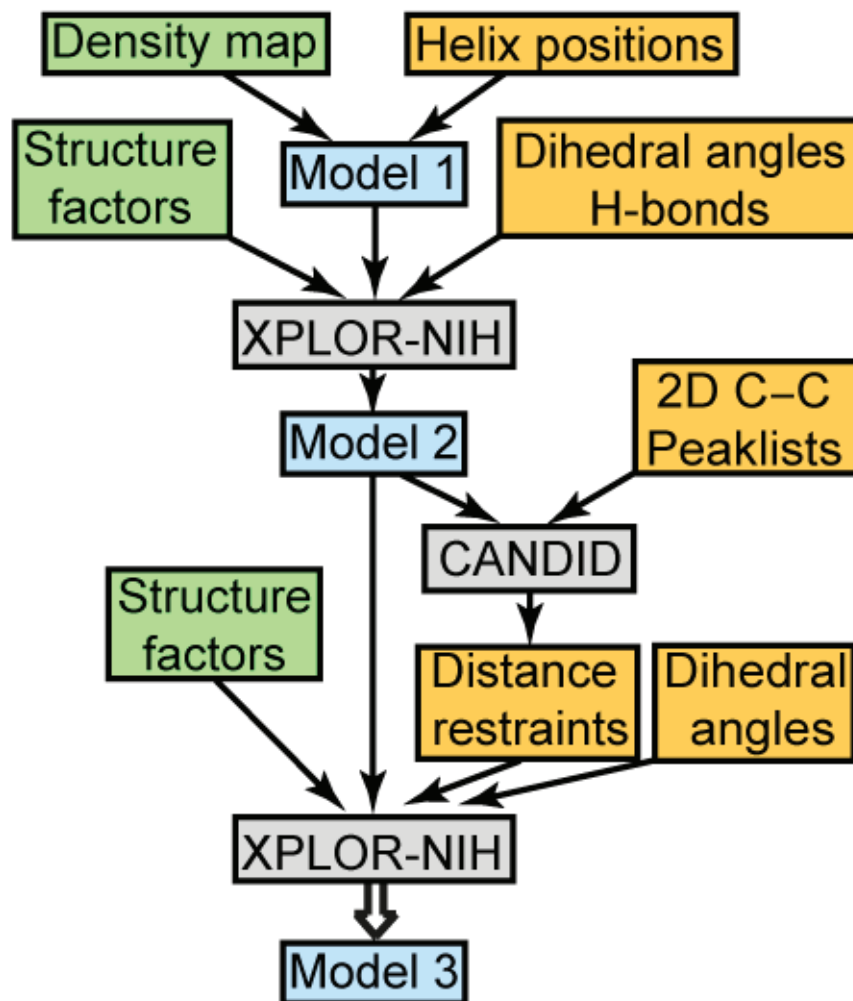


Figure 3.10: Flowchart of the ab initio structure determination of the mouse ASC - PYD filament. The data contributions from solid - state NMR spectroscopy and cryo - EM are indicated by yellow and green rectangles, respectively. The individual structural models 1 - 3 are shown in light blue. Software packages are identified in gray rectangles.

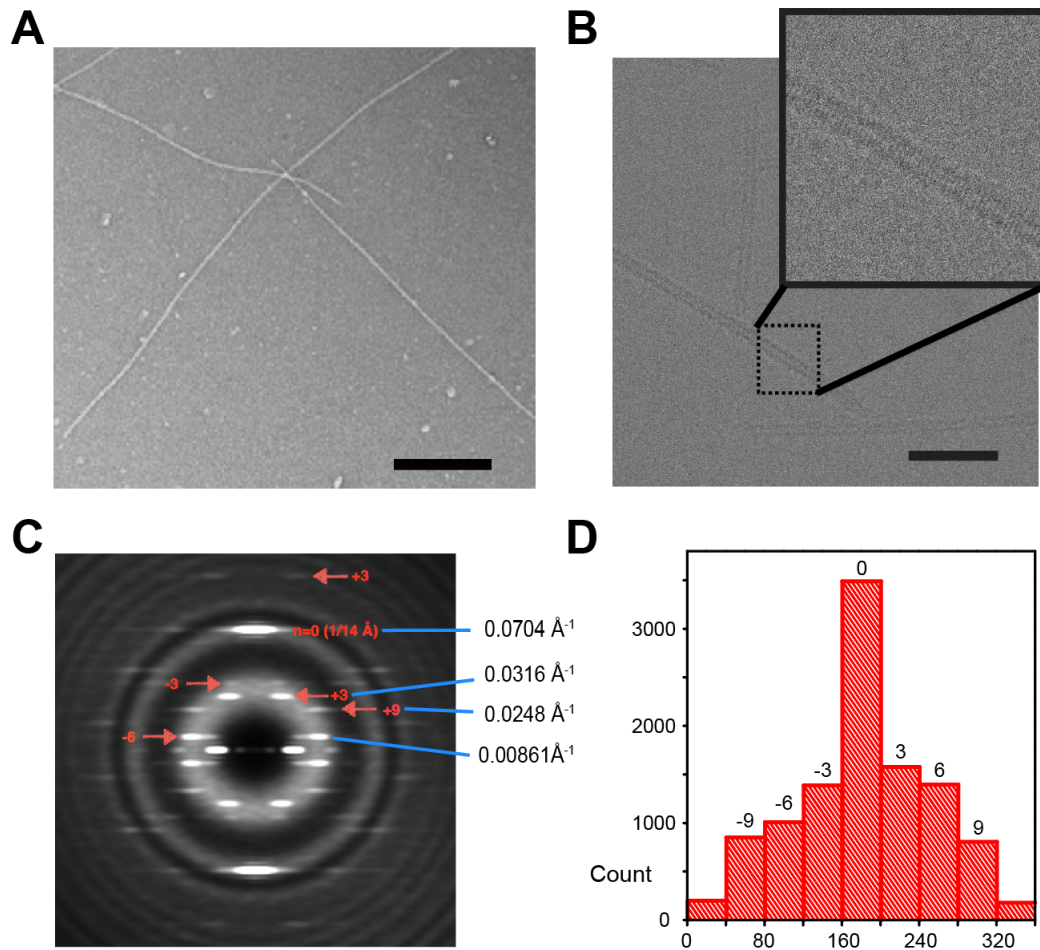


Figure 3.11: Cryo - EM with the mouse ASC - PYD filament. (A) Filaments of the ASC - PYD obtained by dilution of denatured protein with phosphate buffer are well - ordered and separated. (Scale bar, 100 nm.) (B) Cryo - EM image of ASC - PYD filaments. (Scale bar, 50 nm.) (C) Layer - line analysis of average power spectra of ASC - PYD filaments, showing the axial rise per subunit of 14.2 \AA ($n = 0$ layer line). Because of the well - ordered nature of the filaments, there is no variable twist feature. (D) Statistics of filament segments divided into separate bins according to out-of-plane tilts of -12° to 12° .

Table 3.3: Structural statistics for the mouse ASC - PYD filaments for model 3.

NMR distance and dihedral constraints	
Distance constraints*	
Total	674
Intraresidue	19
Interresidue	655
Sequential, $ i - j = 1$	89
Medium range, $ i - j < 4$	209
Long-range, $ i - j > 5$	179
Intermolecular	65
Hydrogen bonds	0
Total dihedral angle restraints	140
ϕ	70
ψ	70
Cryo-EM	
Resolution, Å	3.7
No. reflections	50,317 (work: 48,264; test: 2,572)
R_{work}/R_{free}	0.32/0.33
Structure statistics	
Violations (mean and SD)	
Distance constraints, Å	0
Dihedral angle constraints, °	2 (0)
Max. dihedral angle violation, °	10.5 (0.3)
Max. distance constraint violation, Å	0.0
Deviations from idealized geometry	
Bond lengths, Å	0.0028
Bond angles, °	0.51
Impropers, °	0.46
Ramachandran analysis	
Most favored regions, %	99.0
Disallowed regions, %	0.0
Average pairwise rmsd [†] , Å	
Heavy	0.48
Backbone	0.14

*Obtained from 2D [¹³C,¹³C]-CHHC and 2D [¹³C,¹³C]-PAR, interpreted by CANDID.

[†]Pairwise rmsd was calculated among 10 refined structures.

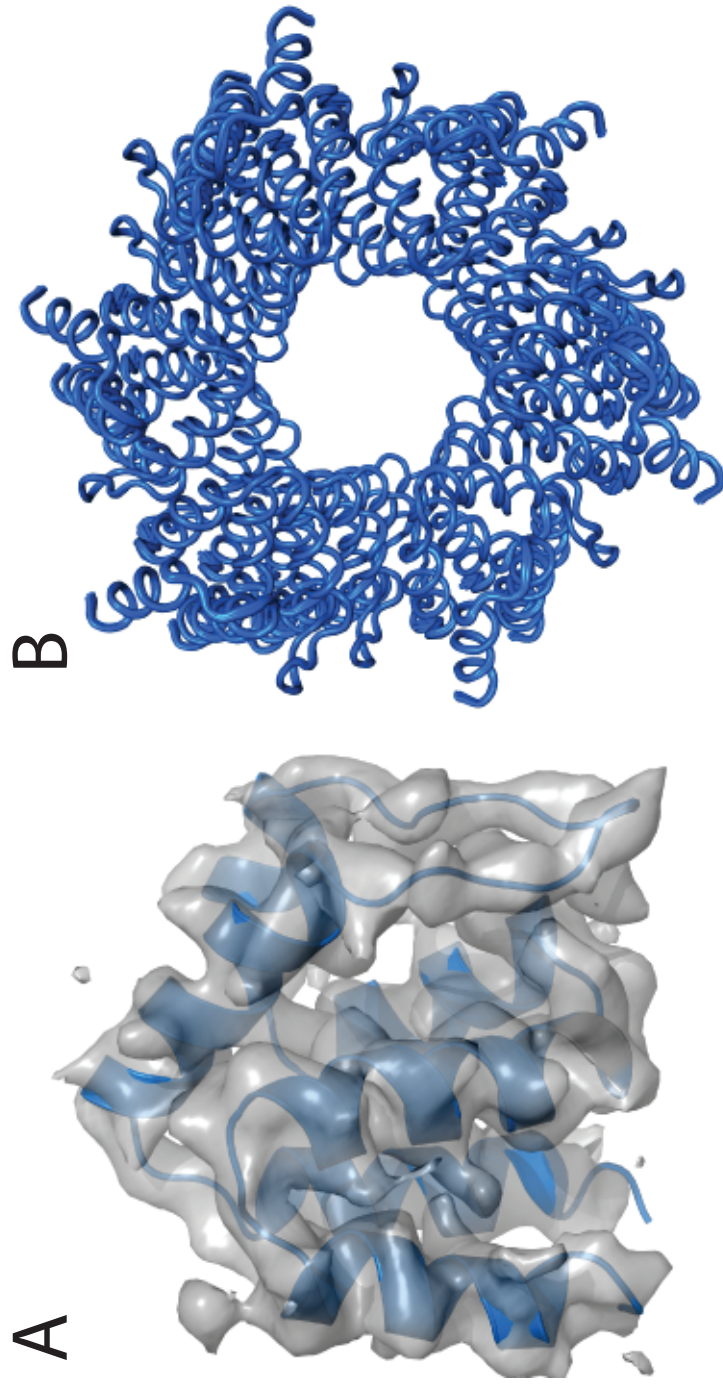


Figure 3.12: (A)Cryo - EM density reconstruction superimposed with the single-subunit ASC - PYD structure. (B)Backbone superimposition of the 20 lowest - energy conformers of the ASC - PYD filament

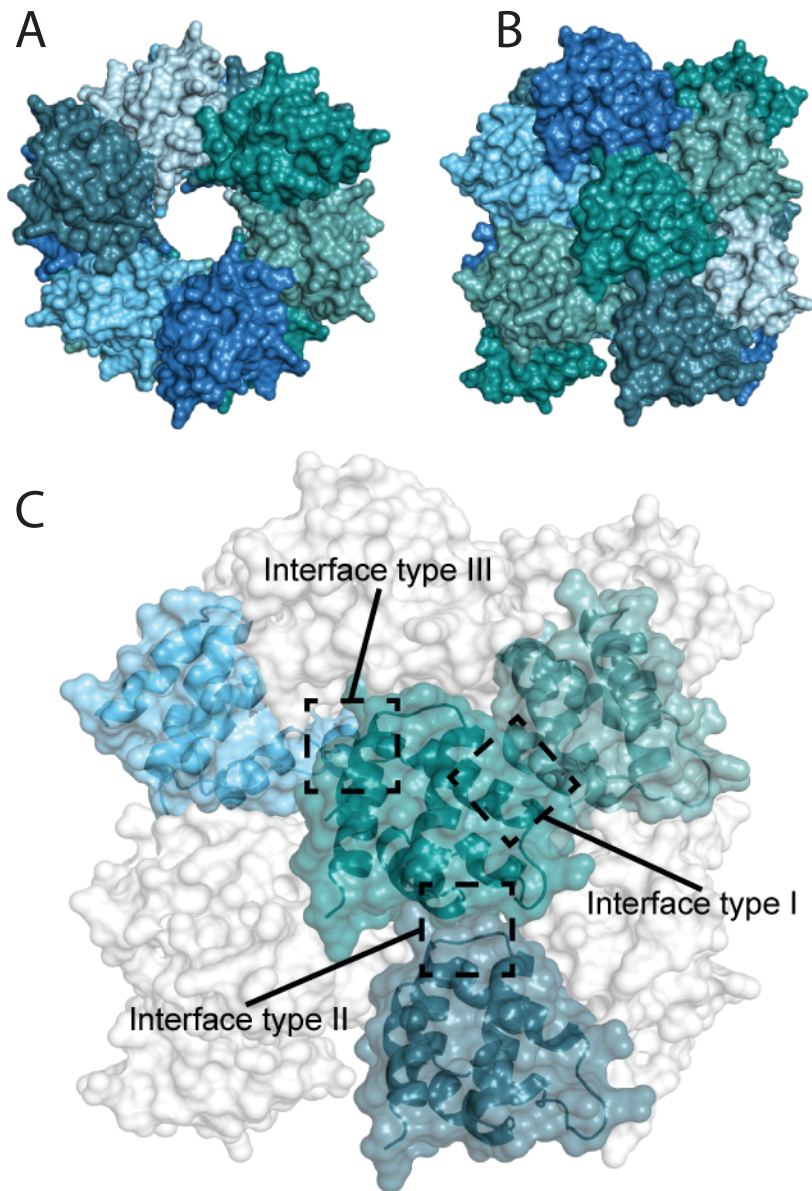


Figure 3.13: Top (A) and side (B) views of the ASC - PYD filament in surface representation. The three helical oligomer strands are colored blue, teal, and dark blue, and individual ASC - PYD subunits have alternating darker and lighter shades. C Four ASC - PYD monomers are shown in surface representation as part of the filament using the color code in A and B. Three interaction interfaces I-III are indicated by dashed square rectangles.

3.2.6 The structure of mouse ASC filament

The so obtained structure of the mouse ASC filament forms a triple-stranded, right-handed helical filament in which each PYD interacts with six adjacent subunits through three asymmetric interfaces, types I-III (Figure 3.13, 3.15, 3.16). The first interface (type I) is formed by interactions between helices 1 and 4 on one monomer and helix 3 in the adjacent one. This interactions happens between residues of opposite charges that

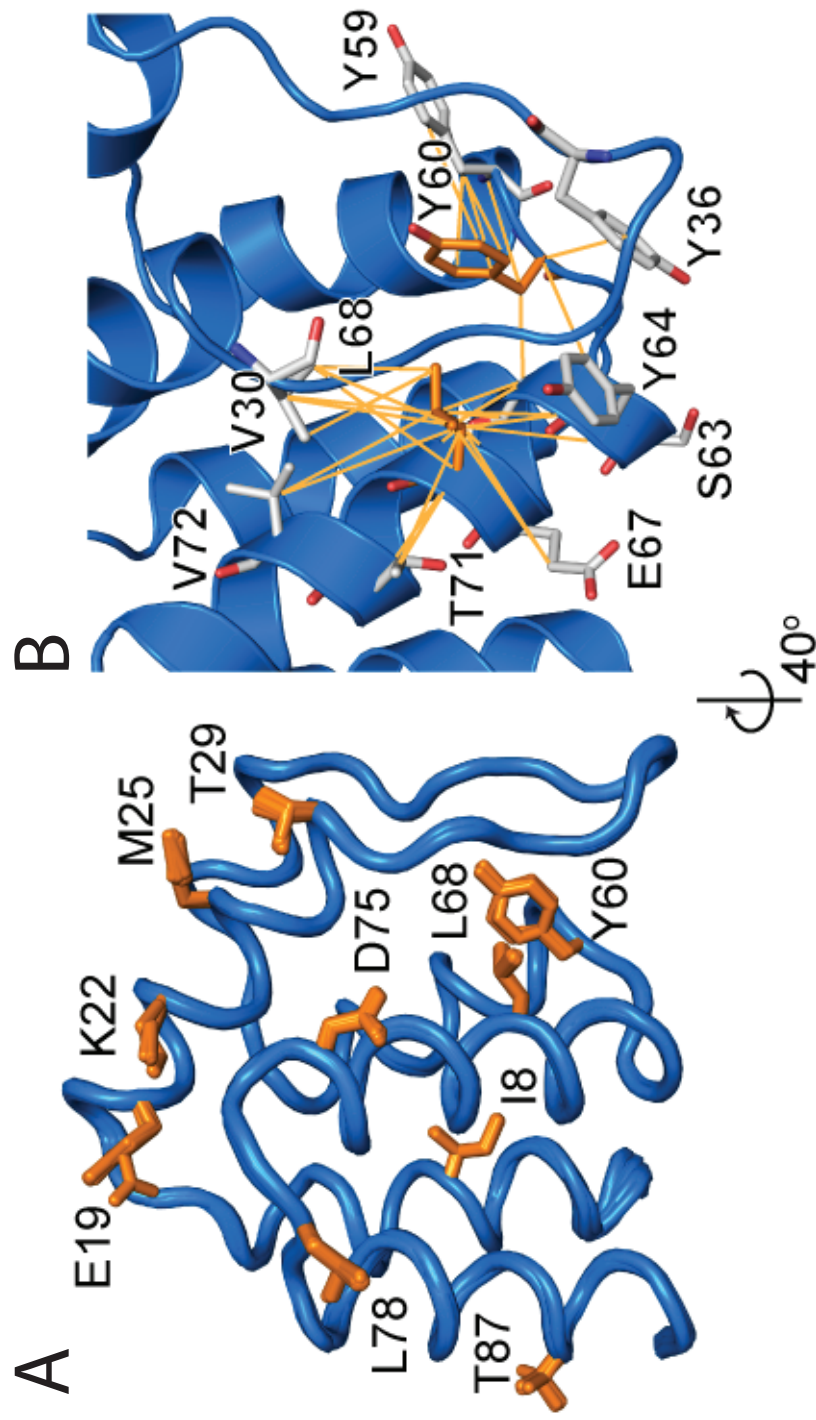


Figure 3.14: **A** Backbone superimposition of the 20 lowest - energy conformers for a single monomer within the assembled filament. **B** Structural features of a single ASC - PYD monomer as part of the filament. The spectrally ambiguous distance constraints between Tyr 60 and Leu 68 (orange) and the neighbouring residues (gray), obtained from solid - state NMR experiments are shown as orange lines.

contribute to the stability of the filament: the solvent - exposed positively charged side chains of Lys 22, Lys 26 and Lys 21 from helix 2 and Arg 41 from helix 3 are involved in electrostatic interactions with the negatively charged side chain of residues Glu 13 and Asp 6 from helix 1 and residues Asp 48 and Asp 54 from helix 4 of the neighbouring monomer. In addition, a network of hydrophobic interactions is formed by Leu 9, Met 25, Val 30, and Ile 50.

The lateral contact of strands parallel to the filament axis emerges from interface type II. Residues in helices 4 and 5 and in the central part of the loop between helices 2 and 3 on one subunit interact with residues at the corner of helices 5 and 6 of the next subunit by specific hydrophobic interactions. The interactions of Tyr 59 and Tyr 60 from the loop between helices 4 and 5 and Gly 77 and Leu 78 from the loop between helices 5 and 6 of the neighbouring subunit define the contact surface between two helical layers.

The type III interface is formed by residues from the end of helix 1 and the sequential short loop on one subunit with helix 3 on the adjacent subunit, mediating the contact of a helical strand with an adjacent helical layer. It is defined by interactions involving both polar and hydrophobic side chains. The charged residues Glu 13, Glu 19, and Arg 41 are located close to this interface but do not form specific salt-bridge interactions.

The so obtained structure of the mouse ASC filaments present similarities with the filament of the human ASC [85], suggesting a functional conservation of the ASC polymerization mechanism as part of the innate immune response system in mouse, human, and possibly other species.

Moreover, the comparison of ^{15}N , $^{13}\text{C}\alpha$ and $^{13}\text{C}\beta$ chemical shifts of the mouse ASC filament with the mouse ASC monomer, shown in Figure 3.16, suggested that the structure of the monomeric form of the PYD is preserved in the filament form. Notable difference of chemical shifts (i.e. $\sum \text{N}, \text{C}\alpha, \text{C}\beta |\delta_{solid} - \delta_{solution}| \geq 2.5 \text{ ppm}$) pointed towards residue responsible of the intra - monomer interactions.

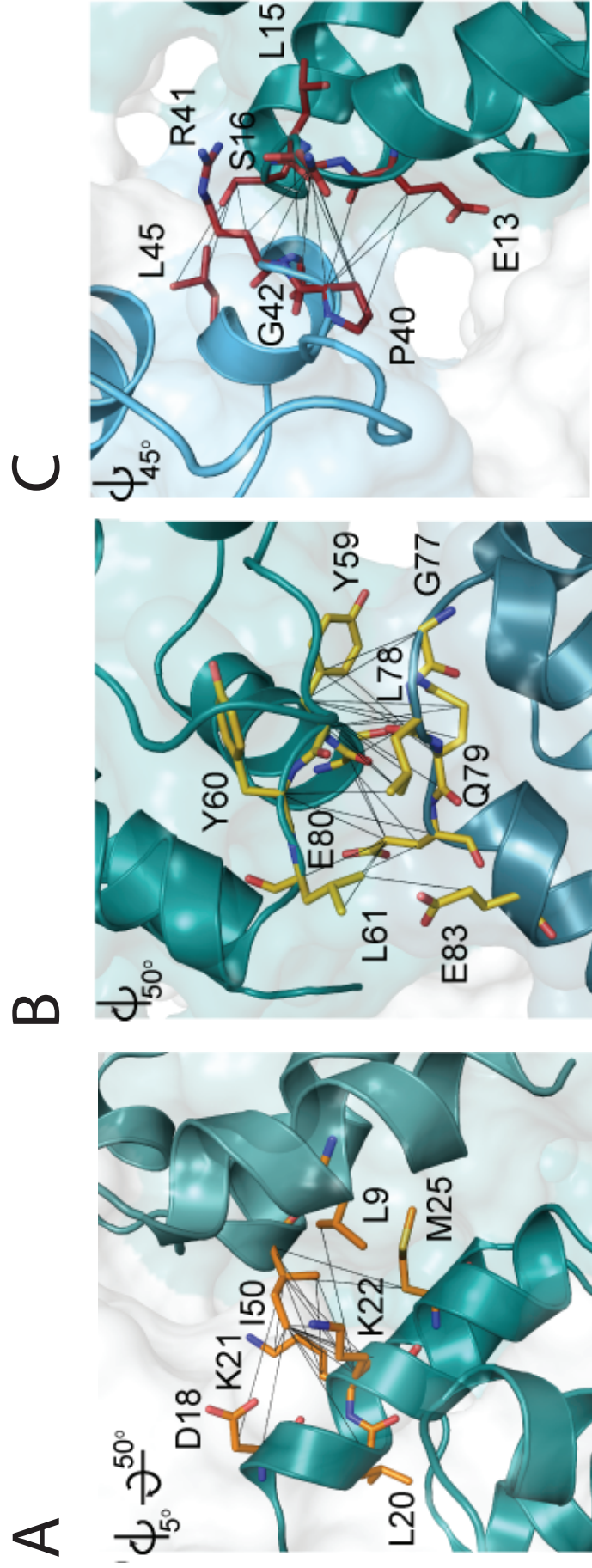


Figure 3.15: A, B, C Detailed view of interaction interfaces I-III, respectively. Intermolecular atom pair contacts observed as ambiguous peaks by solid - state NMR spectroscopy and identified by CANDID are indicated by solid black lines. The residues defining interfaces I, II, and III are labeled and coloured orange, yellow, and red, respectively.

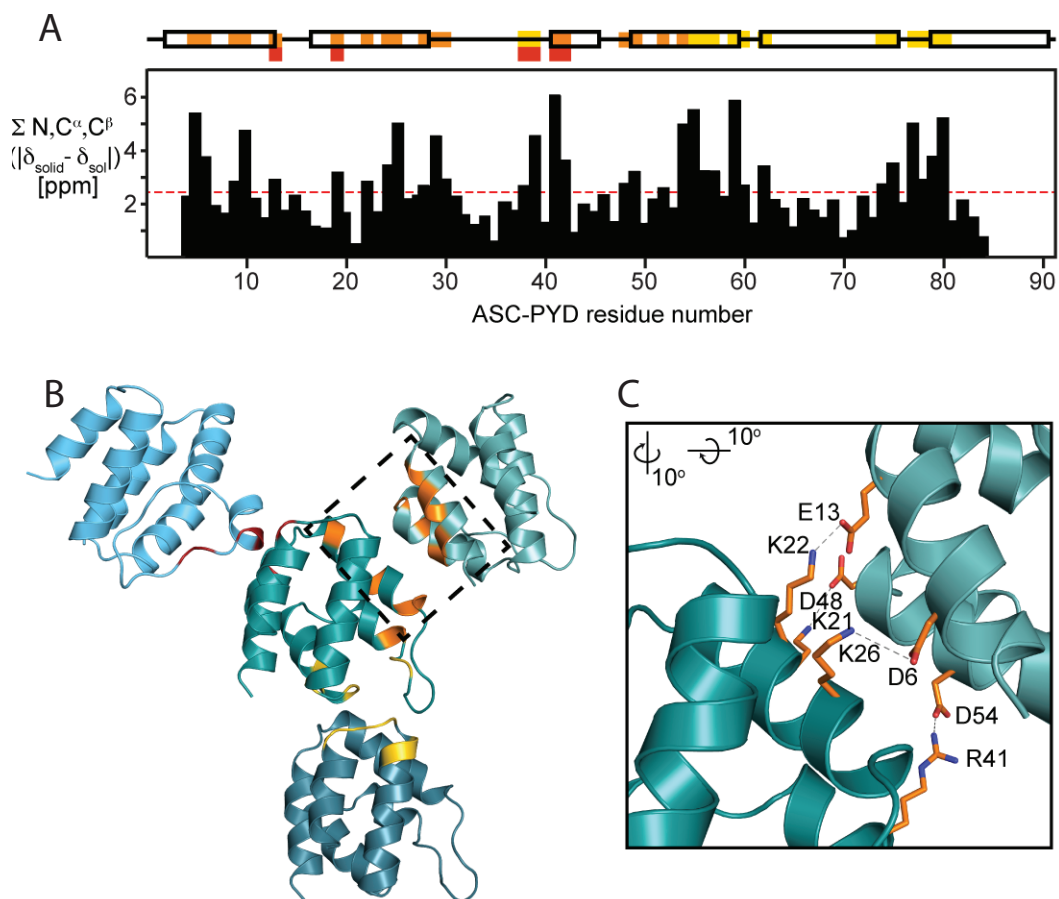


Figure 3.16: **A** Chemical shift differences between solution - and solid - state chemical shifts for the nucleus ^{15}N , $^{13}\text{C}\alpha$ and $^{13}\text{C}\beta$. Chemical shift variations larger than the mean value are marked with different color codes on the secondary structure elements. Residues that belong to the type I, II, and III interfaces are marked in orange, yellow, and red, respectively. **B** Structural location of the residues with significant chemical shift differences between the monomeric and filament forms, as identified and using the color code in **A**. **C** Structural details of interface type I as indicated by the dashed square rectangle in **B**. Side chains involved in inter subunit salt bridges are shown as stick models and with their sequence labels.

3.2.7 The CARD domain

The sample of mouse ASC - FL filament shows similar dipolar based spectra then the ASC - PYD filament, as discussed in Paragraph 3.2.1. These type of experiment filter for rigid parts of the assembly while J - coupled based experiments are sensitive to flexible regions.

We therefore performed INEPT - based experiments [10] to obtain spectral information on the conformation and dynamics of the CARD domain. The [^{15}N - ^1H] double INEPT spectrum of mouse ASC - FL filaments, shown in Figure 3.17, presents ~ 105 strong backbone amide correlation cross peaks. The chemical shift distribution is small (i.e. typical of flexible polypeptide chains) and is in the random coil region.

These correlations must arise from the CARD domain or the flexible linker, since the [^{15}N - ^1H] double INEPT spectrum of ASC - PYD is devoid of peaks. Furthermore, the narrow dispersion of amide proton chemical shifts indicates that the linker and probably a major part of or all the CARD populates a conformational ensemble of flexibly unfolded structures in fast equilibrium, similar to a random coil ensemble. Similarly, the 2D [^{13}C - ^1H] INEPT we measured on the ASC - FL sample shows no major chemical shifts dispersion and the correlations fits the random coil shifts.

We conclude that in our preparations of the mouse ASC filament, the CARD thus is flexible while attached to the well - folded, rigid filament core.

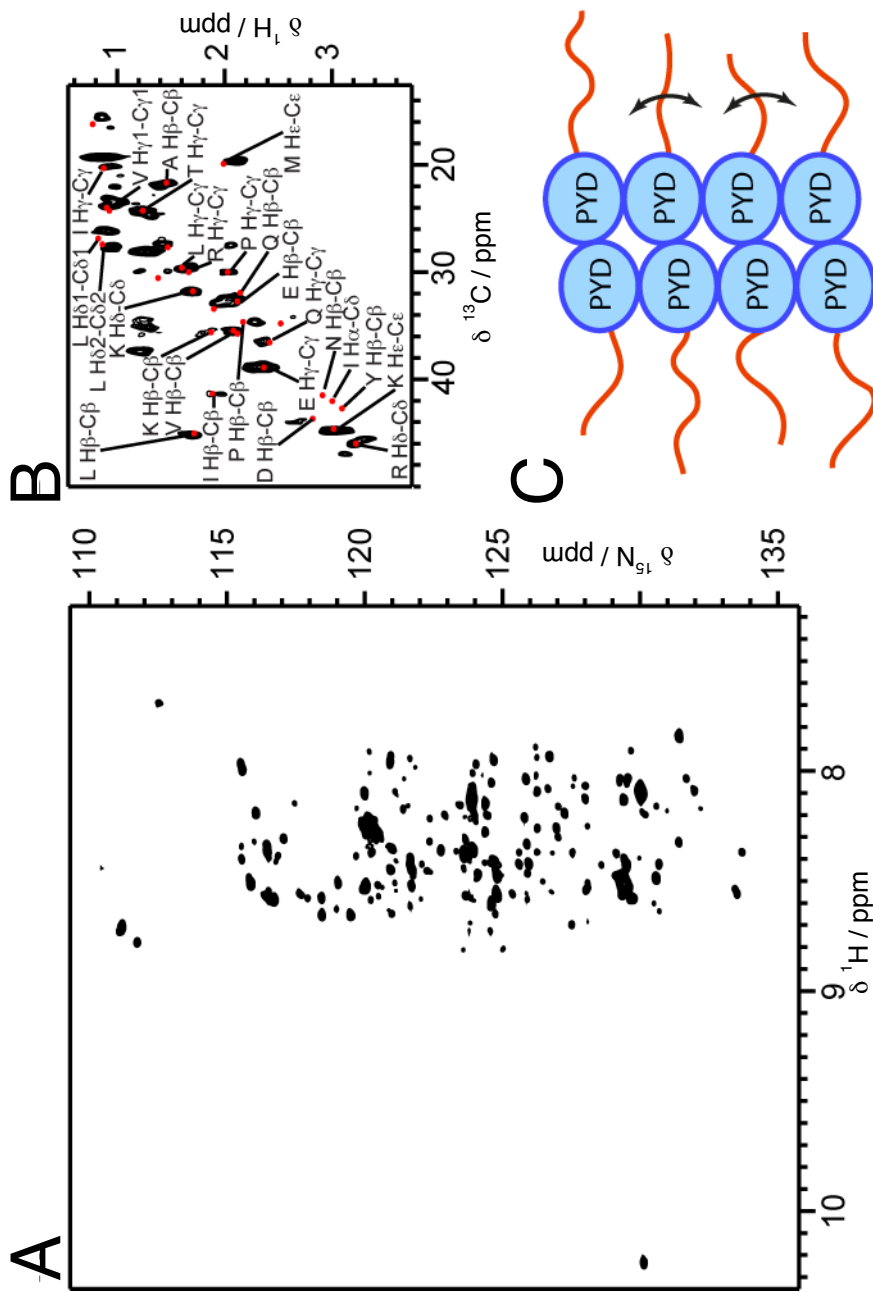


Figure 3.17: The CARD in the mouse ASC - FL filament is flexibly unfolded. **A** Solid - state 2D [^{15}N - ^1H] double INEPT spectrum of mouse ASC - FL filaments. **B** Carbon - detected refocused INEPT spectrum of mouse ASC - FL filaments. Random coil chemical shift positions for the 20 common amino acids are reported as red dots. **C** Model of the ASC - FL filament. Multiple ASC - PYDs (blue) provide the structural scaffold for the filament formation; the ASC - CARDS (orange) remain flexible relative to the ordered filament core and probably exist in random - coil form.

3.3 Conclusions

The integration of solid - state NMR data with a cryo - EM density map proposed in this chapter and applied on the structure determination of the mouse ASC filament is one of the very few recent example of this approach. The other published example comprises structural studies of the type III secretion needle, also a helical arrangement [86], [87]. Importantly, the two techniques provide complementary information, leading to an overall comprehensive description extending beyond the power and resolution of cryo - EM or solid - state NMR alone. The information obtained from the EM density map in combination with the identification of secondary structure elements and the use of individual dihedral backbone angle restraints from solid - state NMR data allowed us to determine the backbone structure de novo.

Solid state NMR can provide additional information about side chains orientation and inter molecular correlation via distance restraints spectra. However, the information from the secondary structure elements and the dihedral angle restraints was proven to be sufficient for the convergence of the backbone of the protein.

3.4 Experimental methods

3.4.1 Expression and purification

The production of full-length protein ASC (residue 1 - 193) and for the PYD domain (residues 1 - 91) was performed using a PET28a vector under the control of a T7 promoter. A GSGSLE linker and a His6 - tag was added to the C - termini of the sequences. ASC - FL and ASC - PYD were produced in BL21(DE3) *E. coli* strains and expressed by growing the cultures at 37°C to an OD600 of 0.8 and by inducing with 1 mM IPTG for 4 hours. The uniform [¹⁵N - ¹³C] - labeling was obtained using ¹³C - glucose and ¹⁵NH₄Cl. The cells were harvested by centrifugation and the pellet was resuspended in 50 mM Phosphate buffer pH = 7.5, 300 mM NaCl, 0.1 mM protease inhibitor. The obtained cells were incubated for 1 h at room temperature with DNase I and then sonicated on ice and centrifuged at 13,000 rpm at 4°C for 30 minutes. The pellet was resuspended in 50 mM phosphate buffer pH = 7.5, 300 mM NaCl, 6M guanidinium hydrochloride and centrifuged at 13,000 rpm at 4°C for 30 minutes. The supernatant was incubated for 2 hours at room temperature with pre - equilibrated Ni-NTA affinity resin (Thermo Scientific) and than passed through a plastic body column for gravity flow purification. The column was washed with 20 column volumes of resuspension buffer containing 20 mM imidazole and the fusion protein was eluted with 3 column volumes of the same buffer with 500 mM imidazole. To avoid aggregation, all the purification steps were carried out at 4°C and further addition of 2 mM DTT to all the buffers were used for the ASC - FL purification.

For the preparation of the filaments of ASC - FL and ASC - PYD, two different approaches were used, based on a pH - or dialysis - step. For the pH - step based method, the elution fraction from NiNTA column was concentrated to half of the volume (~ 5 ml) using Vivaspin and then diluted in a volume ratio of 1 to 9 with 150 mM acetic acid pH = 2.5. The neutral pH condition was achieved by the addition of 3M Tris buffer pH = 8 in a volume ratio of 1 to 5. The solution was incubated overnight at room temperature under continuous stirring condition to facilitate filament formation. The solution was centrifuged at 13,000 rpm at 4°C for 30 minutes yielding a gel - like pellet of ASC filaments that was resuspended in water for a wash step and stored at 4°C. For dialysis based filament formation, the elution fraction of NiNTA purification was dialysed overnight against 25 mM phosphate buffer pH = 7.5, 100 mM NaCl. The gel - like containing ASC filament were centrifuged, washed and stored as previously described.

3.4.2 Rotor filling

The filaments so obtained were packed into 3.2mm ZrO₂ rotors (Bruker Biospin) by ultracentrifugation using a homemade filling device [65] in a SW41 - T1 swing - out rotor in an optima L90 - K ultracentrifuge (Beckmann). The sample was spun for 12h, setting the spinning to 25,000 rpm at 4°C. The drive tip of the rotor was finally sealed with epoxy glue (Araldit) in order to prevent the dehydration of the sample.

3.4.3 Solid - state NMR spectroscopy

All spectra for the sequential assignment, as well as the experiments measured to derive distance restraints were measured on a Bruker Avance II+ 850 MHz using a Bruker 3.2 mm triple-resonance probe. The sample temperature was determined, using the water resonance frequency, to be around 14°C. All spectra were apodized with a Shifted Sine Bell window function (SSB of 2.2 - 2.7). The processing was done by TopSpin 3.1 (Bruker Biospin) and the analysis was performed with CcpNMR analysis 2.3 [47], [48]. All experimental parameters are displayed in Table 3.4 and Table 3.5.

Experiment	NCACO	NCOCA	NCACB	CANCO	CCC	NCA	NCO	DARR 20ms	N(CO)CACB	CAN(CO)CA	N(CA)CBCX
¹ H Larmor frequency	850 MHz	850 MHz	850 MHz	850 MHz	850 MHz	850 MHz	850 MHz	850 MHz	850 MHz	850 MHz	850 MHz
Isotope labeling	[UL ¹³ C- ¹⁵ N]	[UL ¹³ C- ¹⁵ N]	[UL ¹³ C- ¹⁵ N]	[UL ¹³ C- ¹⁵ N]	[UL ¹³ C- ¹⁵ N]	[UL ¹³ C- ¹⁵ N]	[UL ¹³ C- ¹⁵ N]	[UL ¹³ C- ¹⁵ N]	[UL ¹³ C- ¹⁵ N]	[UL ¹³ C- ¹⁵ N]	[UL ¹³ C- ¹⁵ N]
MAS frequency [kHz]	17	17	17	17	17	17	17	17	17	17	17
Transfer 1	HN-CP	HN-CP	HN-CP	HC-CP	HC-CP	HN-CP	HN-CP	HC-CP	HN-CP	HN-CP	HN-CP
Field [kHz] - ¹ H	66.7	66.7	66.7	69.1	81.2	66.7	66.7	69.1	71.5	81.2	81.2
Field [kHz] - ¹³ C	48.9	48.9	48.9	52.0	62.5	48.9	48.9	52.0	47.2	62.5	63.0
Field [kHz] - ¹⁵ N	tangent	tangent	tangent	tangent	tangent	tangent	tangent	tangent	tangent	tangent	tangent
Shape	-	-	-	Cα	-	-	-	-	-	Cα	-
Carrier [ppm]	-	-	-	-	-	-	-	-	-	-	-
Time [ms]	1.2	1.2	1.2	0.35	0.4	1.2	1.2	0.9	1.2	0.4	1.2
Transfer 2	NC-CP	NC-CP	NC-CP	CN-CP	DREAM	NC-CP	NC-CP	DARR	NC-CP	CN-CP	NC-CP
Field [kHz] - ¹ H	-	-	-	-	89.1	-	-	21.3	-	-	-
Field [kHz] - ¹³ C	5.2	5.2	5.2	5.2	7.7	5.2	5.2	-	5.2	5.2	5.2
Field [kHz] - ¹⁵ N	21.0	20.4	21.0	21.1	-	21.0	20.4	-	20.3	21.8	20.5
Shape	tangent	tangent	tangent	tangent	tangent	tangent	tangent	-	tangent	tangent	tangent
Carrier [ppm]	Cα	CO	Cα	Cα	52	Cα	CO	-	CO	Cα	Cα
Time [ms]	7	7	7	7	4	7	7	20	7	7	7
Transfer 3	DARR	DARR	DREAM	NC-CP	DARR	-	-	-	CO-Cα CP	NC-CP	DREAM
Field [kHz] - ¹ H	21.3	21.3	85.1	-	18.1	-	-	-	87.1	-	87.1
Field [kHz] - ¹³ C	-	-	8.1	5.2	-	-	-	-	8.1	5.2	5.3
Field [kHz] - ¹⁵ N	-	-	-	20.4	-	-	-	-	-	21.8	-
Shape	-	-	tangent	tangent	-	-	-	-	tangent	tangent	tangent
Carrier [ppm]	-	-	52	CO	-	-	-	-	CO	Cα	Cα
Time [ms]	60	50	4	7	80	7	7	20	10	7	4
Transfer 4	-	-	-	-	-	-	-	-	DREAM	CO-Cα CP	DREAM
Field [kHz] - ¹ H	-	-	-	-	-	-	-	-	89.1	100	87.1
Field [kHz] - ¹³ C	-	-	-	-	-	-	-	-	8.8	9.2	8.3
Shape	-	-	-	-	-	-	-	-	tangent	tangent	tangent
Carrier [ppm]	-	-	-	-	-	-	-	-	55	177	27
Time [ms]	-	-	-	-	-	-	-	-	4	6	4
t ₁ increments	86	88	86	96	208	992	864	3072	82	140	86
Sweep width (t ₁) [kHz]	4.8	4.8	4.8	8	20	25	25	100	4.6	9	4.8
Max acq time (t ₁) [ms]	8.96	9.17	8.96	6.00	5.20	19.84	17.28	15.36	8.91	7.78	8.96
t ₂ increments	108	72	108	80	208	3072	3072	4096	168	86	192
Sweep width (t ₂) [kHz]	9	6	9	4.5	20	100	100	100	14	4.8	15
Max acq time (t ₂) [ms]	6.00	6.00	6.00	8.89	5.20	15.36	15.36	20.48	6.00	8.96	6.40
t ₃ increments	2560	2560	2560	2560	2560	-	-	-	2560	2560	2560
Sweep width (t ₃) [kHz]	100	100	100	100	100	-	-	-	100	100	100
Max acq time (t ₃) [ms]	12.80	12.80	12.80	12.80	12.80	-	-	-	12.80	12.80	12.80
¹ H SPINAL64 Dec. [kHz]	90	90	90	90	90	90	90	90	90	90	90
Interscan delay [s]	2.3	2.5	2.3	3	2.1	3	2	3.5	3.1	3.5	3
Number of scans	8	8	8	8	4	16	16	8	8	8	8
Measurement time [h]	47.8	35.4	47.8	51.5	101.4	13.3	7.8	12.1	95.4	94.1	110.7

Table 3.4: Experimental parameters for the NMR spectra used for the sequential assignment procedure. All fields in kHz are calculated from reference fields (100 kHz, 62.5 kHz, 50.0 kHz). Actual values might deviate significantly from calculated ones.

Experiment	CHHC 200 μ s	CHHC 200 μ s	PAR 8ms	PAR 8ms
^1H Larmor frequency	850 MHz	850 MHz	850 MHz	850 MHz
Isotope labeling	[UL ^{13}C - ^{15}N]	Diluted	[UL ^{13}C - ^{15}N]	Diluted
MAS frequency [kHz]	15	15	15	15
Transfer 1	HC-CP	HC-CP	HC-CP	HC-CP
Field [kHz] - ^1H	82.3	83.2	78.7	73.4
Field [kHz] - X	63.5	63.5	68.8	68.6
Shape	tangent	tangent	tangent	tangent
Carrier [ppm]	C α	C α	-	-
Time [ms]	0.5	0.5	0.9	0.9
Transfer 2	H-H mixing	H-H mixing	PAR	PAR
Field [kHz] - ^1H	-	-	59.6	58.7
Field [kHz] - ^{13}C	-	-	57.6	55.8
Shape	-	-	-	-
Carrier [ppm]	-	-	60	60
Time [ms]	0.2	0.2	8	8
t_1 increments	2048	2048	2048	2048
Sweep width (t_1) [kHz]	100	100	100	100
Max acq time (t_1) [ms]	10.24	10.24	10.24	10.24
t_2 increments	3072	3072	2560	2560
Sweep width (t_2) [kHz]	100	100	100	100
Max acq time (t_2) [ms]	15.36	15.36	12.80	12.80
^1H SPINAL64 Dec. [kHz]	90	90	90	90
Interscan delay [s]	2.3	2.3	2.5	2.5
Number of scans	48	120	80	168
Measurement time [h]	72.2	128.0	104.0	218.3

Table 3.5: Experimental parameters for the NMR spectra used for structure calculation. All fields in kHz are calculated from reference fields (100 kHz, 62.5 kHz, 50.0 kHz). Actual values might deviate significantly from calculated ones.

Part II

Methods development for solid - state NMR

Chapter 4

Higher resolution ^{13}C spectra by removing the J - couplings

Dr. Jacco van Beek was working on this project when I started my PhD. We performed together the first experiments on alanine. I performed the S³E and analysed the DS³E performances on alanine. I have finally applied these sequences on ubiquitin.

4.1 Introduction

^{13}C Carbon detected experiments are widely used in solid - state NMR for sequential resonances assignment [49] and for structure determination of repetitive filaments, including protein fibrils [88], [31], [33], membrane [89] and protein complexes [90], [91] and injectosome [60]. A factor that hampers these applications is the lack of resolution, caused by anisotropic and isotropic interactions. Many methods have been developed in the past to decrease the linewidth in solid - state NMR, such as sample preparation [92], particular isotope labelling [93], use of faster MAS rate [94] and developing of sequences for homonuclear and heteronuclear decoupling [5], [8].

The combination of these methods have contributed to a narrowing of ^{13}C linewidth, in the order of 150Hz. Under this regime, the main factor that limits resolution is the presence of homonuclear ^{13}C scalar J-coupling. These coupling are typically ~ 55 Hz for $\text{C}\alpha\text{-C}'$ and ~ 35 Hz for $\text{C}\alpha\text{-C}\beta$ [95]. The need to decouple this isotropic interaction is becoming more important in solid - state NMR, to obtain high resolution ^{13}C spectra.

A possibility to obtain a J-decoupled spectrum without using particular sequences is to apply special labelling procedure, in which each ^{13}C nucleus is directly bonded to ^{12}C nuclei [93]. Moreover, the use of these special labelling reduces the dipolar truncation, rendering them useful for obtaining distance information. However this requires a different sample and limits the application for distance restraints information, since a uniformly labeled [^{15}N - ^{13}C] is required for assignment purposes [49].

The combination of hard and selective refocusing pulse placed in the middle of the t_1

evolution can be used to obtain a J-decoupled [^{13}C - ^{13}C] spectrum in the indirect dimension [96]. The removal of the homonuclear J-coupling during acquisition is a more complex task: methods based on soft irradiation [97] or taken from Solution State NMR [98], [99] have been discussed. In this chapter, we show a procedure to obtain high resolution solid - state NMR J-decoupled ^{13}C spectra using variations of the Spin State Selective Excitation (S^3E), initially proposed in [100], [101] for solution-state NMR. These sequences rely on selecting coherences using fixed evolution times and selective π pulses. We finally present a possible application for backbone walk assignment of ubiquitin.

4.2 Theoretical background

Let us consider a system of ^{13}C nuclei coupled with ^{15}N and ^1H in a solid sample (i.e. an amino acid).

As shown in Paragraph 1.1, under average MAS rate, the ^{13}C - ^{13}C and ^{15}N - ^{13}C dipolar coupling, as well as the anisotropy of the chemical shifts, are averaged out in first-order Average Hamiltonian Theory (AHT).

Moreover, the application of designed composite pulse sequences on ^1H can suppress the strong heteronuclear ^1H - ^{13}C dipolar coupling. Under the regime of fast MAS ($\nu_r \geq 55$ kHz), low-power decoupling schemes become efficient and can be used as an alternative of high power ones. This allows to reduce dramatically the amount of rf-load during an experiment and permits longer acquisition times for ^{15}N - and ^{13}C - detected experiments. Typical examples of such low-power sequences are SW_fTPPM [102] and XiX^{CW} [8].

Using these assumptions, the general Hamiltonian ?? for this system without rf-irradiation, can be simplified onto

$$\hat{\mathcal{H}} = \hat{\mathcal{H}}_{CS} + \hat{\mathcal{H}}_{J,Hom.} + \hat{\mathcal{H}}_{J,Het.} \quad (4.1)$$

The heteronuclear J-coupling $\hat{\mathcal{H}}_{J,heteronuclear}$ between ^1H - ^{13}C is removed during the application of low-power rf decoupling, while the ^{15}N - ^{13}C J-coupling can be neglected by low-level ^{15}N sequences, as WALTZ [103].

Equation 4.1 can be simplified as follows

$$\hat{\mathcal{H}} = \hat{\mathcal{H}}_{CS} + 2\pi \sum_{i<j} J_{(i,j)} \hat{S}_i \cdot \hat{S}_j, \quad (4.2)$$

where \hat{S}_i is the operator describing a ^{13}C nucleus (i.e. $^{13}\text{C}\alpha$). Equation 4.2 can be further simplified, since the CS differences between ^{13}C in an amino acid are much bigger than the J-coupling value $J_{(i,j)}$. Therefore the terms $\hat{S}_{ix}\hat{S}_{jx}$ and $\hat{S}_{iy}\hat{S}_{jy}$ become time dependent and can be neglected. The effective Hamiltonian that we are going to use to describe interactions in the system described above is of the form

$$\hat{\mathcal{H}} = \hat{\mathcal{H}}_{CS} + 2\pi \sum_{i<j} J_{(i,j)} \hat{S}_{iz}\hat{S}_{jz}. \quad (4.3)$$

Further contributions for the J-coupling are the homonuclear 2 bonds J-couplings. In the case of ^{13}C , these couplings are usually quite small ($\leq 2 - 3$ Hz) and will be therefore neglected in this work.

4.2.1 The S^3E building block

The Spin State Selective Excitation (S^3E) block, shown in Figure 4.1, can be used to fully J-decouple ^{13}C spins that are directly bonded with a single ^{13}C nucleus (i.e. C' , which is directly bonded to $C\alpha$).

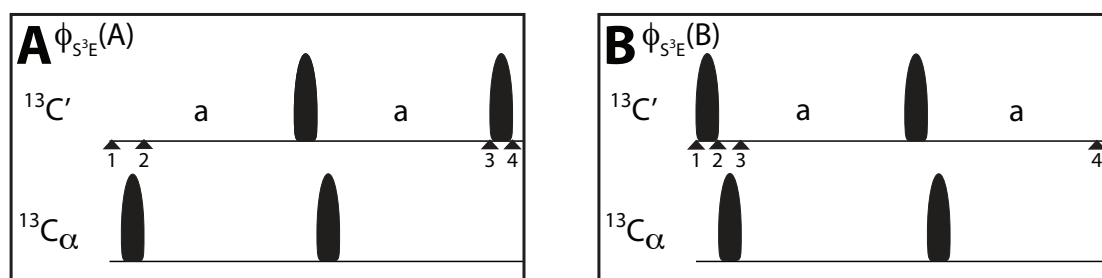


Figure 4.1: The S^3E building block, composed by experiment (A) and (B) that are necessary to separate, via linear combination, the two components of the C' multiplet. The starting magnetization has phase $\phi_{\text{S}^3\text{E}}(\text{A})$ and $\phi_{\text{S}^3\text{E}}(\text{B})$. The delay a is set to allow the evolution of one-bond $^{13}\text{C}'$ - $^{13}\text{C}\alpha$ coupling for a total evolution time $2a = 1/(4J_{\text{C}\alpha\text{C}'}) = 4.5$ ms. The minimum phase cycle for this building block is $\phi_{\text{S}^3\text{E}}(\text{A}) = -y, y$, $\phi_{\text{S}^3\text{E}}(\text{B}) = x, -x$ and the phase at the end is $\phi_{\text{end}} = x, -x$ for both experiments. The black shaped pulses represent selective π rotations on the irradiated spin. Numbers are added to aid in the analysis of the pulse sequence.

The S^3E block can be applied prior acquisition of any experiment with direct detection on C' . It is composed by two experiments, (A) and (B), that have to be measured independently. The key parts are the π rotations, which invert selectively the spins that are irradiated, and the evolution time a , which is set to $1/(8J_{\text{C}\alpha\text{C}'})$. The main difference with another J-decoupling sequence, IPAP [104], is the reduced total evolution time, which has the effect to reduce relaxation.

Panel A

As depicted in Figure 4.2.1, the initial magnetization for (A) is on the C' with phase $-y$:

$$(1) -\hat{C}'_y$$

The initial π pulse on $C\alpha$ does not change the magnetization on the C' .

$$(2) -\hat{C}'_y$$

Then there is the evolution for $2a = 1/(4J_{C\alpha C'})$ under the Hamiltonian 4.3. The central π_x pulse on the carbonyl is applied refocus the C' CS, so that the effective Hamiltonian is purely J-coupling. Moreover, this pulse change the sign of the original \hat{C}'_y , while the central π_x pulse on $C\alpha$ changes the sign of the $\hat{C}\alpha_z$.

$$(3) +\hat{C}'_y \cos(\pi J_{C\alpha C'} 2a) - 2\hat{C}'_x \hat{C}\alpha_z \sin(\pi J_{C\alpha C'} 2a)$$

The final π_x pulse on C' changes the sign of \hat{C}'_y , obtaining

$$(4) -\hat{C}'_y \cos(\pi J_{C\alpha C'} 2a) - 2\hat{C}'_x \hat{C}\alpha_z \sin(\pi J_{C\alpha C'} 2a)$$

We obtain the final density operator for the panel (**A**) of S^3E , substituting $2a = 1/(4J_{C\alpha C'})$:

$$\rho_{S^3E}^A = -\frac{\sqrt{2}}{2} \hat{C}'_y + \sqrt{2} \hat{C}'_x \hat{C}\alpha_z \quad (4.4)$$

Panel B

As depicted in Figure 4.2.1, the initial magnetization for (**B**) is on the C' with phase x :

$$(1) \hat{C}'_x$$

The initial π_x pulse on C' and the following one on $C\alpha$ do not change the sign of the magnetization on the C' .

$$(3) \hat{C}'_x$$

Then there is the evolution for $2a = 1/(4J_{C\alpha C'})$ under the Hamiltonian 4.3. The central π_x pulse on the carbonyl is applied refocus the C' CS, so that the effective Hamiltonian is purely J-coupling. Moreover, this pulse does not change the sign of the original \hat{C}'_x , while the central π_x pulse on $C\alpha$ changes the sign of the $\hat{C}\alpha_z$.

$$(4) +\hat{C}'_x \cos(\pi J_{C\alpha C'} 2a) + 2\hat{C}'_y \hat{C}\alpha_z \sin(\pi J_{C\alpha C'} 2a)$$

We obtain the final density operator for the panel (**B**) of S^3E , substituting $2a = 1/(4J_{C\alpha C'})$:

$$\rho_{S^3E}^B = \frac{\sqrt{2}}{2} \hat{C}'_x + \sqrt{2} \hat{C}'_y \hat{C}\alpha_z \quad (4.5)$$

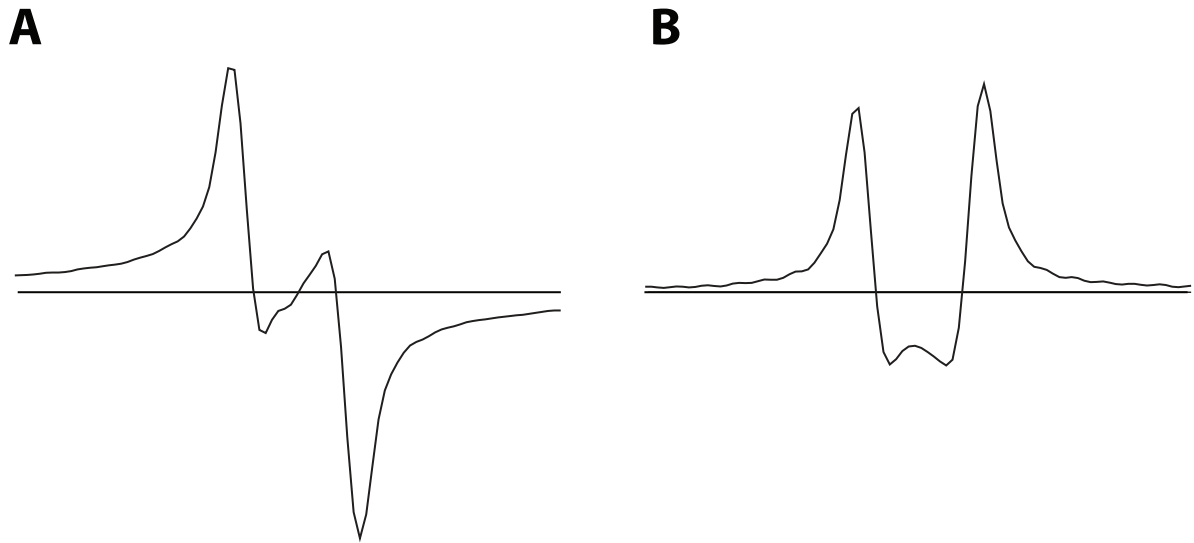


Figure 4.2: C' patterns obtained measuring the experiments (**A**) and (**B**) of S^3E on UL [^{15}N - ^{13}C] alanine, relative to equation 4.4 and 4.5. Experiment details are presented in Paragraph 4.5.2

The operator obtained in the two blocks can be associated with the experimental patterns, as shown in Figure 4.2. Performing linear combinations of the two experiments ($\mathbf{A+B}$ and $\mathbf{A-B}$, with 90° phase correction of the latter one) allows the separation of the C' components of the multiplet. They can then be shifted to the center of the original multiplet by $\pm J_{C\alpha C'}/2$ and summed together, as shown in Paragraph 4.3.1.

4.2.2 The DS³E building block

The S³E block presented above cannot fully remove the homonuclear J-coupling in the case of ¹³C nuclei directly bonded with two other ¹³C spins (i.e. C_α, which is directly bonded to C' and C_β, with the exception of glycine). For this purpose, we have used the Double Spin State Selective Excitation, presented in Figure 4.3

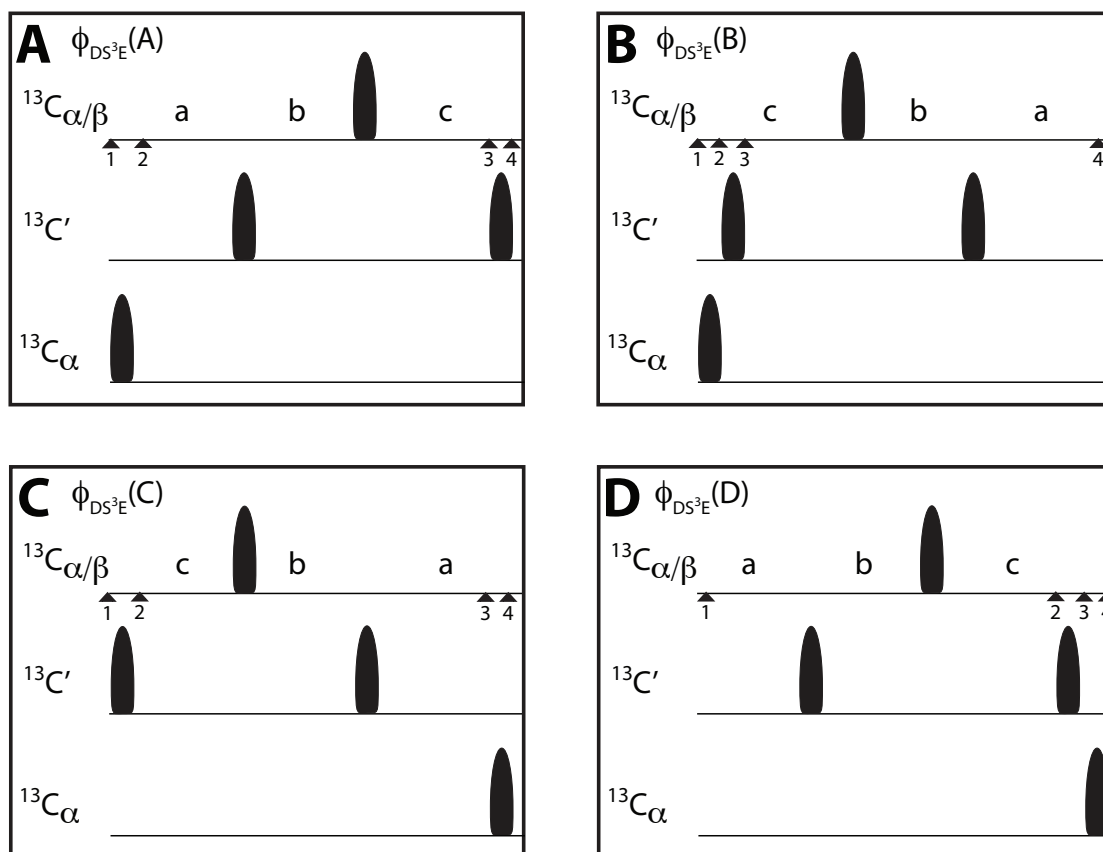


Figure 4.3: The DS³E building block, composed by experiment (A), (B), (C) and (D) that are necessary to separate, via linear combination, the four components of the C_α multiplet. The starting magnetization has phase $\phi_{DS^3E}(A)$, $\phi_{S^3E}(B)$, $\phi_{DS^3E}(C)$, $\phi_{S^3E}(D)$ respectively. The delays a , b and c are set to allow the evolution of one-bond ¹³C_α-¹³C' and ¹³C_α-¹³C_β couplings for a total evolution time of $1/(4J)$ each ($a + b + c = 1/(4J_{C\alpha C\beta}) = 7.2$ ms and $a - b + c = 1/(4J_{C\alpha C'}) = 4.5$ ms, with $a + b = c$). The minimum phase cycle are $\phi_{DS^3E}(A) = -y, y$, $\phi_{DS^3E}(B) = x, -x$, $\phi_{DS^3E}(C) = -x, x$, $\phi_{DS^3E}(D) = -y, y$. The black shaped pulses represent selective π rotations on the irradiated spin. Numbers are added to aid in the analysis of the pulse sequence.

The DS³E block can be applied prior acquisition of any experiment with direct detection on C_α. It is composed by four experiments, (A) - (D), that have to be measured independently. Similarly for the S³E the key parts are the π rotations, which invert selectively the spins that are irradiated, and the evolution times a , b and c , which are set to allow the evolution of the one-bond ¹³C_α-¹³C' and ¹³C_α-¹³C_β couplings.

The total evolution time is $1/(4J)$ each ($a + b + c = 1/(4J_{C\alpha C\beta}) = 7.2$ ms and $a - b + c = 1/(4J_{C\alpha C'}) = 4.5$ ms, with $a + b = c$). The minimal duration of each experiment is determined by the smaller J-coupling to be suppressed (i.e. $J_{C\alpha C\beta} \sim 35$ Hz). The four experiments have the central π pulse on $C\alpha/\beta$ placed in the middle of the evolution time ($a + b = c$) to refocus the $C\alpha$ CS and they differ because of the position of the π pulses on C' (that are always applied in pairs, to compensate for the Bloch-Siegert shifts [105]) and on $C\alpha$.

Panel A

As depicted in Figure 4.2.2, the initial magnetization for (A) is on the C' with phase $-y$:

$$(1) -\hat{C}\alpha_y$$

The initial π_x pulse on $C\alpha$ changes the sign of the initial operator.

$$(2) \hat{C}\alpha_y$$

Then there is the evolution of the two couplings $J_{C\alpha C\beta}$ and $J_{C\alpha C'}$: the central π_x pulse on the $C\alpha/\beta$ is applied refocus the $C\alpha$ CS and allows the evolution of the $C\alpha C\beta$ coupling for $a + b + c = 2c = 1/(4J_{C\alpha C\beta})$. Moreover, this pulse change the sign of the $\hat{C}\alpha_y$ operator. On the other hand, the $J_{C\alpha C'}$ coupling evolves for a total time of $a - b + c = 2a = 1/(4J_{C\alpha C'})$: the coupling evolves for a time a , then the it is partially refocused for a time b (due to the π_x pulse on C') and finally evolves for a time c (after the π_x pulse on $C\alpha/\beta$). Combining this information, we obtain at position (3)

$$(3) -\hat{C}\alpha_y \cos(\pi J_{C\alpha C'} 2a) \cos(\pi J_{C\alpha C\beta} 2c) \\ + 2\hat{C}\alpha_x \hat{C}'_z \sin(\pi J_{C\alpha C'} 2a) \cos(\pi J_{C\alpha C\beta} 2c) \\ + 2\hat{C}\alpha_x \hat{C}\beta_z \cos(\pi J_{C\alpha C'} 2a) \sin(\pi J_{C\alpha C\beta} 2c) \\ + 4\hat{C}\alpha_y \hat{C}'_z \hat{C}\beta_z \sin(\pi J_{C\alpha C'} 2a) \sin(\pi J_{C\alpha C\beta} 2c)$$

The final π_x pulse on C' changes the sign of \hat{C}'_z , obtaining

$$(4) -\hat{C}\alpha_y \cos(\pi J_{C\alpha C'} 2a) \cos(\pi J_{C\alpha C\beta} 2c) \\ - 2\hat{C}\alpha_x \hat{C}'_z \sin(\pi J_{C\alpha C'} 2a) \cos(\pi J_{C\alpha C\beta} 2c) \\ + 2\hat{C}\alpha_x \hat{C}\beta_z \cos(\pi J_{C\alpha C'} 2a) \sin(\pi J_{C\alpha C\beta} 2c) \\ - 4\hat{C}\alpha_y \hat{C}'_z \hat{C}\beta_z \sin(\pi J_{C\alpha C'} 2a) \sin(\pi J_{C\alpha C\beta} 2c)$$

We obtain the final density operator for the panel (A) of DS³E, substituting $2a =$

$1/(4J_{C\alpha C'})$ and $2c = 1/(4J_{C\alpha C\beta})$:

$$\rho_{DS^3E}^A = -\frac{1}{2}\hat{C}\alpha_y - \hat{C}\alpha_x\hat{C}'_z + \hat{C}\alpha_x\hat{C}\beta_z - 2\hat{C}\alpha_y\hat{C}'_z\hat{C}\beta_z. \quad (4.6)$$

Panel B

As depicted in Figure 4.2.2, the initial magnetization for (B) is on the $C\alpha$ with phase x :

$$(1) \hat{C}'_x$$

The initial π_x pulse on $C\alpha$ does not change the sign of the magnetization.

$$(2) \hat{C}'_x$$

The π_x pulse on C' invert the effective J-coupling Hamiltonian between $C\alpha$ and C' . Then there is the evolution of the two couplings $J_{C\alpha C\beta}$ and $J_{C\alpha C'}$: the central π_x pulse on the $C\alpha/\beta$ is applied refocus the $C\alpha$ CS and allows the evolution of the $C\alpha C\beta$ coupling for $a + b + c = 2c = 1/(4J_{C\alpha C\beta})$. Moreover, this pulse does not affect the sign of the $\hat{C}\alpha_x$ operator. On the other hand, the $J_{C\alpha C'}$ coupling evolves for a total time of $c - b + a = 2a = 1/(4J_{C\alpha C'})$, in an analogue way as for panel (A). Combining this information, we obtain at position (4)

$$\begin{aligned} (4) & \hat{C}\alpha_x \cos(\pi J_{C\alpha C'} 2a) \cos(\pi J_{C\alpha C\beta} 2c) \\ & + 2\hat{C}\alpha_y \hat{C}'_z \sin(\pi J_{C\alpha C'} 2a) \cos(\pi J_{C\alpha C\beta} 2c) \\ & + 2\hat{C}\alpha_y \hat{C}\beta_z \cos(\pi J_{C\alpha C'} 2a) \sin(\pi J_{C\alpha C\beta} 2c) \\ & - 4\hat{C}\alpha_x \hat{C}'_z \hat{C}\beta_z \sin(\pi J_{C\alpha C'} 2a) \sin(\pi J_{C\alpha C\beta} 2c) \end{aligned}$$

We obtain the final density operator for the panel (B) of DS³E, substituting $2a = 1/(4J_{C\alpha C'})$ and $2c = 1/(4J_{C\alpha C\beta})$:

$$\rho_{DS^3E}^B = -\frac{1}{2}\hat{C}\alpha_x - \hat{C}\alpha_y\hat{C}'_z + \hat{C}\alpha_y\hat{C}\beta_z - 2\hat{C}\alpha_x\hat{C}'_z\hat{C}\beta_z. \quad (4.7)$$

Panel C

As depicted in Figure 4.2.2, the initial magnetization for (C) is on the $C\alpha$ with phase x :

$$(1 - 2) - \hat{C}'_x$$

The π_x pulse on C' invert the effective J-coupling Hamiltonian between $C\alpha$ and C' . Then there is the evolution of the two couplings $J_{C\alpha C\beta}$ and $J_{C\alpha C'}$: the central π_x pulse on the $C\alpha/\beta$ is applied refocus the $C\alpha$ CS and allows the evolution of the $C\alpha C\beta$ coupling for $a + b + c = 2c = 1/(4J_{C\alpha C\beta})$. Moreover, this pulse does not affect the sign

of the $\hat{C}\alpha_x$ operator. On the other hand, the $J_{C\alpha C'}$ coupling evolves for a total time of $c - b + a = 2a = 1/(4J_{C\alpha C'})$, in an analogue way as for panel (A). Combining this information, we obtain at position (3)

$$(3) -\hat{C}\alpha_x \cos(\pi J_{C\alpha C'} 2a) \cos(\pi J_{C\alpha C\beta} 2c) \\ -2\hat{C}\alpha_y \hat{C}'_z \sin(\pi J_{C\alpha C'} 2a) \cos(\pi J_{C\alpha C\beta} 2c) \\ -2\hat{C}\alpha_y \hat{C}'_{\beta_z} \cos(\pi J_{C\alpha C'} 2a) \sin(\pi J_{C\alpha C\beta} 2c) \\ +4\hat{C}\alpha_x \hat{C}'_z \hat{C}'_{\beta_z} \sin(\pi J_{C\alpha C'} 2a) \sin(\pi J_{C\alpha C\beta} 2c)$$

The final π_x pulse on C α changes the sign of the $\hat{C}\alpha_y$ operator

$$(4) -\hat{C}\alpha_x \cos(\pi J_{C\alpha C'} 2a) \cos(\pi J_{C\alpha C\beta} 2c) \\ +2\hat{C}\alpha_y \hat{C}'_z \sin(\pi J_{C\alpha C'} 2a) \cos(\pi J_{C\alpha C\beta} 2c) \\ +2\hat{C}\alpha_y \hat{C}'_{\beta_z} \cos(\pi J_{C\alpha C'} 2a) \sin(\pi J_{C\alpha C\beta} 2c) \\ +4\hat{C}\alpha_x \hat{C}'_z \hat{C}'_{\beta_z} \sin(\pi J_{C\alpha C'} 2a) \sin(\pi J_{C\alpha C\beta} 2c)$$

We obtain the final density operator for the panel (C) of DS³E, substituting $2a = 1/(4J_{C\alpha C'})$ and $2c = 1/(4J_{C\alpha C\beta})$:

$$\rho_{DS^3E}^C = -\frac{1}{2}\hat{C}\alpha_x + \hat{C}\alpha_y \hat{C}'_z + \hat{C}\alpha_y \hat{C}'_{\beta_z} + 2\hat{C}\alpha_x \hat{C}'_z \hat{C}'_{\beta_z}. \quad (4.8)$$

Panel D

As depicted in Figure 4.2.2, the initial magnetization for (D) is on the C' with phase $-y$:

$$(1) -\hat{C}\alpha_y$$

Then there is the evolution of the two couplings $J_{C\alpha C\beta}$ and $J_{C\alpha C'}$: the central π_x pulse on the C α/β is applied refocus the C α CS and allows the evolution of the C α C β coupling for $a+b+c = 2c = 1/(4J_{C\alpha C\beta})$. Moreover, this pulse change the sign of the $\hat{C}\alpha_y$ operator. On the other hand, the $J_{C\alpha C'}$ coupling evolves for a total time of $a - b + c = 2a = 1/(4J_{C\alpha C'})$, in an analogue way as for panel (A). Combining this information, we obtain at position (3)

$$(3) +\hat{C}\alpha_y \cos(\pi J_{C\alpha C'} 2a) \cos(\pi J_{C\alpha C\beta} 2c) \\ +2\hat{C}\alpha_x \hat{C}'_z \sin(\pi J_{C\alpha C'} 2a) \cos(\pi J_{C\alpha C\beta} 2c) \\ -2\hat{C}\alpha_x \hat{C}'_{\beta_z} \cos(\pi J_{C\alpha C'} 2a) \sin(\pi J_{C\alpha C\beta} 2c) \\ -4\hat{C}\alpha_y \hat{C}'_z \hat{C}'_{\beta_z} \sin(\pi J_{C\alpha C'} 2a) \sin(\pi J_{C\alpha C\beta} 2c)$$

The final π_x pulse on C α changes the sign of $\hat{C}\alpha_y$, obtaining

$$\begin{aligned}
(4) & -\hat{C}\alpha_y \cos(\pi J_{C\alpha C'} 2a) \cos(\pi J_{C\alpha C\beta} 2c) \\
& +2\hat{C}\alpha_x \hat{C}'_z \sin(\pi J_{C\alpha C'} 2a) \cos(\pi J_{C\alpha C\beta} 2c) \\
& -2\hat{C}\alpha_x \hat{C}'\beta_z \cos(\pi J_{C\alpha C'} 2a) \sin(\pi J_{C\alpha C\beta} 2c) \\
& -4\hat{C}\alpha_y \hat{C}'_z \hat{C}'\beta_z \sin(\pi J_{C\alpha C'} 2a) \sin(\pi J_{C\alpha C\beta} 2c)
\end{aligned}$$

We obtain the final density operator for the panel **(D)** of DS³E, substituting $2a = 1/(4J_{C\alpha C'})$ and $2c = 1/(4J_{C\alpha C\beta})$:

$$\rho_{DS^3E}^D = -\frac{1}{2}\hat{C}\alpha_y + \hat{C}\alpha_x \hat{C}'_z - \hat{C}\alpha_x \hat{C}'\beta_z - 2\hat{C}\alpha_y \hat{C}'_z \hat{C}'\beta_z. \quad (4.9)$$

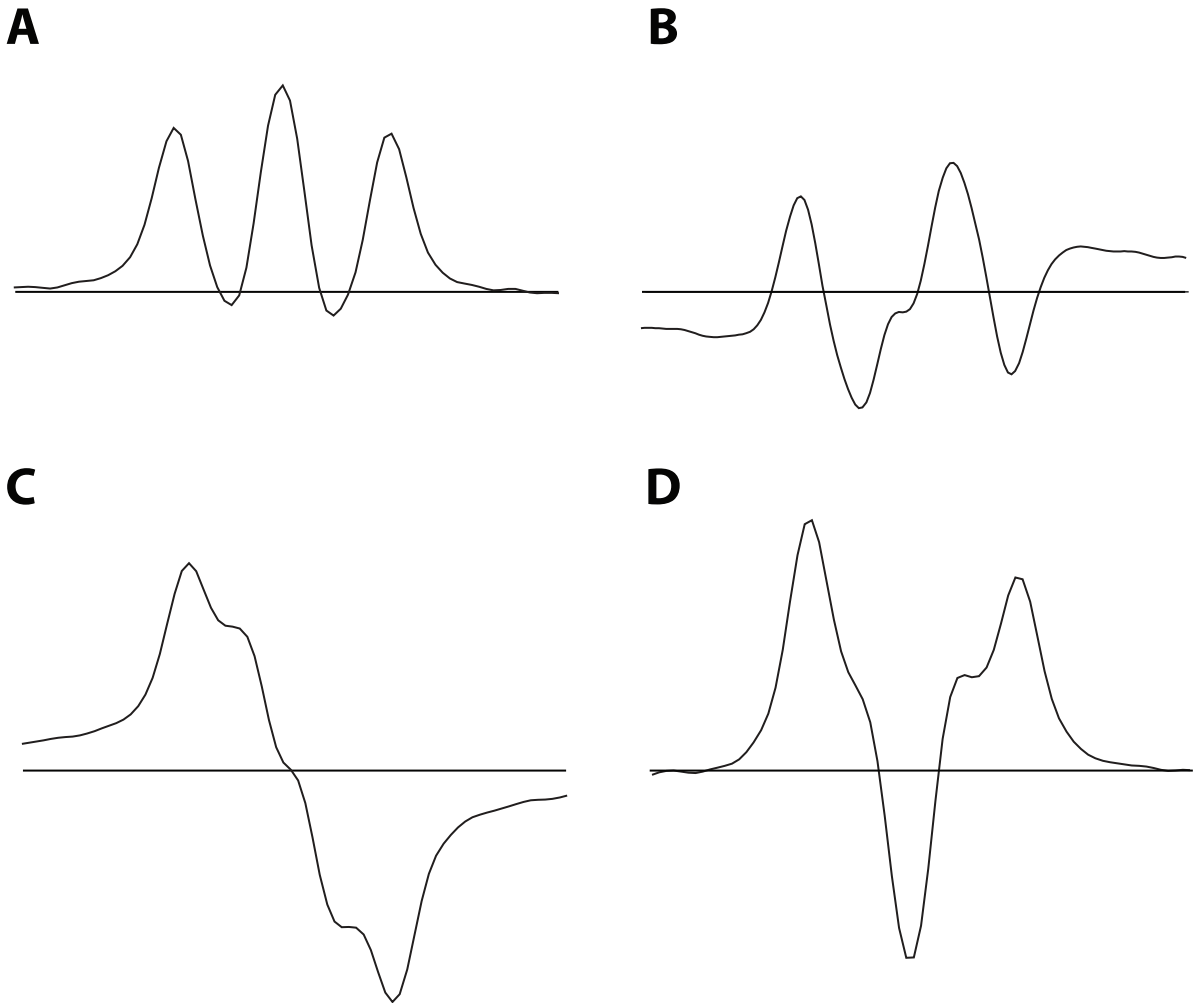


Figure 4.4: C α patterns obtained measuring the experiments **(A)**, **(B)**, **(C)** and **(D)** of DS³E on UL [¹⁵N - ¹³C] alanine, relative to equation 4.6 and 4.7. Experiment details are presented in Paragraph 4.5.2

The operator obtained in the four blocks can be associated with the experimental patterns shown in Figure 4.2. Performing linear combinations of the four experiments allows the separation of the C α multiplet, as shown in Paragraph 4.3.1: **A+B+C+D**

yields the first component of the multiplet from the left (after a correction of the phase by 180°), **A+B-C-D** yields the second one from the left (after a correction of the phase by 90°), **A-B+C-D** yields the third one from the left (after a correction of the phase by -90°) and **A+B-C-D** yields the final one.

The four components can therefore be shifted by $\pm J_{C\alpha C'}/2$ and $\pm J_{C\alpha C\beta}/2$ to the center of the original multiplet and sum together, as presented in Paragraph 4.3.1.

4.3 Results and discussion

The S^3E and DS^3E building block can be used prior to acquisition to homonuclear J-decouple C' and $C\alpha$ respectively, as explained in Paragraph 4.2.1 and 4.2.2. In Paragraph 4.3.1, we will analyse the effect of the value of J-coupling, $J_{C\alpha C'}$ and $J_{C\alpha C\beta}$, which regulates the total evolution time, on the efficiency of the experiments.

These measurement were performed at a magnetic field of 11.75 T, setting the MAS frequency to 60 kHz and using [UL ^{15}N - ^{13}C] alanine as a model system.

In Paragraph 4.3.2 we will present possible applications of these sequences on a model protein, ubiquitin, to obtain J-resolved high resolution ^{13}C spectra. These measurements were performed at a magnetic field of 20.0 T, and setting the MAS frequency to 60 kHz.

4.3.1 Sequence optimization

The basic pulse program used for this Paragraph is depicted in Figure 4.5:

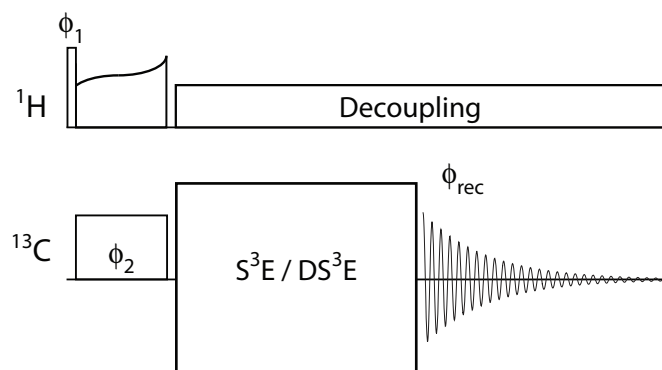


Figure 4.5: ^{13}C CP experiment followed by S^3E / DS^3E building block (Figures 4.1 and 4.3, respectively). 90° pulses are represented by white rectangle. 1H decoupling is applied during the evolution period and the acquisition. Experiment details are discussed in Paragraph 4.5.2. All pulses, except indicated differently, have phase x , while $\phi_1 = y, y, -y, -y$ and $\phi_{rec} = x, -x, -x, x$. ϕ_2 is set equal to $\phi_{S^3E}(X)/\phi_{DS^3E}(X)$, where X denotes the experiment of the building block.

The S³E applied on alanine

We performed the CP - S³E experiment to obtain a J-decoupled carbonyl region. The experiments parameter are discussed in detail in section 4.5.2.

We initially applied a correction from the original sequence (Figure 4.1) changing the value of the evolution time a , originally set to $a = 1/(8J_{C\alpha C'})$, to a new value a' to take into account the finite length of the selective pulse τ_{Q_3} :

$$a' = a - \tau_{Q_3}/2 \quad (4.10)$$

The suggested value in literature is $J_{C\alpha C'} = 55$ Hz, corresponding to a value $a = 2.270$ ms. Considering the length of the inversion pulse $\tau_{Q_3} = 300 \mu s$, the theoretical value for the delay, according to Equation 4.10, would be $a' = 2.120$ ms.

We therefore performed the two experiments (**A**) and (**B**) using the condition described above followed by a reference measurement without the S³E block. The total measurement time for (**A**) and (**B**) is the same as for the reference experiment.

In Figure 4.6 (left) the reference experiment (in black) and the two components of the C' multiplet separated using the S³E sequence (in red and in green) are shown. The signal loss of the green and red spectra compared to the reference one is mainly due to transverse relaxation.

The components were then shifted towards the center of the original multiplet by $J_{C\alpha C'}/2 = 27.5$ Hz and summed together (blue spectrum). The resulting S/N gain, compared to a reference experiment without J-decoupling in the same experimental time, is 1.34.

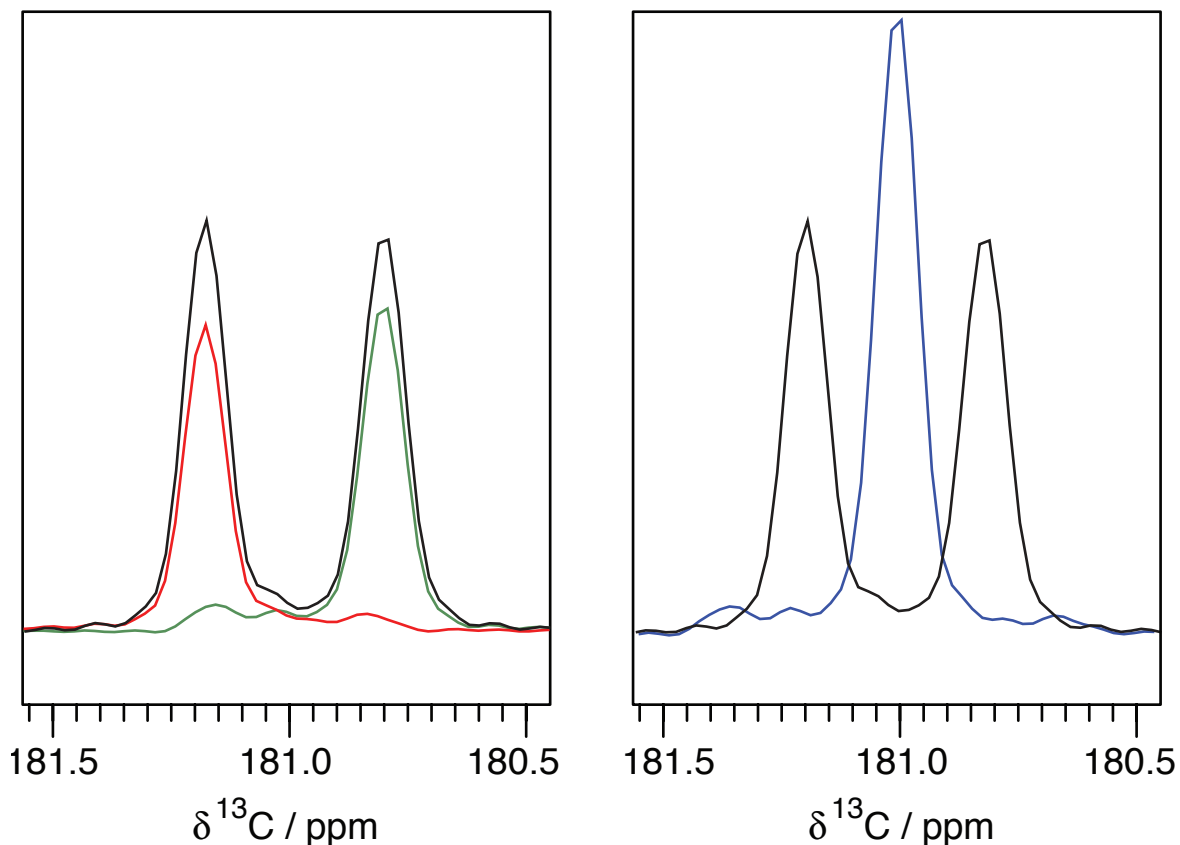


Figure 4.6: S³E applied on alanine C'. Left: reference CP experiment without S³E building block (black, NS = 32) and overlaid with the two components of the multiplets obtained with S³E experiments, shown in Figure 4.1, after the linear combination (red and green). Each experiment of S³E was measured with NS = 16. Right: Overlay of the reference experiment (black) with the singlet obtained shifting the components by $\pm J_{C\alpha C'}/2 = 27.5$ Hz and summing the red and green spectra.

We then analysed the robustness of the sequence toward the choice of the value of the J-coupling between C α and C'. This parameter can be optimized experimentally to obtain the best separation of the components.

We performed the S³E experiments and we analysed the efficiency of the obtained components in function of the parameter a . The result of this optimization is shown in Figure 4.7, where the right component of the original multiplet is presented. In case of alanine, a nice separation of the components is obtained for a broad range of J-couplings values (53 Hz - 57 Hz).

The second component starts to appear for $|J_{C\alpha C'}^{set} - J_{C\alpha C'}^{theor}| \geq 5$ Hz.

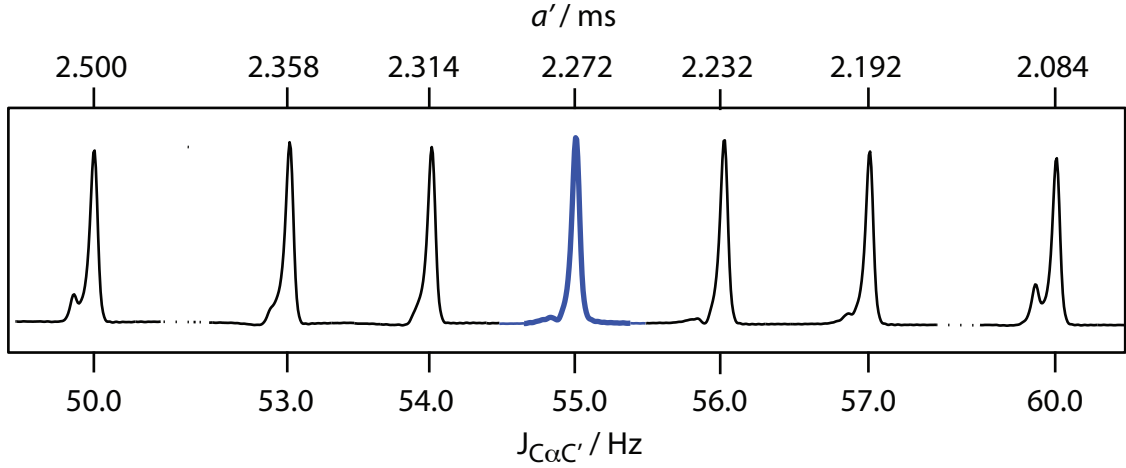


Figure 4.7: Right component of the multiplet obtained by linear combination of the S³E experiment in function of the evolution time a . The separation of the components is well obtained for a broad range of couplings (53 Hz - 57 Hz).

The DS³E applied on alanine

We performed the CP - DS³E experiment to obtain the separation of the four components of the C α multiplets, which are due to the $J_{C\alpha C'}$ and $J_{C\alpha C\beta}$ couplings. In this case, there are two independent variables, a and c , which are related to $J_{C\alpha C'}$ and $J_{C\alpha C\beta}$, respectively: $a' = 1/(8J_{C\alpha C'})$ and $c' = 1/(8J_{C\alpha C\beta})$. The third parameter, b' , is defined as $b' = c' - a'$, as explained in Paragraph 4.2.1.

Similarly to the case of S³E, we have modified the theoretical values of the evolution times a' , b' and c' to take into account the finite length of the selective pulses on C', to have the correct evolution time on the C α : $a = a' - \tau_{Q_3}/2$, $b = b'$ and $c = c' - \tau_{Q_3}$.

We have therefore performed the four DS³E experiments using the pulse sequence shown in Figure 4.5. In the first try, we set the J-couplings to the average values suggested in literature [95] ($J_{C\alpha C'} = 55$ Hz, $J_{C\alpha C\beta} = 35$ Hz) and we performed the DS³E experiments.

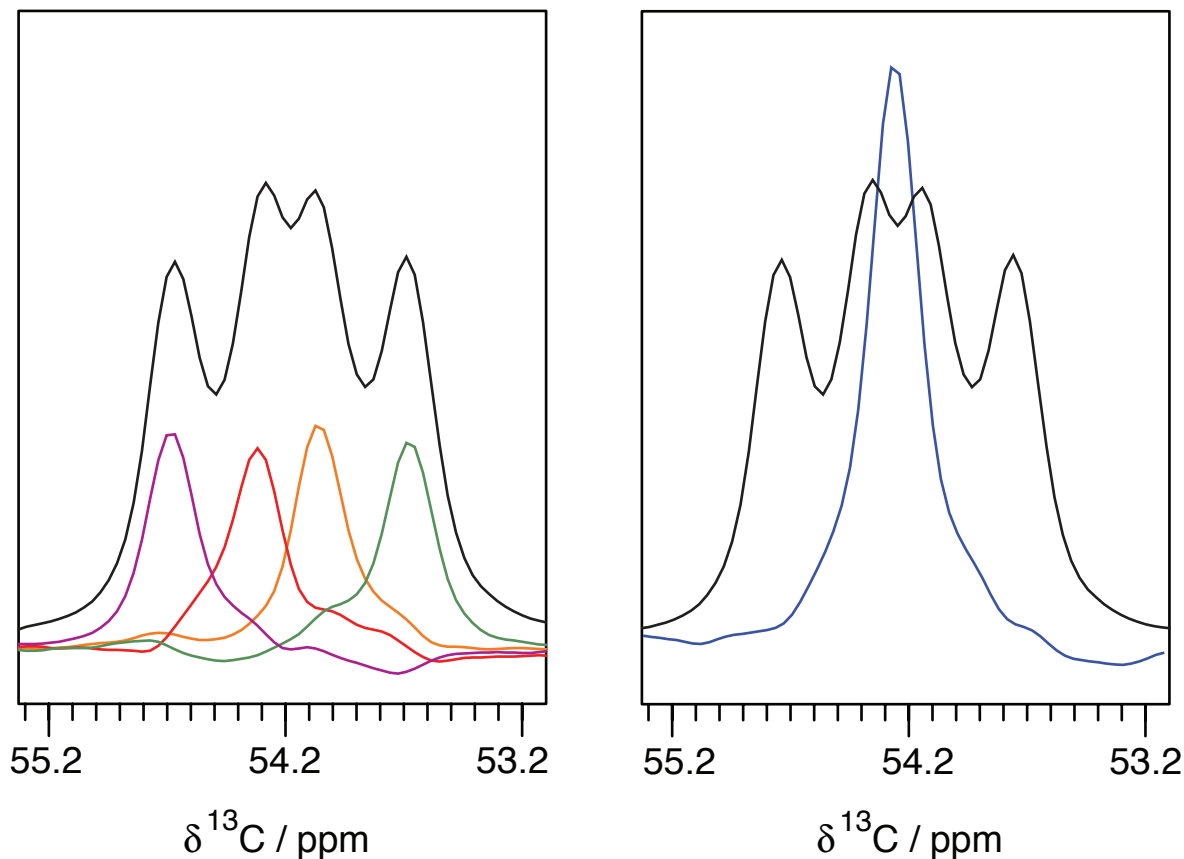


Figure 4.8: DS³E applied on alanine C α . Left: reference CP experiment without DS³E building block (black, NS = 64) overlaid with the four components of the multiplets obtained with DS³E experiments, shown in Figure 4.3, after linear combinations (purple, red, orange and green). Each experiment of DS³E was measured with NS = 16. Right: Overlay of the reference experiment (black) with the singlet obtained by shifting the purple and green components by $\pm J_{C\alpha C'}/2 = 27.5$ Hz and the red and orange by $\pm J_{C\alpha C\beta}/2 = 17.5$ Hz and summing them.

We performed linear combinations of the four DS³E experiments (Paragraph 4.2.2) and, after phase corrections, we obtained the purple (**A+B+C+D**), the red (**A+B-C-D**) the orange (**A-B+C-D**) and the green (**A+B-C-D**) components, shown in Figure 4.8 (left). In the right part of Figure 4.8, the purple and green components were shifted by $\pm J_{C\alpha C'}/2 = 27.5$ Hz and the red and orange by $\pm J_{C\alpha C\beta}/2 = 17.5$ Hz and summed together. The resulting S/N gain of the so obtained singlet compared to the reference experiment is 1.13.

Similarly to the S³E case, the J-decoupling of the C α region can be achieved. On the other hand, the separation of the components results less precise than the previous experiment (Figure 4.8 left). We then carefully analyse the effect of the chosen value for the J-couplings in the performance of the experiments, repeating the experiments varying the evolution times a and c independently. We choose a range of ± 5 Hz for $J_{C\alpha C'}$ and $J_{C\alpha C\beta}$, changing the value by 0.25 Hz for each series of DS³E experiments (data not shown). From the qualitative analysis of the results, we concluded that the performance of the

sequence is not strongly influenced by the chosen value for the J-couplings. Therefore, in the following experiments, we defined $J_{C\alpha C'} = 55$ Hz and $J_{C\alpha C\beta} = 35$ Hz

4.3.2 Applications of S³E and DS³E

We applied the S³E and DS³E building blocks described above on [UL ¹⁵N - ¹³C] crystalline ubiquitin to obtain high resolution J-resolved ¹⁵N - ¹³C and ¹³C - ¹³C correlation spectra.

We performed the following experiments, NCO - S³E, NCA - DS³E and DREAM - S³E, at a magnetic field of 20.0 T and setting the MAS frequency to 60 kHz. Further experiment details are shown in Paragraph 4.5.2. The pulse sequences used for these measurements are shown in Figure 4.9 and 4.10

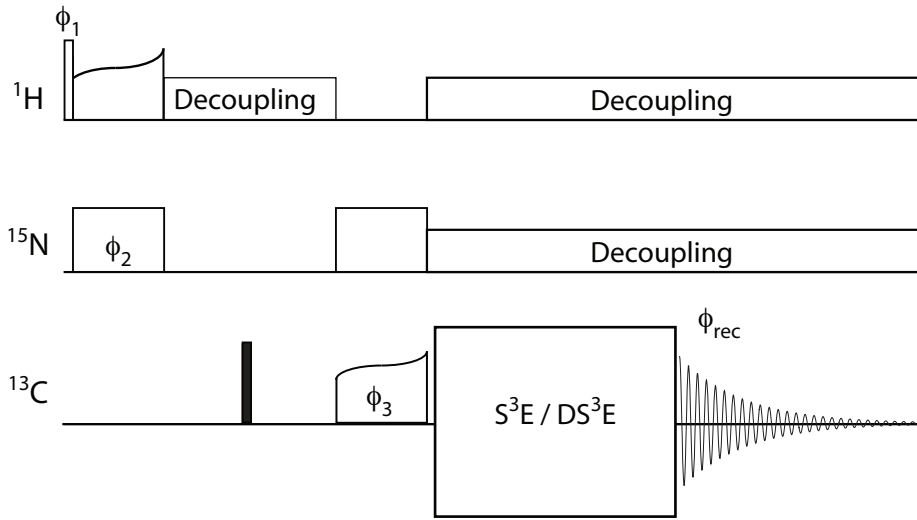


Figure 4.9: 2D NCA - DS³E and 2D NCO - S³E pulse sequences. White and black rectangle represent $\frac{\pi}{2}$ and π pulses respectively. All pulses have phase x , if not specified differently. The pulse sequence starts with the initial ¹H $\frac{\pi}{2}$ pulse, followed by CP to ¹⁵N. During the ¹⁵N evolution time t_1 XiX^{CW} [8] is applied on ¹H and a refocusing π pulse on the ¹³C channel is placed in the center of the evolution. Then the ¹⁵N - ¹³C CP brings the magnetization on the C α / C' followed by DS³E / S³E building block, according to the choice of experiment. The minimum phase cycle for this pulse sequence is $\phi_1 = y, y, -y, -y, \phi_2 = x, x, x, x, -x, -x, -x, -x, \phi_3 = \phi_{S^3E}(X)/\phi_{DS^3E}(X)$ and $\phi_{rec} = x, -x, -x, x, -x, x, x, -x$. X denotes the experiment of the building block. XiX^{CW} [8] and WALTZ [103] decoupling is applied on ¹H and ¹⁵N during acquisition.

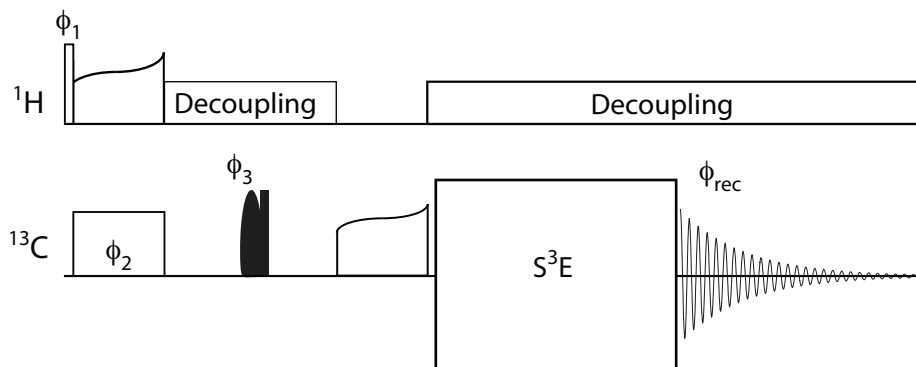


Figure 4.10: 2D DREAM - S³E pulse sequences. White and black rectangle represent $\frac{\pi}{2}$ and π pulses respectively. Shaped black pulse represents selective π pulse. All pulses have phase x , if not specified differently. The pulse sequence starts with the initial ^1H $\frac{\pi}{2}$ pulse, followed by CP to ^{13}C . During the ^{13}C evolution time t_1 , XiX^{CW} [8] is applied on ^1H . The combination of a selective π pulse on $C\alpha$ and hard π pulse are applied in the middle of ^{13}C evolution [96] to refocus the $J_{C\alpha C\beta}$ and $J_{C\alpha C'}$ in the indirect dimension. The DREAM transfer [14] brings the magnetization on C' and is followed by S³E building block. The minimum phase cycle for this pulse sequence is $\phi_1 = y, y, -y, -y$, $\phi_2 = \phi_{S^3E}(X)$, $\phi_3 = x, x, x, x, y, y, y, y$ and $\phi_{rec} = x, -x, -x, x, -x, x, x, -x$. X denotes the experiment of the building block. XiX^{CW} [8] decoupling is applied on ^1H during acquisition.

The DREAM S³E

We performed the DREAM S³E experiments to obtain high resolution $C\alpha - C'$ intra-residue correlation spectrum. The pulse sequence starts with $\frac{\pi}{2}$ pulse on ^1H , followed by an optimized CP to $C\alpha$. In the center of the t_1 evolution, a combination of soft and hard π pulse is applied, as proposed in [96].

The selective π pulse is optimized to invert the $C\alpha$ region, refocussing the homonuclear J-couplings $J_{C\alpha C\beta}$ and $J_{C\alpha C'}$ in the indirect dimension. The presence of these pulses does not create strong phase shifts in the spectrum and the effect of the non-zero minimal t_1 evolution could be removed by moderate first order phase correction.

The following optimized DREAM [14] sequence transfers the magnetization from the $C\alpha$ to the C' of the same residue. Note that, due to the regime of fast MAS ($\nu_r \geq 55$ kHz), no CW decoupling is applied on ^1H during the transfer, as shown in [106].

Prior to acquisition, the S³E building block is applied. As discussed previously, we set $J_{C\alpha C'} = 55$ Hz, leading to a total evolution time of $2a' = 4.54$ ms.

We finally performed a 2D DREAM reference experiment, with J-decoupling in the indirect dimension but without the S³E building block, shown in grey in Figures 4.11, 4.12. The total measurement time of the two S³E experiments was set equal to the reference spectrum. Representative traces (dotted lines in Figure 4.11) are shown in Figure 4.13

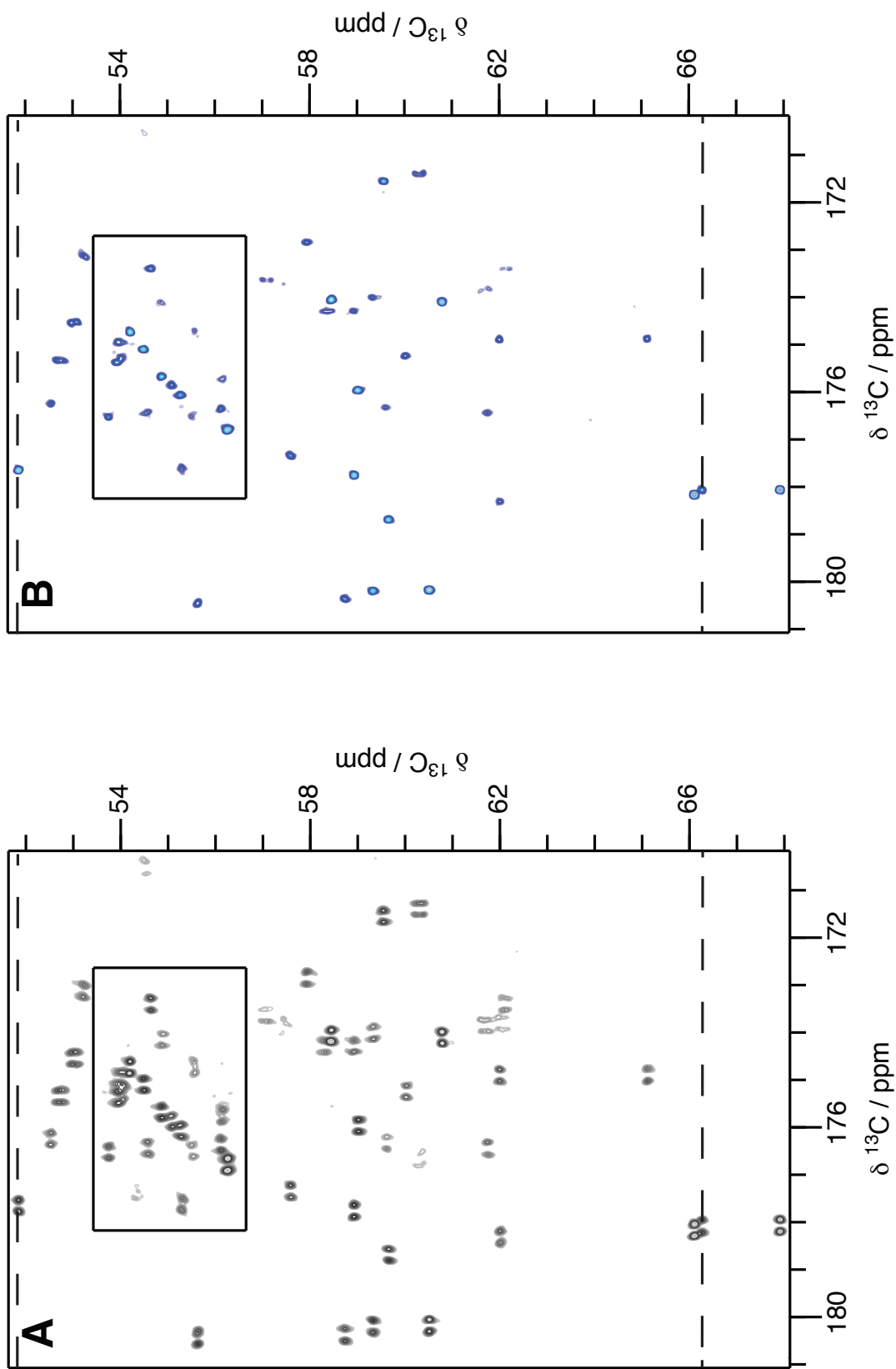


Figure 4.11: 2D C α - C' DREAM. **A** 2D C α - C' DREAM with J-decoupling in the indirect dimension (NS = 32). **B** 2D C α - C' DREAM with S³E spectrum, obtained after shifting and summing the spectra obtained by linear combination of the two S³E experiments. Each experiment of the S³E has NS = 16. Traces of the peaks marked with dotted lines are shown in Figure 4.13.

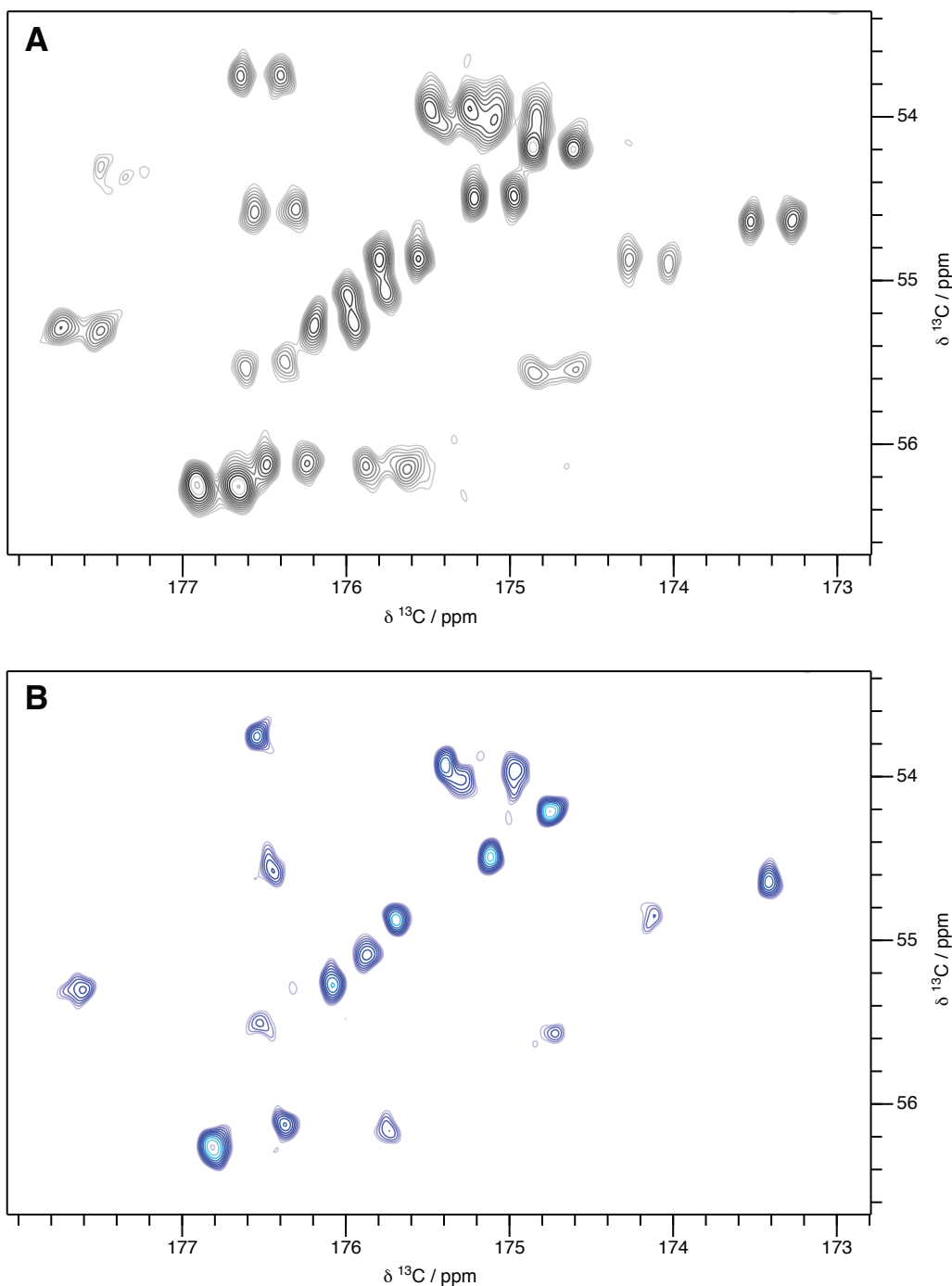


Figure 4.12: Overlap region of 2D DREAM (box of Figure 4.11) to show the gain in resolution. **A** 2D $C\alpha - C'$ DREAM with J-decoupling in the indirect dimension. **B** 2D $C\alpha - C'$ DREAM with S^3E spectrum, obtained after shifting and summing the spectra obtained by linear combination of the two S^3E experiments.

The so-obtained S^3E spectrum of Figure 4.11 presents excellent resolution and higher S/N ratio compared to the reference experiment. The best resolved peak has a linewidth of 20 Hz in the direct dimension and 22 Hz in the indirect one. The average linewidth of the cross peaks is 32 Hz in the direct dimension and 37 Hz in the indirect one.

We automatically picked 61 correlations from 2D $C\alpha - C'$ DREAM - S^3E spectrum of

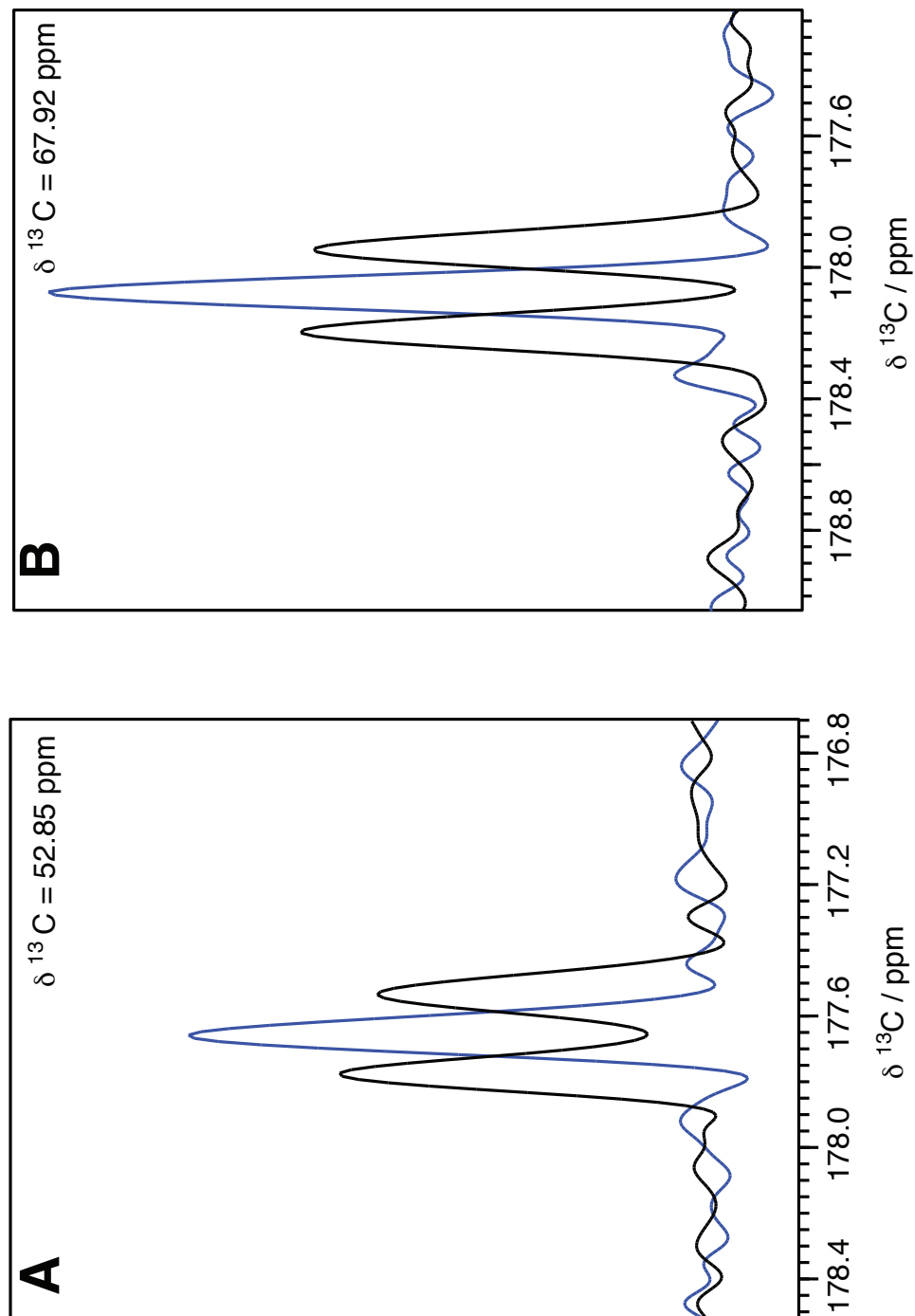


Figure 4.13: **A, B:** 1D traces obtained from 2D $\text{C}\alpha - \text{C}'$ DREAM: comparison between the singlet obtained by shifting and summing the two components from S^3E (blue) and the original multiplet (grey).

Figure 4.11 out of the 66 expected cross peaks, as shown in [107].

The NCO - S³E

We performed the 2D NCO S³E experiments to obtain high resolution N - C' correlation spectrum. The pulse sequence starts with $\frac{\pi}{2}$ pulse on ¹H, followed by CP to nitrogen. A hard π pulse is placed in the center of the ¹⁵N t₁ evolution to refocus the heteronuclear ¹⁵N - ¹³C J-coupling (~ -10 Hz).

The following optimized DQ DCP [108] transfers the magnetization from nitrogen to the C' of the previous residue. Similarly to the DREAM, no CW decoupling is applied on ¹H during the DCP.

Prior to acquisition, the S³E building block is applied. We set $J_{C\alpha C'} = 55$ Hz without further optimization, leading to a total evolution time of $2a' = 4.54$ ms.

We finally performed a 2D NCO reference experiment, with J-decoupling in the indirect dimension but without the S³E building block, shown in grey in Figures 4.14, 4.15. The total measurement time of the two S³E experiments was set equal to the reference spectrum.

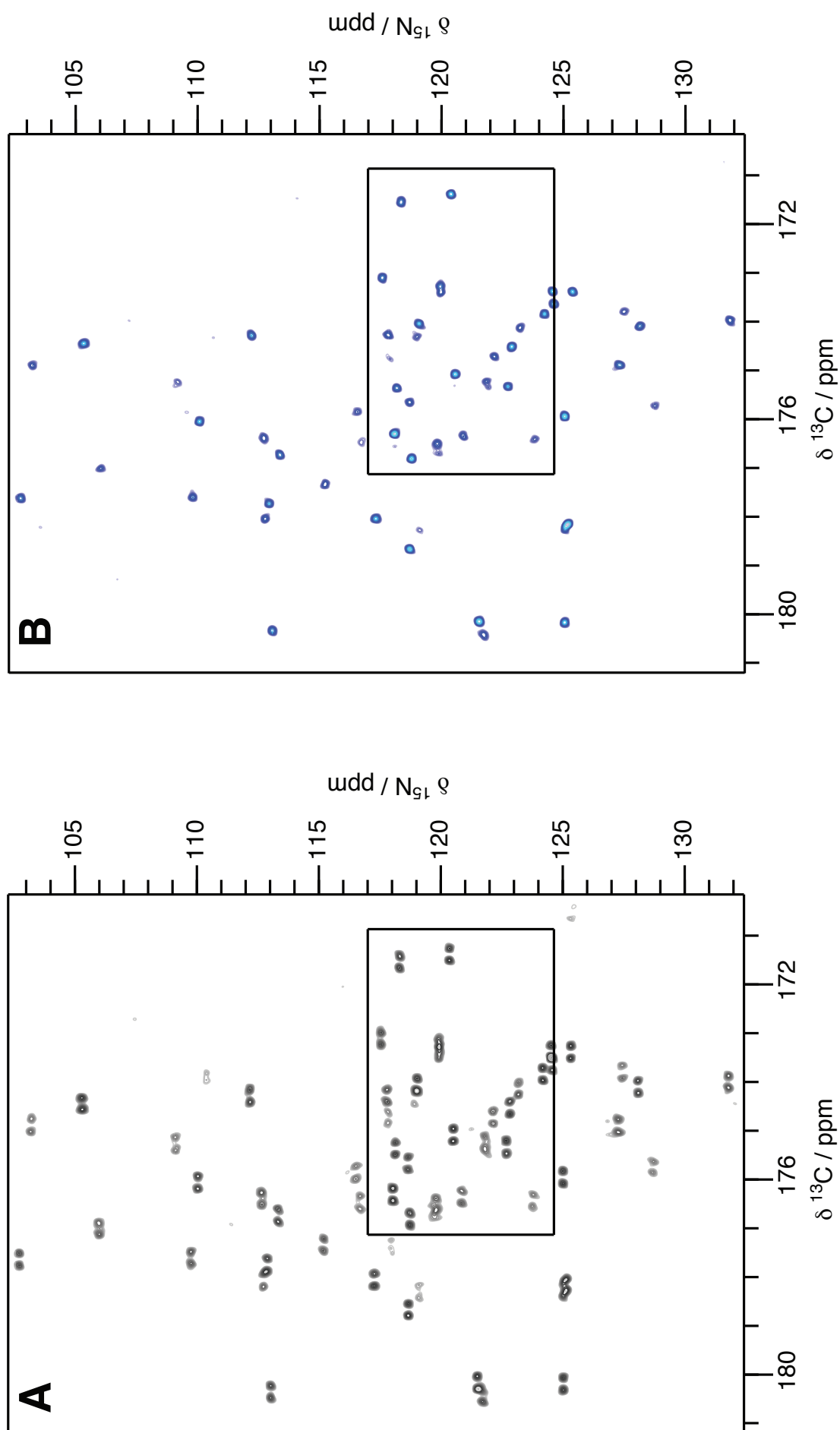


Figure 4.14: 2D NCO spectra. **A:** reference 2D NCO ($\text{NS} = 32$). **B:** 2D NCO with S^3E spectrum, obtained after shifting and summing the spectra obtained by linear combination of the two S^3E experiments. Each experiment of the S^3E has $\text{NS} = 16$.

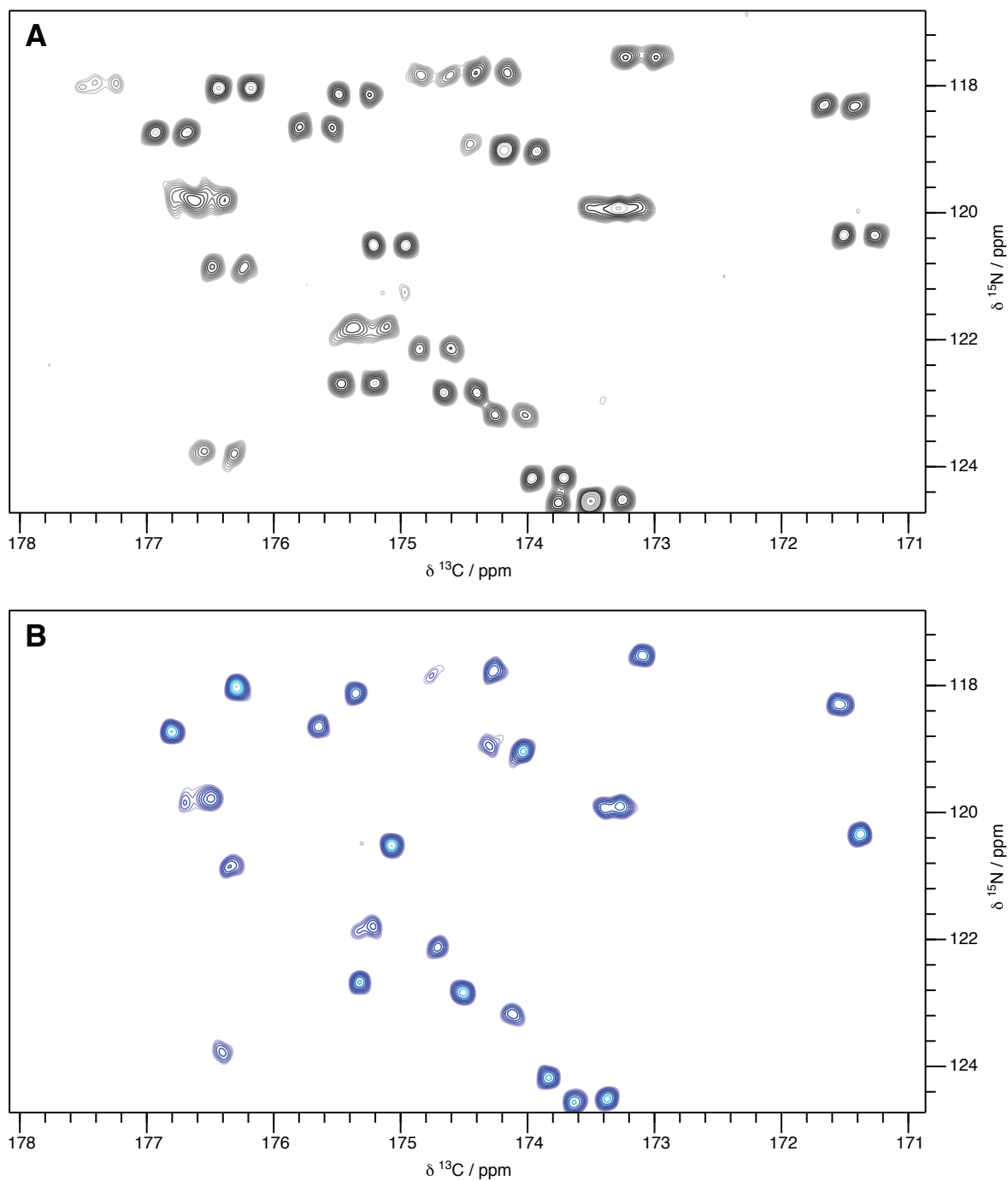


Figure 4.15: Overlap region of 2D NCO (box of Figure 4.14) to show the gain in resolution. **A:** reference 2D NCO. **B** 2D NCO with S³E spectrum, obtained after shifting and summing the spectra obtained by linear combination of the two S³E experiments.

The so-obtained S³E spectrum of Figure 4.14 presents excellent resolution and higher S/N ratio compared to the reference experiment, similarly as with the DREAM - S³E. We automatically picked 60 correlations from 2D C α - C' DREAM - S³E spectrum of Figure 4.11 out of the 66 expected cross peaks, as shown in [107].

The NCA - DS³E

We finally performed the 2D NCA DS³E experiments to obtain high resolution N - C α correlation spectrum. The pulse sequence starts with $\frac{\pi}{2}$ pulse on ¹H, followed by CP to nitrogen. A hard π pulse is placed in the center of the ¹⁵N t₁ evolution to refocus the heteronuclear ¹⁵N - ¹³C J-coupling (~ -10 Hz).

The following optimized DQ DCP [108] transfers the magnetization from nitrogen to the C α of the same residue. Similarly to the experiments listed above, no CW decoupling is applied on ¹H during the DCP.

Prior to acquisition, the DS³E building block is applied. We set $J_{C\alpha C'} = 55$ Hz and $J_{C\alpha C\beta} = 55$ Hz without further optimization, leading to a total evolution time of $2c' = 7.15$ ms.

We finally performed a 2D NCA reference experiment, with J-decoupling in the indirect dimension but without the DS³E building block, shown in grey in Figures 4.16, 4.17. The total measurement time of the four DS³E experiments was set equal to the reference spectrum.

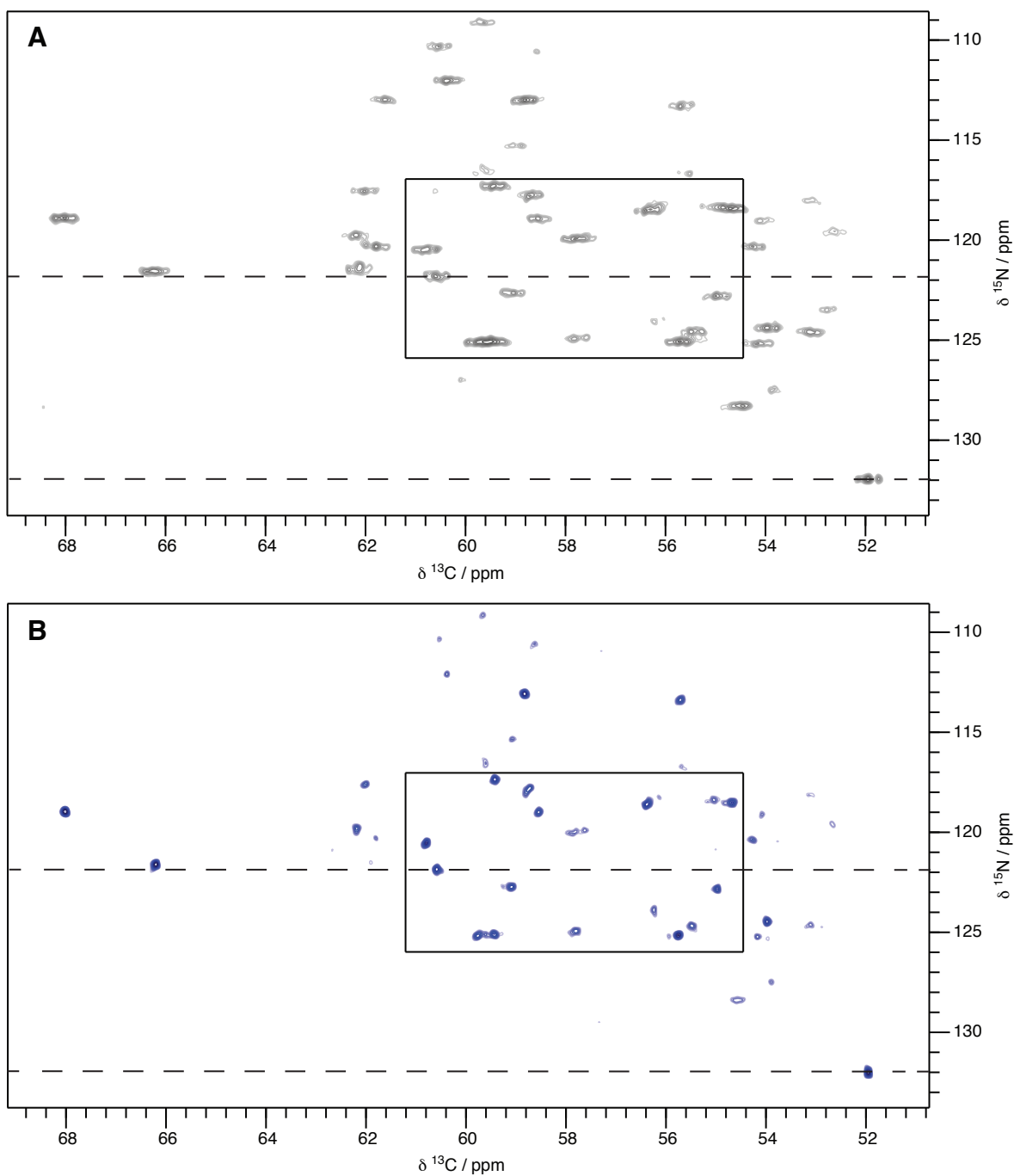


Figure 4.16: 2D NCA spectra. **A:** reference 2D NCA (NS = 32). **B** 2D NCA with DS³E spectrum, obtained after shifting and summing the spectra obtained by linear combination of the four S³E experiments. Each experiment of the DS³E has NS = 8.

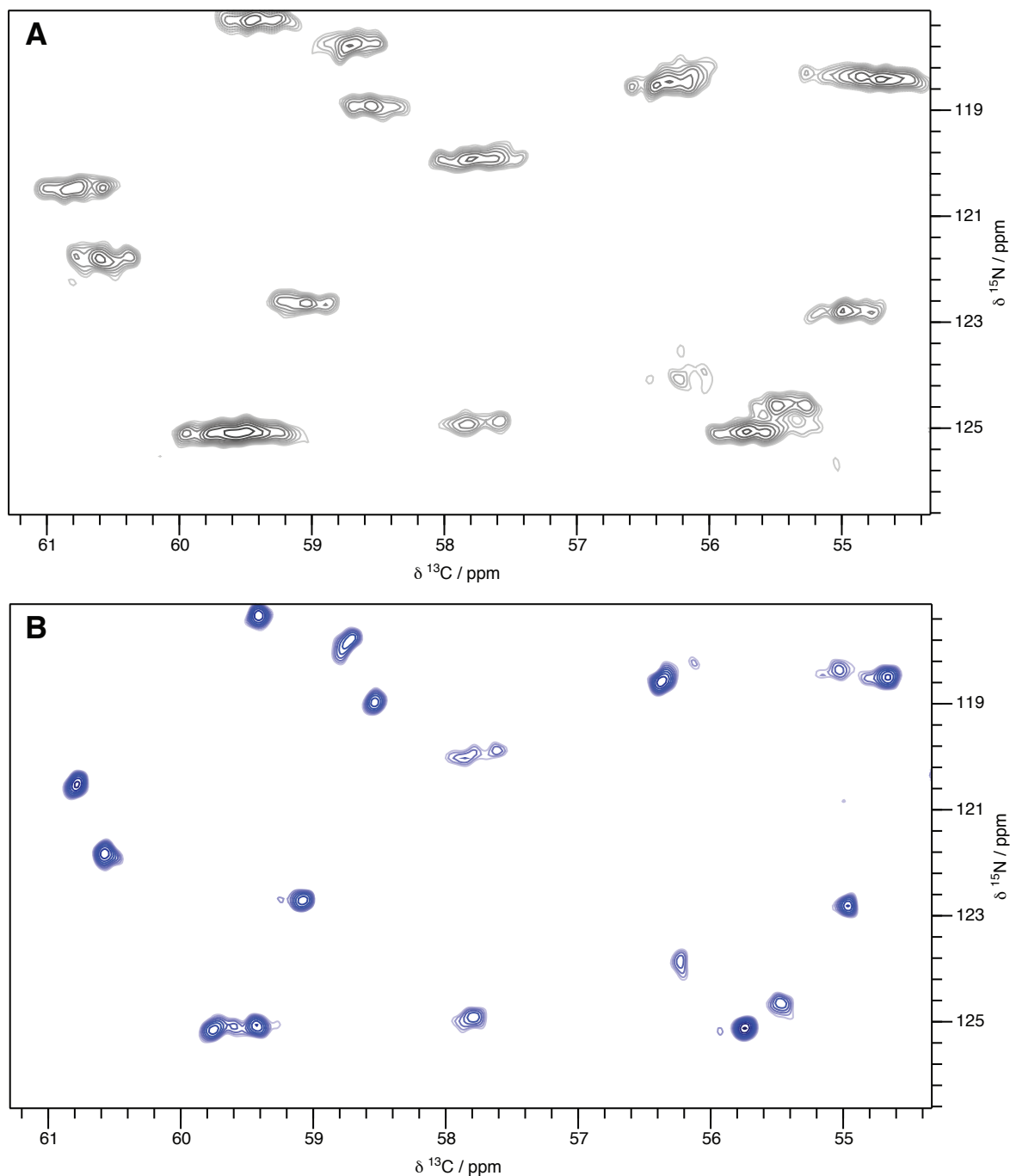


Figure 4.17: Overlap region of 2D NCO (box of Figure 4.14) to show the gain in resolution. **A:** reference 2D NCA. **B** 2D NCA with DS³E spectrum, obtained after shifting and summing the spectra obtained by linear combination of the four DS³E experiments.

The so-obtained DS³E spectrum of Figure 4.16 presents excellent resolution and higher S/N ratio compared to the reference experiment, similarly to the spectra discussed above. On the other hand, the presence of two independent evolution times a and c makes the separation of the components more difficult: in Figure 4.17, for instance, it's possible to see that some of the singlets present a small component on the left of the main peak. These artefacts are due to the non-perfect separation of the components during the DS³E

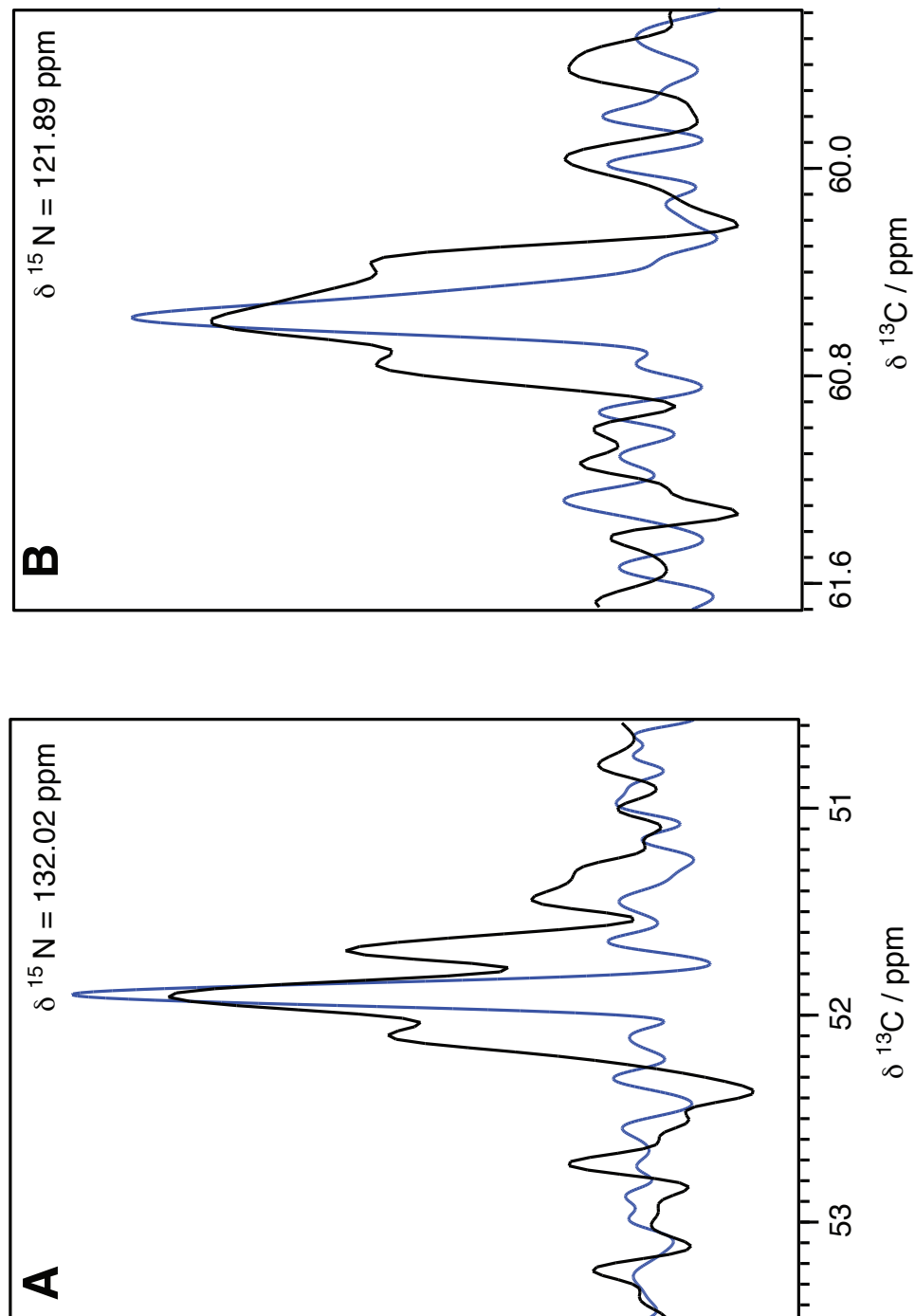


Figure 4.18: A, B: 1D traces obtained from 2D NCA: comparison between the singlet obtained by shifting and summing the four components from DS³E (blue) and the original multiplet (grey).

experiments.

Moreover, as shown in Figure 4.19, the components from DS³E are not symmetric, in comparison with the one extracted from S³E. Nonetheless, we automatically picked 53 highly resolved N-C α crosspeaks. This correlations can be used, together with the one obtained from the NCO - S³E and C α - C' DREAM - S³E, to identify spin systems and to perform 2D backbone walk.

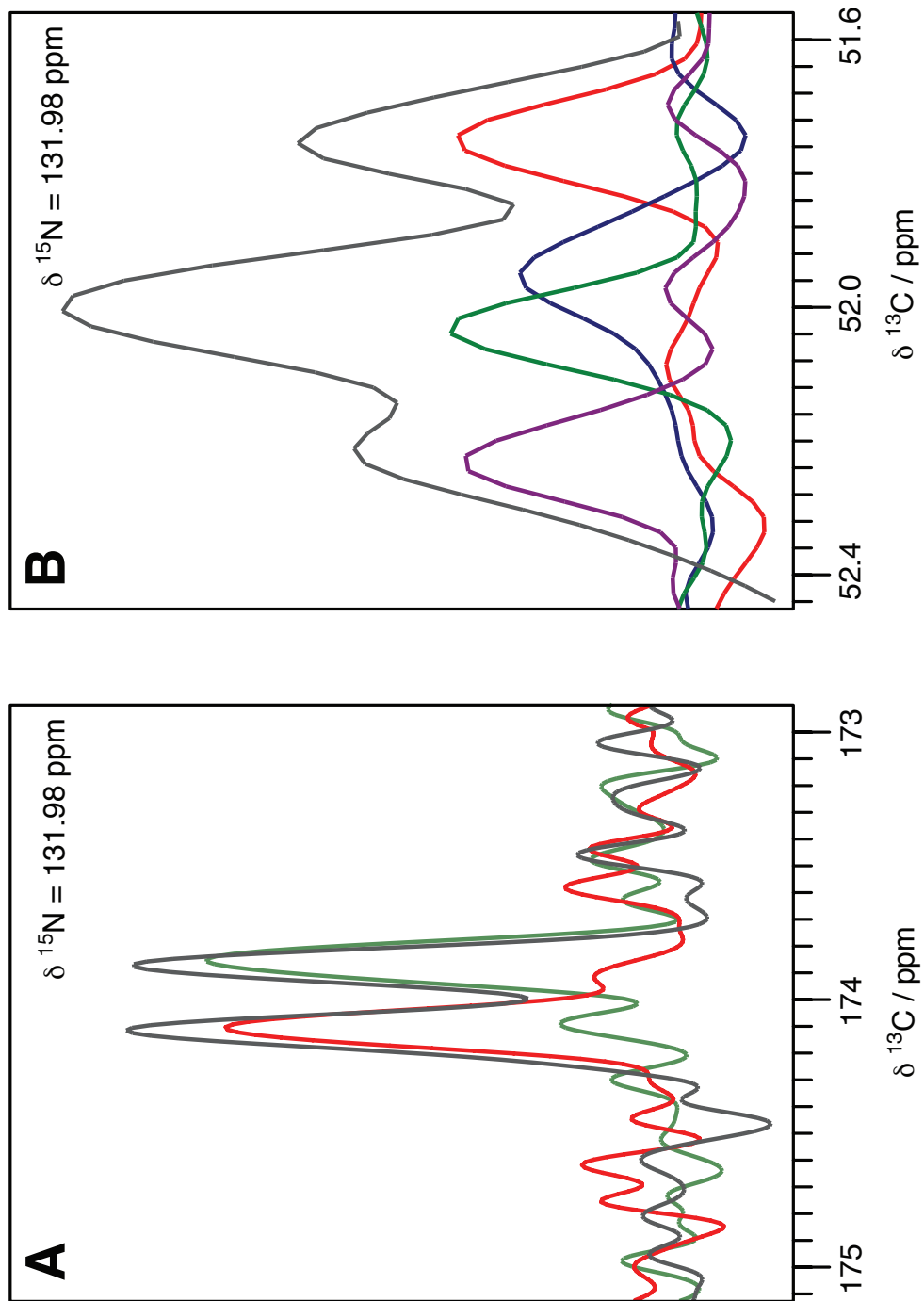


Figure 4.19: 1D traces obtained from 2D NCO S³E (A) and 2D NCA - DS³E (B) at ^{15}N frequency of 131.98 ppm. The components obtained from the C α multiplets are not nicely separated and not symmetric, compared to the C'.

4.4 Conclusions

In this chapter we presented some possible applications of spin state selective excitation type sequences in solid - state NMR. These sequences are designed to suppress the homonuclear ^{13}C J-coupling during acquisition. Two variations of these sequences can be applied on the C' and on the $C\alpha$ region, namely S^3E and DS^3E respectively. These are based on the evolution of the operators for a fixed time and the presence of selective π pulses during this evolution. We can separate the components of the original J-coupling multiplets by linear combining the S^3E and DS^3E experiments, as described above.

We first tested both sequences on a simple amino acid, alanine, to J-resolve the $C\alpha$ and C' . We have investigated the role of the evolution times in the sequences, concluding that both the S^3E and DS^3E do not require careful optimization of these parameters. This fact allowed us to move to a more complex system, ubiquitin, with the aim to obtain high resolution ^{13}C spectra.

We added the spin state selective excitation blocks in standard 2D correlation experiments for backbone atoms (NCA, NCO and $C\alpha$ - C' DREAM), obtaining J-resolved spectra in both dimensions.

These sequences work best in a fast MAS regime ($\nu_r \geq 55$ kHz), where application of low power decoupling sequences become effective. Under this regime, the maximum acquisition time is not limited by sample heating due to high power rf pulses.

With the homonuclear J-coupling, we obtained linewidth in the order of ~ 25 Hz for ^{13}C and ~ 35 Hz for ^{15}N . Moreover, the overlapping was drastically reduced, with almost all the peaks resolved in these 2D spectra.

Finally, the possibility of shifting and summing the components of the multiplet allowed us to obtain higher S/N ratio than the reference experiment, rendering this method competitive for samples screening in the case of low quantity of material where ^1H detection schemes [109] can't be applied (i.e. low ^1H resolution in proton detected spectra).

4.5 Experimental methods

4.5.1 Sample preparation

To prepare the ubiquitin sample, the procedure starts with an overnight pre - culture, which is used to inoculate the desired medium. Cells are grown at 37°C and 100 - 120 rpm until OD600 reaches 0.8 in LB. The culture is induced and grown for 3 - 4 hours in LB and the cells are then centrifuged for 10 minutes at 6000 g and re suspended in lysis buffer for the Microfluidizer.

Perchloric acid is added to the lysis supernatant to a concentration of 3.5 % w/v and vigorously shaken for a short time. After an incubation of 10 minutes at 40°C , precipitated proteins are pelleted 4°C and 20 minutes at 48,000 g. The supernatant is neutralized using saturated Tris buffer. The solution is exchanged with ubiquitin binding buffer by

gel filtration using a HiPrep 26/10 desalting column. The protein is boiled at 85°C for 10 minutes and the precipitated pelleted at 4°C and 48,000 g.

The supernatant is loaded on a 6 ml Resource S ion exchange column, washed with 5 column volumes of binding buffer and eluted with a gradient of 0 - 100 % elution buffer over 20 column volumes. The fractions containing ubiquitin are dialysed against MilliQ water overnight at 4°C and then lyophilized.

Ubiquitin is dissolved in 20 mM ammonium acetate buffer at pH 4.3 containing 0.05% sodium azide. The final ubiquitin concentration is 25 mg/ml ($M_{ubiquitin} = 8.56$ kDa). The protein solution is filter sterilized and centrifuged for 5 minutes at 15,000 rpm at 4°C.

The precipitation buffer consists of 2-methylpentanediol-2,4 and citrate buffer at pH 4.1 in a 3:2 volume ratio, containing 0.05% sodium azide. The citrate buffer can be prepared from citric acid and adjusted carefully with 1M NaOH to the desired pH of 4.1. The final concentration of citric acid in the precipitation buffer is 20 mM.

In each crystallization reservoir 500 μ l of precipitation buffer is added. 37 μ l of protein solution and 10 μ l of precipitation buffer are mixed in the crystallization well. The crystallization reservoir are sealed at 4°C. After a few weeks the wells should contain crystals, which were harvested and put in a 1.3 mm rotor by ultracentrifugation.

4.5.2 Solid - state NMR spectroscopy

All the experiments performed on alanine were measured at a static magnetic field of 11.75 T on a Bruker 1.3 mm probe. The MAS frequency was set to 60 kHz and no cooling was added. The rf fields applied during the CP were set to $\omega_H = 110$ kHz and $\omega_C = 52$ kHz, while the carrier was set to 55 ppm for DS³E and 175 ppm for S³E. The length of the CP was optimized for $C\alpha$ and C' separately, $\tau_{CP}^{C\alpha} = 900$ μ s and $\tau_{CP}^{C'} = 1700$ μ s.

The selective π pulses used in these experiments are Gaussian cascade Q_3 [105], [110] optimized experimentally for the best inversion of the $C\alpha$ and C' region. The length of the pulses was set to $\tau_{Q_3}^{C\alpha} = 1.25$ ms and $\tau_{Q_3}^{C'} = 300$ μ s, while the average rf field was $\omega_{Q_3}^{C\alpha} = 1.2$ kHz and $\omega_{Q_3}^{C'} = 0.7$ kHz. Care was taken to avoid phase distortions and partial inversion on the $C\beta$ while optimizing the selective π pulse on $C\alpha$.

We set the value of the J couplings to $J_{C\alpha C\beta} = 35$ Hz for DS³E and $J_{C\alpha C'} = 55$ Hz for both DS³E and S³E, correspondin to a total evolution time of $\tau_{S^3E} = 2a = 4.54$ ms and $\tau_{DS^3E} = 2c = 7.14$ ms. XiX^{CW} [8] decoupling was applied on ¹H during acquisition and during the DS³E/S³E, with $\tau_{XiX} = 68$ μ s, $\omega_{XiX} = 10$ kHz and $\omega_{XiX}^{CW} = 2$ kHz. The total acquisition time was set to 45 ms.

2D experiments

All the experiments performed on ubiquitin were measured at a static magnetic field of 20 T on a Bruker 1.3 mm probe. The MAS frequency was set to 60 kHz and the sample

temperature was set to 10° C, calibrated on the position of the water line.

We used, as in the case of the experiments on alanine, Q_3 selective π pulses for the inversion of the $C\alpha$, C' and $C\alpha+C\beta$ regions. The length of the pulses was set to $\tau_{Q_3}^{C\alpha} = 1.25$ ms and $\tau_{Q_3}^{C'} = \tau_{Q_3}^{C\alpha+C\beta} = 300\mu\text{s}$, while the average rf field was $\omega_{Q_3}^{C\alpha} = 1.2$ kHz and $\omega_{Q_3}^{C'} = \omega_{Q_3}^{C\alpha+C\beta} = 0.7$ kHz. Details on the optimization of the selective pulses are shown in Appendix B.1.

We set the evolution times during the DS³E and S³E for the three experiments to $\tau_{S^3E} = 2a = 4.54$ ms and $\tau_{DS^3E} = 2c = 7.14$ ms, as described above in the case of the experiments on alanine.

XiX^{CW} [8] decoupling was applied on ¹H during acquisition, t_1 evolution and during the DS³E/S³E, with $\tau_{\text{XiX}} = 68\mu\text{s}$, $\omega_{\text{XiX}} = 10$ kHz and $\omega_{\text{XiX}}^{CW} = 2$ kHz. 5 kHz ¹⁵N WALTZ decoupling [103] was applied during acquisition and during the DS³E/S³E.

For the NCO and NCA experiments, the rf fields applied during the CP were set to $\omega_H = 110$ kHz and $\omega_N = 58$ kHz, with $\tau_{CP}^N = 1.2$ ms for both NCO and NCA experiments and $\omega_H = 110$ kHz and $\omega_C = 55$ kHz, with $\tau_{CP}^C = 850\mu\text{s}$ for DREAM experiment. The length of the DCP to C' and $C\alpha$ was optimized to $\tau_{DCP} = 6.5$ ms, using a double-quantum (DQ) condition [108] $\omega_N = 35$ kHz, $\omega_{C\alpha} = 26$ kHz and $\omega_{C'} = 29$ kHz. No CW irradiation on ¹H was added during the DCP [106]. The maximum acquisition time for ¹⁵N was set to $t_1^{15N} = 35.2$ ms, while the total acquisition time for ¹³C was set to $t_1^{13C} = 50.0$ ms for both NCA - DS³E and NCO - S³E.

Each experiment of the NCO-S³E took 12 hours, while each of the NCA-DS³E took 6 hours. The NCO and NCA reference experiment took 1 day each. For the DREAM experiment, the rf fields applied during the ¹H - ¹³C CP were set to $\omega_H = 110$ kHz and $\omega_C = 49$ kHz, with with $\tau_{CP}^C = 900\mu\text{s}$. The DREAM transfer was optimized experimentally to have maximum $C\alpha - C'$ transfer: the carrier was placed at 100 ppm and we optimized the $\omega_{DREAM} = 35$ kHz and the contact time $\tau_{DREAM} = 3.5$ ms. No ¹H CW decoupling was applied during the transfer.

The maximum evolution time for the $C\alpha$ evolution was set to 40.5 ms, while the acquisition time for the C' detection was set to 50.0 ms.

Each experiment of the DREAM-S³E took 12 hours, while DREAM reference experiment took 1 day.

Chapter 5

Applications of TEDOR sequence

I started this project with the aim to find a robust approach to obtain intermolecular long range contacts at fast MAS. I thank Susanne Penzel and Matthias Ernst for discussions about the TEDOR sequence. The chemical shifts of deuterated HET-s were obtained by Dr. Albert Smith. The sample of HET-s was prepared by Riccardo Cadalbert.

5.1 Introduction

In recent years, advances in magic angle spinning (MAS) [3] together with the introduction of new methods for dipolar recoupling [52], have increased the possible applications of solid-state NMR.

These approaches have been used to establish a standard procedure for resonances sequential assignment [49] and for measuring distance restraints [111], [45], [46] for proteins, which are fundamental steps for the *de novo* structure determination.

These methods are particularly useful for systems that cannot be studied via other techniques (such as X-ray crystallography and solution state NMR), namely big protein complexes [90], [91], amyloid fibrils [88], [31], [33] and membrane proteins [89]. Furthermore, the use of deuterated samples and the introduction of probes that can achieve MAS frequencies of 50 - 100 kHz [3] have made feasible the use of multidimensional ^1H detected experiments [109], [94], [112], [113], [114] in solid - state NMR.

Consequently this has stimulated interest in introducing a standard procedure for assignment [109] and for structure determination [94] in this regime. It has been shown that the use of 3D and 4D ^1H - ^1H distance restraints spectra alone can lead to a *de novo* structure determination of micro crystalline ubiquitin [94]. This approach, however, does not provide any specific information on intermolecular contacts, which have been proven fundamental for the structure determination of amyloid fibrils [33] and protein complexes. In the slow MAS regime, this information can be obtained from ^{15}N - ^{13}C contacts of a 50% ^{15}N - 50% ^{13}C labeled sample (ML sample), as shown in Chapter 2. This can be achieved using sequences that either relies on ^1H - ^1H spin diffusion (NHHC [53])

or on the effect of a third ^1H spin (PAIN-CP [52]). Both approaches rely on a second order recoupling technique which would be less effective in the fast MAS regime ($\nu_r > 55$ kHz) and with the use of deuterated samples. It has been shown recently that third spin assisted recoupling (TSAR) like the heteronuclear PAIN-CP and the homonuclear PAR [115] can be used for ($\nu_r > 20$ kHz). However, care has to be taken in the choice of the used radio frequency fields, to avoid unwanted resonance conditions depending on the spinning frequency. Furthermore, the transfer does not directly depend on the ^{15}N - ^{13}C coupling but on the geometry of the system and, in a less important way, also on the presence of additional ^1H spins.

In this chapter, we present a new approach to obtain long distance intermolecular ^{15}N - ^{13}C constraints based on a modified transferred echo double resonance TEDOR experiment [13], [116] including ^1H detection, differently from [117]. This sequence has been applied for protein sequential assignment and we propose using this first order recoupling technique in the context of structure determination. The aim is to propose a procedure to obtain such information in the fast MAS regime for protein structure determination. We tested this technique on a mixed 50% ^{13}C and 50% ^{15}N labeled ^2H 100 % back exchanged HET-s(218-289) sample.

5.2 Theoretical background

The basic TEDOR sequence transfers the magnetization from two heteronuclear-coupled spins (I-S) and it consists of two REDOR [119] blocks separated by two $\frac{\pi}{2}$ pulses on I and S. Recently, different variations of the original sequence have been proposed [116] to overcome effects related with ^{13}C - ^{13}C dipolar coupling, ^{13}C - ^{15}N chemical shift anisotropy (CSA) and homonuclear ^{13}C - ^{13}C J-coupling. There, the initial magnetization is on the ^{13}C channel (I spin) and it is transferred to the ^{15}N after the first TEDOR block, followed by nitrogen evolution. Finally, it is back transferred on the carbon and detected. In the two versions proposed, the effect of ^{13}C - ^{13}C homonuclear J-coupling during the TEDOR period was solved by including a z-filter before the detection or by adding a selective refocusing pulse in the middle of the TEDOR mixing.

The 3D - TEDOR version we propose (shown in Figure 5.1) is optimized to be efficient in the fast MAS regime with a deuterated sample 100% back exchanged on the amide proton. To obtain only intermolecular information, we consider a mixed 50% ^{13}C and 50% ^{15}N labeled (ML) sample.

The sequence starts with a cross polarization between $^1\text{H}_\text{N}$ - ^{15}N of the nitrogen labeled monomer, followed by the ^{15}N evolution (t_1). In this case, an initial CP between $^1\text{H}_\text{N}$ - ^{13}C as proposed in the previous version [116], would be less effective due to the longer $^1\text{H}_\text{N}$ - ^{13}C distance. Moreover, no selective π pulses or z-filter are used in this version. We assumed that the effective Hamiltonian during the transfer contains only the heteronuclear ^{13}C - ^{15}N dipolar coupling terms since

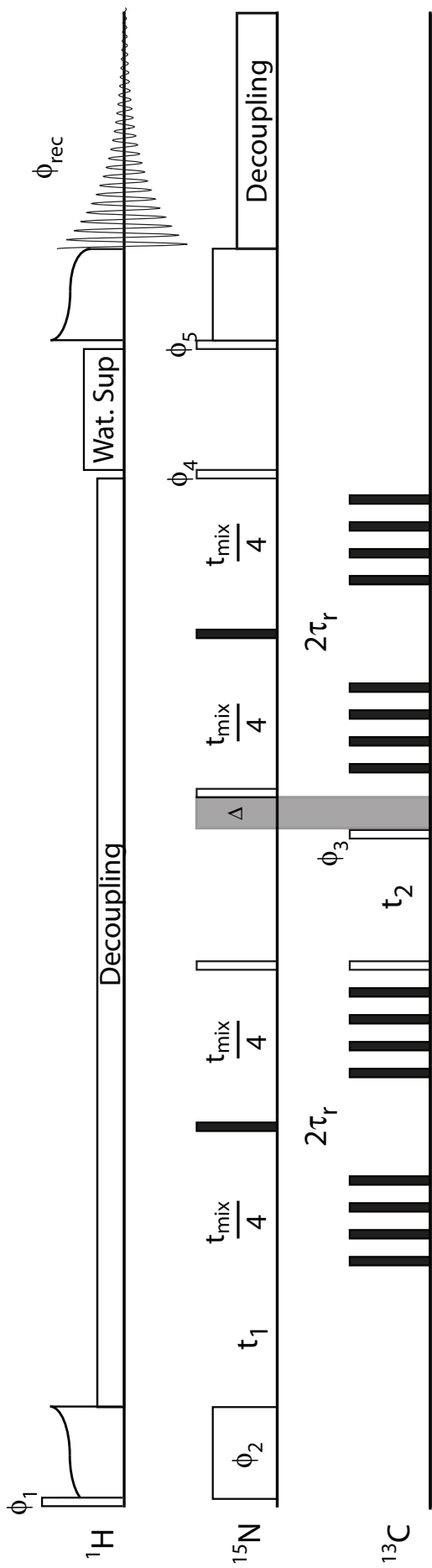


Figure 5.1: 3D ^{15}N - ^{13}C - ^1H TEDOR pulse sequence. White and black rectangles represent $\frac{\pi}{2}$ and π pulses, respectively. During the REDOR periods, two π pulses per rotor period are applied on the ^{13}C channel and phase cycled according to the xy -4 scheme [118]. The separation between the trains of π pulses on the ^{13}C channel is set to $2\tau_r$, to maintain the rotor synchronization. The delay Δ is added after the t_2 evolution to fulfil for each increment $t_2 + \Delta = n\tau_r$. A water suppression period was added after the second REDOR period, prior to the final ^{15}N - ^1H CP. All pulses have phase x if not specified differently. The minimum phase cycle is $\phi_1 = y, -y, \phi_3 = x, x, -x, -x, \phi_4 = y, \phi_5 = y, y, y, y, -y, -y, -y, -y$ and $\phi_{\text{rec}} = x, -x, -x, x, -x, x, -x$. ϕ_2 and ϕ_3 are incremented for the ^{15}N and ^{13}C evolution, respectively. Low power SW $_f$ TPPM [102] is applied during the TEDOR mixing and the t_1 and t_2 evolution. WALTZ-16 decoupling is applied on ^{15}N during acquisition.

(i) The π pulse in the middle of the REDOR period refocusses the ^{15}N chemical shifts,

(ii) Homonuclear ^{15}N J-coupling is not existing and heteronuclear ^{15}N - ^{13}C is not present in a ML sample (neglecting the NA ^{13}C in the ^{15}N labeled molecule), The

(iii) Heteronuclear ^{15}N - ^1H J-coupling and dipolar coupling are suppressed due to the ^1H decoupling in first order approximation.

effective Hamiltonian during the two REDOR blocks for spin I - S can be written as

$$\hat{\mathcal{H}}_{\text{Eff}} = \hat{\mathcal{H}}_D = 2d_{IS}\hat{I}_z\hat{S}_z, \quad (5.1)$$

where d_{IS} is the dipolar coupling constant between the ^{15}N - ^{13}C intermolecular pair, as defined in 1.1. Under this assumptions, we can calculate the propagator for the TEDOR sequence for an isolated ^{15}N (I) - ^{13}C (S) pair.

In a powder sample, each crystallite is modulated in function of the mixing time t_{mix} , as described analytically in [120].

$$\begin{aligned} & I_x \xrightarrow{t_1} I_x e^{i\Omega_I t_1} \xrightarrow{\text{REDOR}} \\ & 2I_y S_z \sin(\delta t_{\text{mix}}/2) e^{i\Omega_I t_1} \xrightarrow{90_x(I)90_x(S)} \\ & -2I_z S_x \sin(\delta t_{\text{mix}}/2) e^{i\Omega_I t_1} \xrightarrow{t_2} \\ & -2I_z S_x \sin(\delta t_{\text{mix}}/2) e^{i\Omega_I t_1} e^{i\Omega_S t_2} \xrightarrow{90_x(S)} \\ & -2I_z S_z \sin(\delta t_{\text{mix}}/2) e^{i\Omega_I t_1} e^{i\Omega_S t_2} \xrightarrow{90_x(I)} \\ & -2I_y S_z \sin(\delta t_{\text{mix}}/2) e^{i\Omega_I t_1} e^{i\Omega_S t_2} \xrightarrow{\text{REDOR}} \\ & I_x \sin^2(\delta t_{\text{mix}}/2) e^{i\Omega_I t_1} e^{i\Omega_S t_2} \end{aligned} \quad (5.2)$$

The magnetization after the initial ^1H - ^{15}N CP is in the nitrogen transverse plane. This coherence is frequency labeled during t_1 with the S spin chemical shift, Ω_I . During the first REDOR period, the heteronuclear dipolar coupling is reintroduced and an anti-phase I coherence with respect to the S spin is generated, as shown in equation 5.2. The following couple of $\frac{\pi}{2}$ pulses on the I and S spins resulted in coherence transfer to the S spin ($\propto I_z S_y$).

The selected coherence is frequency labeled during t_2 with the S chemical shift, Ω_S . The time Δ , after the $\frac{\pi}{2}$ pulse on S ($\propto I_z S_z$) is used to keep the whole TEDOR block rotor synchronised. The following $\frac{\pi}{2}$ pulse on I transfers the coherence back to the I spin ($\propto I_y S_z$). The so-generated anti-phase coherence is back transferred to observable I_x magnetization after the second REDOR period. After a z-filter with water suppression on ^1H , the magnetization is back transferred to the amide proton and detected. The combination of proton detected experiment and TEDOR has been used in [121] to measure ^1H - ^{15}N bond length.

We performed quadrature detection in t_1 and t_2 [95], [122] and a 3D Fourier transform of the time-domain results in a 3D spectrum with cross peaks in the indirect dimensions at frequency Ω_I and Ω_S , while the information on ^1H chemical shift is recorded in the

direct dimension.

In the version we propose, the rotor synchronized π pulses are situated on the ^{13}C channel, while in the published 3D sequence [116] this approach was avoided. The reason was to avoid any homonuclear ^{13}C recoupling during the mixing period due to RFDR - type effects [123], [16].

Having the magnetization on the ^{13}C transverse plane, however, leads to homonuclear J-coupling evolution during the TEDOR mixing time. This effect generates additional frequencies, that reduce transfer efficiency and additional anti - phase multiple - quantum (MQ) spin coherences, which leads to phase twisted lines and spurious cross - peaks. The proposed solutions for these issues are either adding a z - filter prior to acquisition or replacing the hard refocusing π pulse with a selective one [116].

We nonetheless decided to use the modified version shown in Figure 5.1 because, as discussed above, the initial and final $^1\text{H}_\text{N} - ^{15}\text{N}$ CP is more efficient in the case of a deuterated 100% back - exchanged sample. Moreover, the selective π pulse will remove all information of the ^{13}C spins outside the inversion window and, furthermore, increase the total length of the sequence (i.e. $\tau_{Q_3}^{C\alpha} \sim 1.5\text{ms}$, as shown in Appendix B.1). The effect of the z - filter is only to remove the MQ coherences, and it does not suppress the J - coupling evolution.

We investigated the possibility of RFDR - type recoupling during the TEDOR period by performing simulations with SIMPSON [124]. In the first calculation, we simulate the TEDOR performance in function of the mixing time for an isolated $^{15}\text{N} - ^{13}\text{C}$ spin pair. For the second calculation, we added two strongly coupled carbon atoms to the ^{13}C spin of interest (i.e $C\alpha - C'$ and $C\alpha - C\beta$). We set the values for dipolar coupling constants to $\delta_{N-C} = 100$ Hz, $\delta_{C\alpha-C\beta} = 2100$ Hz and $\delta_{C\alpha-C'} = 2200$ Hz. In Figure 5.2 the normalized intensities of the TEDOR transfer for the simulations described above are shown: the black curve represents the case of an isolated $^{15}\text{N} - ^{13}\text{C}$ pair while the red curve represents the simulation with two additional coupled ^{13}C spins.

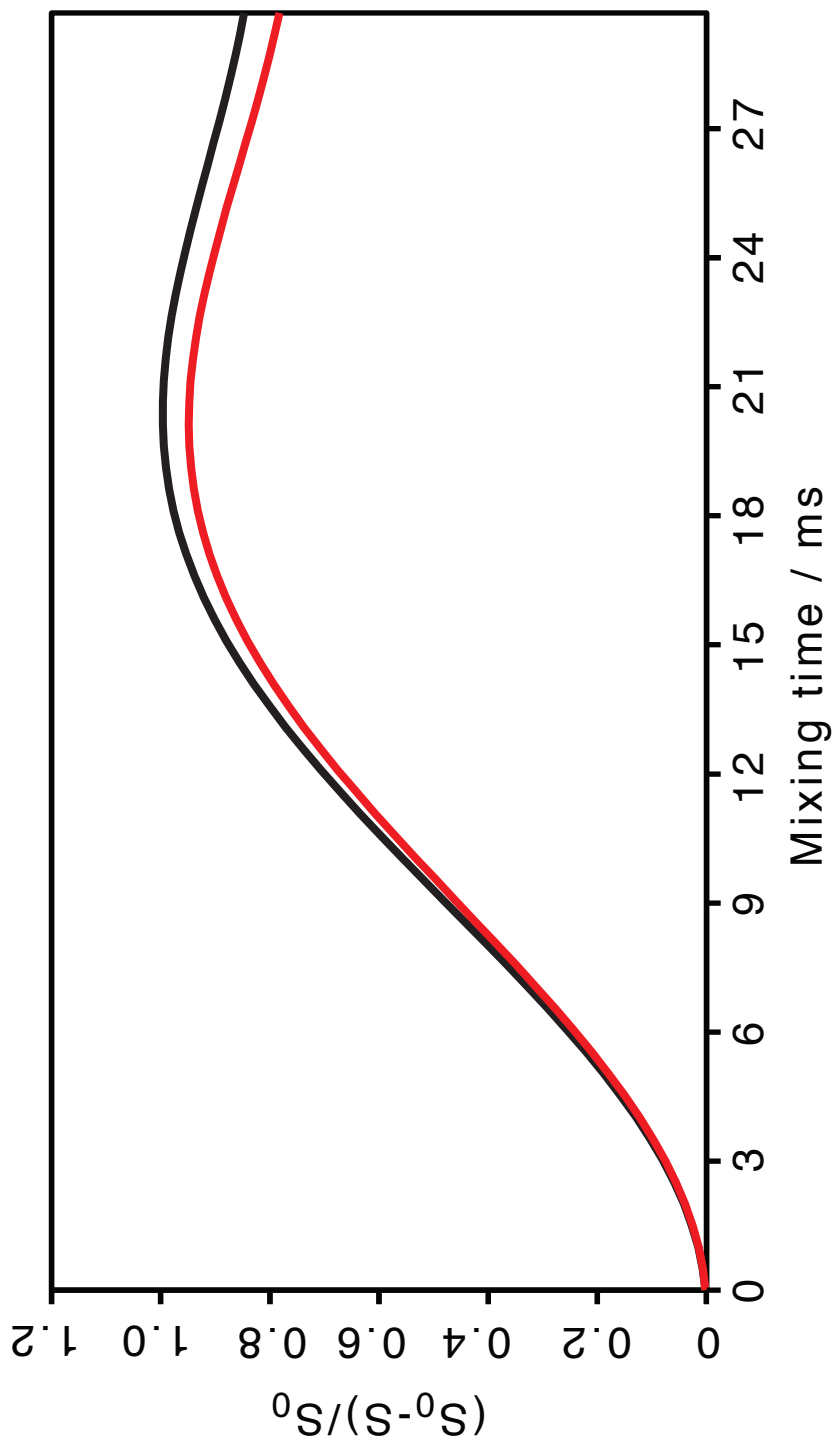


Figure 5.2: Normalized intensity of the TEDOR for a transfer between a coupled ^{15}N - ^{13}C pair. The black curve represents the build up for an isolated spin pair while the red curve represents the simulation with additional ^{13}C spins. The values for dipolar coupling constants are $\delta_{\text{N-C}} = 100$ Hz, $\delta_{\text{C}\alpha-\text{C}\beta} = 2100$ Hz and $\delta_{\text{C}\alpha-\text{C}'}$ = 2200 Hz. The spinning frequency was set to 55.555 kHz.

Looking at Figure 5.2, one can see that the presence of π pulses on the ^{13}C leads to a loss in the signal due to RFDR - type recoupling. This effect, however, is much less severe than the loss of signal due to the double CP to ^{13}C (Appendix B.2) and the effects of homonuclear J-coupling evolution.

5.3 Results and discussion

5.3.1 ^1H detected TEDOR

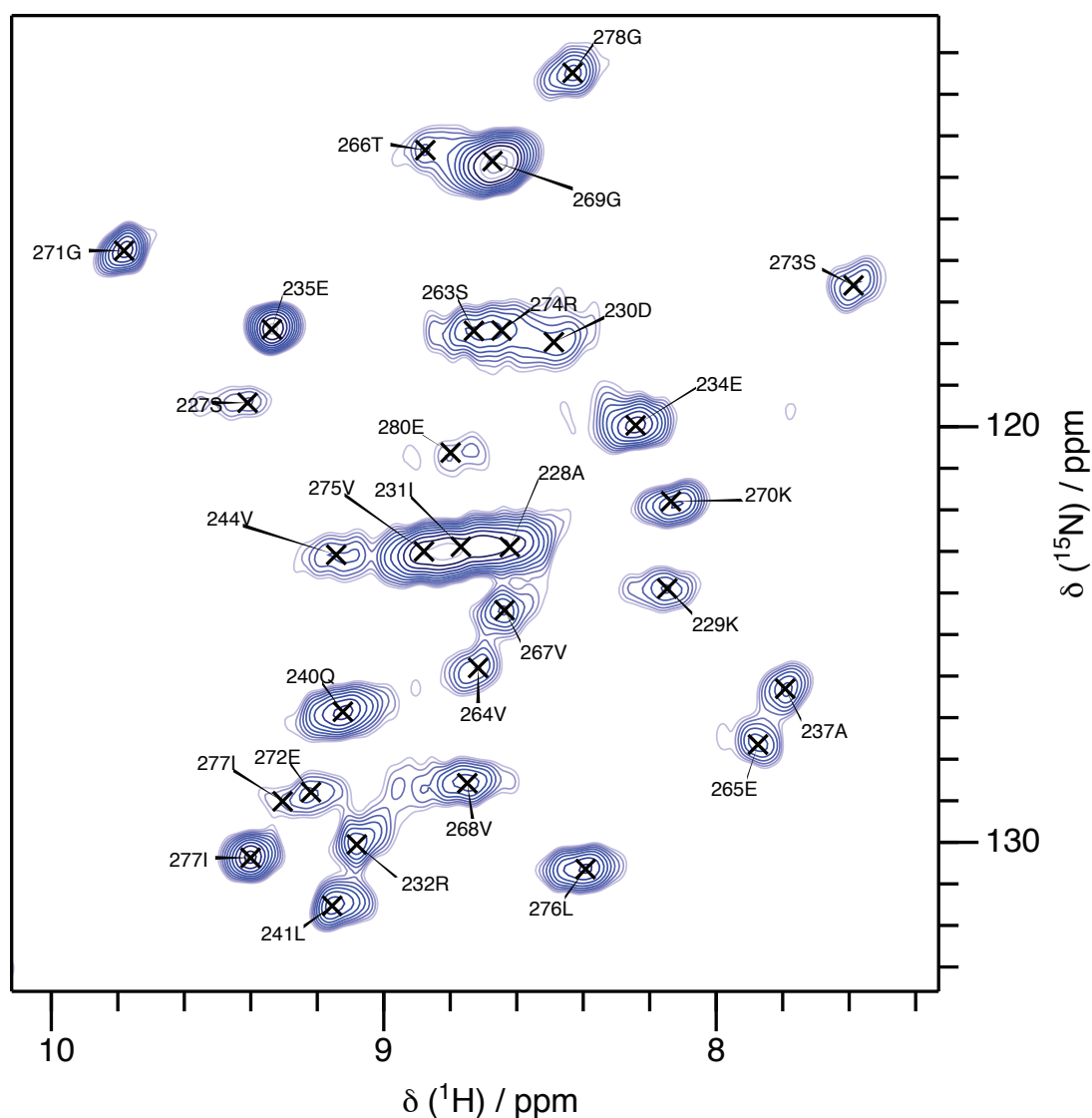


Figure 5.3: 2D ^{15}N - ^1H TEDOR measured on a ML sample of deuterated 100 % back exchanged HET-s(218-289) fibril. The experiment was performed at a magnetic field of 20.0 T and setting the MAS frequency to 55.555 kHz. Cross peaks are present only if the ^{15}N - ^{13}C transfer had taken place. Visible correlations are labeled with 1 - letter code from the assigned ^{15}N - ^1H chemical shifts.

We performed a 2D variation of the pulse sequence shown in Figure 5.1 with only ^{15}N evolution on a ML sample of fully deuterated 100 % back exchanged HET-s(218-289) fibril. The experiment was performed at a magnetic field of 20.0 T and setting the MAS frequency to 55.555 kHz (corresponding to $\tau_r = 18\mu\text{s}$). The TEDOR mixing time was set to $t_{mix} = 14.4$ ms and the resulting spectrum is shown in Figure 5.3.

A cross peak appears in the 2D ^{15}N - ^1H spectrum only if there was transfer between the ^{15}N of the nitrogen labeled molecule to the ^{13}C of the carbon labeled monomer. The relative transfer mechanism is depicted in Figure 5.4.

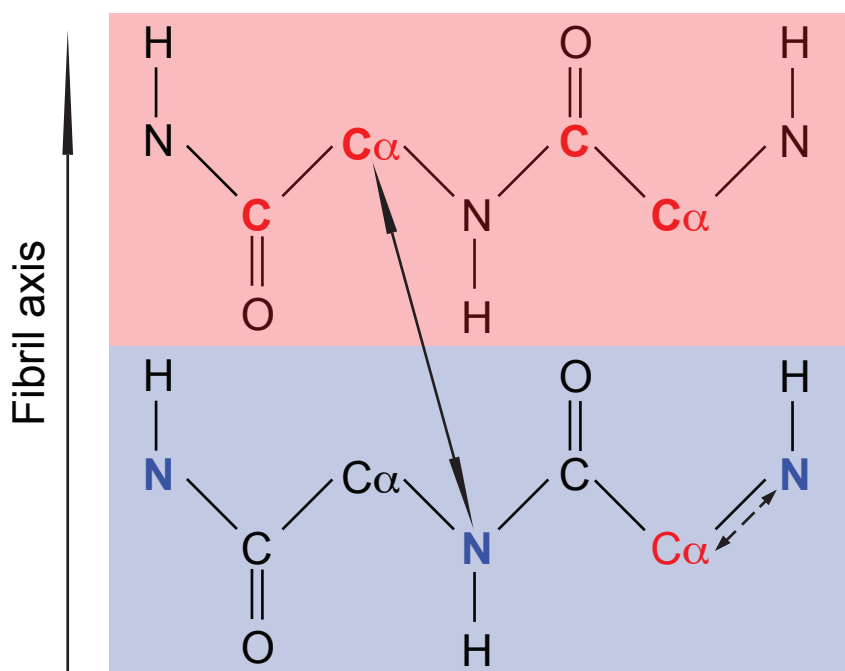


Figure 5.4: Possible transfer mechanisms for TEDOR experiment. A cross peaks appear in the spectrum only if ^{15}N - ^{13}C transfer had taken place. The wanted transfer is between the ^{15}N of the nitrogen labeled molecule to the ^{13}C of the carbon labeled molecule (plain arrow). The unwanted transfer between ^{15}N to the ^{13}C NA of the nitrogen labeled molecule (dotted arrow) could in principle take place.

In principle, cross peak might arise due to an intra - molecular transfer of the ^{15}N molecule, because of the presence of natural abundance ^{13}C . This is a well known issue in the structure calculation procedure with standard solid - state NMR methods. To exclude this possibility we have initially performed a series of 1D TEDOR experiments, varying the mixing time, in order to qualitatively identify the nature of the transfer. The integration of the signal of the $^1\text{H}_N$ in function of the TEDOR mixing time (Figure 5.5) shows that the maximum transfer happens at a mixing time of 14.4 ms. If the transfer would happen mainly due to the short intramolecular ^{15}N - $^{13}\text{C}\alpha$ contacts ($d \sim 1.3\text{\AA}$), then the maximum would appear at $t = 2.4$ ms, as also shown in [116].

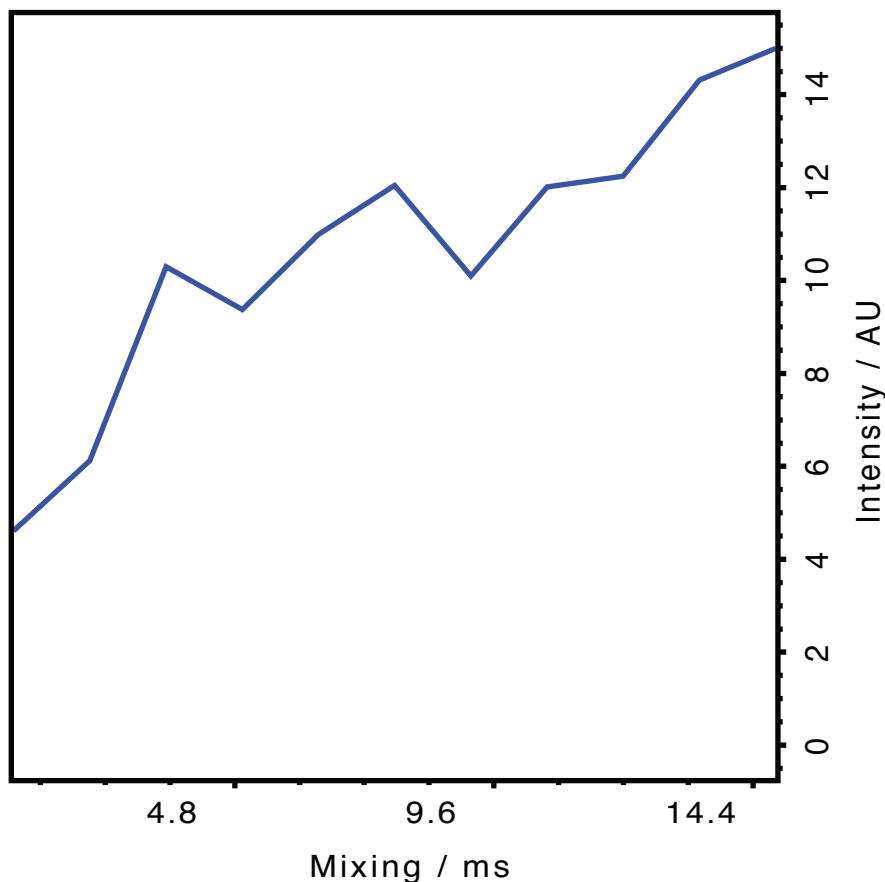


Figure 5.5: Integrated intensity of the ${}^1\text{H}_N$ region for 1D TEDOR in function of the mixing time

We performed a 3D ${}^{15}\text{N}$ - ${}^{13}\text{C}$ - ${}^1\text{H}$ TEDOR experiment to have site-specific long distance intermolecular information between carbon of the ${}^{13}\text{C}$ labeled molecule with nitrogen of the ${}^{15}\text{N}$ labeled molecule. This experiment was measured at a magnetic field of 20.0 T and setting the MAS frequency to 55.555 kHz. The TEDOR mixing time was set to $t_{mix} = 14.4$ ms, according to the maximum of the transfer from the 1D optimization. More experimental details are shown in Paragraph 5.5.2. Some representative ${}^{15}\text{N}$ planes of the 3D experiment are shown in Figure 5.6. A projection on the ${}^{15}\text{N}$ - ${}^{13}\text{C}$ plane is shown in Figure 5.7. In total, we could identify and select automatically 81 cross peaks in the spectrum, which corresponds to a intra - residue correlation ${}^1\text{H}_N$ - ${}^{15}\text{N}$ with the long range contact between the selected ${}^{15}\text{N}$ frequency to the ${}^{13}\text{C}$. Most peaks are well separated and can be manually assigned for the ${}^1\text{H}_N$ and ${}^{15}\text{N}$ dimension, due to the pair belongs to the same amino acid, which can be distinguished in a 2D spectrum (Figure 5.3). We were then able to neglect the presence of correlation coming from NA ${}^{13}\text{C}\alpha$ of the nitrogen labeled molecule: at the expected position, marked with a red cross in Figure 5.3 **A** and in Figure 5.8, no peak is present. The spectrum has, moreover, good S/N ratio, as shown in Figure 5.9 for two representative correlations.

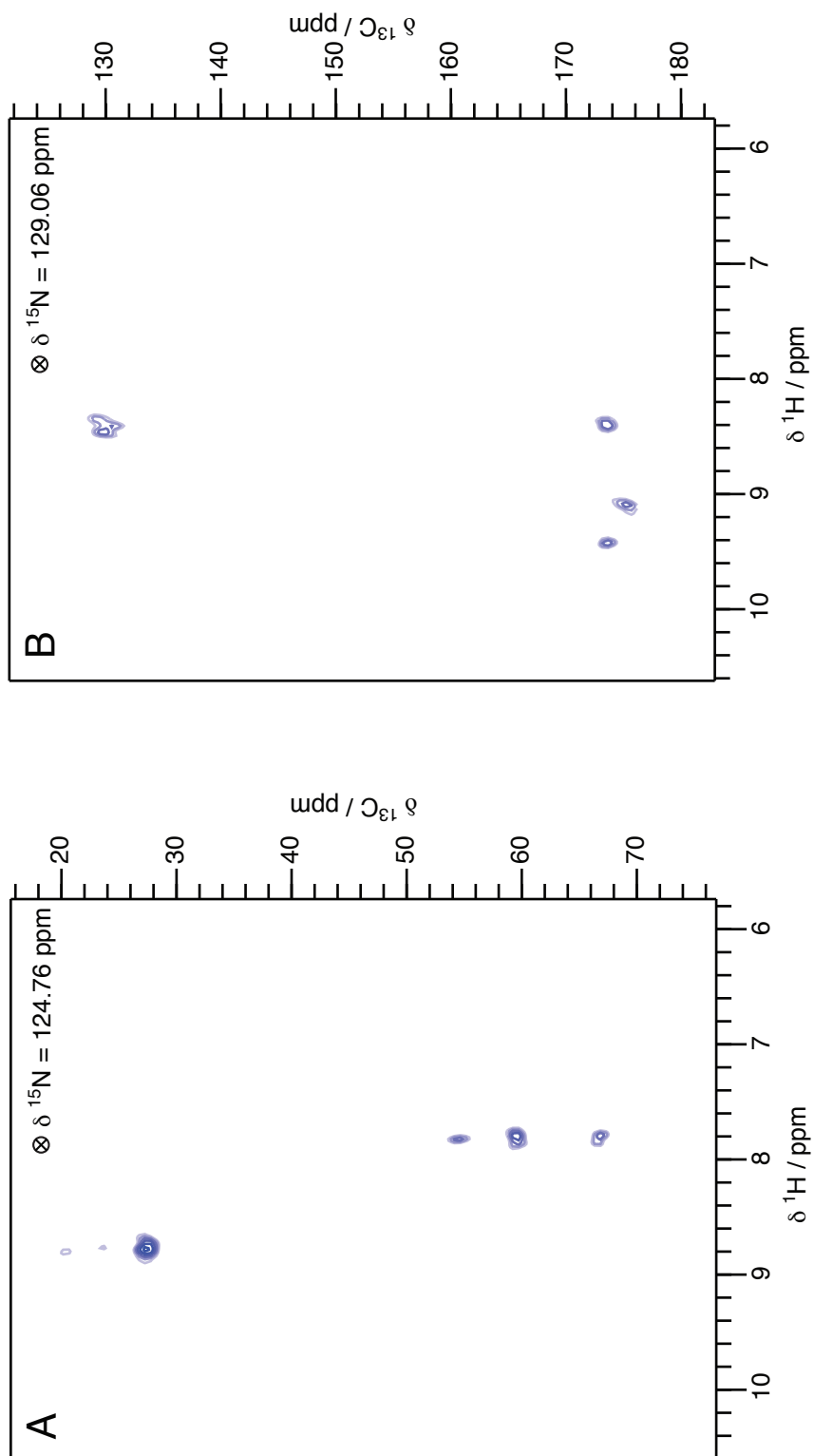


Figure 5.6: Representative 2D planes of TEDOR experiment. We could identify 81 cross peaks, each of them indicates a correlation of the ^{15}N and ^1H of the same residue with the long range ^{13}C . Cross peaks are present in the aliphatic (**A**), in the carbonyl and in the aromatic region (**B**)

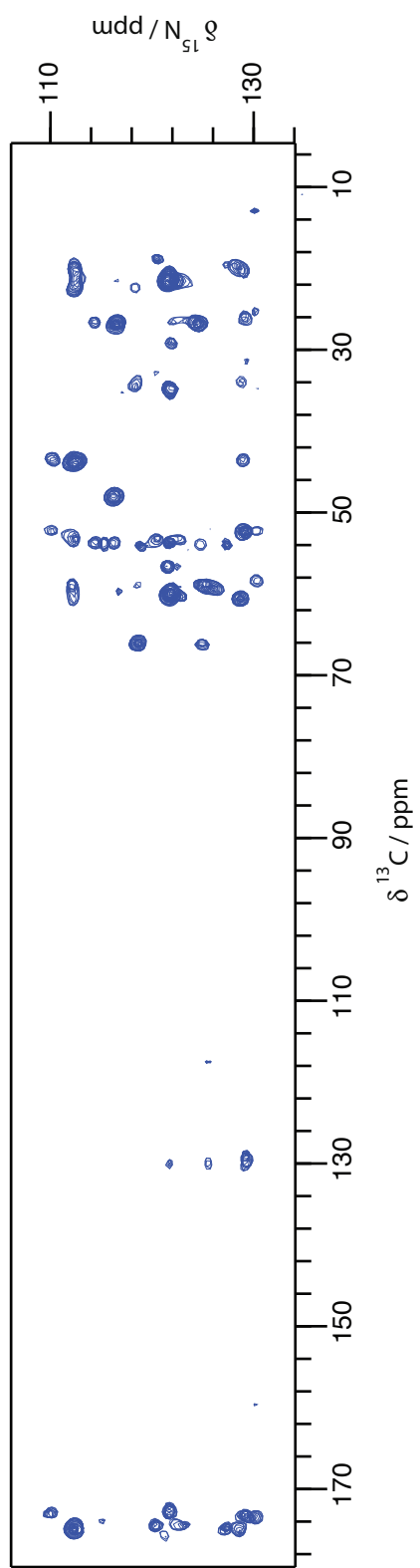


Figure 5.7: Projection of 3D TEDOR on 2D ^{15}N - ^{13}C plane.

5.3.2 Intermolecular restraints

The so obtained correlations contain valuable inter - molecular information but, with a few exceptions, the ^{13}C dimension cannot unambiguously assigned (with 0.2 ppm of tolerance). We therefore performed an automatic structure calculation of the HET-s(218-289) fibril using the software CYANA [58] using the peak list obtained from 3D TEDOR as an input. Additional inputs that we used come from the original calculation of the HET-s(218-289) fibril, namely intra molecular ^{13}C - ^{13}C distance restraints as well as the position of H - bonds, as shown in [60]. This allowed us to obtain a convergent structure similar to the published one (RMSD to heavy atoms compared to the published one 1.1 Å).

We have used the ^{15}N , $^{13}\text{C}\alpha$ and ^1H chemical shifts obtained from HNCA experiment [125] of UL [^2H - ^{13}C - ^{15}N] 100% back exchanged HET-s(218-289) fibrils. Additional ^{13}C chemical shifts were obtained by 2D DREAM [14] and 3D DREAM - TOBSY [126] measured at a magnetic field of 14.0 T and setting the MAS frequency to 13 kHz (Appendix B.3). The newly assigned ^{13}C chemical shifts mainly belong to $\text{C}\beta$ of serines, alanines and threonines.

We tried to apply the so - called deuterium correction to predict the effect of the ^2H on the ^{13}C chemical shifts [127]. This effect takes place from nuclei that are separated by as many as four covalent bonds, according to the formula 5.3.

$$\Delta^{13}\text{C}_{1\text{H}\rightarrow^2\text{H}} = {}^1\Delta^{13}\text{C} d_{1\text{bond}} + {}^2\Delta^{13}\text{C} d_{2\text{bond}} + {}^3\Delta^{13}\text{C} d_{3\text{bond}}, \quad (5.3)$$

where ${}^n\Delta^{13}\text{C}$ represents the n -bond isotope effect per deuteron and $d_{2\text{bond}}$ the number of deuterons n bonds away from ^{13}C nucleus. We therefore tried to apply this corrections on the $\text{C}\beta$ we have assigned ((Appendix B.3) and confront the values, finding out that the agreement is not perfect and way above the desired precision (in average, $|\delta_{\text{assigned}} - \delta_{\text{calculated}}| \geq 0.2$ ppm).

Moreover, the dihedral angles play a role in this correction for backbone atoms (i.e. $\text{C}\alpha$, C' and N) as shown in [128]. We therefore used only the assigned chemical shifts in the calculation, shown in Table 5.2.

Furthermore, we defined the rule in CYANA for the assignment of the peaks as follows: intra residue contact between the ^{15}N and ^1H dimension and long range intermolecular contact between ^{15}N and ^{13}C dimension. The syntax used in CYANA for the defining the contact is written as follows

```
SPECTRUM PAIN3D C N HN
0.1 C:C_* ~ N:N_AMI HN:H_AMI
0.1 HN:H_AMI N:N_AMI ~ C:C_*
```

The upper distance limit (upl) between the ^{15}N and ^{13}C was set to 7 Å. We set the tolerance for the assignment to 0.55 ppm for the nitrogen dimension, 0.30 ppm for the carbon dimension and 0.03 ppm for the proton dimension.

The 81 correlations from TEDOR, shown in Table 5.1, were tentatively assigned and used as constraints during the structure calculation procedure, obtained the results summarized in Table 5.3.

1	53.078	129.015	9.360	9 T	2.731e+06	0.00e+00	a	0	0	0	0	0
2	66.752	118.623	8.210	9 T	2.467e+06	0.00e+00	a	0	0	0	0	0
3	34.960	118.378	8.207	9 T	1.768e+06	0.00e+00	a	0	0	0	0	0
5	23.087	118.338	8.183	9 T	1.497e+06	0.00e+00	a	0	0	0	0	0
6	44.470	112.364	8.616	9 T	3.341e+06	0.00e+00	a	0	0	0	0	0
7	23.131	112.268	8.639	9 T	1.965e+06	0.00e+00	a	0	0	0	0	0
8	21.440	112.438	8.531	9 T	1.647e+06	0.00e+00	a	0	0	0	0	0
9	20.744	112.358	8.662	9 T	2.085e+06	0.00e+00	a	0	0	0	0	0
10	54.491	116.259	9.271	9 T	1.865e+06	0.00e+00	a	0	0	0	0	0
11	48.778	116.257	9.279	9 T	3.437e+06	0.00e+00	a	0	0	0	0	0
13	35.795	116.417	9.268	9 T	1.179e+06	0.00e+00	a	0	0	0	0	0
16	59.120	130.306	9.087	9 T	1.729e+06	0.00e+00	a	0	0	0	0	0
17	52.931	130.335	9.095	9 T	1.516e+06	0.00e+00	a	0	0	0	0	0
18	26.000	130.159	9.115	9 T	1.381e+06	0.00e+00	a	0	0	0	0	0
19	13.623	130.089	9.147	9 T	1.342e+06	0.00e+00	a	0	0	0	0	0
21	53.077	129.254	8.327	9 T	1.856e+06	0.00e+00	a	0	0	0	0	0
22	26.880	129.204	9.336	9 T	1.698e+06	0.00e+00	a	0	0	0	0	0
23	44.303	128.984	9.372	9 T	1.816e+06	0.00e+00	a	0	0	0	0	0
24	61.326	128.668	9.047	9 T	2.422e+06	0.00e+00	a	0	0	0	0	0
25	34.655	128.686	9.025	9 T	1.460e+06	0.00e+00	a	0	0	0	0	0
26	20.681	128.633	9.028	9 T	2.239e+06	0.00e+00	a	0	0	0	0	0
27	54.721	127.461	9.203	9 T	1.444e+06	0.00e+00	a	0	0	0	0	0
29	54.745	127.348	8.726	9 T	1.480e+06	0.00e+00	a	0	0	0	0	0
30	59.969	126.008	7.821	9 T	2.324e+06	0.00e+00	a	0	0	0	0	0
31	66.949	124.927	7.711	9 T	1.729e+06	0.00e+00	a	0	0	0	0	0
32	59.687	124.988	7.725	9 T	2.107e+06	0.00e+00	a	0	0	0	0	0
33	54.633	124.755	7.739	9 T	1.592e+06	0.00e+00	a	0	0	0	0	0
34	27.490	124.517	8.696	9 T	2.672e+06	0.00e+00	a	0	0	0	0	0
35	57.346	122.451	8.125	9 T	1.371e+06	0.00e+00	a	0	0	0	0	0
36	54.081	122.418	8.613	9 T	1.613e+06	0.00e+00	a	0	0	0	0	0
37	22.227	122.409	8.130	9 T	1.800e+06	0.00e+00	a	0	0	0	0	0
38	60.534	121.936	8.592	9 T	1.987e+06	0.00e+00	a	0	0	0	0	0
39	53.989	122.245	8.577	9 T	1.481e+06	0.00e+00	a	0	0	0	0	0
40	27.224	122.124	8.587	9 T	1.444e+06	0.00e+00	a	0	0	0	0	0
41	60.910	121.682	8.751	9 T	3.192e+06	0.00e+00	a	0	0	0	0	0
42	54.699	121.865	8.894	9 T	1.325e+06	0.00e+00	a	0	0	0	0	0
43	54.419	121.781	8.711	9 T	1.607e+06	0.00e+00	a	0	0	0	0	0
44	54.348	121.695	8.646	9 T	1.679e+06	0.00e+00	a	0	0	0	0	0
45	35.547	121.654	8.844	9 T	1.854e+06	0.00e+00	a	0	0	0	0	0
46	35.513	121.697	8.779	9 T	2.051e+06	0.00e+00	a	0	0	0	0	0
47	35.679	121.642	8.695	9 T	1.764e+06	0.00e+00	a	0	0	0	0	0
48	35.416	121.803	8.610	9 T	1.709e+06	0.00e+00	a	0	0	0	0	0
49	35.524	121.836	8.547	9 T	1.686e+06	0.00e+00	a	0	0	0	0	0
50	29.894	121.869	8.659	9 T	1.626e+06	0.00e+00	a	0	0	0	0	0
51	22.359	121.571	8.775	9 T	3.131e+06	0.00e+00	a	0	0	0	0	0
52	22.412	121.890	8.593	9 T	2.327e+06	0.00e+00	a	0	0	0	0	0
53	57.375	121.526	8.565	9 T	1.826e+06	0.00e+00	a	0	0	0	0	0
54	53.900	120.567	8.039	9 T	1.372e+06	0.00e+00	a	0	0	0	0	0
55	19.603	120.547	8.034	9 T	1.582e+06	0.00e+00	a	0	0	0	0	0
56	54.152	120.450	8.112	9 T	1.914e+06	0.00e+00	a	0	0	0	0	0
57	54.776	118.793	8.191	9 T	1.516e+06	0.00e+00	a	0	0	0	0	0
58	59.686	118.507	8.238	9 T	1.343e+06	0.00e+00	a	0	0	0	0	0
59	60.378	116.747	8.437	9 T	1.403e+06	0.00e+00	a	0	0	0	0	0
60	27.637	116.395	8.659	9 T	2.542e+06	0.00e+00	a	0	0	0	0	0
61	54.616	115.288	7.563	9 T	1.544e+06	0.00e+00	a	0	0	0	0	0
62	54.455	115.229	7.499	9 T	1.559e+06	0.00e+00	a	0	0	0	0	0
63	54.394	114.415	9.745	9 T	1.775e+06	0.00e+00	a	0	0	0	0	0
64	27.395	114.330	9.751	9 T	1.675e+06	0.00e+00	a	0	0	0	0	0
66	60.120	112.276	8.627	9 T	1.790e+06	0.00e+00	a	0	0	0	0	0
67	59.564	112.147	8.589	9 T	1.561e+06	0.00e+00	a	0	0	0	0	0
68	54.008	112.196	8.618	9 T	1.747e+06	0.00e+00	a	0	0	0	0	0
69	59.539	112.099	8.665	9 T	1.539e+06	0.00e+00	a	0	0	0	0	0
70	52.875	110.125	8.400	9 T	1.571e+06	0.00e+00	a	0	0	0	0	0
71	44.147	110.204	8.391	9 T	1.996e+06	0.00e+00	a	0	0	0	0	0
72	174.209	130.165	9.100	9 T	1.880e+06	0.00e+00	a	0	0	0	0	0
73	174.037	129.313	8.330	9 T	1.899e+06	0.00e+00	a	0	0	0	0	0
77	173.971	128.918	9.358	9 T	1.681e+06	0.00e+00	a	0	0	0	0	0
78	175.698	128.517	9.026	9 T	1.930e+06	0.00e+00	a	0	0	0	0	0
79	175.403	127.252	8.800	9 T	1.499e+06	0.00e+00	a	0	0	0	0	0
80	175.635	127.199	8.709	9 T	1.737e+06	0.00e+00	a	0	0	0	0	0
81	130.700	125.537	9.102	9 T	1.421e+06	0.00e+00	a	0	0	0	0	0
82	175.121	123.105	8.618	9 T	1.474e+06	0.00e+00	a	0	0	0	0	0
83	175.105	122.519	8.576	9 T	1.674e+06	0.00e+00	a	0	0	0	0	0
84	173.405	121.617	8.760	9 T	1.818e+06	0.00e+00	a	0	0	0	0	0
85	173.319	121.802	8.679	9 T	1.686e+06	0.00e+00	a	0	0	0	0	0
87	176.508	121.245	8.738	9 T	1.449e+06	0.00e+00	a	0	0	0	0	0
88	175.234	120.402	8.157	9 T	1.703e+06	0.00e+00	a	0	0	0	0	0
89	175.182	120.247	8.078	9 T	1.685e+06	0.00e+00	a	0	0	0	0	0
90	174.649	115.097	7.495	9 T	1.300e+06	0.00e+00	a	0	0	0	0	0
91	175.689	112.350	8.772	9 T	1.421e+06	0.00e+00	a	0	0	0	0	0
92	175.553	112.243	8.616	9 T	2.674e+06	0.00e+00	a	0	0	0	0	0
93	173.603	110.086	8.423	9 T	1.692e+06	0.00e+00	a	0	0	0	0	0

Table 5.1: 3D TEDOR peak list used for the structure calculation.

Residue	H _N	N	C _α	C _β	C _γ
224 Gly	8.64	111.31	42.62	-	-
225 Arg	-	-	-	-	-
226 Asn	9.04	124.60	51.75	-	-
227 Ser	9.43	118.18	56.32	66.41	-
228 Ala	8.57	121.89	49.11	22.87	-
229 Lys	8.21	122.45	59.35	31.50	-
230 Asp	8.52	116.82	52.71	-	-
231 Ile	8.70	121.71	60.45	40.70	26.51 / 16.76
232 Arg	9.03	128.64	53.67	32.91	32.16
233 Thr	8.62	112.35	59.30	71.23	22.84
234 Glu	8.20	118.72	53.45	-	-
235 Glu	9.28	116.25	58.37	-	-
236 Arg	8.75	122.01	54.17	-	-
237 Ala	7.79	124.78	52.73	18.98	-
238 Arg	8.30	117.42	54.01	-	-
239 Val	8.58	121.81	59.72	-	-
240 Gln	9.12	125.63	52.37	-	-
241 Leu	9.10	130.33	52.39	-	-
242 Gly	8.71	112.60	43.41	-	-
243 Asn	8.39	109.22	50.88	-	-
244 Val	9.13	122.01	61.56	-	-
245 Val	9.02	128.63	60.75	-	-
246 Thr	8.32	115.61	62.02	70.44	20.08
247 Ala	8.73	119.93	55.53	16.30	-
248 Ala	8.34	118.91	54.49	17.57	-
249 Ala	7.72	119.43	53.58	18.23	-
261 Thr	8.37	123.30	61.00	70.11	20.44
262 Asn	8.95	126.78	52.12	-	-
263 Ser	8.73	116.62	55.95	65.42	-
264 Val	8.71	124.41	56.69	34.63	19.69 / 22.19
265 Glu	7.87	126.40	58.98	-	-
266 Thr	8.62	112.27	60.57	71.17	21.36
267 Val	8.66	123.71	60.01	34.96	21.37
268 Val	8.78	127.41	60.62	33.17	20.05
269 Gly	8.64	112.30	43.81	-	-
270 Lys	8.12	120.51	53.96	34.41	-
271 Gly	9.75	114.40	48.01	-	-
272 Glu	9.12	127.35	53.73	-	-
273 Ser	7.57	115.30	58.85	66.17	-
274 Arg	8.66	117.29	54.59	-	-
275 Val	8.86	121.95	60.02	-	-
276 Leu	8.40	129.30	52.29	43.53	26.77
277 Ile	9.37	129.34	58.19	34.71	25.26 / 17.76
278 Gly	8.40	110.20	43.61	-	-
279 Asn	8.53	113.84	51.36	-	-
280 Glu	8.80	119.74	54.10	-	-
281 Tyr	9.87	128.15	55.74	39.89	-
282 Gly	9.75	108.91	45.56	-	-
283 Gly	8.37	111.85	43.36	-	-
284 Lys	-	-	-	-	-
285 Gly	9.12	107.79	43.90	-	-

Table 5.2: Chemical shifts of deuterated HET-s (218-289) fibrils in ppm used for the calculation

Unassigned	41
No assignment possibilities for ^{13}C	40
Violations	1
Assigned	40
Unambiguous assignment	27
2 possibilities in the ^{13}C dimension	10
Ambiguous assignment (≥ 3 possibilities)	3

Table 5.3: Summary of the structure calculation results for the TEDOR peak list assignment. The 40 unassigned peaks are because of lacking of information about ^{13}C assignment. The violation corresponds to a ^{15}N - ^{13}C distance of 8.2 Å.

41 cross peaks were not assigned during this process, mostly due to of the lack of the ^{13}C side chains information (18 peaks in the carbonyl region and 7 in the aromatic). We had 1 correlation that violated the 7 Å distance limit: in the final structure, the distance between the ^{15}N - ^{13}C pair was 8.2 Å.

40 cross peaks were assigned in the structure calculation process, 27 of them in an unambiguous way (i.e. only one assignment possibility with the set tolerance). The other 13 correlations could be ambiguously assigned, mainly because of the ^{13}C dimension.

We plotted the assigned correlations on the TEDOR spectrum, as shown representatively in Figure 5.8 and on the resulting structure with the relative distances, as shown in Figure 5.10. It is interesting to note that the TEDOR transfer works for residue in β strands (Figure 5.10 **A**) and in loops (Figure 5.10 **B**). As a comparison, we plotted the so obtained restraints in the PAIN spectrum measured for [60] on a ML sample of HET-s(218-289) fibrils (Figure 5.11).

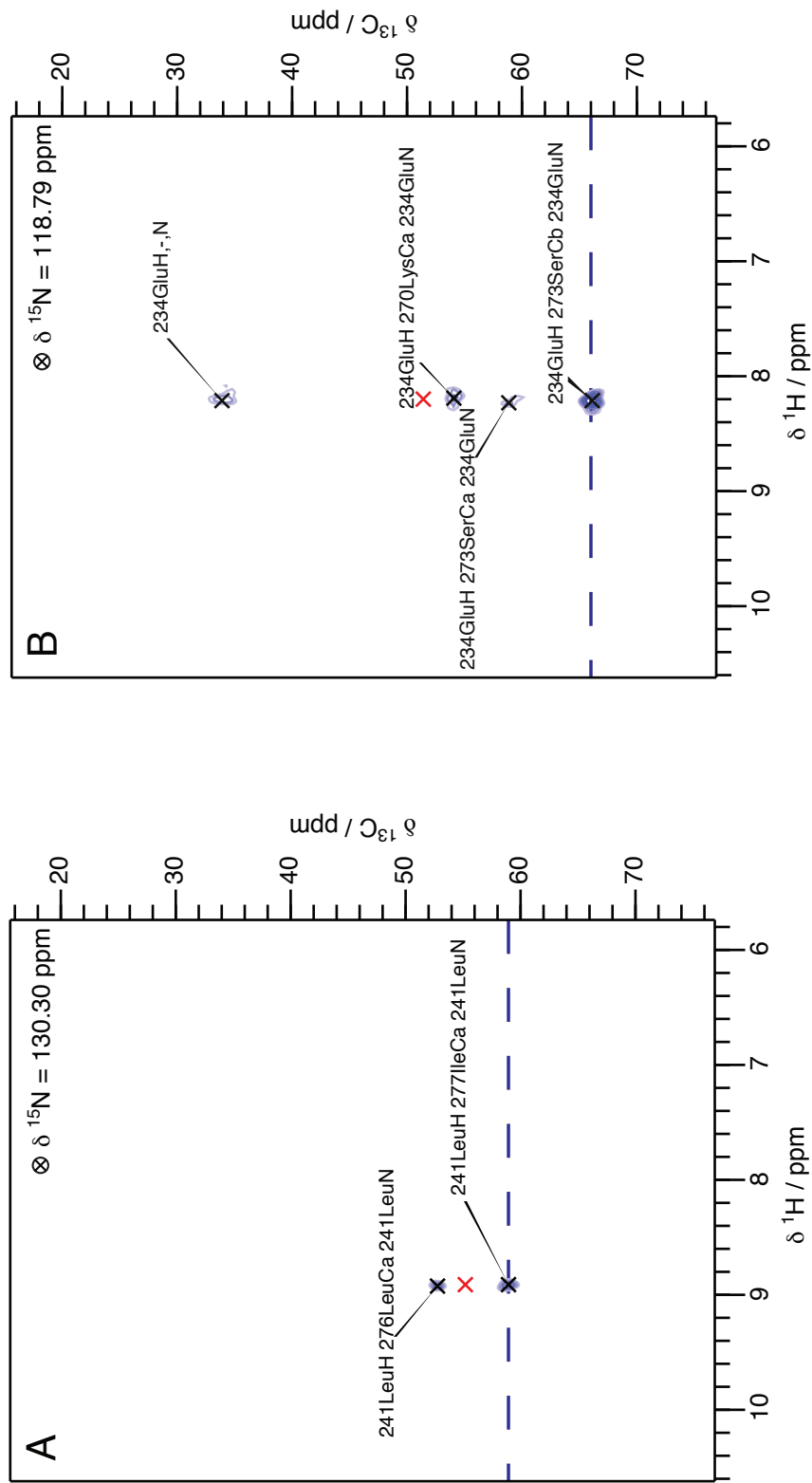


Figure 5.8: Representative 2D planes of TEDOR experiment. Cross peaks are assigned automatically during the structure calculation and are shown in the spectrum. These correlation are assigned unambiguously in the $^{15}\text{N} - ^{13}\text{C} - ^1\text{H}$ dimension, with set tolerance to 0.55 ppm - 0.30 ppm - 0.03 ppm, respectively. The position of the eventual intra residue $^{15}\text{N} - ^{13}\text{C}\alpha$ correlation is marked with a red cross.



Figure 5.9: Representative 1D traces of TEDOR experiment obtained at the position of the dashed lines in Figure 5.8. The S/N ratio is 6.73 for (A) and 3.95 for (B)

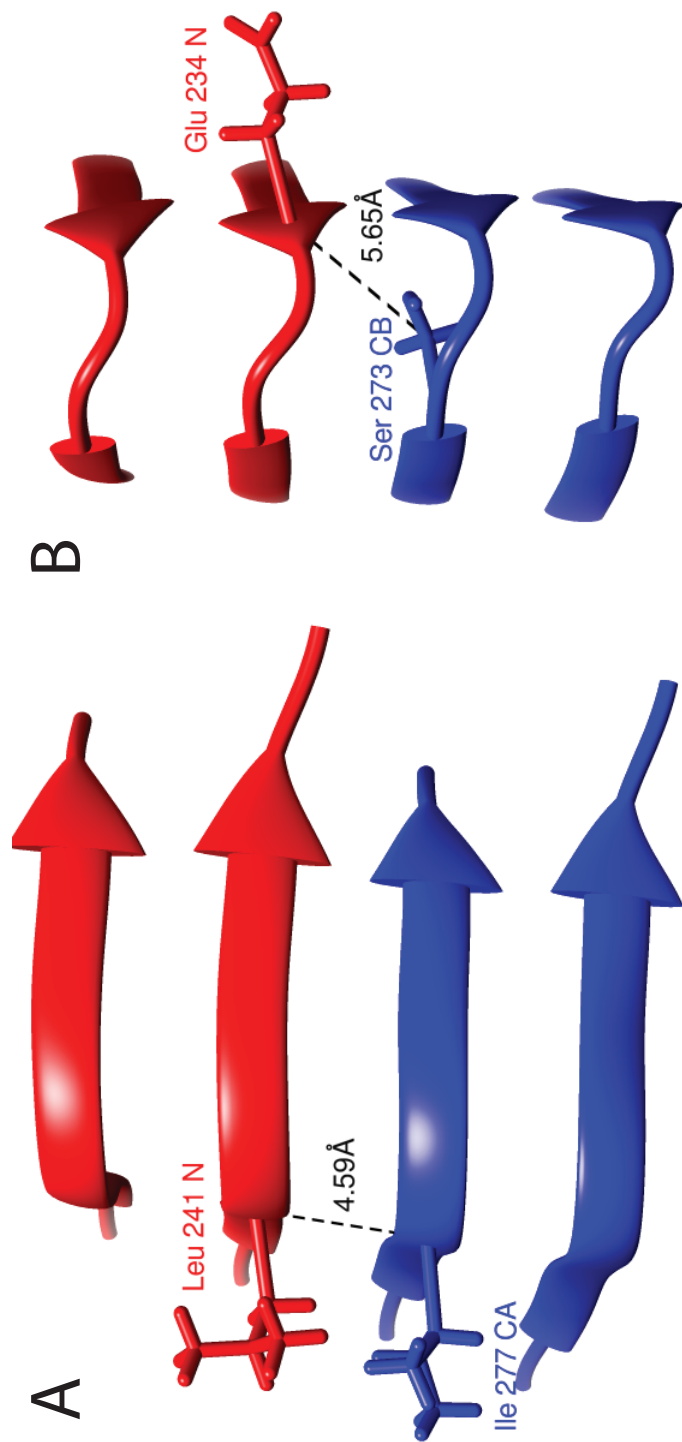


Figure 5.10: Two representative $^{15}\text{N} - ^{13}\text{C}$ intermolecular correlations obtained from 3D TEDOR and identified in the structure calculation process between residues in β strands (**A**) and in loops (**B**). Distance between selected atoms is shown in \AA

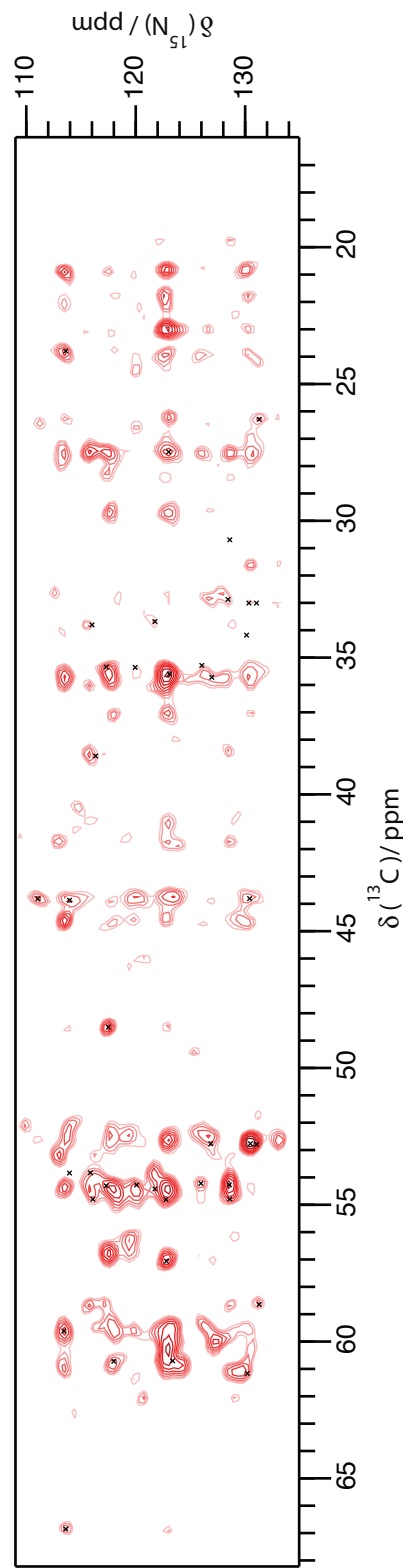


Figure 5.1.1: Restraints obtained from the 3D TEDOR spectrum are marked with a black cross on a 2D PAIN spectrum measured on ML [^{15}N - ^{13}C] of HET-s(218-289) fibrils

5.4 Conclusions

In this chapter we have presented a new approach to obtain highly resolved ^{15}N - ^{13}C intermolecular correlations using a variation of the TEDOR sequence. This sequence directly reintroduces the ^{15}N - ^{13}C dipolar coupling, differently from other sequences based on the ^1H network (i.e. PAIN, NHHC). Therefore, it can provide complementary information on the stacking of the protein.

This method works nicely in the fast MAS regime ($\nu_r \geq 50$ kHz) in combination with a deuterated 100% back-exchanged sample. In this regime, the use of low power decoupling schemes reduces drastically the sample heating because of rf irradiation and the proton detection boosts the sensitivity of the experiment.

The 3D TEDOR ^{15}N - ^{13}C - ^1H experiment we performed shows good S/N and, due to the high dimensionality of the spectrum, allowed us to obtain valuable structural information with low ambiguity. We have used the so-obtained correlation in an automatic structure calculation of HET-s(218-289) and subsequently assigned them. The strong restriction that the ^{15}N and ^1H have to belong to the same residue allowed to dramatically reduce the ambiguities of the inter-molecular ^{15}N - ^{13}C constraints.

We have moreover demonstrated that correlation from NA ^{13}C , that could provide wrong information on the stacking, are too weak to be visible in the spectrum in this specific compound.

A further improvement of the experiment can be obtained by scalar ^2H decoupling during the TEDOR mixing and the ^{13}C evolution, as shown in [129]. In conclusion, the approach we proposed provides low ambiguity intermolecular constraints and can therefore be used in the context of protein structure determination in the fast MAS regime.

5.5 Experimental methods

5.5.1 Sample preparation

The competent cells were placed in BL 21 star (DE3) (50 μL) and the plasmid was put in solution for ten minutes in the fridge. 0.5 μL of the plasmid was added to the competent cells and kept in the fridge for 30 minutes. The preparation was incubated overnight at 37°C. After that, the cells were harvested and centrifuged at 5000 rpm for 30 minutes. After that, the cells were re-suspended in a 150 mM NaCl / 50mM Tris-HCl, pH 8 buffer.

The cells were lysed in 150 mM NaCl and 50 mM Tris-HCl, pH 8 and disrupted using a microfluidizer (Microfluidics). The lysate was centrifuged for 120 min at 8,250 g. The pellet was re-suspended in buffer (150 mM NaCl and 50 mM Tris-HCl, pH 8) and guanidinium HCl powder was added until the solution had doubled the volume.

The sample was incubated overnight at 60°C and rotated 1 hour at room temperature. The supernatant was cleared by centrifugation for 5 hours at 186,000 g and filtered over

0.2 μm pore-size filters.

Equilibrated Ni-Sepharose was added to the sample and the protein was binding over 72 hours to the resin. The sample was transferred to a column and the resin was washed with eight times column volumes buffer (6M guanidinium HCl, 20 mM Imidazole, 0.5 M NaCl, 50 mM Tris-HCl, pH 8). The protein was eluted with elution buffer (6M guanidinium HCl, 500 mM Imidazole, 0.5 M NaCl, 50 mM Tris-HCl, pH 8). 1 ml fractions were taken and the fractions with protein were pooled in one falcon.

The buffer was exchanged with 150 mM acetic acid pH 2.5 using a HiPrep 26/10 desalting column (GE Healthcare). The pH was then immediately adjusted to 7.4 by addition of 3 M Tris at room temperature, which triggers fibrilization. After fibrillation the sample was stored at 4°C. The protein was centrifuged at 30,000 g over night, the supernatant was discarded and the fibrils were packed into a 1.3 mm Bruker rotor by ultracentrifugation using a filling device. The drive tip was sealed with epoxy glue (Araldit blue) in order to prevent dehydration of the sample.

5.5.2 Solid - state NMR spectroscopy

All experiments were performed at a magnetic field of 20.0 T using a commercial BRUKER 1.3 mm probe. The MAS frequency was set to 55.555 kHz (corresponding to $\tau_r = 18\mu\text{s}$) and the temperature of the sample was calibrated on the water line peak to 15°C.

All π and $\frac{\pi}{2}$ pulses on ^{15}N and ^{13}C are 100 kHz pulses ($\tau_\pi = 5.0\mu\text{s}$ and $\tau_{\pi/2} = 2.5\mu\text{s}$). The rf fields for the first and last CP were optimized to $\omega_H = 120$ kHz and $\omega_N = 68$ kHz. Low power SW_fTPPM [102] is applied during the TEDOR mixing and the t_1 and t_2 evolution with $\omega_{\text{TPPM}} = 12$ kHz and $\tau_{\text{TPPM}} = 42\mu\text{s}$. WALTZ-16 is applied during the proton detection on the ^{15}N channel with $\omega_{\text{WALTZ}} = 6$ kHz and $\tau_{\text{TPPM}} = 49\mu\text{s}$.

For the 2D ^{15}N - ^1H experiment, the TEDOR mixing time was set to 14.4 ms. The spectral width was set to 20 kHz for ^{15}N and 100 kHz for ^1H , with total acquisition time of 12.5 ms for ^{15}N ms and 51.2 ms for ^1H . The recycle delay was set to $d_1 = 1.5$ s and $NS = 64$, corresponding to a total measurement time of 13.3 hours.

For the 3D ^{15}N - ^{13}C - ^1H experiment, the TEDOR mixing time was set to 14.4 ms. The spectral width was set to 8 kHz for ^{15}N , 55.555 kHz for ^{13}C and 100 kHz for ^1H , with total acquisition time of 7.18 ms for ^{15}N ms, 2.6 ms for ^{13}C and 20.48 ms for ^1H . The recycle delay was set to $d_1 = 1.0$ s and $NS = 16$, corresponding to a total measurement time of 148.8 hours.

Part III

Conclusions and Outlook

In the first part of this thesis we presented applications of solid - state NMR techniques on the structure determination of proteins.

In Chapter 2, we measured solid - state NMR experiments on the amyloid β 1-42. The first step was to obtain the sequential assignment of the protein, achieved by a combination of 2D and 3D spectroscopy. Residues between 11 to 14 were invisible in both solid - and solution - state NMR experiments, implying that this stretch presents an intermediate range of dynamics.

Using the so obtained backbone chemical shifts, we identified the presence of five β -sheets, namely between residues 2 - 6 (β 1), 15 - 18 (β 2), 26 - 28 (β 3), 30 - 32 (β 4), 39 - 42 (β 5). The identified beta - strands could be verified by measurements of ^{15}N - ^{13}C long range spectra on a ML 50% ^{15}N - 50% ^{13}C sample, namely PAIN and NHHC.

We performed long range experiments on a UL and on a 1:3 diluted sample to obtain distance restraints, namely CHHC, DARR and PAR. From the analysis of these spectra we obtained 38 restraints with low spectral ambiguity (i.e. less than 2 assignment possibilities per dimension with 0.2 ppm of tolerance).

We used the so obtained information, together with additional peak lists from the restraints spectra and dihedral angle restraints obtained from the assigned CS to perform a structure calculation of the A β 1-42 fibrils. We furthermore used the information obtained from M/L about the lateral stacking of 2 A β monomers per unit. This procedure yielded 551 additional constraints and resulted in a well converged structure with an average target function of 1.90 \AA^2 for the final bundle comprising the 10 best conformers and a backbone RMSD of 0.89 \AA for residues 15 - 42 of the two molecules in the central layer.

In the second chapter, we have proposed a new hybrid approach for protein structure determination, combining a iterative combination of solid - state NMR and cryo - EM data.

This method was applied successfully for the structure determination of the mouse ASC - PYD filaments, which would probably haven't been possible with the single techniques alone.

The solid state NMR part was performed by the sequential assignment of the ASC - PYD filaments. The complete assignment of the backbone atoms between residue 4 to 84 was achieved, together with most of the side chains. Residues 1 - 3 and 85 - 91 were not visible neither in solid - state or solution - state NMR experiments, implying that these residues presented a intermediate range of motion that renders them invisible in the experiments, similarly to what has been shown in Chapter 1.

From the combination of secondary CS and TALOS+ analysis, we could identify 6 α helices at position 3 - 14 (α ₁), 17 - 29 (α ₂), 41 - 46 (α ₃), 49 - 59 (α ₄), 62 - 76 (α ₅), 80 - 84 (α ₆). This information was used, together with dihedral angle restraints, in the first step of the calculation with the cryo - EM density map. The so obtained model was converging and presented a well defined backbone structure.

To increase the precision of the final structure, we performed 2D distance restraints spectra, namely PAR and CHHC, to obtain distance restraints and constraints. The spectra were measured on both a UL and a 1:3 diluted sample, so that the dilution analysis was possible. From the analysis of these spectra, 13 spectral unambiguous (i.e. only 1 assignment possibility for each dimensions with 0.2 ppm of tolerance) restraints were identified and used in the second step of the calculation, together with structural information from cryo - EM.

In the final step of the calculation, the peak lists obtained from the distance restraints spectra were used as input and iteratively assigned by the program, giving additional constraints. These constraints were used to better defined the position of the side chains atoms, obtaining a backbone rmsd of 0.17 Å and an overall heavy atom rmsd of 0.63 Å of the 10 best structures.

Furthermore, using INEPT - based experiments, we proposed that the CARD domain is flexible and attached to the well - folded filament core, composed by the PYD domain. Moreover, the CARD presence does not influence the structure of the PYD filament.

In the second part of the thesis we have proposed two techniques that can be applied in solid - state NMR in the fast MAS regime.

In Chapter 3, we have proposed an approach to obtain high resolved ^{13}C spectra. It is based on the application of the Spin State Selective Excitation sequences, which were developed for solution state NMR with the aim to obtain J - resolved ^{13}C spectra by suppressing the homonuclear J - coupling during acquisition.

We first have tested these sequences, namely S³E for the carbonyl region and DS³E for the C α region, on a simple amino acid, alanine. These experiments were performed to test the sequences and to obtain information about their robustness towards the parameters, such as the evolution times and the selective π pulses.

We applied these sequences on a model protein, ubiquitin, to obtain high resolved 2D correlation spectra for the backbone atoms N, C α and C'.

In Chapter 4 we proposed a new approach to obtain highly resolved long distance inter molecular restraints using a variation of the TEDOR sequence. This sequence directly reintroduce the ^{15}N - ^{13}C dipolar coupling, differently from other sequences. Therefore, it can provide complementary information on the stacking of the protein.

This method has proven itself extremely efficient in the fast MAS regime ($\nu_r \geq 50$ kHz) in combination with a deuterated 100% back exchanged HET-s(218-289) sample.

The 3D TEDOR ^{15}N - ^{13}C - ^1H experiment we performed shows good S/N and, due to the high dimensionality of the spectrum, allowed us to obtain valuable structural information with low ambiguity. We have used the so-obtained correlation in an automatic structure calculation of HET-s(218-289) and subsequently assigned them. The strong restriction that the ^{15}N and ^1H have to belong to the same residue allowed to dramatically reduce the ambiguities of the inter molecular ^{15}N - ^{13}C constraints.

In conclusion, the approach we proposed provides low ambiguity intermolecular con-

straints and can therefore be applied for protein structure determination in the fast MAS regime.

Appendix

A Structure determination of the Amyloid β (1-42) fibril

A.1 Screening of conditions

Nr.	Seeding	A β (1-42) concentration [μ M]	Shaking	Additives / salt	Polymorphisms
0	No	150	Gently	No	Many
1	Yes	30	350 rpm	100 mM NaCl, 30 μ M heparin	-
2	Yes	30	350 rpm	100 mM NaCl, 100 μ M ZnCl	1
3	Yes	30	350 rpm	100 mM NaCl	\sim 2
4	Yes	100	350 rpm	100 mM NaCl, 100 μ M ZnCl	1

Table 5.4: Condition screening of A β (1-42) fibrils. All conditions are in a 100 mM phosphate buffer at pH 7.4 and fibrilization was performed at 37° C

A.2 Dot blot measurement

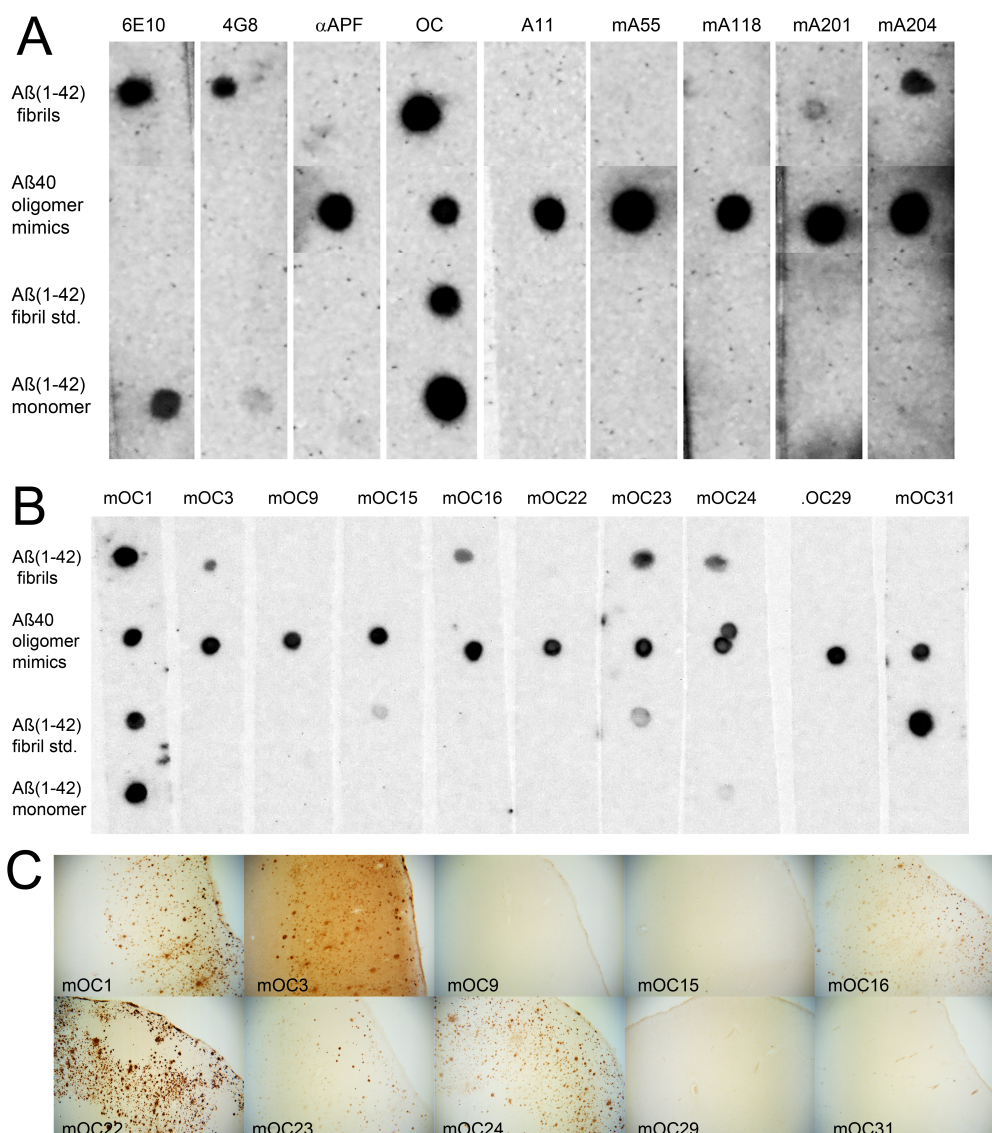


Figure 5.12: (A) Dot blot results of the A β (1-42) fibrils used for the solid - state NMR experiments show that the fibrils are OC+ and A11-. In addition to the solid - state NMR-analyzed A β (1-42) fibrils, A β (1-40) oligomer mimics, A β (1-42) fibril standard (from the Glabe lab), and A β (1-40) monomers were spotted as positive controls for antibodies on each membrane. The A β samples on each membrane were then probed with one of the anti-A β antibodies (6E10 and 4G8), anti-amyloid antisera (α APF, A11, and OC), or anti-oligomer monoclonal antibodies (mAs) (mA55, mA118, mA201, and mA204). The 6E10 and 4G8 are commercially available anti-A β antibodies. Amyloid conformation specific antisera, α APF, A11, and OC, are specific for A β -annular protofibrils (APF), oligomer mimic, and fibrils, respectively. The results show that the A β (1-42) fibrils used for the solid - state NMR analysis (top row) were strongly detected by 6E10, 4G8, and OC but not by α APF, A11, nor by majority of the A11-like mAs. The same results show that the A β (1-42) fibrils were positive for mA201 (weakly) and mA204. (B) A β (1-42) fibrils used for the solid - state NMR analysis show reactivity to OC-like, fibril-specific monoclonal antibodies (mOCs).

Figure 5.12: In addition to the fibril sample, the three different conformations of $A\beta$ samples (same as (A)) were spotted on each membrane as positive controls for antibodies. The four samples were probed with all available 23 OC-like mOCs. Here we show ten representative dot blot results, the samples screened with mOC1, mOC3, mOC9, mOC15, mOC16, mOC22, mOC23, mOC24, mOC29 and mOC31. The $A\beta$ (1-42) fibrils used for the solid - state NMR analysis were detected by mOC 1, mOC3, mOC16, mOC23, and mOC24, but not by mOC9, mOC15, mOC22, mOC29, and mOC31. (C) The same mOCs that showed reactivity to the $A\beta$ (1-42) fibrils from Panel (B) also stain plaques in human AD brain tissues as demonstrated by immunostaining. AD brain tissues probed by mOC1, mOC3, mOC16, mOC23, and mOC24 showed plaque staining. AD brain tissues probed by mOC9, mOC15, mOC22, mOC29, and mOC31 were mostly unstained.

A.3 Chemical shifts comparison

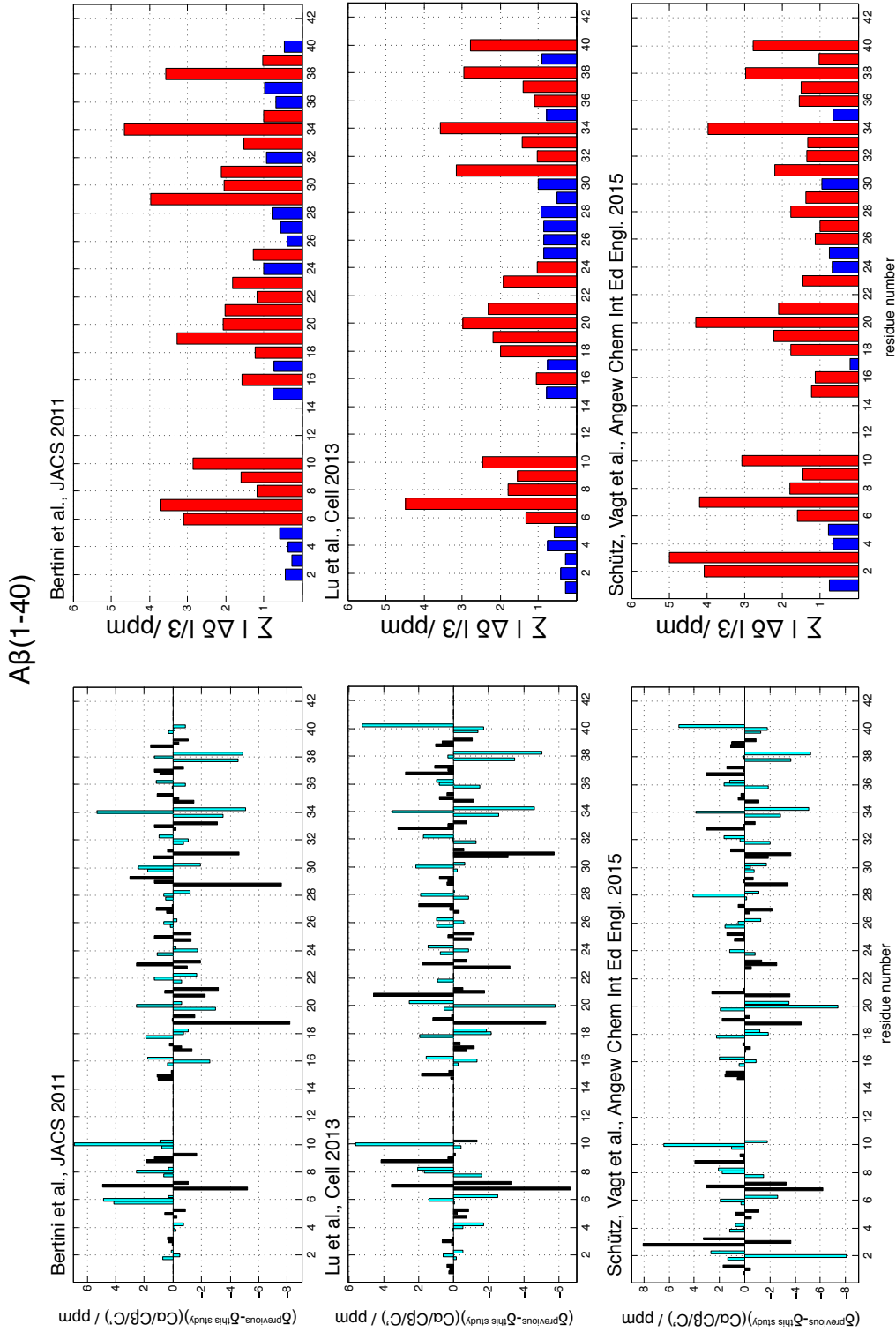


Figure 5.13: Left: differences between chemical shifts of the A β (1-42) fibrils of this study with previously published A β (1-40) fibrils [130], [32] and A β (1-40) E22 Δ fibrils [33]. The first bar of each residue shows the chemical shift difference of ^{13}C , the second ^{13}C , and the third $^{13}\text{C}'$, respectively. For readability of the graphs the bars of the even residues are color coded in cyan and the odd ones in black, respectively. Right: residue-resolved average absolute values of the ^{13}C , ^{13}C , and $^{13}\text{C}'$ chemical shift differences between chemical shifts of the A β (1-42) fibrils of this study with previously published A β fibrils with $\Sigma|\Delta\delta|/3 = (|\delta C_{\alpha_{previous}} - \delta C_{\alpha_{this\ study}}| + |\delta C_{\beta_{previous}} - \delta C_{\beta_{this\ study}}| + |\delta C_{\gamma_{previous}} - \delta C_{\gamma_{this\ study}}|)/3$. Bars with differences larger than 1 ppm are depicted in red, the ones equal or smaller in blue.

A β (1-42)

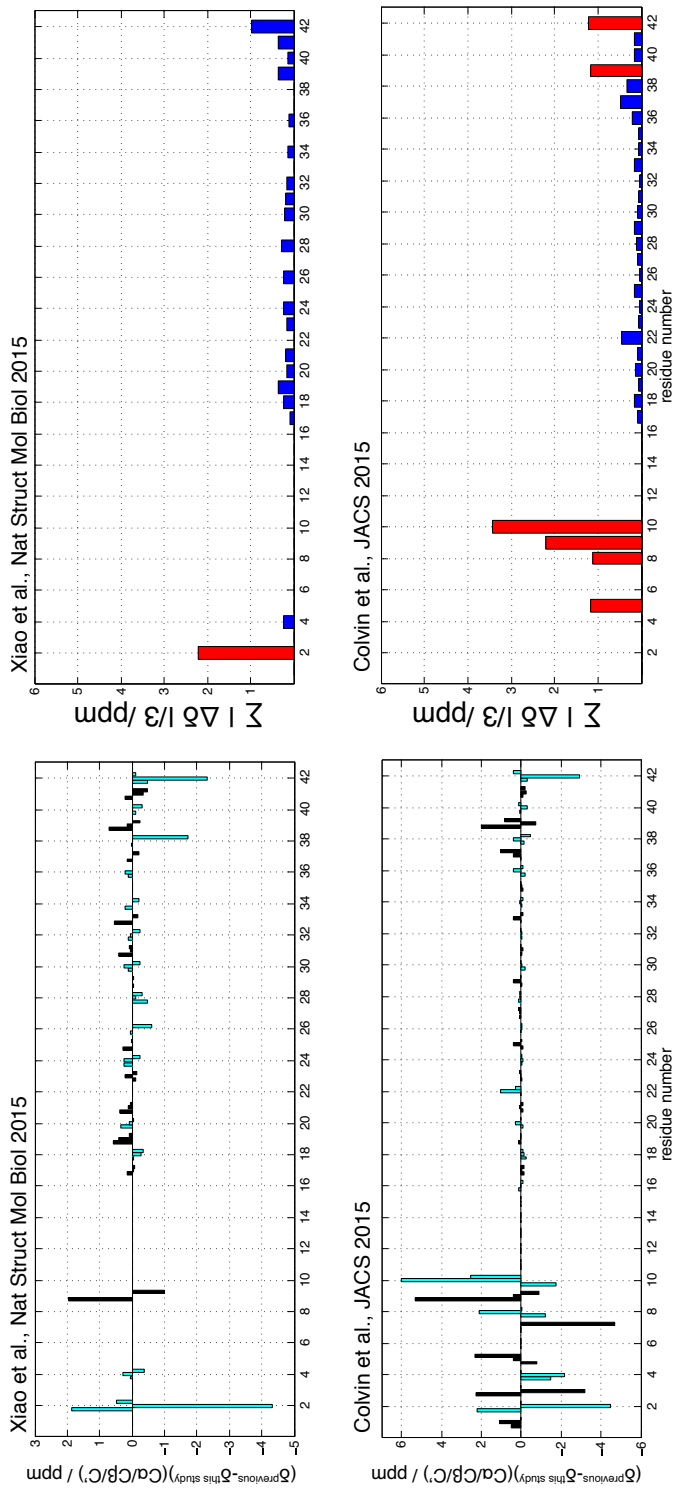


Figure 5.14: Left: differences between chemical shifts of the A β (1-42) fibrils of this study with previously published A β (1-42) fibrils [41], [61]. The first bar of each residue shows the chemical shift difference of ^{13}C , the second $^{13}\text{C}'$, and the third ^{13}C , respectively. Right: residue-resolved average absolute values graphs the bars of the even residues are color coded in cyan and the odd ones in black, respectively. Right: residue-resolved average absolute values of the ^{13}C , $^{13}\text{C}'$, and ^{13}C chemical shift differences between chemical shifts of the A β (1-42) fibrils of this study with previously published A β fibrils with $\Sigma|\Delta\delta|/3 = (|\delta C_{\alpha}^{\text{previous}} - \delta C_{\alpha}^{\text{this study}}| + |\delta C_{\beta}^{\text{previous}} - \delta C_{\beta}^{\text{this study}}| + |\delta C_{\gamma}^{\text{previous}} - \delta C_{\gamma}^{\text{this study}}|)/3$. Bars with differences larger than 1 ppm are depicted in red, the ones equal or smaller in blue.

A.4 H/D exchange

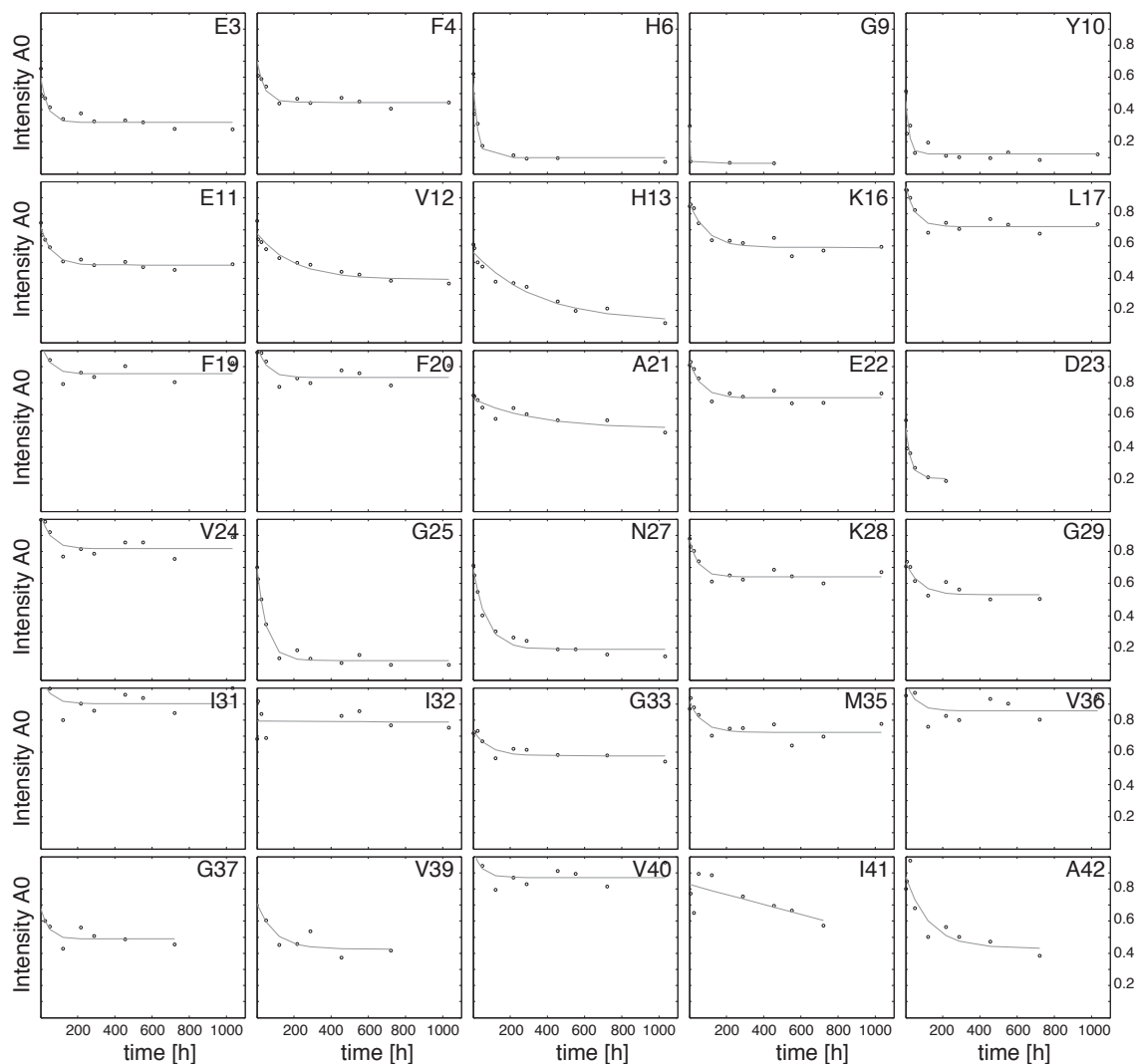


Figure 5.15: Residue-resolved Quenched H/D exchange data for the identification of solvent protected ^{15}N - ^1H moieties of $\text{A}\beta$ (1-42) fibrils. The relative peak intensities in DMSO back predicted to time zero for each exchange time in D_2O are shown. Smooth solid lines represent the mono-exponential fits of the raw data. Some residues (for example His 6, Gly 9, Tyr 10, Gly 25) show a clear decay to zero, whereas others (for example Phe 19, Phe 20, Ile 31, and Ile 32) remain at high intensity indicative of a high solvent protection.

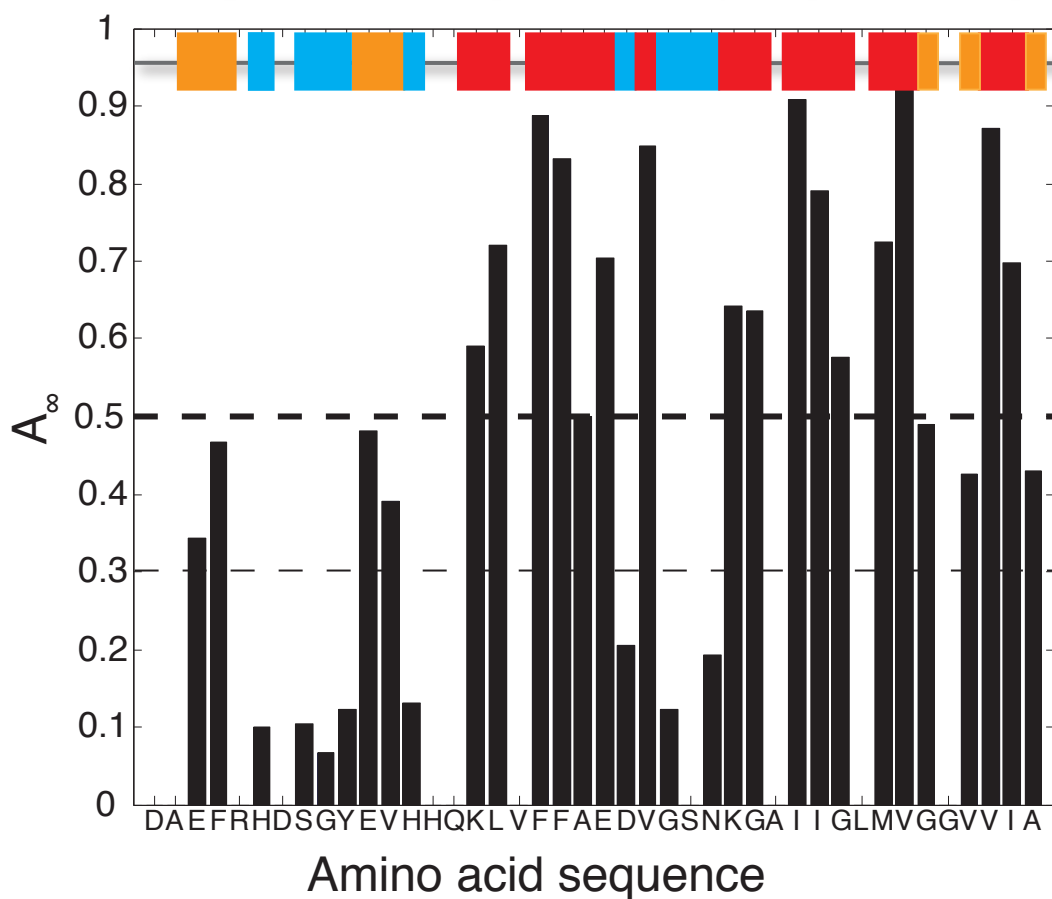


Figure 5.16: Residue-resolved identification of solvent protected ^{15}N - ^1H moieties of $\text{A}\beta$ (1-42) fibrils based on the quenched H/D exchange measurements. The extend of solvent protection is represented by the relative peak intensities at infinite times from the fit of the exchange data shown in Figure 5.15. In the top row, the filled squares indicate the segments that are most protected (red) and semi-protected (orange), and solvent exposed (blue), respectively.

A.5 Dilution analysis

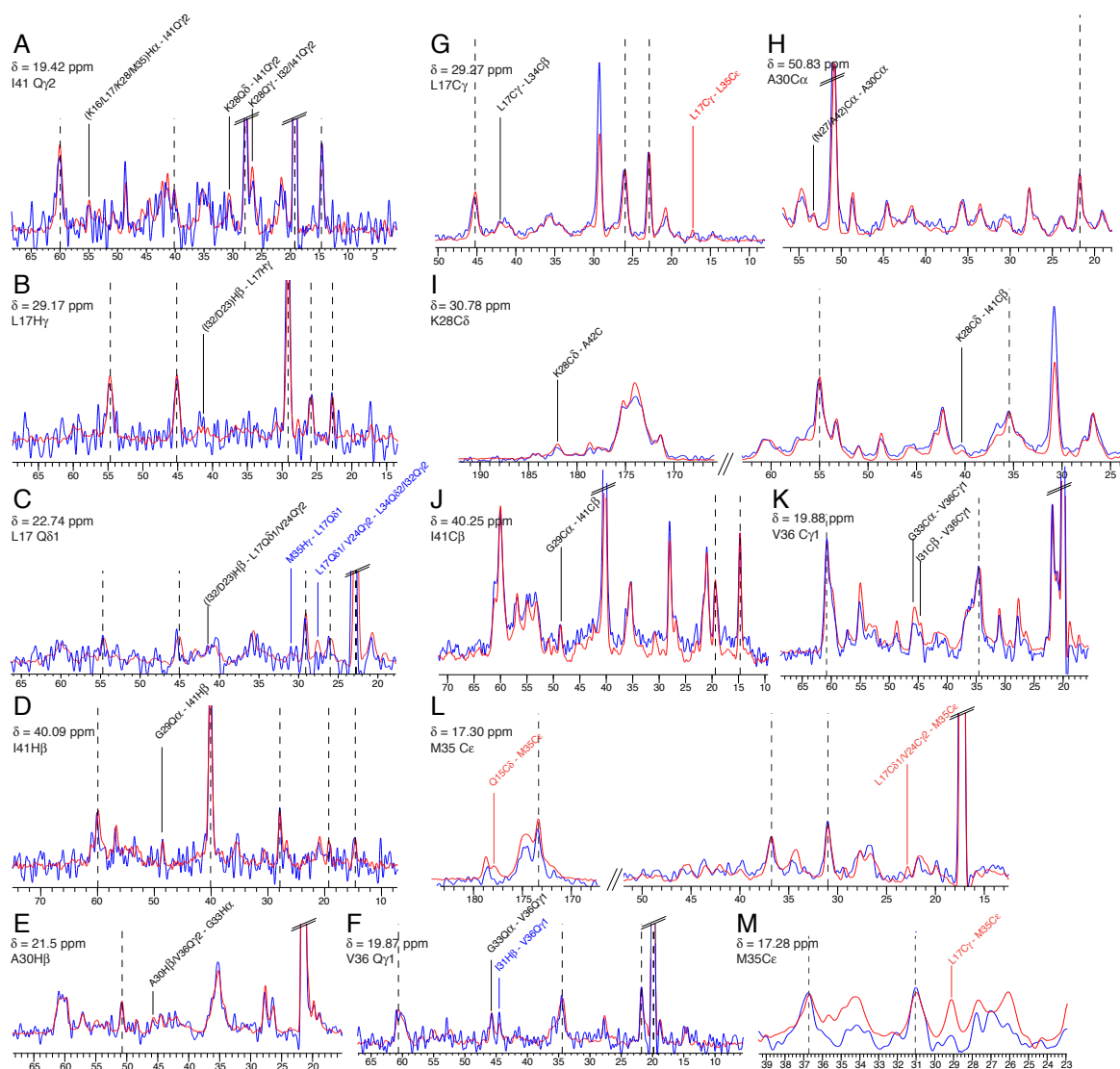


Figure 5.17: Selected traces from the 400 μ s CHHC (A-F), 400 ms DARR (G-L) and PAR (M) spectrum of A β (1-42) fibrils. In red are the traces from the [UL ^{13}C - ^{15}N] sample, while in blue are the corresponding traces from the diluted sample. The frequency of the trace together with the corresponding assignments are listed on the top left of each subfigure. Cross-peaks of interest are labeled black if they are considered to be intra-molecular, red inter-molecular, and blue if they are spectrally unambiguous intra- or intermolecular. The calibration of the diluted spectra was performed using the intra-residual peaks (black dashed line).

A.6 Limited proteolysis

B Methods development

B.1 Selective π pulses optimization

The pulse sequence used to optimize the selective π pulses is shown in Figure 5.19. After the $\frac{\pi}{2}$ pulse on ^1H , the magnetization is transferred to the ^{13}C via CP, optimized for the region of the inversion. The first $\frac{\pi}{2}$ on ^{13}C brings the magnetization on the z - axis and, after a dephasing delay Δ , the inversion pulse Q_3 is placed. The last $\frac{\pi}{2}$ pulse brings the magnetization on the transverse plane and it is detected. ^1H decoupling is applied during the inversion and detection.

We exploited the feature of universal inversion pulse to optimize it for a rotation $z \rightarrow -z$, avoiding CS evolution of the spins outside the inversion window.

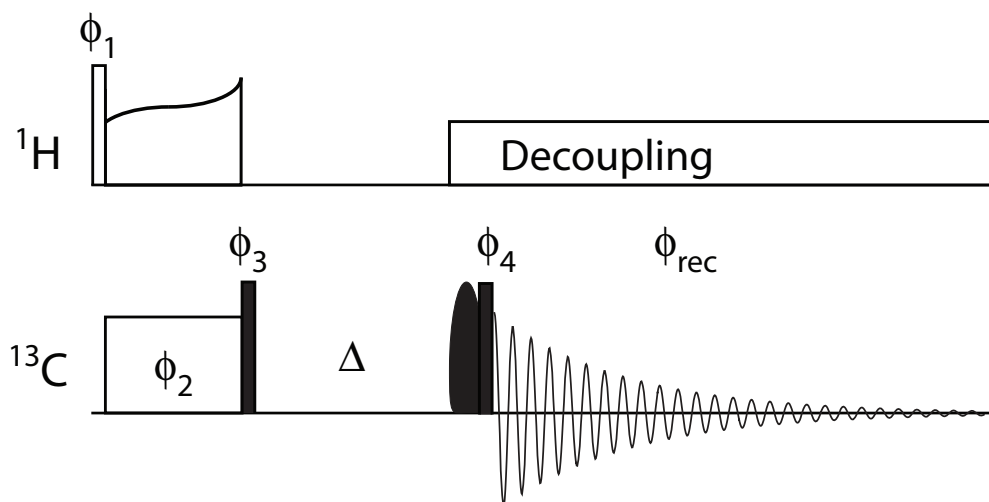


Figure 5.19: Pulse sequence used to optimize the selective π pulses on ^{13}C . White and black boxes represent $\frac{\pi}{2}$ and π pulses, respectively. The shaped pulses represents the selective inversion pulse. All pulses have phase x if not specified differently. The used phase cycle is $\phi_1 = y, -y$, $\phi_3 = y, y, -y, -y$, $\phi_4 = y, y, y, y, -y, -y, -y, -y$, $\phi_{rec} = x, -x, -x, x, -x, x, x, -x$

The so described pulse sequence was used on ubiquitin to invert selectively the C' , the $C\alpha+C\beta$ and the $C\alpha$, obtaining the results shown in Figure 5.20. Care was taken to minimize the effects on the spins outside the inversion window. We compare the results of this pulse sequence (shown in red) with the one in which the rf field of the selective inversion pulse was set to zero (shown in blue).

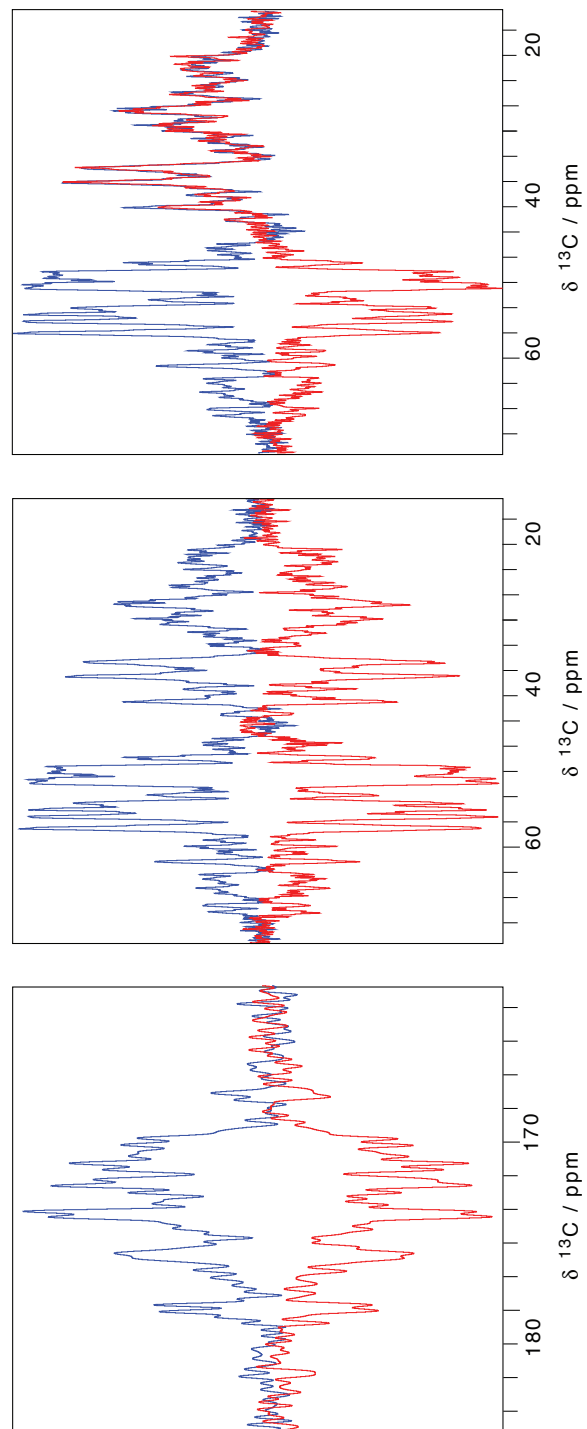


Figure 5.20: Results of the selective π pulses optimization on ubiquitin to invert the C' , the $\text{C}\alpha+\text{C}\beta$ and the $\text{C}\alpha$ (red spectra). The reference experiments (i.e. with the rf power for the selective inversion set to zero) are shown in blue.

B.2 Comparison of ^{13}C and ^{15}N MISSISSIPI experiment

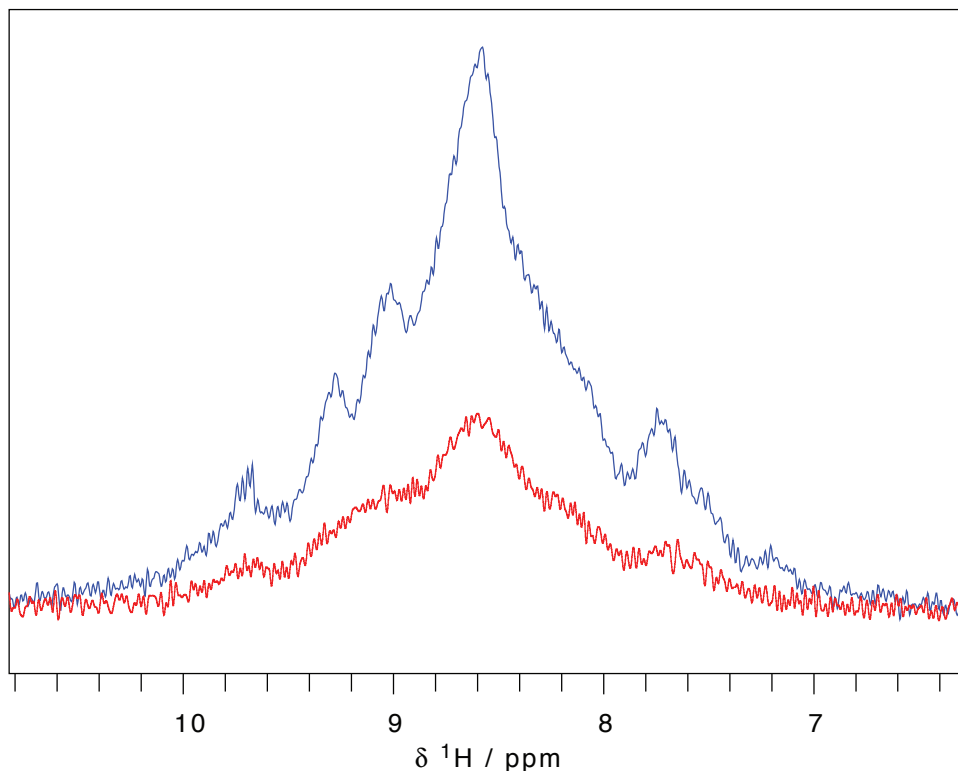


Figure 5.21: 1D ^{13}C - ^1H (red) and 1D ^{15}N - ^1H (blue) MISSISSIPI experiment performed on ^2H - ML HET-s(218-289) fibril 100 % back exchanged. The CP steps were optimized separately and NS = 16 for both experiment. The S/N of the red spectrum is $\sim 30\%$ of the blue spectrum.

B.3 Assignment of ^2H - 100% back - exchanged HET-s(218-289)

The assignment for the ^2H - 100% back - exchanged HET-s(218-289) was obtained by HNCA experiment, thus giving the CS for H^{N} , N and $\text{C}\alpha$. We obtained additional carbon shifts from the analysis of 2D [^{13}C - ^{13}C] DREAM spectrum. This experiment was measured at a magnetic field of 14 T on a BRUKER 3.2 mm rotor, setting the MAS frequency to 13 kHz, on a ^2H - 100% back - exchanged HET-s(218-289) fibrils sample. The $\text{C}\beta$ shifts were obtained from the combination of the $\text{C}\alpha$ shifts from the deuterated sample with the help of the $\text{C}\beta$ of the fully protonated one [60].

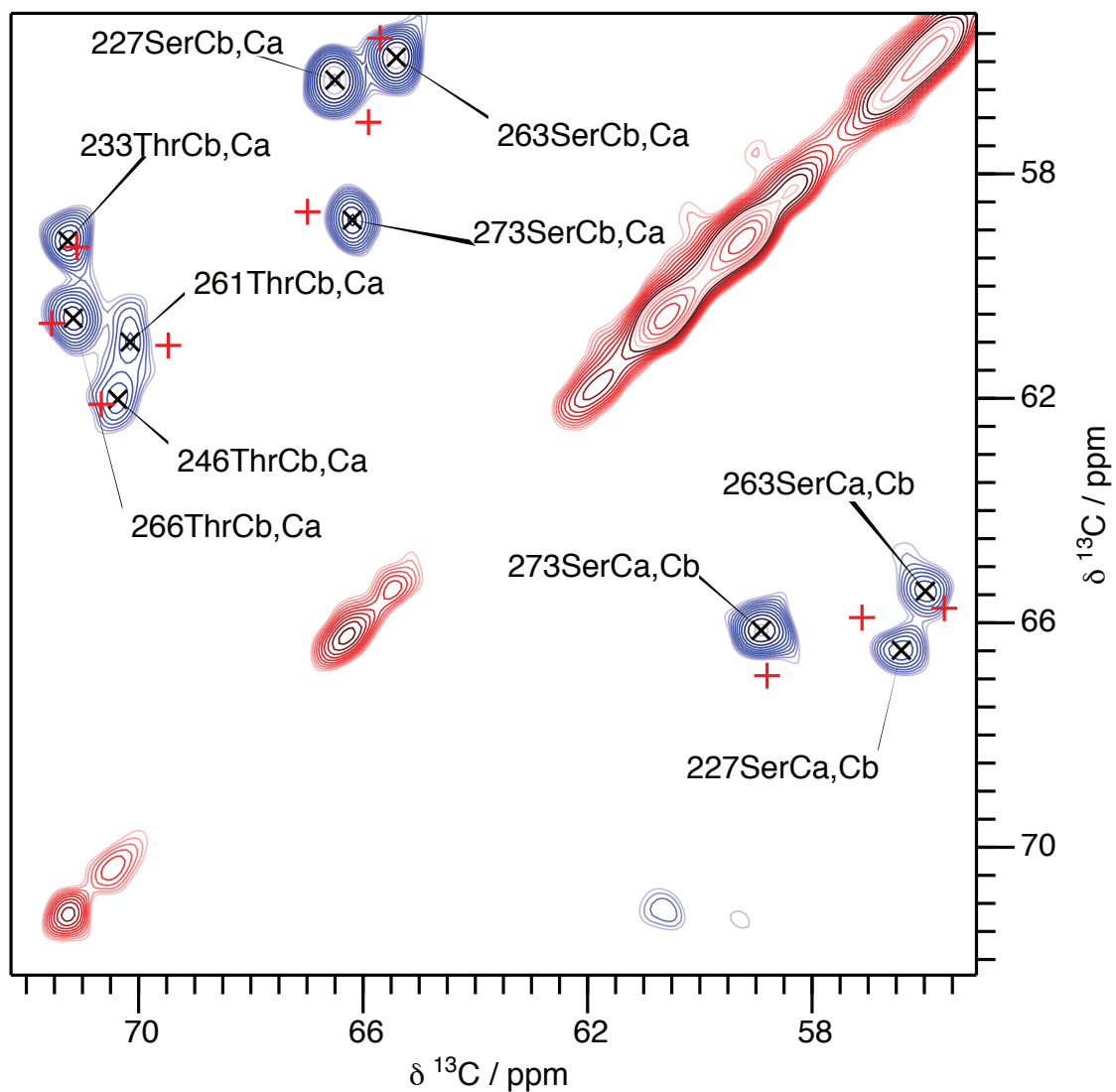


Figure 5.22: Part of 2D [^{13}C - ^{13}C] DREAM spectrum of a ^2H - 100% back - exchanged HET-s(218-289) fibrils, measured at a magnetic field of 14 T and setting the MAS frequency to 13 kHz. $C\beta$ shifts were obtained with the help of the $C\alpha$ of the deuterated sample. Red crosses indicate the position of the expected peak after the isotope correction, as shown in Equation 5.3.

Acknowledgements

When I started writing my thesis, I thought writing acknowledgments would be an easy task. Only now, on the verge of writing them, I realize how complicated it is to acknowledge all the people that have helped, supported, motivated or comforted me during these years. To begin with, I apologize now for each mistake, repetition or lapse of memory I will have for these acknowledgments. I have decided to write them spontaneously and not read them again. In a similar way, I apologize if I will offend someone (not intended at all, except for some exceptions) or for writing too little or too much about you. As I said, these are spontaneous because, for each of you, I should write a chapter at least. This is not clearly possible.

First of all, I'd like to thank my thesis supervisor, Prof. Dr Beat H. Meier. First of all, without you, I'd not have started this PhD and I'd not have become interested in NMR. I thank you for this great opportunity you gave me, to work in your group and for the interesting projects you gave me. I am also grateful for our discussions, about the projects, research and various other topics.

I want also to thank my co-referees, Dr. Anja Böckmann and Prof. Roland Riek, not only for the work related for the thesis and for their comments and support, but for all the scientific discussions, suggestions during the years of my PhD.

During these years, I have spent quite a big percentage of my time in the lab. I have had the luck to work in an open and stimulating environment and so I want to spend some time in thanking all the people I have worked with, starting with Prof. Dr. Matthias Ernst. Matthias, even if I was not your student, your door was always open to me (despite your threats to lock the door for me), to my questions and discussions about the more theoretical projects. Moreover, I enjoyed a lot the sporadic coffee breaks with you and with Dr. Giorgia Zandomenighi, my first "Italian connection". Giorgia, thanks a lot for all your help during these years, for the pleasant discussions about various themes, from work related topics to fundamental debates on Italian languages and dialects, supercazzole, coffee and politics (Travaglio and Berlusconi, remember?). From the "Post-doc" side of the lab, I want to thank all the post-doc I had the pleasure to work with: Dr. Thomas Wiegand, Dr. Nils Lakomek, Dr. Anders Nielsen, Dr. Albert Smith, Dr. Vlastimil Jirasko, Dr. Lauriane Leqoc, Dr Vipin Agarwal, Dr. Chandrakala Gowda and Dr. Mariana Sardo and Dr. Paul Schanda.

Thomas, it was a real pleasure to work with you. I'm going to miss our discussions with

a cup of coffee from the red car on scientific stuff and best combinations of food and drinks. I really found out that you are a very nice person, who takes care of the others and manage also to do great research.

Nils, or "Posty", I haven't really had the opportunity to work on a project with you, but I enjoyed discussing with you about work. Moreover, thanks for the nice time also outside work, at the happy hours mainly!

Anders, how can I forget your sentence: "Yes, I can play chess a little". Thanks to that, I understood the meaning of "a little" in Danish: "Extremely well and blindfolded". Apart from this chess parenthesis, I am grateful for all the things I have learned from you, starting from NMR theory to chess theory. It has been a pleasure to work with you. Andy, we shared the duty of responsible people for the 2 850 MHz magnet and I was involved in your HET-s project. I will always remember the summer school in Brno we have attended.

Vlasta, I had fun in helping you joining the dark side of NMR and for our discussions about holiday in the best country in the world.

Lauriane, was a pleasure to meet you and I'm grateful for the funny time we have spent together with the group.

Vipin, thanks for all the discussions on decoupling and for the introduction to Indian Cuisine.

Chandra, without you, I'd not have realized the difference between harm and arm and thanks for your laughs, so full of energy.

Paul, we had an overlap of only 2 months, I believe. Thanks for having helped me to enter the group.

Mariana, dear Mariana! Thanks a lot, you also have helped me to enter the group, you were able to make me feel at home! Thanks.

Leaving the Post-doc side, let's move to the dark side of the lab. I had the pleasure to meet wonderful people during my PhD, people who have helped me, motivated me, taught me and discussed with me about a lot of themes. It's definitely true, I have to thank all of you for that, starting from the people I had the pleasure to share the office: Matthias Huber, Emilie Testori, Joeri Verasdonck, Dr. Marcin Krajewski, Dr. Greg Kwiatkowski. Matthias, I've learned a lot from you during the long years of my PhD! It was a pleasure sharing the office with you, as well as spending time together outside ETH. Emilie, we started almost together our PhD (maybe a day earlier, since I got the better desk.. But it was on Matthias suggestion!) and I can say it was a pleasure to work, to talk and spend time with you for all these years. I am glad to have improved your knowledge in Italian, teaching you extremely useful words and sentences. Joeri, another Dutch. I was seriously afraid that you will behave like the other one. Luckily (or unluckily) I was wrong! It was extremely pleasant and funny to share the office with you. Thanks also for the good selection of Dutch words I have learned from you. Marcin and Greg, the Polish connection of the Meier's group! Marcin, we haven't discussed a lot about work

because of the different topics, but I've enjoyed the discussions with you. Greg, thanks for teaching me the importance of always saying "I'm doing well" or "I am fine" even when everything was going bad. It started as a "joke", but I learned that, with a bit of optimism, even a horrible day can become better.

From the other office, I'd like to thank Anne Schtz, Kathrin Szekely, Alons Lends, Fabian Jaehnig, Maarten Schledorn and Thomas Westfeld.

Anne, it was nice to work with you and also sharing the duties for the 850 MHz. Many thanks for teaching me protein NMR and for the useful advice on A-beta project.

Kathrin, thanks for the nice atmosphere you have contributed to create in the group. Was fun also the teaching we have done together.

Alons, it was a pleasure to get to know you. I really appreciate our discussions about NMR and about other themes, sport, football (NOT soccer!), movies and comics, maybe with a good glass of beer. I wish you all the best with the TEDOR project.

Fabian, unfortunately we really had not too much contact, but you were always nice and it was a pleasure to discuss with someone about the OLD Spinsight (or whatever is written).

Maarten, I had to check 2-3 times how to write your first name (and I am positively sure I have saved it wrongly on my mobile). It was nice to work with you; your enthusiasm and your will to learn were absolutely great.

Thomas Nr₂, even though we only have worked together briefly, I keep a nice memory of you! Thanks for helping me out in setting up my first experiment on the 600.

Speaking of that, I am forced hereby to mention another postdoc of the group, that comes into my mind thanks to the sentence before. Dr. Jacco van Beek, thanks for having me introduced into the wonderful world of NMR, you taught me the basics of a good experiment. You always had a good word for me ("Ah, you are a physicist, you don't know it" or "You are a physicist and you don't know it?" or my favourite one "Whatever you do, don't do anything stupid"), you probably gave me the worst week of my life at the 600 but, after that baptism, I was able to handle almost everything.

From the other part of the lab, I do not want to thank Kong Ooi Tan.

No way, I am not going to thank you for getting me almost arrested twice in Italy (my fault, perhaps, since I taught you too much Italian), for the trip to Malaysia (with the cave tour that almost killed us all and the relaxing hikes to the volcanoes), for your political incorrectness and for the facts you were able to annoy me with each of your sentence (as well as any other nationalities in the world), for always reminding me about my neighbour.. God, I miss you so much, how can I insult you in a thesis? I wish you good luck for your future career, at the Malaysian Institute of Technology.

Back to the "normal" acknowledgements, I'd like to thank Christian Wasmer, Andreas Grommek, Michael Batel, Julia Gath, Johannes Hellwagner, Susanne Penzel and the people from the other office, Ingo Sholz, Ivan Tomka, Rosemarie Joss, Johannes Wittmann, Thomas Bauer and Sebastian Schnoz.

Christian, thanks a lot for teaching me the basics of protein NMR and for helping me measuring my first 2D and 3D experiments. I have learned a lot from you.

Andreas, thanks for your (sadly) unsuccessful attempts to push me to learn German. I hope that this will change in the future.

Michael, I think I have asked you so many times about which national football team are you supporting. It was nice to know you and I remember nicely the trip to Ireland, for EUROMAR.

Julia, thanks a lot! I really have learned a lot from you, from NMR experiments to structure calculation. I really appreciate your contributions for the group, with your spontaneous invitations for brunch or dinner. Thanks a lot also for that.

”Small” Johannes, was really nice to get to know you! I had fun times with you and I will always remember with a smile our discussion on South Tirol.

Susanne, Supe, we have shared for so much time the responsibility for the 850 MHz. Thanks for that, for the chats we had during the otherwise boring helium and nitrogen filling.

Ingo, we had an overlap of only 1 semester. Thanks for having helped me during the first teaching I had to do (PC VI, 7:45 Tuesday morning. I do not want to add more to that) and for the book (in German!) about statistical thermodynamic.

Igor, even though I did not always appreciate your sense of humour, I am really glad that I got to know you. Otherwise, the dinners with the Dutch guy would have been extremely boring.

Rosemarie, I... would like to thank you... for ... ok, I am positively sure I will learn German in the future. Yes. Thanks anyway for having tried that and for the Pirates of Caribbean soundtrack with your orchestra.

Jowi, we had similar problems with the stomach at the end of our PhD. Thanks for all the advices you gave me, they really have helped. Thanks also for showing me the world of the Rubik’s cube.

Toba, Mr.-I-Forgot-To-Acknowledge- Francesco-In-My-Thesis. A sin like this one is difficult to forget and my revenge will come sloooooowly. Just, please, do not leave Facebook open. Thanks for not having replaced me, for your sense of humour and for having taught me to always lock my computer (or, at least, to log out).

Schnozel, thanks for the atmosphere you have contributed to create. Your laughs, your imitations and your sense of humour are just unique.

From the group, I also want to thank Alexander Daepf, Andreas Hunkeler and Riccardo Cadalbert and Gabriele Roder.

Alex, I am really really glad to have met you! Probably the first Swiss person I have met who can be later than me for an appointment. Thanks a lot for being my friend, for your valuable help for work and for the support you gave me.

Andreas, I also want to thank you for your help during work or for helium related matters.

Riccardo, you were always nice to me and helped me a lot with the otherwise stressful and scaring part of samples preparation. Thanks a lot also for your Aperol and for the good atmosphere they have created.

Gabriele, thanks a lot for your support in different cases and for the possibility to discuss about various themes with you.

Continuing with work related acknowledgements, I'd like to thank all the people I have collaborated with: Marielle Waelti, Peter Guentert, Nina Luckgei, Nadezhda Nespovitaya and Dr. Lorenzo Sborgi.

Marielle, thanks really a lot! I have enjoyed working with you on the big A-beta project! I think I can write a lot about that, from the beginning, the sample preparation, the assignment, the problems, the discussions! But, above all and despite the stress, it was always nice to discuss with you and work with you. Thanks also for having taught me that "Cazzo Merda" in Finnish is not a bad sentence.

Peter, I really learned a lot from you for the structure calculation. Your patience and your availability to answer my questions were great, thanks!

Nina, how can't I remember when, at the 850 MHz in the evening, I started to speak to you in Italian (because of tiredness)? And you, instead of laughing or insulting me, said that it was not a problem that you could understand a bit. Thanks a lot for the funny times we had together.

Nadja and Lorenzo, I had two projects with you. Thanks for your support and help.

Meier's group was my working group. But I cannot forget (and I do not want to!) the other group, the Real's group! Christopher, Alain, Jonny, Louisa, Jagna, Annick, Pavel, Lenka, David, Noah, Vicki, Stephi, Maike, Pascal, Ali.

Guys, thanks really a lot! You have made the time of my PhD so nice, I can't really thank you enough for that! It's also difficult to thank each of you with a sentence, seriously!

Christopher, talking with you was always nice, especially during Happy Hours, in which we have had so wonderful ideas!

Alain, I'll never be able to pronounce your name correctly, despite my countless efforts!

Jonny, Louisa, the trip I had in Hamburg with you was just great! No words to describe it! Jonny, thanks a lot for your support, I really have appreciated it!

Jagna, best NMR student I have ever had! It was so nice and FRAnny to help you with the exam! Pointless to say, that you have "repaid" this during my PhD, with your support, your laughs and your "shots"!

Annick, I really enjoyed our chats! I am really happy I got to know you!

Pavel, Lenka, thanks a lot for all the time we have spent together, you are both extremely nice, friendly and it was always a pleasure to talk to you and to party with you! David, thanks for your jokes, your sense of humor, your partying skills and, especially, for not having burnt Claudia!

Noah, thanks for having started the Fra's Jokes, on the Gotthard! Thanks a lot again for the thousands discussions on so many topics!

Vicki, thanks for your way to laugh! Seriously, it's the funniest way of laughing I have ever seen! Doesn't matter if you are frustrated or sad, 2 minutes of hearing you laughing fixes everything.

Stephi! We met on the first week of our PhD in the office of Veronika. Immediately, I realized asked myself, who the hell was this guy. I could not have imagined back then, that you would have become a great friend and that we would have had so many coffees, so many chats (curtains, ideas for movies, jokes to someone!) Thanks a lot for that!

Maike, it has been a real pleasure to get to know you! I will always remember the trip to visit you and Stephi in Belgium as well as your fantastic birthday party in Germany! Moreover, thanks for your support when I needed it! Thanks a lot!

Pascal, how can I start? Thanks a lot for your constant help to decide what the best meal to order and to always remind me the alternative! Thanks also for your support, you were there when I was down and also when I was up again! Thanks for not being only the boyfriend (should I say that?) of my best friend, but for being one of my best friend, a person I can count of, even when we take a shortcut!

Ali, a full chapter of my thesis would not be enough to thank you, even when you stole the Italian speaking group in PC1! Grazie, grazie davvero! Dal nostro corso/i di Tedesco, alle bibliche chat su gmail, alla ricerca delle luci sberlucanti, al tuo supporto, per i tuoi compleanni. Grazie!

Rimanendo in Italiano, voglio ringraziare i degni rappresentanti del Canton Ticino, Ognò e Alessia.

Ognò, grazie per gli innumerevoli caffè', iniziati con la tua assistenza a PC1, che mi hanno permesso di conoscerti meglio e di conoscere il lato oscuro del Ticino.

Alessia, grazie per le birrette in Zwielfplatz, per l'incoraggiamento, per i racconti sulle coinquiline!

Scendendo pi a sud, voglio ringraziare Isaberta Mantani e Max!

Isa, in pratica sei stata tu a consigliarmi il Dottorato a Zurigo! Grazie per questo, e grazie per i postantani momenti passati insieme, dalla Street Parade alle serate Zurighesi.

Max, grazie per il tempo passato assieme, per le discussioni e per i viaggi della speranza Torino/Zurigo.

Ale, anche se ultimamente non ci siamo pi sentiti, grazie per esserci stata, grazie per le battute di caccia al pollo per Zurigo e per le tue avventure con la macchina.

Joelle, grazie per gli innumerevoli pranzi assieme, per gli stropuli, le scoiattole e le lezioni di Italiano.

Andando nella mia città natale, vorrei ringraziare tutti i miei amici, che mi hanno sopportato e supportato durante questa mia avventura Zurighese, a cominciare dai survival del Team Violaciocche, Ivo, Paolo, Fede e Ale.

Ivo, grazie davvero ! Sei stato un amico fantastico, mi hai aiutato tantissimo in questi anni e, nonostante la distanza, abbiamo sempre avuto modo di parlare e discutere assieme, come se il tempo non fosse passato. In ugual modo, con Paolo (anche se ancora mi rode

il fatto delle ferie) e con Ale. Grazie davvero.

Un grazie particolare a Fede (e metto insieme anche Alfio e Vero) per aver organizzato il capodanno durante il quale ho incontrato la mia futura moglie, Cla.

Cla, a te in particolare, voglio ringraziarti per avermi aiutato nel periodo finale della tesi, forse il pi stressante, di avermi incoraggiato e per essermi stato vicino. Grazie!

Voglio infine ringraziare la mia famiglia, che prima di tutto ha reso possibile la mia avventura Zurighese!

Mamma, pap, mi avete sempre spinto a seguire e a cercare la mia strada, sostenendomi e aiutandomi come nessun altro avrebbe potuto fare durante questi anni, partendo dal supporto arrivando a aiuti molto concreti. Grazie!

Dade, sebbene tu abbia imboccato la strada della matematica perdizione, grazie!

Sei un fratello fantastico e il tuo aiuto, il tuo supporto e incoraggiamento (condito da commenti sarcastici, ovviamente) mi son stati fondamentali in questi anni!

Curriculum Vitae

Francesco Ravotti

Date of birth 13.05.1985
Nationality Italian
Address Bergellerstrasse 18, 8049 Zurich, Switzerland
Email francesco.ravotti@phys.chem.ethz.ch

Education and Research

Doctoral student with Prof. B.H. Meier at **ETH Zürich** 09/2010-present
MSc Bio-medical Physics at **University of Torino** 09/2007-12/2009
BSc Physics at **University of Torino** 09/2004-09/2007

Conferences:

EUROMAR, Zurich, Switzerland, 2014
ENC, Pacific Grove, USA, 2013
NMR Summer School, Brno, Czech Republic, 2012
EUROMAR, Dublin, Ireland, 2012
7th Alpine Conference on Solid-State NMR, Chamonix, France, 2011

Presentations

Analysis and applications of S^3E sequence in ^{13}C experiments for proteins, *EUROMAR 2012*, Dublin, Ireland

Publications

Atomic-resolution structure of a disease-relevant $A\beta(1-42)$ amyloid fibril. M. A. Wälti, F. Ravotti, H. Arai, C. G. Glabe, J. S. Wall, A. Böckmann, P. Güntert, B. H. Meier and R. Riek, *PNAS* 113, 84 (2016)
Solid-state NMR sequential assignment of an Amyloid- $\beta(142)$ fibril polymorph. F. Ravotti, M. A. Waelti, P. Guentert, R. Riek, A. Boeckmann and B. H. Meier *Biomol. NMR Assignment* 10, 1 (2016)
Solid-state NMR sequential assignments of the N-terminal domain of HpDnaB helicase. T. Wiegand, C. Gardiennet, F. Ravotti, A. Bazin, B. Kunert, D. Lacabanne, R. Cadal-

bert, P. Guentert, L. Terradot, A. Boeckmann and B. H. Meier *Biomol. NMR Assignment* 10, 1 (2016)

Sequence-specific solid-state NMR assignments of the mouse ASC PYRIN domain in its filament form. F. Ravotti, L. Sborgi, R. Cadalbert, M. Huber, A. Mazur, P. Broz, S. Hiller, B. H. Meier, and A. Bckmann, *Biomol. NMR Assignment* 10, 1 (2016)

Structure and assembly of the mouse ASC inflammasome by combined NMR spectroscopy and cryo-electron microscopy. L. Sborgi, F. Ravotti, V. P. Dandey, M. S. Dick, A. Mazur, S. Reckel, M. Chami, S. Scherer, M. Huber, A. Boeckmann, E. H. Egelman, H. Stahlberg, P. Broz, B. H. Meier and S. Hiller, *PNAS* 112, 43 (2015)

Solid-state NMR sequential assignments of the C-terminal oligomerization domain of human C4b-binding protein. N. Luckgei, B. Habenstein, F. Ravotti, S. Megy, F. Penin, J.-B. Marchand, F. Hill, A. Boeckmann, and B. H. Meier *Biomol. NMR Assignment* 8, 1 (2014)

Automated solid-state NMR resonance assignment of protein microcrystals and amyloids. E. Schmidt, J. Gath, B. Habenstein, F. Ravotti, K. Szkely, M. Huber, L. Buchner, A. Boeckmann, B. H. Meier, and P. Guentert *Journal Biomol. NMR* 56, 3 (2013)

Amyloids seen by solid-state NMR: Atomic-resolution structure, dynamics, and characterization of the pharmacophore. B. H. Meier, A. Boeckmann, M. Ernst, R. Melki, R. Riek, L. Bousset, J. Gath, B. Habenstein, M. Huber, N. Luckgei, F. Ravotti, A. Schuetz, C. Seuring, and C. Wasmer *FEBS* 279, S1 (2012)

Bibliography

- [1] IJ Lowe. Free induction decays of rotating solids. *Physical Review Letters*, 2(7):285, 1959.
- [2] ER Andrew, A Bradbury, and RG Eades. Nuclear magnetic resonance spectra from a crystal rotated at high speed. 1958.
- [3] Ago Samoson, Tiit Tuhern, Jaan Past, Andres Reinhold, Ivo Heinmaa, Tiit Anupõld, Mark E Smith, and Kevin J Pike. Fast magic-angle spinning: Implications. *eMagRes*, 2010.
- [4] BM Fung, AK Khitrin, and Konstantin Ermolaev. An improved broadband decoupling sequence for liquid crystals and solids. *Journal of Magnetic Resonance*, 142(1):97–101, 2000.
- [5] A.E. Bennet, C.M. Rinestra, M. Augr, K.V. Lakshmi, and R.G. Griffin. Heteronuclear Decoupling in rotating solids. *JOURNAL OF CHEMICAL PHYSICS*, 103(16):6951–6958, OCT 22 1995.
- [6] Andreas Detken, Edme H Hardy, Matthias Ernst, and Beat H Meier. Simple and efficient decoupling in magic-angle spinning solid-state nmr: the xix scheme. *Chemical Physics Letters*, 356(3):298–304, 2002.
- [7] Matthias Ernst, Ago Samoson, and Beat H Meier. Low-power xix decoupling in mas nmr experiments. *Journal of Magnetic Resonance*, 163(2):332–339, 2003.
- [8] Vipin Agarwal, Tiit Tuhern, Andres Reinhold, Jaan Past, Ago Samoson, Matthias Ernst, and Beat H. Meier. Amplitude-modulated low-power decoupling sequences for fast magic-angle spinning {NMR}. *Chemical Physics Letters*, 583:1 – 7, 2013.
- [9] Barbara Leiting, Frank Marsilio, and John F O’Connell. Predictable deuteration of recombinant proteins expressed in *escherichia coli*. *Analytical biochemistry*, 265(2):351–355, 1998.
- [10] Gareth A Morris and Ray Freeman. Enhancement of nuclear magnetic resonance signals by polarization transfer. *Journal of the American Chemical Society*, 101(3):760–762, 1979.

- [11] SR Hartmann and EL Hahn. Nuclear double resonance in the rotating frame. *Physical Review*, 128(5):2042, 1962.
- [12] S Hediger, BH Meier, and RR Ernst. Adiabatic passage hartmann-hahn cross polarization in nmr under magic angle sample spinning. *Chemical Physics Letters*, 240(5):449–456, 1995.
- [13] A. W. Hing, S. Vega, and J. Schaefer. Transferred-echo double-resonance nmr. *Journal of Magnetic Resonance (1969)*, 96(1):205–209, 1992.
- [14] Ren Verel, Matthias Ernst, and Beat H. Meier. Adiabatic dipolar recoupling in solid-state nmr: The {DREAM} scheme. *Journal of Magnetic Resonance*, 150(1):81 – 99, 2001.
- [15] Marvin J Bayro, Matthias Huber, Ramesh Ramachandran, Timothy C Davenport, Beat H Meier, Matthias Ernst, and Robert G Griffin. Dipolar truncation in magic-angle spinning nmr recoupling experiments. *The Journal of chemical physics*, 130(11):114506, 2009.
- [16] A. E. Bennett, C. M. Rienstra, J. M. Griffiths, W. Zhen, P. T. Lansbury Jr, and R. G. Griffin. Homonuclear radio frequency-driven recoupling in rotating solids. *The Journal of chemical physics*, 108(22):9463–9479, 1998.
- [17] Yoshitaka Ishii. ^{13}C – ^{13}C dipolar recoupling under very fast magic angle spinning in solid-state nuclear magnetic resonance: applications to distance measurements, spectral assignments, and high-throughput secondary-structure determination. *The Journal of Chemical Physics*, 114(19):8473–8483, 2001.
- [18] DP Raleigh, MH Levitt, and RG Griffin. Rotational resonance in solid state nmr. *Chemical Physics Letters*, 146(1):71–76, 1988.
- [19] Rasmus Linser, Uwe Fink, and Bernd Reif. Proton-detected scalar coupling based assignment strategies in mas solid-state nmr spectroscopy applied to perdeuterated proteins. *Journal of Magnetic Resonance*, 193(1):89–93, 2008.
- [20] C. L. Masters, G. Simms, N. A. Weinman, G. Multhaup, B. L. McDonald, and K. Beyreuther. Amyloid plaque core protein in Alzheimer disease and Down syndrome. *Proc. Natl. Acad. Sci. U.S.A.*, 82(12):4245–4249, Jun 1985.
- [21] G. G. Glenner and C. W. Wong. Alzheimer’s disease and Down’s syndrome: sharing of a unique cerebrovascular amyloid fibril protein. *Biochem. Biophys. Res. Commun.*, 122(3):1131–1135, Aug 1984.
- [22] J. Kang, H. G. Lemaire, A. Unterbeck, J. M. Salbaum, C. L. KangMasters, K. H. Grzeschik, G. Multhaup, K. Beyreuther, and B. Muller-Hill. The precursor of

- Alzheimer's disease amyloid A4 protein resembles a cell-surface receptor. *Nature*, 325(6106):733–736, 1987.
- [23] M. Costanzo and C. Zurzolo. The cell biology of prion-like spread of protein aggregates: mechanisms and implication in neurodegeneration. *Biochem. J.*, 452(1):1–17, May 2013.
- [24] A. E. Roher, J. D. Lowenson, S. Clarke, A. S. Woods, R. J. Cotter, E. Gowing, and M. J. Ball. beta-Amyloid-(1-42) is a major component of cerebrovascular amyloid deposits: implications for the pathology of Alzheimer disease. *Proc. Natl. Acad. Sci. U.S.A.*, 90(22):10836–10840, Nov 1993.
- [25] D. J. Selkoe. The molecular pathology of Alzheimer's disease. *Neuron*, 6(4):487 – 498, April 1991.
- [26] T. Iwatsubo, A. Odaka, N. Suzuki, H. Mizusawa, N. Nukina, and Y. Ihara. Visualization of A beta 42(43) and A beta 40 in senile plaques with end-specific A beta monoclonals: evidence that an initially deposited species is A beta 42(43). *Neuron*, 13(1):45–53, Jul 1994.
- [27] S. A. Gravina, L. Ho, C. B. Eckman, K. E. Long, L. Otvos, L. H. Younkin, N. Suzuki, and S. G. Younkin. Amyloid beta protein (A beta) in Alzheimer's disease brain. Biochemical and immunocytochemical analysis with antibodies specific for forms ending at A beta 40 or A beta 42(43). *J. Biol. Chem.*, 270(13):7013–7016, Mar 1995.
- [28] J. T. Jarrett, E. P. Berger, and P. T. Lansbury. The carboxy terminus of the beta amyloid protein is critical for the seeding of amyloid formation: implications for the pathogenesis of Alzheimer's disease. *Biochemistry*, 32(18):4693–4697, May 1993.
- [29] J. T. Jarrett, E. P. Berger, and P. T. Lansbury. The C-terminus of the beta protein is critical in amyloidogenesis. *Ann. N. Y. Acad. Sci.*, 695:144–148, Sep 1993.
- [30] O. M. El-Agnaf, D. S. Mahil, B. P. Patel, and B. M. Austen. Oligomerization and toxicity of beta-amyloid-42 implicated in Alzheimer's disease. *Biochem. Biophys. Res. Commun.*, 273(3):1003–1007, Jul 2000.
- [31] A. T. Petkova, Y. Ishii, J. J. Balbach, O. N. Antzutkin, R. D. Leapman, F. Delaglio, and R. Tycko. A structural model for Alzheimer's beta -amyloid fibrils based on experimental constraints from solid state NMR. *Proc. Natl. Acad. Sci. U.S.A.*, 99(26):16742–16747, Dec 2002.
- [32] A. K. Paravastu, R. D. Leapman, W. M. Yau, and R. Tycko. Molecular structural basis for polymorphism in Alzheimer's beta-amyloid fibrils. *Proc. Natl. Acad. Sci. U.S.A.*, 105(47):18349–18354, Nov 2008.

- [33] A. K. Schuetz, T. Vagt, M. Huber, O. Y. Ovchinnikova, R. Cadalbert, J. Wall, P. Guntert, A. Bockmann, R. Glockshuber, and B. H. Meier. Atomic-resolution three-dimensional structure of amyloid fibrils bearing the Osaka mutation. *Angew. Chem. Int. Ed. Engl.*, 54(1):331–335, Jan 2015.
- [34] T. Luhrs, C. Ritter, M. Adrian, D. Riek-Loher, B. Bohrmann, H. Dobeli, D. Schubert, and R. Riek. 3D structure of Alzheimer’s amyloid-beta(1-42) fibrils. *Proc. Natl. Acad. Sci. U.S.A.*, 102(48):17342–17347, Nov 2005.
- [35] A. Olofsson, M. Lindhagen-Persson, A. E. Sauer-Eriksson, and A. Ohman. Amide solvent protection analysis demonstrates that amyloid-beta(1-40) and amyloid-beta(1-42) form different fibrillar structures under identical conditions. *Biochem. J.*, 404(1):63–70, May 2007.
- [36] M. Schmidt, A. Rohou, K. Lasker, J. K. Yadav, C. Schiene-Fischer, M. Fandrich, and N. Grigorieff. Peptide dimer structure in an A(1-42) fibril visualized with cryo-EM. *Proc. Natl. Acad. Sci. U.S.A.*, 112(38):11858–11863, Sep 2015.
- [37] M. Ahmed, J. Davis, D. Aucoin, T. Sato, S. Ahuja, S. Aimoto, J. I. Elliott, W. E. Van Nostrand, and S. O. Smith. Structural conversion of neurotoxic amyloid-beta(1-42) oligomers to fibrils. *Nat. Struct. Mol. Biol.*, 17(5):561–567, May 2010.
- [38] A. Morimoto, K. Irie, K. Murakami, Y. Masuda, H. Ohigashi, M. Nagao, H. Fukuda, T. Shimizu, and T. Shirasawa. Analysis of the secondary structure of beta-amyloid (Abeta42) fibrils by systematic proline replacement. *J. Biol. Chem.*, 279(50):52781–52788, Dec 2004.
- [39] R. Nelson, M. R. Sawaya, M. Balbirnie, A. ?. Madsen, C. Riek, R. Grothe, and D. Eisenberg. Structure of the cross-beta spine of amyloid-like fibrils. *Nature*, 435(7043):773–778, Jun 2005.
- [40] O. N. Antzutkin, R. D. Leapman, J. J. Balbach, and R. Tycko. Supramolecular structural constraints on Alzheimer’s beta-amyloid fibrils from electron microscopy and solid-state nuclear magnetic resonance. *Biochemistry*, 41(51):15436–15450, Dec 2002.
- [41] Y. Xiao, B. Ma, D. McElheny, S. Parthasarathy, F. Long, M. Hoshi, R. Nussinov, and Y. Ishii. A(1-42) fibril structure illuminates self-recognition and replication of amyloid in Alzheimer’s disease. *Nat. Struct. Mol. Biol.*, 22(6):499–505, Jun 2015.
- [42] M. Fandrich, J. Meinhardt, and N. Grigorieff. Structural polymorphism of Alzheimer Abeta and other amyloid fibrils. *Prion*, 3(2):89–93, 2009.

- [43] L. Bousset, L. Pieri, G. Ruiz-Arlandis, J. Gath, P. H. Jensen, B. Habenstein, K. Mardona, V. Olieric, A. Bockmann, B. H. Meier, and R. Melki. Structural and functional characterization of two alpha-synuclein strains. *Nat Commun*, 4:2575, 2013.
- [44] B. H. Meier and A. Bockmann. The structure of fibrils from 'misfolded' proteins. *Curr. Opin. Struct. Biol.*, 30:43–49, Feb 2015.
- [45] K. Takegoshi, Shinji Nakamura, and Takehiko Terao. $^{13}\text{C}1\text{h}$ dipolar-assisted rotational resonance in magic-angle spinning {NMR}. *Chemical Physics Letters*, 344(56):631 – 637, Aug 2001.
- [46] K. Takegoshi, Shinji Nakamura, and Takehiko Terao. $^{13}\text{C}1\text{h}$ dipolar-driven $^{13}\text{C}13\text{c}$ recoupling without ^{13}C rf irradiation in nuclear magnetic resonance of rotating solids. *The Journal of Chemical Physics*, 118(5):2325–2341, 2003.
- [47] T. J. Stevens, R. H. Fogh, W. Boucher, V. A. Higman, F. Eisenmenger, B. Bardiaux, B. J. van Rossum, H. Oschkinat, and E. D. Laue. A software framework for analysing solid-state MAS NMR data. *J. Biomol. NMR*, 51(4):437–447, Dec 2011.
- [48] W. F. Vranken, W. Boucher, T. J. Stevens, R. H. Fogh, A. Pajon, M. Llinas, E. L. Ulrich, J. L. Markley, J. Ionides, and E. D. Laue. The CCPN data model for NMR spectroscopy: development of a software pipeline. *Proteins*, 59(4):687–696, Jun 2005.
- [49] A. Schuetz, C. Wasmer, B. Habenstein, R. Verel, J. Greenwald, R. Riek, A. Bockmann, and B. H. Meier. Protocols for the sequential solid-state NMR spectroscopic assignment of a uniformly labeled 25 kDa protein: HET-s(1-227). *Chembiochem*, 11(11):1543–1551, Jul 2010.
- [50] B. Habenstein, C. Wasmer, L. Bousset, Y. Sourigues, A. Schutz, A. Loquet, B. H. Meier, R. Melki, and A. Bockmann. Extensive de novo solid-state NMR assignments of the 33 kDa C-terminal domain of the Ure2 prion. *J. Biomol. NMR*, 51(3):235–243, Nov 2011.
- [51] D. S. Wishart and B. D. Sykes. The ^{13}C Chemical-Shift Index: A simple method for the identification of protein secondary structure using ^{13}C chemical-shift data. *Journal of Biomolecular NMR*, 4(2):171–180, Mar 1994.
- [52] J. R. Lewandowski, G. De Paepe, and R. G. Griffin. Proton assisted insensitive nuclei cross polarization. *J. Am. Chem. Soc.*, 129(4):728–729, Jan 2007.
- [53] A. Lange, S. Luca, and M. Baldus. Structural constraints from proton-mediated rare-spin correlation spectroscopy in rotating solids. *J. Am. Chem. Soc.*, 124(33):9704–9705, Aug 2002.

- [54] G. De Paepe, J. R. Lewandowski, A. Loquet, A. Bockmann, and R. G. Griffin. Proton assisted recoupling and protein structure determination. *J Chem Phys*, 129(24):245101, Dec 2008.
- [55] S. A. Muller and A. Engel. Structure and mass analysis by scanning transmission electron microscopy. *Micron*, 32(1):21–31, Jan 2001.
- [56] A. A. Sousa and R. D. Leapman. Mass mapping of amyloid fibrils in the electron microscope using STEM imaging. *Methods Mol. Biol.*, 950:195–207, 2013.
- [57] D. Thomas, P. Schultz, A. C. Steven, and J. S. Wall. Mass analysis of biological macromolecular complexes by STEM. *Biol. Cell*, 80(2-3):181–192, 1994.
- [58] P. Guntert, C. Mumenthaler, and K. Wuthrich. Torsion angle dynamics for NMR structure calculation with the new program DYANA. *J. Mol. Biol.*, 273(1):283–298, Oct 1997.
- [59] P. Guntert and L. Buchner. Combined automated NOE assignment and structure calculation with CYANA. *J. Biomol. NMR*, 62(4):453–471, Aug 2015.
- [60] C. Wasmer, A. Lange, H. Van Melckebeke, A. B. Siemer, R. Riek, and B. H. Meier. Amyloid fibrils of the HET-s(218-289) prion form a beta solenoid with a triangular hydrophobic core. *Science*, 319(5869):1523–1526, Mar 2008.
- [61] M. T. Colvin, R. Silvers, B. Frohm, Y. Su, S. Linse, and R. G. Griffin. High resolution structural characterization of A42 amyloid fibrils by magic angle spinning NMR. *J. Am. Chem. Soc.*, 137(23):7509–7518, Jun 2015.
- [62] R. Riek. Cell biology: infectious Alzheimer’s disease? *Nature*, 444(7118):429–431, Nov 2006.
- [63] M. Meyer-Luehmann, J. Coomaraswamy, T. Bolmont, S. Kaeser, C. Schaefer, E. Kilger, A. Neuenschwander, D. Abramowski, P. Frey, A. L. Jaton, J. M. Vigouret, P. Paganetti, D. M. Walsh, P. M. Mathews, J. Ghiso, M. Staufenbiel, L. C. Walker, and M. Jucker. Exogenous induction of cerebral beta-amyloidogenesis is governed by agent and host. *Science*, 313(5794):1781–1784, Sep 2006.
- [64] M. A. Walti, J. Orts, B. Vogeli, S. Campioni, and R. Riek. Solution NMR studies of recombinant A(1-42): from the presence of a micellar entity to residual β -sheet structure in the soluble species. *Chembiochem*, 16(4):659–669, Mar 2015.
- [65] A. Bockmann, C. Gardiennet, R. Verel, A. Hunkeler, A. Loquet, G. Pintacuda, L. Emsley, B. H. Meier, and A. Lesage. Characterization of different water pools in solid-state NMR protein samples. *J. Biomol. NMR*, 45(3):319–327, Nov 2009.

- [66] Y. J. Lin, D. K. Kirchner, and P. Guntert. Influence of H chemical shift assignments of the interface residues on structure determinations of homodimeric proteins. *J. Magn. Reson.*, 222:96–104, Sep 2012.
- [67] L. Buchner and P. Guntert. Increased reliability of nuclear magnetic resonance protein structures by consensus structure bundles. *Structure*, 23(2):425–434, Feb 2015.
- [68] L. Franchi, R. Munoz-Planillo, and G. Nunez. Sensing and reacting to microbes through the inflammasomes. *Nat. Immunol.*, 13(4):325–332, Apr 2012.
- [69] M. Lamkanfi and V. M. Dixit. Mechanisms and functions of inflammasomes. *Cell*, 157(5):1013–1022, May 2014.
- [70] S. K. Vanaja, V. A. Rathinam, and K. A. Fitzgerald. Mechanisms of inflammasome activation: recent advances and novel insights. *Trends Cell Biol.*, 25(5):308–315, May 2015.
- [71] K. Schroder and J. Tschopp. The inflammasomes. *Cell*, 140(6):821–832, Mar 2010.
- [72] J. G. Walsh, D. A. Muruve, and C. Power. Inflammasomes in the CNS. *Nat. Rev. Neurosci.*, 15(2):84–97, Feb 2014.
- [73] T. Strowig, J. Henao-Mejia, E. Elinav, and R. Flavell. Inflammasomes in health and disease. *Nature*, 481(7381):278–286, Jan 2012.
- [74] M. Lamkanfi and V. M. Dixit. Inflammasomes and their roles in health and disease. *Annu. Rev. Cell Dev. Biol.*, 28:137–161, 2012.
- [75] Z. Hu, C. Yan, P. Liu, Z. Huang, R. Ma, C. Zhang, R. Wang, Y. Zhang, F. Martinon, D. Miao, H. Deng, J. Wang, J. Chang, and J. Chai. Crystal structure of NLRC4 reveals its autoinhibition mechanism. *Science*, 341(6142):172–175, Jul 2013.
- [76] E. de Alba. Structure and interdomain dynamics of apoptosis-associated speck-like protein containing a CARD (ASC). *J. Biol. Chem.*, 284(47):32932–32941, Nov 2009.
- [77] E. Liepinsh, R. Barbals, E. Dahl, A. Sharipo, E. Staub, and G. Otting. The death-domain fold of the ASC PYRIN domain, presenting a basis for PYRIN/PYRIN recognition. *J. Mol. Biol.*, 332(5):1155–1163, Oct 2003.
- [78] J. Masumoto, S. Taniguchi, K. Ayukawa, H. Sarvotham, T. Kishino, N. Niikawa, E. Hidaka, T. Katsuyama, T. Higuchi, and J. Sagara. ASC, a novel 22-kDa protein, aggregates during apoptosis of human promyelocytic leukemia HL-60 cells. *J. Biol. Chem.*, 274(48):33835–33838, Nov 1999.

- [79] J. X. Lu, W. Qiang, W. M. Yau, C. D. Schwieters, S. C. Meredith, and R. Tycko. Molecular structure of α -amyloid fibrils in Alzheimer’s disease brain tissue. *Cell*, 154(6):1257–1268, Sep 2013.
- [80] V. Chevelkov, C. Shi, H. K. Fasshuber, S. Becker, and A. Lange. Efficient band-selective homonuclear CO-CA cross-polarization in protonated proteins. *J. Biomol. NMR*, 56(4):303–311, Aug 2013.
- [81] Yang Shen, Frank Delaglio, Gabriel Cornilescu, and Ad Bax. Talos+: a hybrid method for predicting protein backbone torsion angles from nmr chemical shifts. *Journal of Biomolecular NMR*, 44(4):213–223, 2009.
- [82] P. Emsley and K. Cowtan. Coot: model-building tools for molecular graphics. *Acta Crystallogr. D Biol. Crystallogr.*, 60(Pt 12 Pt 1):2126–2132, Dec 2004.
- [83] C. D. Schwieters, J. J. Kuszewski, N. Tjandra, and G. M. Clore. The Xplor-NIH NMR molecular structure determination package. *J. Magn. Reson.*, 160(1):65–73, Jan 2003.
- [84] T. Herrmann, P. Guntert, and K. Wuthrich. Protein NMR structure determination with automated NOE assignment using the new software CANDID and the torsion angle dynamics algorithm DYANA. *J. Mol. Biol.*, 319(1):209–227, May 2002.
- [85] A. Lu, V. G. Magupalli, J. Ruan, Q. Yin, M. K. Atianand, M. R. Vos, G. F. Schroder, K. A. Fitzgerald, H. Wu, and E. H. Egelman. Unified polymerization mechanism for the assembly of ASC-dependent inflammasomes. *Cell*, 156(6):1193–1206, Mar 2014.
- [86] A. Loquet, N. G. Sgourakis, R. Gupta, K. Giller, D. Riedel, C. Goosmann, C. Griesinger, M. Kolbe, D. Baker, S. Becker, and A. Lange. Atomic model of the type III secretion system needle. *Nature*, 486(7402):276–279, Jun 2012.
- [87] J. P. Demers, B. Habenstein, A. Loquet, S. Kumar Vasa, K. Giller, S. Becker, D. Baker, A. Lange, and N. G. Sgourakis. High-resolution structure of the Shigella type-III secretion needle by solid-state NMR and cryo-electron microscopy. *Nat Commun*, 5:4976, 2014.
- [88] Hlne Van Melckebeke, Christian Wasmer, Adam Lange, Eiso AB, Antoine Loquet, Anja Bckmann, and Beat H. Meier. Atomic-resolution three-dimensional structure of het-s(218289) amyloid fibrils by solid-state nmr spectroscopy. *Journal of the American Chemical Society*, 132(39):13765–13775, 2010. PMID: 20828131.
- [89] Sarah D. Cady, Klaus Schmidt-Rohr, Jun Wang, Cinque S. Soto, William F. De-Grado, and Mei Hong. Structure of the amantadine binding site of influenza M2 proton channels in lipid bilayers. *NATURE*, 463(7281):689–U127, FEB 4 2010.

- [90] Stefan Jehle, Ponni Rajagopal, Benjamin Bardiaux, Stefan Markovic, Ronald Kuehne, Joseph R. Stout, Victoria A. Higman, Rachel E. Klevit, Barth-Jan van Rossum, and Hartmut Oschkinat. Solid-state NMR and SAXS studies provide a structural basis for the activation of alpha B-crystallin oligomers. *NATURE STRUCTURAL & MOLECULAR BIOLOGY*, 17(9):1037–U1, SEP 2010.
- [91] Andi Mainz, Stefan Jehle, Barth J. van Rossum, Hartmut Oschkinat, and Bernd Reif. Large Protein Complexes with Extreme Rotational Correlation Times Investigated in Solution by Magic-Angle-Spinning NMR Spectroscopy. *JOURNAL OF THE AMERICAN CHEMICAL SOCIETY*, 131(44):15968+, NOV 11 2009.
- [92] J Pauli, B van Rossum, H Forster, HJM de Groot, and H Oschkinat. Sample optimization and identification of signal patterns of amino acid side chains in 2D RFDR spectra of the alpha-spectrin SH3 domain. *JOURNAL OF MAGNETIC RESONANCE*, 143(2):411–416, APR 2000.
- [93] M Hong and K Jakes. Selective and extensive C-13 labeling of a membrane protein for solid-state NMR investigations. *JOURNAL OF BIOMOLECULAR NMR*, 14(1):71–74, MAY 1999.
- [94] Vipin Agarwal, Susanne Penzel, Kathrin Szekely, Riccardo Cadalbert, Emilie Testori, Andres Oss, Jaan Past, Ago Samoson, Matthias Ernst, Anja Bckmann, and Beat H. Meier. Denovo 3d structure determination from sub-milligram protein samples by solid-state 100khz mas nmr spectroscopy. *Angewandte Chemie International Edition*, 53(45):12253–12256, 2014.
- [95] J Cavanagh, WJ Fairbrother, AG Palmer, M Rance, and NJ Skelton. *Protein NMR Spectroscopy: Principles and Practice, 2nd Edition.* , 2007.
- [96] SK Straus, T Bremi, and RR Ernst. Resolution enhancement by homonuclear J decoupling in solid-state MAS NMR. *CHEMICAL PHYSICS LETTERS*, 262(6):709–715, NOV 29 1996.
- [97] V Chevelkov, ZJ Chen, W Bermel, and B Reif. Resolution enhancement in MAS solid-state NMR by application of C-13 homonuclear scalar decoupling during acquisition. *JOURNAL OF MAGNETIC RESONANCE*, 172(1):56–62, JAN 2005.
- [98] L Duma, WC Lai, M Carravetta, L Emsley, SP Brown, and MH Levitt. Principles of spin-echo modulation by J-couplings in magic-angle-spinning solid-state NMR. *CHEMPHYSICHEM*, 5(6):815–833, JUN 21 2004.
- [99] L Duma, S Hediger, A Lesage, and L Emsley. Spin-state selection in solid-state NMR. *JOURNAL OF MAGNETIC RESONANCE*, 164(1):187–195, SEP 2003.

- [100] A Meissner, JO Duus, and OW Sorensen. Spin-state-selective excitation. Application for E.COSY-type measurement of J(HH) coupling constants. *JOURNAL OF MAGNETIC RESONANCE*, 128(1):92–97, SEP 1997.
- [101] Wolfgang Bermel, Ivano Bertini, Isabella C. Felli, Manolis Matzapetakis, Roberta Pierattelli, Elizabeth C. Theli, and Paola Turano. A method for C-alpha direct-detection in protonless NMR. *JOURNAL OF MAGNETIC RESONANCE*, 188(2):301–310, OCT 2007.
- [102] Rajendra Singh Thakur, Narayanan D Kurur, and PK Madhu. Swept-frequency two-pulse phase modulation for heteronuclear dipolar decoupling in solid-state nmr. *Chemical physics letters*, 426(4):459–463, 2006.
- [103] AJ Shaka, J. Keeler, and R. Freeman. Evaluation of a new broadband decoupling sequence: Waltz-16. *Journal of Magnetic Resonance (1969)*, 53(2):313–340, 1983.
- [104] W. Bermel, I. Bertini, I. C. Felli, R. Kummerle, and R. Pierattelli. Novel ¹³C direct detection experiments, including extension to the third dimension, to perform the complete assignment of proteins. *J. Magn. Reson.*, 178(1):56–64, Jan 2006.
- [105] Lyndon Emsley and Geoffrey Bodenhausen. Phase shifts induced by transient bloch-siegert effects in nmr. *Chemical Physics Letters*, 168(3):297–303, 1990.
- [106] V. Vijayan, J. P. Demers, J. Biernat, E. Mandelkow, S. Becker, and A. Lange. Low-power solid-state nmr experiments for resonance assignment under fast magic-angle spinning. *ChemPhysChem*, 10(13):2205–2208, 2009.
- [107] M. Schubert, T. Manolikas, M. Rogowski, and B. H. Meier. Solid-state nmr spectroscopy of 10% ¹³C labeled ubiquitin: spectral simplification and stereospecific assignment of isopropyl groups. *Journal of Biomolecular NMR*, 35(3):167–173, 2006.
- [108] B.H. Meier. Cross polarization under fast magic angle spinning: thermodynamical considerations. *Chemical Physics Letters*, 188(34):201 – 207, 1992.
- [109] S. Penzel, A. A. Smith, V. Agarwal, A. Hunkeler, M.-L. Org, Ago S., A. Böckmann, M. Ernst, and B. H. Meier. Protein resonance assignment at MAS frequencies approaching 100 kHz: a quantitative comparison of J-coupling and dipolar-coupling-based transfer methods. *Journal of Biomolecular NMR*, 2015.
- [110] Lyndon Emsley and Geoffrey Bodenhausen. Optimization of shaped selective pulses for nmr using a quaternion description of their overall propagators. *Journal of Magnetic Resonance (1969)*, 97(1):135–148, 1992.

- [111] Gaël De Paëpe, Józef R Lewandowski, Antoine Loquet, Anja Böckmann, and Robert G Griffin. Proton assisted recoupling and protein structure determination. *The Journal of chemical physics*, 129(24):245101, 2008.
- [112] Matthias Huber, Sebastian Hiller, Paul Schanda, Matthias Ernst, Anja Boeckmann, René Verel, and Beat H. Meier. A Proton-Detected 4D Solid-State NMR Experiment for Protein Structure Determination. *ChemPhysChem*, 12(5):915–918, April 2011.
- [113] Matthias Huber, Anja Bockmann, Sebastian Hiller, and Beat H. Meier. 4D solid-state NMR for protein structure determination. *Physical Chemistry Chemical Physics*, 14(15):5239–5246, 2012.
- [114] Donghua H Zhou, John J Shea, Andrew J Nieuwkoop, W Trent Franks, Benjamin J Wylie, Charles Mullen, Dennis Sandoz, and Chad M Rienstra. Solid-state protein-structure determination with proton-detected triple-resonance 3d magic-angle-spinning nmr spectroscopy. *Angewandte Chemie International Edition*, 46(44):8380–8383, 2007.
- [115] Jzef R. Lewandowski, Gal De Pape, Matthew T. Eddy, Jochem Struppe, Werner Maas, and Robert G. Griffin. Proton assisted recoupling at high spinning frequencies. *The Journal of Physical Chemistry B*, 113(27):9062–9069, 2009.
- [116] C. P. Jaroniec, C. Filip, and R. G. Griffin. 3D TEDOR NMR experiments for the simultaneous measurement of multiple carbon-nitrogen distances in uniformly ^{13}C , ^{15}N -labeled solids. *Journal of the American Chemical Society*, 124(36):10728–10742, 2002.
- [117] Marvin J Bayro, Galia T Debelouchina, Matthew T Eddy, Neil R Birkett, Catherine E MacPhee, Melanie Rosay, Werner E Maas, Christopher M Dobson, and Robert G Griffin. Intermolecular structure determination of amyloid fibrils with magic-angle spinning and dynamic nuclear polarization nmr. *Journal of the American Chemical Society*, 133(35):13967–13974, 2011.
- [118] T. Gullion, D. B. Baker, and M. S. Conradi. New, compensated carr-purcell sequences. *Journal of Magnetic Resonance (1969)*, 89(3):479–484, 1990.
- [119] T. Gullion and J. Schaefer. Rotational-echo double-resonance nmr. *Journal of Magnetic Resonance (1969)*, 81(1):196–200, 1989.
- [120] Karl T Mueller. Analytic solutions for the time evolution of dipolar-dephasing nmr signals. *Journal of Magnetic Resonance, Series A*, 113(1):81–93, 1995.

- [121] Ingo Schnell and Kay Saalwächter. ^{15}N - ^1H bond length determination in natural abundance by inverse detection in fast-magic-angle spinning solid-state NMR spectroscopy. *Journal of the American Chemical Society*, 124(37):10938–10939, 2002.
- [122] R. R. Ernst, G. Bodenhausen, A. Wokaun, et al. *Principles of nuclear magnetic resonance in one and two dimensions*, volume 14. Clarendon Press Oxford, 1987.
- [123] A.E. Bennett, R.G. Griffin, J.H. Ok, and S. Vega. Chemical shift correlation spectroscopy in rotating solids: Radio frequency-driven dipolar recoupling and longitudinal exchange. *The Journal of chemical physics*, 96(11):8624–8627, 1992.
- [124] M. Bak, J. T. Rasmussen, and N. C. Nielsen. Simpson: A general simulation program for solid-state {NMR} spectroscopy. *Journal of Magnetic Resonance*, 147(2):296 – 330, 2000.
- [125] Lewis E Kay, Mitsuhiro Ikura, Rolf Tschudin, and Ad Bax. Three-dimensional triple-resonance {NMR} spectroscopy of isotopically enriched proteins. *Journal of Magnetic Resonance (1969)*, 89(3):496 – 514, 1990.
- [126] M Baldus, RJ Iulucci, and BH Meier. Probing through-bond connectivities and through-space distances in solids by magic-angle-spinning nuclear magnetic resonance. *Journal of the American Chemical Society*, 119(5):1121–1124, 1997.
- [127] Ronald A. Venters, Bennett T. Farmer II, Carol A. Fierke, and Leonard D. Spicer. Characterizing the use of perdeuteration in {NMR} studies of large proteins: ^{13}C , ^{15}N and ^1H assignments of human carbonic anhydrase {II}. *Journal of Molecular Biology*, 264(5):1101 – 1116, 1996.
- [128] Yang Shen and Ad Bax. Protein backbone chemical shifts predicted from searching a database for torsion angle and sequence homology. *Journal of biomolecular NMR*, 38(4):289–302, 2007.
- [129] Matthias Huber, Oliver With, Paul Schanda, René Verel, Matthias Ernst, and Beat H. Meier. A supplementary coil for ^2H decoupling with commercial HCN MAS probes. *Journal of magnetic resonance*, 214:76–80, January 2012.
- [130] I. Bertini, L. Gonnelli, C. Luchinat, J. Mao, and A. Nesi. A new structural model of A40 fibrils. *J. Am. Chem. Soc.*, 133(40):16013–16022, Oct 2011.